Universität Bonn

Physikalisches Institut

Single-top production t-channel cross section measurement in the electron+jets final state at ATLAS with 35 pb^{-1}of data

Gia Khoriauli

The cross section of the Standard Model electroweak production of a single top quark in the t-channel has been measured using the LHC proton-proton collision data at $\sqrt{s} = 7$ TeV, 35 pb^{-1} of integrated luminosity, recorded by the ATLAS detector during the year 2010. The measurement has been based on a selection of the collision events with an electron and one b-tagged hadronic jet in the central region of the detector and one extra jet in the forward region of the detector. These requirements are dictated by the topology of the final state particles in the t-channel process. They helped to optimize an expected fraction of the t-channel process, according to a study based on Monte-Carlo simulation, in the selected events and suppress the contribution of the background processes. The main background processes such as production of hadronic jets via the strong interaction and production of a single W boson with associated hadronic jets are measured by means of data driven methods developed in this work. The measured cross section of single top quark production in the t-channel process is 59 $^{+44}_{-39}$(stat.) $^{+63}_{-39}$(syst.) pb. The measured upper limit on the cross section is 226 pb at the 95% confidence level. The results are in agreement with the latest theoretical prediction of the t-channel cross section of the Standard Model production of a single top quark calculated at NNLO, 64.6 $^{+3.3}_{-2.6}$ pb, considering $m_{t\text{-quark}} = 172.5$ GeV.

Universität Bonn

Physikalisches Institut

Single-top production t-channel cross section measurement in the electron+jets final state at ATLAS with 35 pb^{-1}of data

Gia Khoriauli

Acknowledgements

Contents

Chapter 1

Introduction

Top quark physics is one fundamental section of contemporary high energy physics (HEP). The top quark production in collisions of high energy elementary particles via the electroweak interaction that is usually called the single-top production is one of the interesting fields of the top quark physics awaiting in-depth experimental exploration. The subject of this thesis is a measurement of the cross section of one of the physics channels of the single-top production in high energy proton-proton collisions. The details of this measurement as well as the theory background and its importance for new physics searches will be discussed in this document.

The successful start of the Large Hadron Collider (LHC) [1] machine at CERN (Switzerland) in late 2009 offered a unique opportunity to advance the frontiers of many interesting fields of HEP including top quark physics. The unique opportunity is opened up due to the energy reached in interactions between elementary particles. The key argument of the motivation for increasing the interaction energy in HEP experiments is that the physics laws that are already known today might be just some low energy projections of more general and fundamental laws of physics that manifest themselves in high energy interactions. Theories that predict some new physics phenomenon, normally also provide some estimate of the energy scale at which the phenomenon would become important.

Besides the energy scale, the luminosity of collider experiments plays an important role in HEP studies, since results of these studies are statistical inferences made from data considering also the theoretical and the instrumental systematic uncertainties of the performed measurements. Thus, large amount of data collected during the LHC operation time will help to perform precise measurements.

The designed energy of the proton beams that are accelerated by the 27 kilometers accelerator ring of the LHC is 7 TeV [1], which allows to have 14 TeV center-of-mass energy (c.m.) in proton-proton collisions. This is a by almost one order of magnitude higher scale with respect to the energy scale of the TEVATRON [2] hadron collider facility operated until 2011 at Fermilab (USA). The designed high rate of the proton-proton collisions at the LHC is determined by the crossing rate of oppositely moving proton bunches at particular collision points that happen once in every 25 ns. This rate is obtained by means of a high number of proton bunches accelerated through the LHC ring, considering of 2808 bunches per beam. Taking the geometrical structure of the proton bunches and the average number of protons per bunch into account, the nominal instantaneous luminosity of the LHC is 10^{34} cm^{-2}s^{-1}. The LHC gradually improves its performance to reach the nominal operation conditions. The intermediate steps were and are still necessary in increasing of the beam energy and intensity. The presented study used data, which was collected during the LHC operation period in 2010

---

[1]For expressing values of the energy and momentum the HEP natural units system is used in the document, while space and time variables are given in SI units. All physics expressions are given in HEP natural units as well.

with 3.5 TeV energy per beam and with varying instantaneous luminosity by $10^7 - 10^2$ times lower than the nominal value. The integrated luminosity of data collected by the ATLAS (A Toroidal LHC Apparatus) detector [3] that is used in this study is 35 pb^{-1}.

ATLAS is one of the major experiments, which uses the proton beams of the LHC to collect high energy collision data. The detector is a complex system of various sub-detectors, the magnet system and the supporting infrastructure. It is built to record large multiplicity of high energy leptons and hadrons created in the proton-proton collisions. It is designed for many years of operation with the intermediate upgrades of the sub-systems.

The ATLAS experiment has a rich list of physics goals. Perhaps, the most interesting and fundamental question that it should answer together with another LHC experiment, CMS [4, 5], is whether the Standard Model (SM) [6–8] Higgs mechanism [9–11] of the mass generation for elementary particles is realized in nature. The mechanism predicts the existence of heavy spin-less Higgs boson. It is the only unobserved particle predicted by the SM. The possible discovery of the Higgs boson would be a real success of this theory.

The SM is a theory of the basic building blocks of the micro-universe and has been, to a large extent, experimentally proven. It is a combined model of the quantized gauge theories, which describe the unified electromagnetic and weak interactions (electroweak) and the strong interaction in a frame of Lagrangian formalism of gauge fields. The building units of the SM Lagrangian are the quantum operators of the matter and the gauge fields and the coupling constants. The quanta of matter fields represent the known fermion particles, quarks and leptons. The quantized gauge fields are included in the theory in order to keep the Lagrangian invariant under local gauge transformations [2] of the matter fields. This means the SM Lagrangian has a certain symmetry group of gauge transformations, which is SU(3)$_C \otimes$SU(2)$_L \otimes$U(1)$_Y$. The construction of the SM Lagrangian invariant to the SU(3)$_C \otimes$SU(2)$_L \otimes$U(1)$_Y$ gauge symmetry group is dictated by the nature of the existing fundamental interactions. In general, the gauge invariance requirement introduces a coupling of matter fields with gauge fields introducing the coupling constants.

SU(2)$_L \otimes$U(1)$_Y$ and SU(3)$_C$ correspond to the unified electroweak interaction and the strong interaction respectively. The number of gauge quanta, called vector bosons, that arise in a gauge theory is equal to the number of generators of the symmetry group of the theory and is $n^2 - 1$, where n is the dimension of the symmetry group. The strong (color) interaction, which acts only in the quark sector of fermions, treats a quark as a color triplet and therefore, the dimension of the symmetry group that is needed to describe the strong interaction is 3. This leads to the 8 massless vector bosons, g (gluons), of the corresponding SU(3)$_C$ gauge symmetry group, which mediate the strong interaction between the quarks. The corresponding part of the SM, which describes the strong interaction is called Quantum Chromodynamics (QCD) [12–17].

The unified electroweak interaction involves the whole fermion sector of elementary particles, quarks and leptons. The weak interaction has a specific (chiral) structure. It treats the matter fields as left-handed and right-handed and the gauge transformations of those are different. The left-handed particles make weak isodoublets and the corresponding gauge symmetry group is SU(2)$_L$. The right-handed particles are weak isosinglets of the SU(2)$_L$ symmetry group. There are three families of quark weak isodoublets consisting of up- and down-

---

[2]This is a rather general requirement to the quantum system Lagrangian meaning that the whole physics picture has to be independent of the choice of the local coordinate basis at each point of the gauge space.

Table 1.1: Three generations of quarks and leptons. Their electric charge and measured masses are provided [25].

Generation	Quarks			Leptons		
	Symbol	Charge	Mass [MeV]	Symbol	Charge	Mass [MeV]
1	u	$+2/3$	1.7 to 3.1	ν_e	0	$< 2 \cdot 10^{-6}$
	d	$-1/3$	4.1 to 5.7	e^-	-1	0.51
2	c	$+2/3$	$(1.18 \text{ to } 1.34) \cdot 10^3$	ν_μ	0	< 0.19
	s	$-1/3$	80 to 130	μ^-	-1	105.7
3	t	$+2/3$	$(172.9 \pm 0.6 \pm 0.9) \cdot 10^3$	ν_τ	0	< 18.2
	b	$-1/3$	$(4.13 \text{ to } 4.37) \cdot 10^3$	τ^-	-1	1777

flavor quarks and three families of lepton weak isodoublets consisting of charged leptons and corresponding neutrinos. The electroweak symmetry group $SU(2)_L \otimes U(1)_Y$ introduces $3 + 1$ gauge fields. The quanta of the electroweak gauge fields, vector bosons, are massless in order to keep the electroweak Lagrangian gauge invariant. This is in contradiction with the experimental fact that the weak interaction is a short-range interaction and therefore, its carrier particles should have non-zero masses. This problem is solved by means of the Higgs mechanism. In this mechanism, a weak isodoublet of a complex scalar field is added to the electroweak Lagrangian. One component of this field is made to acquire a non-zero vacuum expectation value (spontaneous symmetry breaking) that leads to three non-zero mass combinations of the electroweak vector bosons, one massless combination and one massive scalar particle, the Higgs boson. The arisen massive vector bosons are the $W^\pm$ and Z particles and the fourth massless vector boson is the photon, γ. The $W^\pm$ bosons couple only with the left-handed weak isodoublets of quarks and leptons. Other vector bosons, Z and γ, and the scalar Higgs boson couple to both left-handed weak isodoublet and right-handed weak isosinglet fermion fields.

Fermions are also massless before the spontaneous symmetry breaking due to the gauge invariance of the electroweak Lagrangian. The Yukawa coupling [18, 19] terms of the Higgs field with the fermion fields, which are added to the electroweak Lagrangian in the gauge invariant way, are responsible for the generation of fermion masses.

The fourth known type of fundamental interactions, gravity, is not included in the SM formalism. However, gravity, due to its weakness with respect to other interactions, has negligible impact on the theoretical calculations relevant to our study and therefore, is neglected.

Discovery of the top quark in 1995 [20, 21] completed the third family of the strongly interacting sector of the known elementary particles, the quarks. Later, in 2000, the third family of the electroweakly interacting elementary particles, the leptons, was completed [22] with the missing member, the tau neutrino. These discoveries were a great success of the SM, which have required the existence of the top quark and the tau neutrino after the first members, the bottom quark and the tau lepton, of the third family quarks and leptons were found [23, 24]. Table 1.1 presents all three generation fermions, their electric charges and the experimentally measured masses. Table 1.2 presents the vector bosons and the scalar Higgs boson.

In order to account for the fact that fermion flavors are interchanged between the different generations via the electroweak interaction, a mixing mechanism is included in the SM Lagrangian. In the quark sector the Cabibbo-Kobayashi-Maskawa (CKM) 3×3 complex unitary

Table 1.2: Gauge vector and Higgs bosons. Their electric charge and measured masses presented in GeV units, except of the gluon mass, which is a theoretical value, are provided [25].

Symbol	g	γ	Z	W^+	W^-	H
Charge	0	0	0	$+1$	-1	0
Mass [GeV]	0	0	91.1876 ± 0.0021	80.399 ± 0.023		n/a

matrix describes the mixing of the down-type quarks [26, 27] in the electroweak interactions,

$$\begin{pmatrix} d' \\ s' \\ b' \end{pmatrix}_L = \mathbf{V} \begin{pmatrix} d \\ s \\ b \end{pmatrix}_L = \begin{pmatrix} V_{ud} & V_{us} & V_{ub} \\ V_{cd} & V_{cs} & V_{cb} \\ V_{td} & V_{ts} & V_{tb} \end{pmatrix} \begin{pmatrix} d \\ s \\ b \end{pmatrix}_L \qquad (1.1)$$

The up-type quark couples (via the charged vector bosons, $W^{\pm}$) with the down-type quark of the same generation, which is a mixture of all down-type quarks. The strength of the coupling with the specific up-type quark and the down-type quark flavors is proportional to the corresponding CKM matrix element. It is experimentally known that the diagonal elements of the CKM matrix have the largest values [28]. This means that quarks prefer to couple within the same family. The interesting consequence is that the top quark prefers to decay into a bottom quark and a W boson via the electroweak $W - t - b$ vertex and can be produced via this vertex in high energy collisions. This is the SM mechanism of the single-top production that was already mentioned.

The top quark has the largest mass among all SM particles [3] and is about 40 times larger than the bottom quark mass. This significant difference from other fermion masses has some important consequences in the SM theory. It has a large impact on the precise calculations of the electroweak processes via loop corrections. In particularly, it makes the theoretical prediction of the Higgs boson mass very sensitive to the precise value of the top quark mass [29]. The Higgs boson is expected to couple with the top quark stronger than with other fermions due the large mass of the top quark. This makes it possible to search for the associated production of a Higgs boson with top quarks in proton-proton collisions [30, 31]. In contrast to other quarks the top quark decays via the weak interaction before hadronization due to its large mass. This allows to measure its mass and charge directly from its decay products as well as to test the chiral structure of the weak interaction in the quark sector. This later phenomenon is in a tight relationship with the single-top physics and related searches for an evidence for new physics.

The pair production of a top quark and its antiparticle (referred as top-pair or $t\bar{t}$) is mediated by the strong interaction and has high enough cross section at the LHC c.m. energies. Due to the high c.m. energy in the proton-proton collisions at the LHC, the necessary fraction of the proton momentum, x, that is needed to produce two top quarks, is relatively smaller for the colliding constituent partons (quarks, gluons) of the protons. The parton distribution function (PDF) [32] of gluons gets larger than PDFs of quarks for low x values. Therefore, the cross section of the top-pair production is enhanced due to the large contribution of the gluon-gluon fusion. The ATLAS experiment measured the top-pair production cross section

---

[3]The latest studies of the ATLAS and CMS experiments indicate that the Higgs boson mass should be close to 125 GeV if it exists at all.

using $35\,\mathrm{pb}^{-1}$ of recorded data [33], which has shown an agreement with the SM prediction.

The total cross section of all three channels (see Chapter 2) of the SM single-top production, t-channel [34–42] , s-channel [43–47] and the W associated production (Wt-channel) [48–54], is roughly two times smaller (see Table 2.1) than the cross section of the top-pair production [55] for 7 TeV c.m. energy proton-proton collisions at the LHC. The largest cross section among the three channels belongs to t-channel. *The goal of the following study is to measure the t-channel cross section and thus, test the validity of the electroweak SM in the heaviest quark sector.* The measurement is based on a selection of t-channel events with a single high energy electron. We do not use events with muons in the measurement. The reason is that the muon final state is expected to have different background content and kinematics than the electron final state. In this work we developed a measurement of the background specific for the electron final state. A central requirement of the t-channel signal selection is the presence of a b-flavored hadronic jet in the candidate events. The selection requirements are based on the expected topology of the t-channel events in order to minimize any bias due to the contribution of the background processes. The main SM background processes to the single-top production are the top-pair and single W boson production in association with hadronic jets (W+jets). Due to the presence of a W boson in these background processes, they have the same high energy electron signature of the signal. Moreover, given that they have significantly larger cross sections than t-channel, especially W+jets, the rate of the selected background events can be rather high. Another important SM background process is the production of hadronic jets via the strong interaction (QCD multi-jets). Due to the small but non-zero probability that the hadronic jet can be reconstructed as an electron in the ATLAS detector, fake QCD multi-jets events can mimic the t-channel signal. The small probability of selection of a fake electron event is contrasted with the QCD multi-jets production cross section several orders of magnitude higher than the t-channel cross section. Therefore, the fake electron background becomes important to the measurement. Realistic Monte-Carlo simulation of the signal and background processes in the ATLAS detector as well as auxiliary measurements are needed to make reliable predictions for both signal and background event yields. The signal measurement precision in data crucially depends on the precision of these predictions. Figure 1.1 shows the predicted inclusive cross sections and the corresponding event rates of the SM heavy flavor quark and vector boson productions as a function of the c.m. energy of collisions at the typical instantaneous luminosities of the LHC and the TEVATRON. The exclusive cross sections of the light QCD multi-jets production with kinematic requirements on the transverse energy of the hardest jet are also presented. The SM Higgs boson inclusive production cross section is presented for two different assumed Higgs boson masses. The gaps between some of the TEVATRON and the LHC cross section curves at the same c.m. energy are due to the different colliding beams used. The TEVATRON was operated with proton and anti-proton beams.

The document consists of eight remaining chapters. In Chapter 2 the theoretical models and predictions of the single-top production in hadron-hadron collisions are discussed. The SM mechanism of the different channels of single-top production is described. The second part of Chapter 2 is dedicated to the review of the theoretical models of new physics that can have experimentally observable effects on the single-top production rates at the LHC. It is shown that the different channels have different sensitivity to various types of predicted new physics models. This makes a study of the single-top production channels a powerful test of the SM. Deviations from the SM predictions will provide information about the underlying

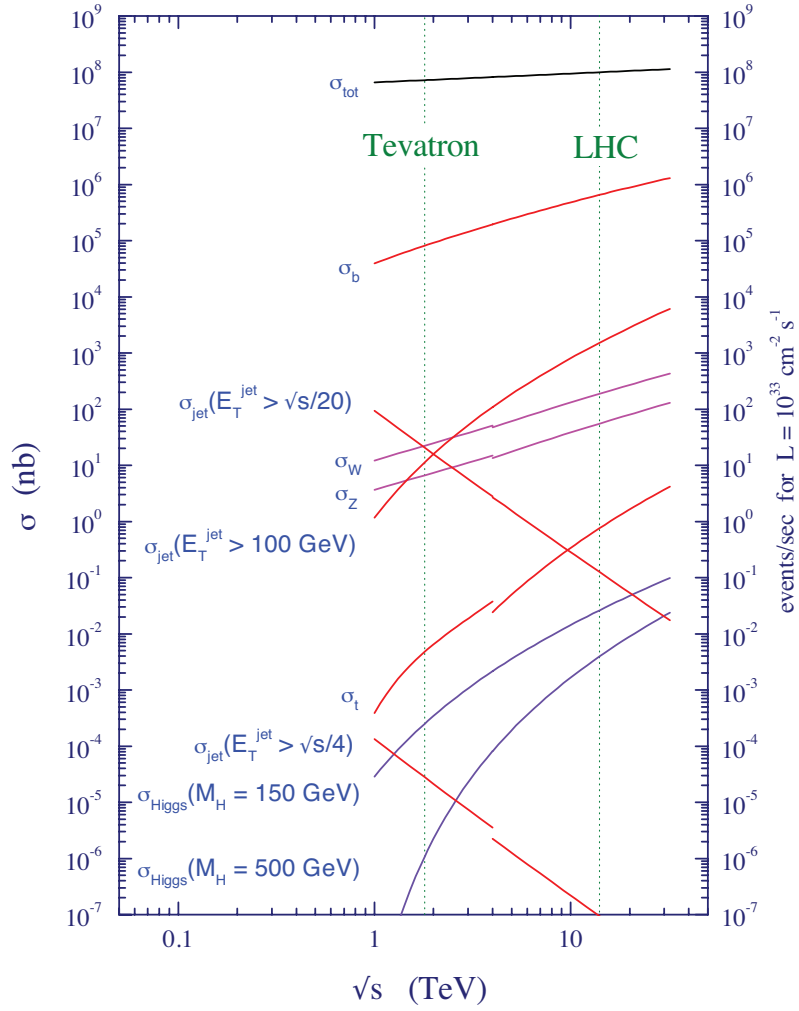Figure 1.1: Dependence of the theoretical cross sections of different physics processes of the Standard Model on the c.m. energy of colliding proton-proton (at LHC) or proton-antiproton (at TEVATRON) beams. The left ordinate represents a cross section, while the right one represents the event production rate per second given a typical operation value of the instantaneous luminosity of the LHC and the TEVATRON.

new physics phenomena.

Chapter 3 provides a description of the ATLAS detector. Geometrical configurations, functionality principles and performance of each sub-detector and the integrated system of magnets are presented. The trigger system and the data acquisition scheme of the ATLAS detector is also described.

Details of the data collected and used in this study are presented in Chapter 4. The overview of the Monte-Carlo model of the ATLAS experiment is provided as well. Monte-Carlo simulation samples of the signal (t-channel) and background processes used in this study are introduced.

Chapter 5 describes the first step of the physics analysis that is the selection of the reconstructed physics objects in both data and Monte-Carlo simulated events. Selection details of each physics object such as electrons, muons, hadronic jets, b-tagged hadronic jets and the missing transverse energy are discussed. Our study is based on these objects. The selection is optimized for the t-channel analysis.

Chapter 6 provides the details of the event selection optimization. The t-channel event topology in terms of the expected multiplicities of the different physics objects and the distributions of the kinematic variables was exploited in order to reach an optimal expected signal to background ratio. Monte-Carlo simulated samples of the t-channel signal and its SM background processes are used in the optimization study.

Chapter 7 describes the details of the data driven measurement of the QCD multi-jets and W+jets background. In spite of using the Monte-Carlo simulated samples for the W+jets production process, its contribution to the final selection has to be measured using data itself. The reason is that the heavy flavored content (hadronic jets initiated with c- and b-quarks) of the W+jets production is not well understood in the existing models of Monte-Carlo simulation. A new data driven method is developed that allows to measure the QCD multi-jets and W+jets background.

Predictions for the selected signal and background event yields have uncertainties due to various reasons. Chapter 8 reviews the sources of these systematic uncertainties.

Chapter 9 provides a description of the statistics methods used in the study for the t-channel cross section measurement. The measurement is done in the frame of an unbinned maximum likelihood. It is performed considering all systematic uncertainties on the event yields. For this goal, the profiling method of the maximum log-likelihood ratio is employed. An upper limit on the t-channel production cross section is also estimated. A dependence of the t-channel cross section measurement on the expectation of the cross section of the W associated production, which is a not yet discovered process, is explored. A summary of the results completes Chapter 9.

Chapter 2

Single-top production in proton-proton collisions

An overview of the theoretical aspects of the single-top production mechanism in the SM is given in the following chapter. The characteristics of three distinct production channels in proton-proton collisions are discussed. The results of the theoretical calculations of cross sections of these channels are provided. Also, the possible non SM physics processes that might influence the single-top production at the LHC are reviewed. New physics can affect cross sections of the different single-top channels in different ways, which depend on the exact type of a new phenomenon. Thus, the precise measurement of the cross sections of the single-top channels at the LHC experiments is important. Deviations from the SM predictions can be linked to the presence of the new physics.

2.1 Standard Model single-top processes

In the SM the top quark interacts with the down-type quarks via the $SU(2)_L$ charged gauge boson $W^\pm$. Only the left-chiral components of the quark fields participate in this interaction, which means the interaction vertex, $W - t - q$, has the vector-minus-axial-vector (V-A) structure and is described by the expression $-i\frac{g}{2\sqrt{2}}V_{tq}\gamma^\mu(1 - \gamma_5)$. Here, g is the electroweak coupling constant, V_{tq} ($q = d, s, b$) is the CKM matrix element and $\gamma^\mu(1 - \gamma_5)$ is the V-A structure constructed with the Dirac matrices, γ. The amplitude of this interaction, which is also known as the charged-current (CC) weak interaction is proportional to V_{tq}.

The CC weak interaction is responsible for decay of the top quark as well as for the single-top production. Both partial decay widths and the production cross section of single-top via the CC weak interaction are proportional to $|V_{tq}|^2$. Indirect measurements point that V_{td} and V_{ts} are small numbers of the orders of 10^{-3} and 10^{-2} respectively [28]. Then considering the CKM matrix unitarity condition, $|V_{td}|^2 + |V_{ts}|^2 + |V_{tb}|^2 = 1$, under the assumption of the existence of only three fermion families, we have that $|V_{tb}| \sim 1$. Therefore, the main decay mode as well as the single-top production mode is via the $W - t - b$ vertex.

From the theoretical or physics analysis point of view it is convenient to distinguish the SM single-top production in three channels according to the virtuality of the involved W boson. Single-top production in t-channel proceeds with the space-like ($q_W^2 < 0$) W boson exchange between a light quark and a b-quark of the colliding protons resulting in the production of an on-shell top quark and light quark [1] pair (see Figure 2.1a). The s-channel production implies the process of different flavor quark and anti-quark pair annihilation into a time-like ($q_W^2 > 0$) W boson, which produces a pair of on-shell top and bottom quarks (see Figure 2.1b).

---

[1]Under 'light' the u, d, c and s quarks are assumed.

The third process, an associated W production has the W boson as a final on-shell ($q_W^2 = 0$) particle produced along a final top quark. Its amplitude is the sum of a t-channel and an s-channel Feynman diagram (see Figure 2.2), when in the first case the space-like top quark from a gluon splitting interacts with a bottom quark producing the on-shell W boson and in the second case the time-like b-quark is the propagator.
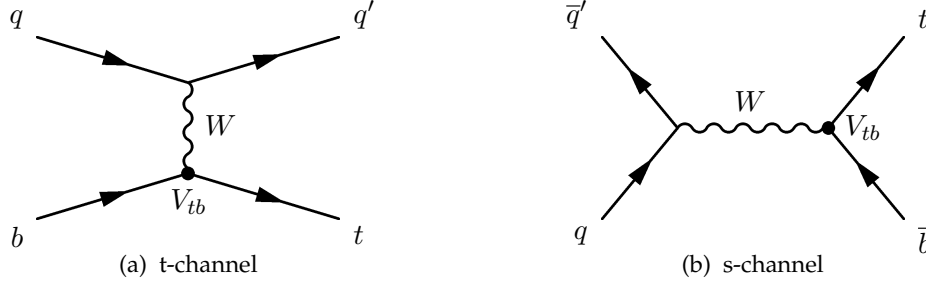
Figure 2.1: Tree level Feynman diagrams of t-channel (left) and s-channel (right) production of single-top.
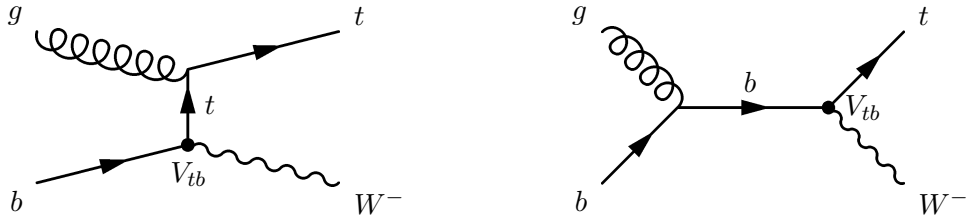
Figure 2.2: Tree level Feynman diagrams of the Wt associated production of single-top.

Due to the W propagator the t-channel differential cross section is proportional to $1/(q_W^2 - m_W^2)^2$. Since $q_W^2 < 0$ the differential cross section is larger in the kinematic region of low absolute value of q_W leading to the total cross section to be proportional to $1/m_W^2$. This fact is (partially) responsible that the t-channel cross section, which is of the order α_W^2 is comparable to the top quark pair production cross section, which is proportional to α_s^2 but scales as $1/4m_t^2$. Here, $\alpha_W \cong 1/127$ is the running electroweak coupling constant calculated at the W mass and $\alpha_s \sim 0.1$ is the strong interaction constant [2].

The spectator light quark created in the t-channel process, which can have rather high momentum, normally has a low transverse momentum. This is the consequence of the fact that the t-channel cross section is dominated by the kinematic region with small $|q_W^2|$. As we will see later, this feature of the spectator quark plays an important role for the identification of the single-top t-channel process (see Chapter 6).

The s-channel cross section is of the order α_W^2 similar to the t-channel cross section although it scales as $1/s$ and therefore, is much smaller at the LHC than the t-channel cross section. The Wt-channel cross section has higher order than the other channels, $\alpha_s\alpha_W$, since it involves a strong interaction vertex. However, the Wt-channel has two massive, on-shell final particles and thus, its production requires the higher kinematic region (momentum fractions, x, of the interacting partons) than the t-channel production. Therefore, at the LHC the Wt-channel

---

[2]It is calculated on a squared value of the transfered momentum that is typical to a given process. In case of the top quark pair production the typical transfered momentum is the two times top quark mass.

cross section is a few times smaller than the t-channel cross section. This can be seen in Figure 2.3, which shows a depndence of the NLO cross sections of all three channels of the SM single top production on the c.m. energy of proton-proton collisions calculated using the MCFM tool [56].
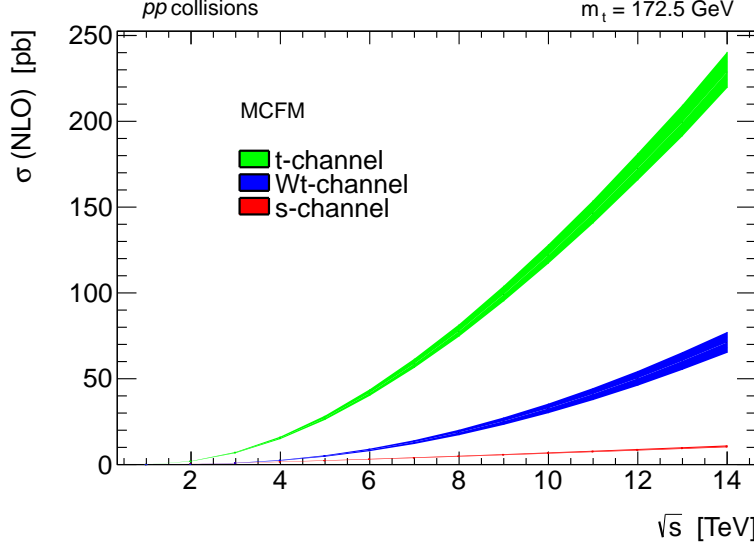
Figure 2.3: Dependence of the NLO cross sections of the single top production channels on the c.m. energy of proton-proton collisions. The cross sections are calculated using the MCFM tool and assuming $m_{t\text{-quark}} = 172.5\,\text{GeV}$.

Single-top production t-channel and Wt-channel imply an initial b-type quark (see Figure 2.2 as an example) interacting with other particles via the weak or the strong vertex. The origin of the b-type quarks is gluon splitting into a virtual $b\bar{b}$ pair as it is shown on the Feynman diagram of the t-channel process in Figure 2.4. The gluon splitting mechanism is responsible for the existence of the c- and s-type quarks in protons. The differential cross section of the process drawn in the diagram is higher when the $\bar{b}$-quark is more collinear to the initial gluon and asymptotically diverges if the mass of b-quark is taken as zero. This divergence is regulated by the b-quark mass and the resulting total cross section is of the order $\alpha_s \ln(m_t^2/m_b^2)$. Any additional gluon emission process adds contributions to the total cross section proportional to the higher powers of $\alpha_s \ln(m_t^2/m_b^2)$ (collinear logarithms). Thus, $\alpha_s \ln(m_t^2/m_b^2)$ serves as the expansion variable for the perturbative approach of the cross section calculation. Considering $m_t \approx 170\,\text{GeV}$, $m_b \approx 4\,\text{GeV}$ and $\alpha_s \approx 0.1$ the expansion parameter is roughly equal to 1 that makes the perturbative calculations irrelevant. An analytical summation of the collinear logarithms of any orders is possible by Dokshitzer-Gribov-Lipatov-Altarelli-Parisi (DGLAP) equations [57–59]. This leads to the introduction of the PDF of the b-quark, which includes the logarithmic terms summed at all orders when calculating cross sections. If the $b\bar{b}$ pair is not collinear, then its contribution in the total cross section is calculated using the perturbative approach.

Both t-channel and s-channel are produced with different amounts of t-quark and $\bar{t}$-quark in proton-proton collisions due to the higher probability to pick-up u-quark or d-quark than their antiparticles. For instance, the charge conjugated process to the process shown in Figure 2.1a is $\bar{u}\bar{b} \to \bar{d}\bar{t}$ and it has a smaller cross section due to the smaller probability to find $\bar{u}$-quark
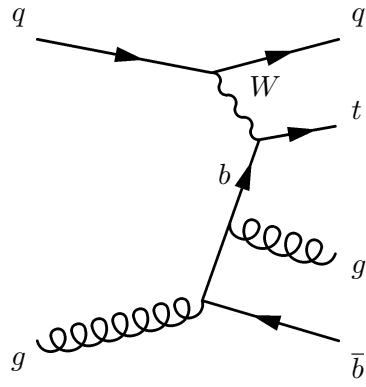
Figure 2.4: t-channel Feynman diagram of t-channel with initial gluon splitting into a virtual $b\bar{b}$ pair. Possible gluon emission from the virtual b-quark is included in the diagram.

rather than u-quark in the colliding protons. Since b-quark and $\bar{b}$-quark arise from gluon splitting, they have the same probability to enter into an interaction. This determines that the charge of the final state top quarks in Wt-channel production is symmetric.

Theoretical calculations of the single-top production cross sections for all three channels exist at the next-to-leading order (NLO) level [60–63]. Calculations of the higher order corrections to the cross section beyond NLO also exist at next-to-next-to-leading-logarithm resummation of soft gluon loops [42, 47, 54]. Figure 2.5 presents the t-channel production NNLL cross sections [42] at the LHC. The NNLO cross sections at 7 TeV for the top quark mass 172.5 GeV are summarized in Table 2.1 including the top quark pair production [55].
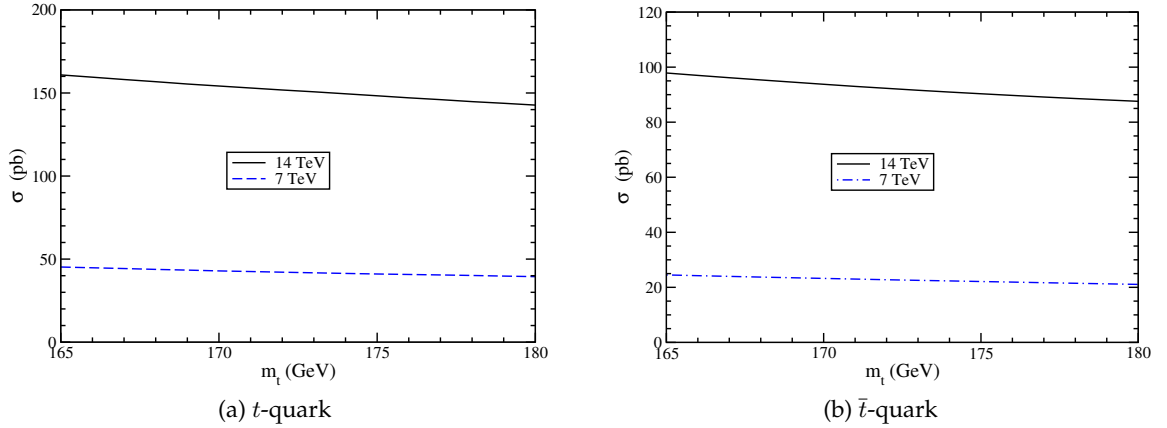
(a) t-quark

(b) $\bar{t}$-quark

Figure 2.5: Single-top production t-channel cross section at the NNLL level for 7 TeV and 14 TeV in proton-proton collisions as a function of the top quark mass. The left plot presents the cross section of the t-quark production and the right one corresponds to the $\bar{t}$-quark production [42].

Top quarks decay due to the CC interaction in much shorter time than is needed for hadronization. Measuring V_{tq} in the top quark decay is a rather challenging experimental exercise. The reason is that the existing experiments are able to identify top quark production events in the Wb decay mode only [3], while distinguishing the other decay modes is much more diffi-

---

[3]Hadronic jets b-tagging is used for this goal.

Table 2.1: Single-top production cross sections for three different channels calculated at NNLL [42, 47, 54]. The top quark pair production cross section calculated at approximate NNLO [55] is also provided for comparison. The values are given in pico-barns.

t-channel	s-channel	Wt-channel	top-pair
$64.57^{+3.32}_{-2.62}$	$4.63^{+0.29}_{-0.27}$	$15.74^{+1.34}_{-1.36}$	$166.8^{+16.5}_{-17.8}$

cult. The D0 and CDF experiments estimated lower limits on $|V_{tb}|$ by measuring the branching ratio $R = (t \to Wb)/(t \to Wq) = |V_{tb}|^2 / \sum_{q=d,s,b} |V_{tq}|^2$. The measurements assumed the unitarity of the CKM matrix and the existence of only three fermion generations. The results for the lower limit of $|V_{tb}|$ are $|V_{tb}| > 0.89$ [64] and $|V_{tb}| > 0.78$ [65] reported by D0 and CDF respectively. The only known way to directly estimate $|V_{tb}|$ without appealing to the CKM matrix unitarity is to measure the cross sections of the single-top production channel(s). The averaged result from D0 [66] and CDF [67, 68] is $|V_{tb}| = 0.88 \pm 0.07$, which is consistent with the above results obtained by studying the top quark decay modes.

All CKM elements are estimated by various measurements. The results are used for a global fit of the SM parameter space [28]. The fit result is $|V_{tb}| = 0.999152^{+0.000030}_{-0.000045}$. In the next section we will see how the measurement of cross sections of all three single-top channels can be linked to new physics. If precise measurements of all channels have smaller cross sections than predicted by the SM this would mean that V_{tb} is significantly less than 1. This would leave room for the 4th generation quarks, still preserving the CKM matrix unitarity.

2.2 Single-top production/physics beyond the Standard Model

Precise measurements of cross sections of single-top production channels can serve as powerful tests for new physics. The possible effect of new physics phenomena can be a modification of the $W - t - b$ weak interaction vertex by introducing some additional non-SM coupling between the top quark and other SM particles. Or it can be an effect of a coupling of the top quark with a new particle or particles. Depending on the exact type of the new phenomenon it would have different effects on the different single-top production channels. These possible effects will also influence the top quark decay width. Although the top quark decay width is rather large, which determines its fast decay, it is still smaller than the experimental resolution in the existing hadron-hadron collision experiments. In general, if new physics appears at some energy scale Λ, its effect on the single-top production would scale as $(\sqrt{s}/\Lambda)^n$, where n is some natural number [69]. In contrast, the same effect in the top quark decay would scale as $(m_t/\Lambda)^n$. At the LHC, $\sqrt{s}$ can be much larger than the top quark mass and the relative effect of the new physics can be much more enhanced in the production of the top quark than in its decay.

New physics can be directly observed in case its characteristic energetic scale Λ is lower than the c.m. energy of an experiment [4]. If this is not the case, then the place where to search for its evidence is the SM couplings between the SM particle fields and gauge bosons. The run-

---

[4]Assuming the possible new particle(s) and/or interaction(s) couple(s) with the existing elementary particles.

ning coupling constants are sensitive (e.g. via the higher order corrections with new particle loops) to the new physics that depends also on the type of the new phenomenon. It can be shown [70–74] that provided that $\sqrt{s} < \Lambda$, then any new physics effect can be parameterized by adding the high ($n \geq 4$) mass dimension gauge invariant terms to the SM Lagrangian. These terms modify the production rates of the different SM processes that can be searched on experiments independently of the particular model of underlying new physics. Due to the large mass of the top quark, the physics processes, which involve the top quark production are expected to be sensitive to new physics. The higher dimension terms of the effective Lagrangian change the coupling strength (anomalous coupling) at the SM vertices like $W - t - b$ and also, introduce new interaction vertices with flavor changing neutral currents (FCNC). FCNC is not possible in the SM at the tree level, the quark flavors are changed only by the weak charged current mediated with $W^\pm$. It is possible via loop diagrams involving a virtual W boson but the corresponding amplitudes are strongly suppressed. For instance, the SM prediction of the branching fractions for $t \to cZ$ is of the order 10^{-12} [75]. Various models of new physics can lead to an excess in the strength of the FCNC vertex also involving the top quark production. Existence of new scalar fields [76–78] or new exotic quarks [79] as well as supersymmetry [80–84] and technicolor [85] theories predict the branching fractions of top quark FCNC decays into a light quark and Z or γ in the range 10^{-3} - 10^{-5}. This has an effect on the t-channel cross section of the single-top production. The enhanced FCNC interaction implies t-channel production involving new propagators but not only W. For instance, the top quark and the spectator light quark in the final state can be produced via the $Z - t - c$ and $\gamma - t - c$ FCNC vertices [5].

The s-channel cross section is also increased by the FCNC interaction. For instance, the strongly coupling underlying new physics might imply the existence of the process $q\bar{q} \to g \to t\bar{c}$. However, this enhancement of the s-channel production rate is not experimentally detectable because c-jets are not easily distinguished from b-jets [6].

The Wt-channel production is insensitive to the FCNC interaction, since it assumes an on-shell W in the final state and therefore, do not interfere with the possible single-top final states mediated with FCNC vertices. It is only sensitive to the possible anomalous couplings at the $W - t - b$ vertex. Hence, the Wt-channel production provides a possibility to study such a non-SM couplings without interfering with the possible FCNC effects [69].

A significant excess of the measured t-channel cross section over its SM prediction, while the s-channel and Wt-channel measurements agree the SM predictions would imply the existence of the FCNC interaction beyond the SM. If no direct evidence of the underlying new physics is observed, this would mean that the characterizing energy scale of the new physics is higher than the c.m. energy of the experiment. The LEP and TEVATRON experiments loosely constrained the $Z - t - c$ and $\gamma - t - c$ FCNC interactions [86]. The LHC experiments will be able to impose stringent constraints. As to FCNC interactions mediated with the non-SM bosons at the tree level, they are experimentally ruled out for low masses of these extra bosons [86–93].

New physics can be directly searched via the tree level couplings of the new bosons or fermions to the top quark. Since the existing experimental data constrain the low mass region of the new particles, the t-channel production, which scales as $1/M_{NP}^2$ is not sensitive to these

---

[5]One gets the corresponding Feynman diagram by replacing b-quark with c-quark and W with Z or γ in the t-channel diagram in Figure 2.1a. Meanwhile, the final light quark remains the same flavor as the initial one.

[6]The charge conjugate final state, $\bar{t}\,c$, is also assumed.

new particles due to their large masses. Here, M_{NP} is the mass of a new particle. In contrast, the s-channel cross section can be largely affected by the new particle if it couples to the top quark and if its mass is not larger than the typical c.m. energy of a parton collision. A charged or neutral extra boson sector is less constrained experimentally than the sector of the extra fermions [69]. One of the interesting new particle is the heavy charged W' boson. Many theoretical models, such as non-commuting extended technicolor [94], composite [95, 96] and little Higgs [97–99], supersymmetric top-flavor [100] predict [101] a charged W' boson with a model dependent coupling properties. It couples with the top quark and the bottom quark but not necessarily has the V-A interaction structure. W' participates in the s-channel production [7] and interferes with the SM s-channel production mediated by W, since the final state is always $t\bar{b}$ or its charge conjugate. It can significantly enhance the channel cross section if the averaged c.m. energy of the experiment is sufficient to have the propagator W' on-shell. Due to the interference term the total cross section of the s-channel production might be enhanced or reduced. The existing models predict [69] enhancement of the total cross section.

New physics theories, which predict a new scalar neutral or/and charged bosons can also influence the s-channel production cross section. In theories such as for instance, the SM and its minimal supersymmetric extensions (MSSM) the fundamental scalar fields arise as a mechanism of the spontaneous symmetry breaking and generation of particle masses. Therefore, they are expected to have rather strong coupling with the top quark. They also can be composite particles consisting of the top quark and a light quark [69, 102–104] and should have large masses [41]. The cross sections of the t-channel and Wt-channel production are not sensitive to the heavy scalar particles, while the s-channel cross section can be significantly boosted by the additional contribution from the tree level diagrams with the charged scalar bosons.

From the above discussion we saw that various possible new physics phenomena can manifest in the single-top production channels in different manners. The t-channel cross section is sensitive to any new physics, which might not be observed directly but modifies the strength and the structure of the $W - t - b$ interaction and leads to FCNC interactions. The experimentally observed cross section of s-channel is not influenced by these effects but is sensitive to new charged gauge or scalar bosons, which couple with the top quark. Since these new bosons should have large masses (otherwise, they would be already observed on the existing experiments), the t-channel production rate has a relatively small contribution from them. The Wt-channel production of single-top is insensitive to the FCNC interaction and the new heavy bosons. Therefore, it is a 'clean' probe for any new physics that leads to the modified coupling at the $W - t - b$ vertex.

---

[7]The corresponding Feynman diagram can be derived from the SM diagram shown in Figure 2.1b by replacing the W propagator with W'.

Chapter 3

ATLAS Detector

In the following chapter, we provide a general description of the ATLAS detector. In a simple but overall picture of the detector, its composition and the functionality is discussed.

The coordinate system of the ATLAS experiment is explained here. The notations of the coordinate variables are used throughout the whole document. The origin of the right-handed coordinate system is the designed interaction point of colliding beams inside the detector. The Cartesian x-axis lies in the LHC ring plane and is directed towards the center of the ring. The y-axis is directed upward. Thus, the z-axis lies along the beam direction at the interaction point. Since the coordinate system is chosen to be right-handed, the positive side of the z-axis is the direction of the beam, that moves anti-clockwise. Coordinates of the the polar and the cylindrical coordinate systems are more useful to work with than the Cartesian ones, that is determined by the global cylindrical symmetry of the detector. The azimuthal angle, ϕ, is measured around the z-axis with $\phi = 0$ at the positive y-axis direction. R is the radial distance from the z-axis. The polar angle, θ, is measured from a positive direction of the z-axis. Instead of θ, which is not a Lorentz invariant quantity, the pseudo-rapidity, η, is often used. The two quantities are related by the formula,

$$\eta = -\ln \tan(\theta/2) \tag{3.1}$$

For massless particles the pseudo-rapidity is the same of the rapidity, which is a Lorentz invariant quantity. It is used in theoretical calculations related to the particle physics. Thus, η, ϕ and R make a set of Lorentz invariant coordinates with respect to the transfer between the ATLAS (laboratory) frame and the beam frame. The granularity of the sensitive (signal detection) regions of the ATLAS calorimeter detector is convenient to represent in terms of $\Delta\phi$ and $\Delta\eta$ of the unite volume of these regions. The detector granularity has the azimuthal symmetry [1] for all sub-detectors but depends on R and η. One more used variable is the angular distance, $\Delta R = \sqrt{\Delta\eta^2 + \Delta\phi^2}$. Here, $\Delta\eta$ and $\Delta\phi$ are differences between η and ϕ coordinates of any two objects (e.g., electron and muon momenta).

3.1 Detector overview

The ATLAS detector [3] is the joint system of various sub-detectors and a magnetic system as well as the electronics, cooling and installation infrastructures. Its design and sizes are determined by the physics performance in proton-proton collisions at the LHC c.m. energies and the luminosity. The detector is characterized by high efficiency, high resolution and an

---

[1]This symmetry is violated by the supporting constructions the largest part of which are the iron feet holding the detector.

unbiased determination of an energy, a momentum, a flavor and a charge sign. The requirement of high resolution is achieved by the fine granularity of the detector read-out system. Fast response and short recovery time of the detector elements and the signal read-out electronics are crucial requirements given the designed bunch crossing rate, 40 MHz, of the LHC. The abundance of high energy particles penetrating into the detector leads to another important requirement to the detector, it has to be radiation resistant in order to operate for several years without significant degradation. This requirement applies especially to the innermost parts of the detector, where the radiation is high. Figure 3.1 shows a cut-away drawing of the detector. The innermost component is the semiconductor pixel tracker (Pixel) detector [3, 105, 106]. It is wrapped by the semiconductor tracker (SCT) detector [3, 107] and both are embedded inside the transition radiation tracker (TRT) detector [3, 108]. These three detectors together are referred to as the inner detector (ID). The goals of ID is to measure the momentum and the sign of the charge of charged particles and provide a good reconstruction resolution of the primary (proton-proton collision) and secondary (particle decay) vertices. It is covered with the central solenoid of the magnet system.

ID is followed (in the radial direction) by the calorimetry system, which consists of two parts. The inner part is the liquid argon calorimeter (LAr) [3, 109] and the outer is the hadronic calorimeter (Tile) [3, 110]. The LAr calorimeter is hermetically embedded in the special cryostat system in order to maintain argon in a liquid phase. The Tile calorimeter is designed for measuring of the energy of hadrons (hadronic jets). The LAr calorimeter has a dual functionality. Its task is to measure the energy of electrons and photons as well as for hadronic jets. Additionally, the forward (close to z-axis) parts of the LAr calorimeter are designed to measure energy of the beam remnants after proton-proton collisions as close as possible to the initial directions of the colliding beams. This is an important measurement for the precise determination of the missing transverse energy.

The calorimeter is surrounded by the muon spectrometer [3, 111], which consist of several layers of the muon detector chambers arranged with the azimuthal symmetry. The task of these chambers is to measure muon trajectories. The muon spectrometer together with the inner detector is used to achieve better precision of the measurement. The layers of the central muon chambers are mounted in a range of the radial distance, which is covered by the central toroid of the magnet system [3, 112], see Figure 3.1. In this region, the magnet coils create a magnetic field with the azimuthal symmetry [2] (see 3.2.1). Charged particles trajectories are bent by this magnetic filed, that gives a possibility to measure their momentum over mass ratios and charge signs.

---

[2]Violated by the non-homogeneity of the supporting infrastructure of the detector.

44m

25m

Tile calorimeters

LAr hadronic end-cap and
forward calorimeters

Pixel detector

LAr electromagnetic calorimeters

Toroid magnets

Transition radiation tracker

Muon chambers

Solenoid magnet

Semiconductor tracker
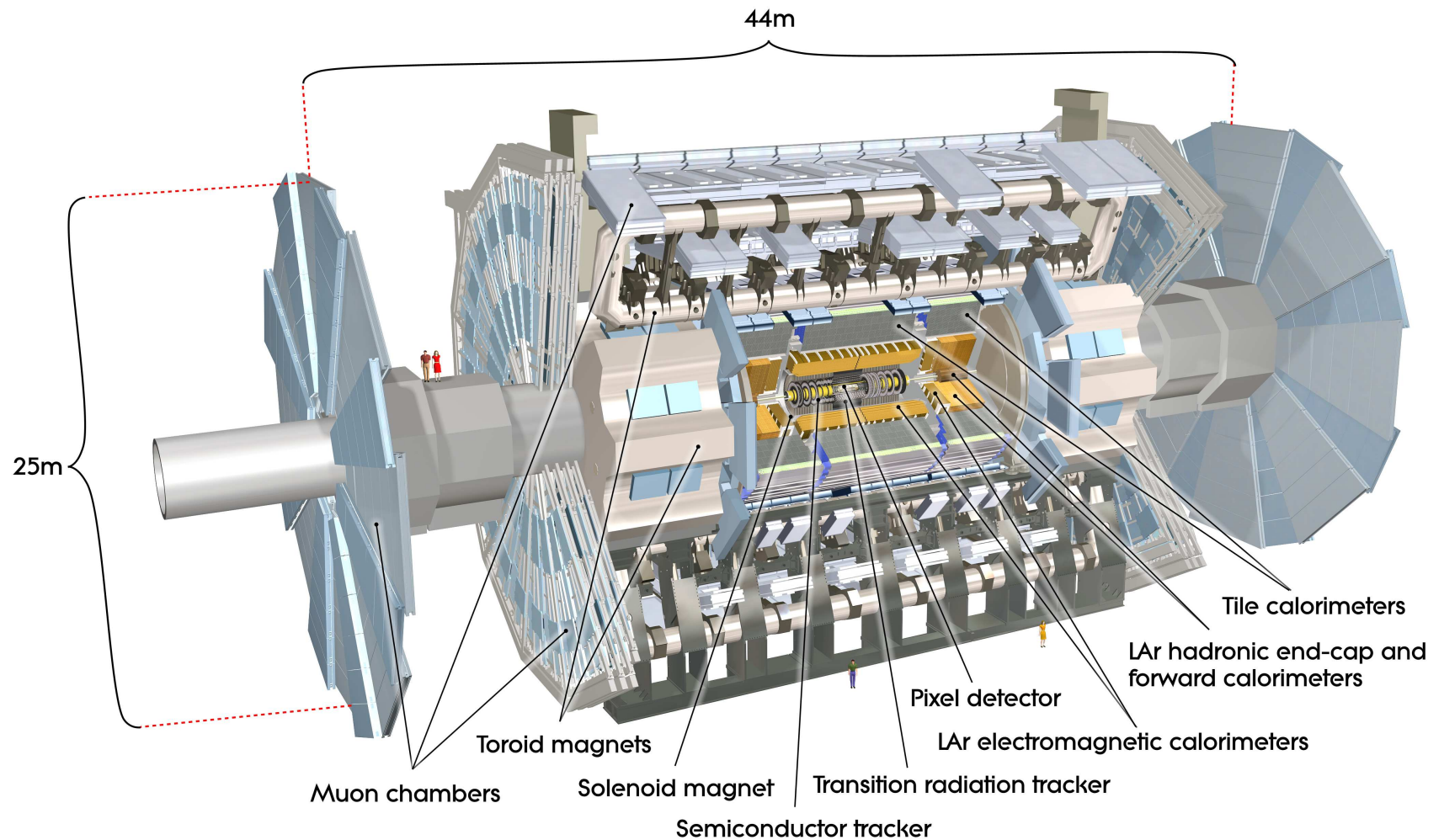
Figure 3.1: View of the ATLAS detector. Front part of the detector is cut away in order to present all sub-detectors [3].

3.2 ATLAS sub-detectors

In this section, a detailed overview of the ATLAS sub-detectors is provided. The magnet system, which is integrated into a construction of the sub-detectors is also described.

3.2.1 Magnet system

The superconductive magnet system of the ATLAS detector, shown in Figure 3.2 can be divided into two main components, the central solenoid and the toroids. The solenoid [113, 114] has a cylindrical shape and is installed inside the calorimeter cryostat. It covers ID within its pseudo-rapidity range and provides the axial magnetic field of 2T with increasing radial component towards the solenoid ends. Thus, the bending of the track of charged particles inside the inner detector volumes happens in the $R - \phi$ plane. The massive iron parts of the detector construction at the outer surface of the Tile calorimeter bends the magnetic field lines back inside the calorimeter region.
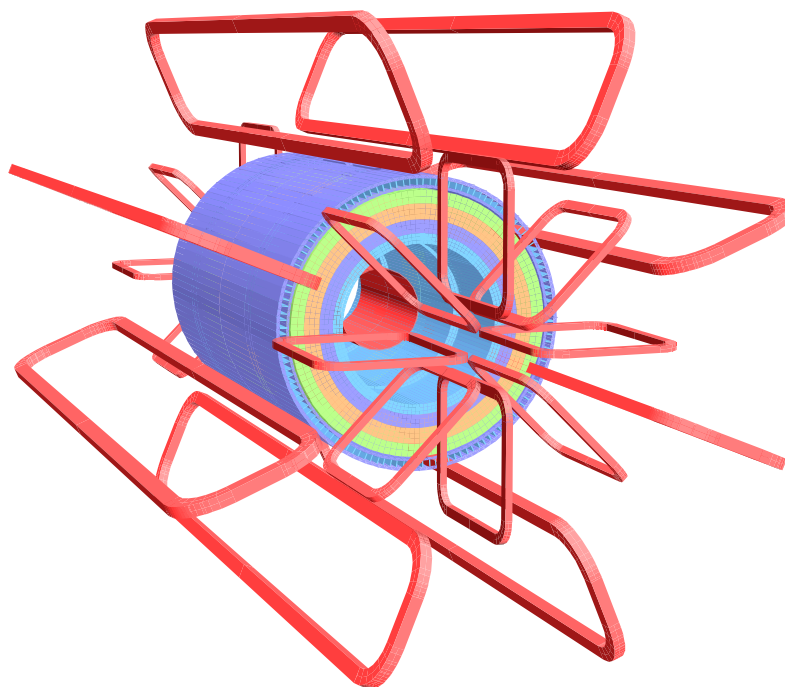
Figure 3.2: Drawing of the magnet system of the ATLAS detector. The solenoid magnet (in the center) and the coils of the barrel and the end-cap magnet toroids are shown [3].

The toroidal magnet system consists of the barrel [115] and two end-cap [116] toroids. Each of them has eight coils arranged in an azimuthal symmetry as shown in Figure 3.2. Each coil is placed inside a separate cooling volume. The end-cap toroids are rotated around the z-axis by $22.5°$ with respect to the barrel. This optimize radial matching between the barrel and the end-cap magnetic fields. The magnetic field strength is at most about 0.5 T for the barrel and about 1 T for the end-caps. Figure 3.3a shows a picture (simulation) [117] of the ATLAS magnetic field strength in the $R - \phi$ plane for z close to the interaction point. Higher strength regions can be seen in dark red, which are created by the central solenoid as well as by the

toroids near to their coils. The recoiled field by the iron constructions of the Tile calorimeter is also seen as the red circle in between the toroid and the solenoid. Figure 3.3b shows the magnetic field strength in the $x - z$ plane with y near to the interaction point.

(a) $R - \phi$ (b) $x - z$
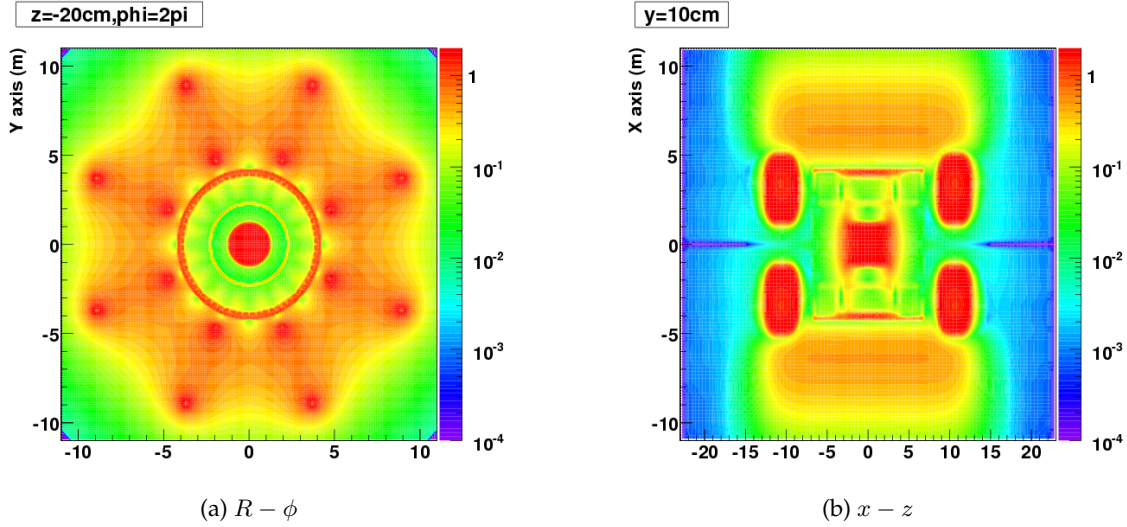
Figure 3.3: 2-dimensional views of the ATLAS magnetic field strength (simulation) on the $R - \phi$ (left) and the $x - z$ (right) planes near to the interaction point. The unit on the axes is meters. The color palette represents the strength of the magnetic field measured in the Tesla units [117].

3.2.2 Inner detector

Figure 3.4 shows the cut-away view of ID. Each sub-detector consists of a barrel and two end-cap segments. All these three segments of each sub-detector are cylindrically symmetric. The whole inner detector cylindrical envelope has a length 7024 mm and a radius 1150 mm.

A geometrical configuration of the different sub-detector modules of both the barrel and the end-cap segments can be seen in Figure 3.5a and Figure 3.5b respectively. The last includes also the barrel layers of SCT and Pixel.

The Pixel barrel consists of three layers of modules. All modules in the barrel and the end-caps have identical functionality and are the smallest building blocks of the Pixel detector. The first layer (called also B-layer) is arranged at 50.5 mm distance from the beam axis. Each end-cap consist of three disks of modules. The geometry of the barrel layers and the end-cap disks guaranties that a particle track initiated from the nominal interaction point traverses at least three of them (within the pseudo-rapidity coverage of Pixel) and one is always B-layer.

The SCT barrel has four cylindrical layers of identical sensor modules. Each SCT end-cap consists of nine discs of sensor modules. End-cap modules have trapezoidal-shaped geometry of five different types. The discs have the equal outer radii, 560 mm, but different inner radii. They are arranged at different distances along the z-axis from the nominal interaction point. This geometrical configuration is chosen such that a track of a particle initiated from the nominal interaction point traverses at least four of them at any pseudo-rapidity within the coverage range of SCT.

The TRT barrel consists of three independent rings with 32 modules per ring. Each end-cap
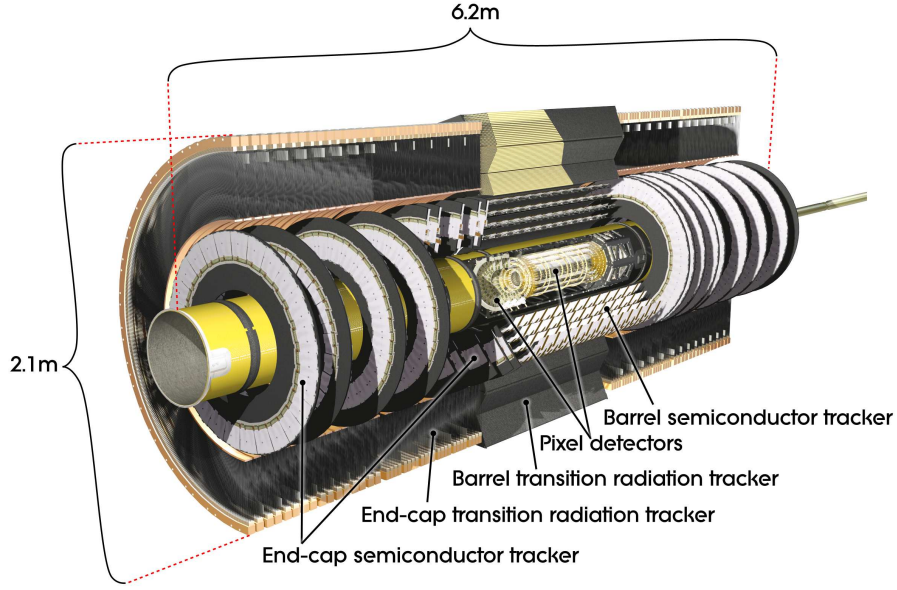
Figure 3.4: View of ID, which consists of the Pixel, SCT and TRT barrel and end-cap modules [3].

consist of two sets of wheels. The inner set has 12 identical wheels and the outer set consists of 8 wheels.

Additional information about the construction of the inner tracker sub-detectors, including their pseudo-rapidity coverage, can be seen in Figure 3.6, which provides a schematic view of one half (axial) of ID. Pixel and SCT provide a particle track measurement in the range of $|\eta| < 2.5$. TRT covers a smaller region of $|\eta| < 2.0$.

The Pixel detector has the finest granularity among all ATLAS sub-detectors. The sensitive unit is a rectangular silicon sensor (pixel) of size $50\,\mu\text{m} \times 400\,\mu\text{m}$ [3]. The Pixel detector consist of 1744 modules that makes about 80 millions of read-out channels (half of the whole ATLAS read-out). With such a fine granularity of the signal read-out, the design goal of Pixel is to have a resolution of the transverse impact parameter, the distance between a given track and a given reconstructed vertex on the plane transverse to the beam axis, of $15\,\mu\text{m}$ and a resolution in the z-coordinate of a reconstructed primary vertex better than 1 mm [118].

The SCT detector consists of silicon microstrip modules. Each strip is connected to a separate read-out channel. The pitch of strips is $80\,\mu\text{m}$ for the modules in the barrel layers. The pitch is a variable quantity for the end-cap modules. It varies in the range close to $80\,\mu\text{m}$ for all types of the modules. The length of strips is approximately the same for all types of modules and is equal roughly to 12 cm. Modules are installed on the barrel layers in such a way that the strips are aligned along the z-axis. In the end-cap modules strips are orthogonal to the z-axis. Therefore, in both regions only two coordinates can be measured with a single-sided microstrip sensor. In case of barrel these are ϕ and R, where the accuracy of the measurement of ϕ is determined by the pitch of the strips. The accuracy of R measurement is determined by the radial alignment precision of the modules of the barrel layers. The precision is of the order of $100\,\mu\text{m}$. In case of end-cap modules the measured coordinates are ϕ and z. The ac-

---

[3]Each module has a small fraction (about 10%) of special pixels with larger dimension, $50\,\mu\text{m} \times 600\,\mu\text{m}$, in the region near the edge of a front-end chip.
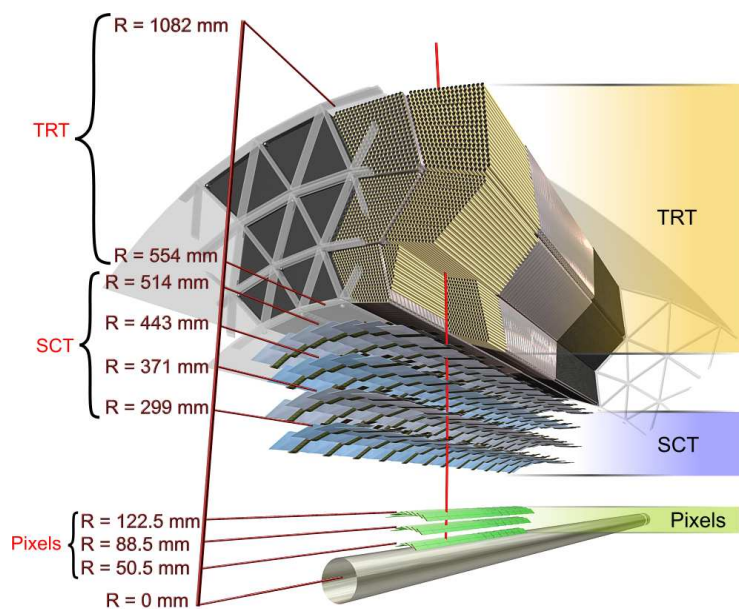
(a) Barrel region
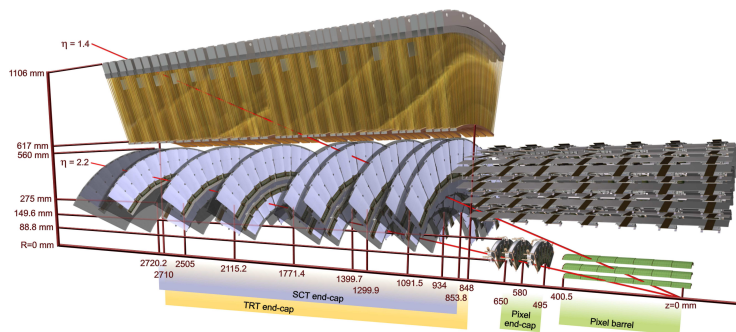
(b) end-cap region

Figure 3.5: Alignment details of the barrel (top) and the end-cap regions (bottom) of the layers of Pixel, SCT and TRT modules. Cut-away pictures [3].
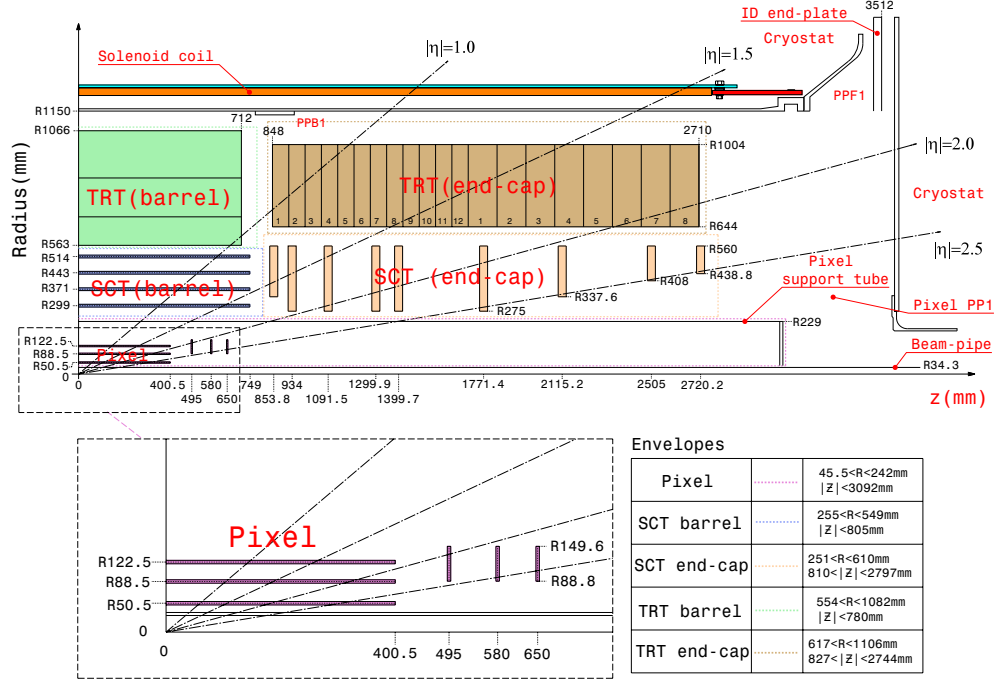
Figure 3.6: Schematic view of the ID positive side in the $R - z$ plane. The sizes of the sub-detectors are presented in the table on bottom right side of the figure. Bottom left figure shows the zoomed view of the Pixel sub-detector. Distances are expressed in millimeters. The dash-dotted lines from the coordinate system origin represent the corresponding pseudo-rapidity bounds [3].

curacy of the z-coordinate measurement is determined by the axial alignment precision of the end-cap modules, which is of the order of 200 μm. In order to measure the third coordinate, a SCT module is a joint system of two back-to-back glued identical single-sided sensors rotated with respect to each other by 40 mrad. Thus, the projection of each strip from one sensor plane to the other crosses several strips. Therefore, the described geometry of a sensor pair allows to measure the third coordinate as well. The coordinate of the crossing point of the two "fired" strips is known with an accuracy of the order of $d(1 + \cos\alpha)/\sin\alpha$, where, d is the pitch of the strips (see above) and α is the stereo angle between the sensor planes of a module. Each sensor (module) consists of 768 (1536) active strips. SCT has 4088 modules in total, 2112 out of which are mounted on four layers of the barrel segment. Thus, the total number of read-out channels of SCT is about 6.2 millions.

Spatial resolution of the SCT modules was studied during a dedicated test beams [119]. It is 17 μm on the $R - \phi$ bending plane for both barrel and end-cap modules. Resolution in the z-coordinate measurement is 580 μm for the barrel modules. Resolution in the R measurement is also 580 μm for the end-cap modules.

The TRT detector unit is a straw tube of 4 mm diameter, which has a 35 μm thick wall. The wall serves as a cathode. The anode is a tungsten wire with 31 μm diameter and stretched at the center of a straw with a tolerance of less than 300 μm. Barrel straws have 1440 mm length and the signal is read from both sides of a straw, since its anode wire is divided into the equivalent parts. They are arranged parallel to the z-axis and form 73 straw layers along the radial direction. End-cap straws are 370 mm long and correspond to only one read-out channel. They are aligned along the radial direction and form an azimuthal uniform distribution

of 768 straws per disc. Each wheel of the inner set of the end-cap wheels (12 in total) consist of 8 discs. The distance between the discs is 8 mm. Wheels from the outer set (8 in total) consist of 8 discs but spacing between them is 15 mm. The construction of barrel and end-cap layers guaranty that a charged particle (with $p_T > 0.5$ GeV) traverses at least 36 straws within the pseudo-rapidity coverage of TRT. The exception is the transition regions between barrel and end-caps, $0.8 < |\eta| < 1.0$, where the minimal number of traversed straws decreases to 22. The total number of read-out channels is about 351 thousands.

A straw operates by collecting the charge of secondary electrons induced by ionization of the gaseous mixture, $Xe/CO_2/O_2$, which fills the tube. The ionization happens due to the transition radiation of low energy photons from an initial charged particle, when it penetrates inside a straw from the inter-straw transition material or vice versa. A charged particle itself also can ionize the gas and induce a signal. Though its amplitude is smaller than the amplitude of the signal due to the transition radiation for the given gaseous mixture. Therefore, we can distinguish two sorts of signals by imposing low and high thresholds on the integrated signal charge (hits). Existence of the large number of the hits, which integrated charge is larger than the high threshold, per reconstructed track can serve as a good identification criterion for electrons, since electrons induce much intensive transition radiation due to their small mass than other charged particles. The gain of a single straw under nominal operation is about 2.5×10^4. The spatial resolution of straws is about $130\,\mu$m in the $R - \phi$ bending plane [108] in both barrel and end-cap segments. The main goal of the TRT detector is to improve reconstruction and identification of electrons. Besides, it helps to improve tracking in general.

3.2.3 Calorimeter

The ATLAS calorimeter is presented in Figure 3.7, which shows a cut-away view of LAr [109] and Tile [110] sub-detectors. The total pseudo-rapidity coverage of the calorimeter is $|\eta| < 4.9$. The LAr calorimeter system consist of the barrel segment (EM) and the two end-cap discs (EMEC) both for the electro-magnetic energy measurement, the two end-cap discs (HEC) for hadronic energy measurement and the two forward detector barrels (FCal) for a measurement of the energy of particles scattered at small angles.

The EM barrel [120] covers the range of $|\eta| < 1.475$. It is divided in two equal parts with axial symmetry. Each half has length of 3.2 m and inner and outer radii of 1.4 m and 2 m respectively. The absorber material is made of accordion-shaped lead plates (see Figure 3.8). The gaps between the absorber plates are filled with liquid argon and cathode plates are also placed. The thickness of the EM barrel corresponds to about $22X_0$, where X_0 is the radiation length [25]. Therefore, the electro-magnetic energy deposition by electrons and photons is normally contained within EM, which allows for a high resolution measurement of the energy. The fine $\eta - \phi$ granularity in the read-out segmentation of the accordion like structure [3] allows for a precise measurement of the η and ϕ coordinates of reconstructed energy clusters of electrons and photons. This structure determines a continuous azimuthal detecting medium without any cracks. It also helps to have a good discrimination of electrons and photons from $\pi^0 \to 2\gamma$ by using electro-magnetic shower shapes. Figure 3.8 shows the read-out granularity of EM composed of three layers of read-out cells. EM is preceded by the thin 11 mm liquid argon detector. This presampler is aimed to measure electron and photon energy loss in the upstream materials ($1.7X_0$ thick) in front of EM barrel. EM, the presampler and the solenoid of the inner magnet system are all contained within the central cryostat. EM has 101760 read-out channels in total. The presampler granularity implies 7808 read-out channels.
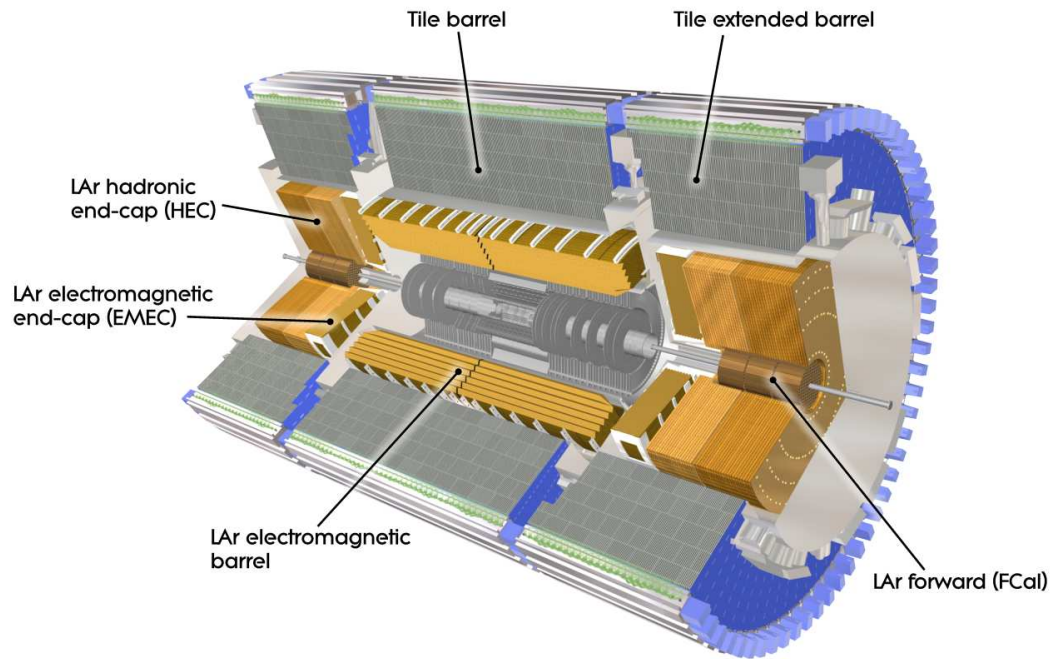
Figure 3.7: A cut-away view of the ATLAS calorimeter sub-detectors [3].
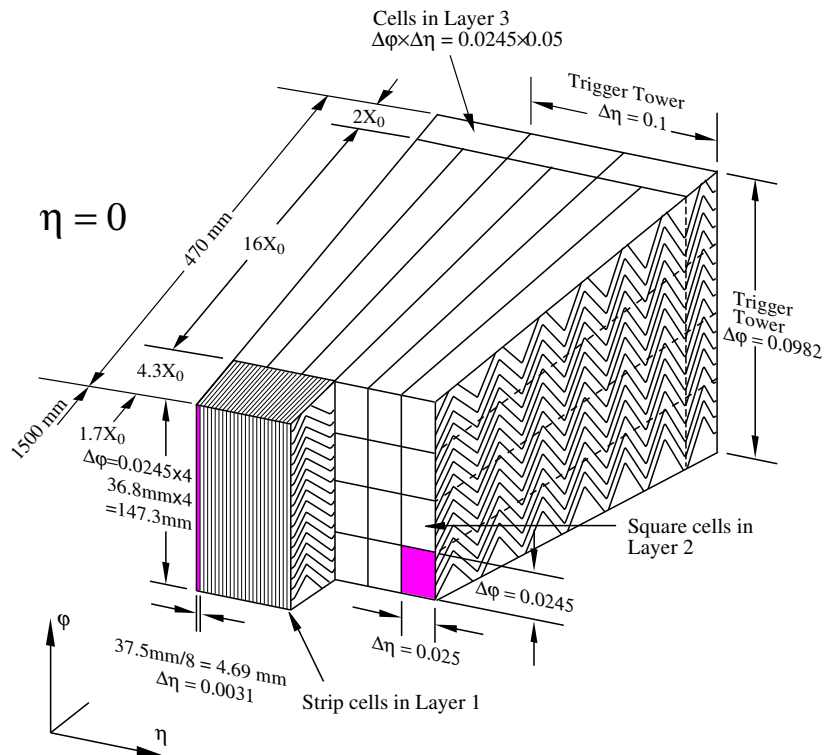
Figure 3.8: Schematic view of the geometrical structure of the LAr barrel and the corresponding $\eta - \phi$ granularity of the three layer read-out segmentation [3].

The EMEC [118] discs extend the pseudo-rapidity coverage of the electro-magnetic calorimeter and cover the range of $1.375 < |\eta| < 3.2$. They also have an accordion-like structure and are $0.63\,$m thick and have inner and outer radii $0.33\,$m and $2.1\,$m respectively. The depth of an EMEC disc in terms of the radiation length is about $24X_0$. Each disc consists of two co-axial outer and inner wheels. The outer wheel covers the range of $1.375 < |\eta| < 2.5$ and the inner one $2.5 < |\eta| < 3.2$. The outer wheel has a fine read-out granularity by η comparable with EM. Together they cover the same pseudo-rapidity range as the inner detector. Using the tracking information together with the EM+EMEC outer wheel information allows to have a high efficiency in reconstruction and identification of electrons, matching the designed physics goals of the detector. Electron and photon energy loss in the transition region, $1.5 < |eta| < 1.8$, between EM and EMEC is measured with the $5\,$mm thick presampler disc of EMEC. EMEC has 62208 channels in both end-caps together. The presampler has 1536 channels in both sides together.
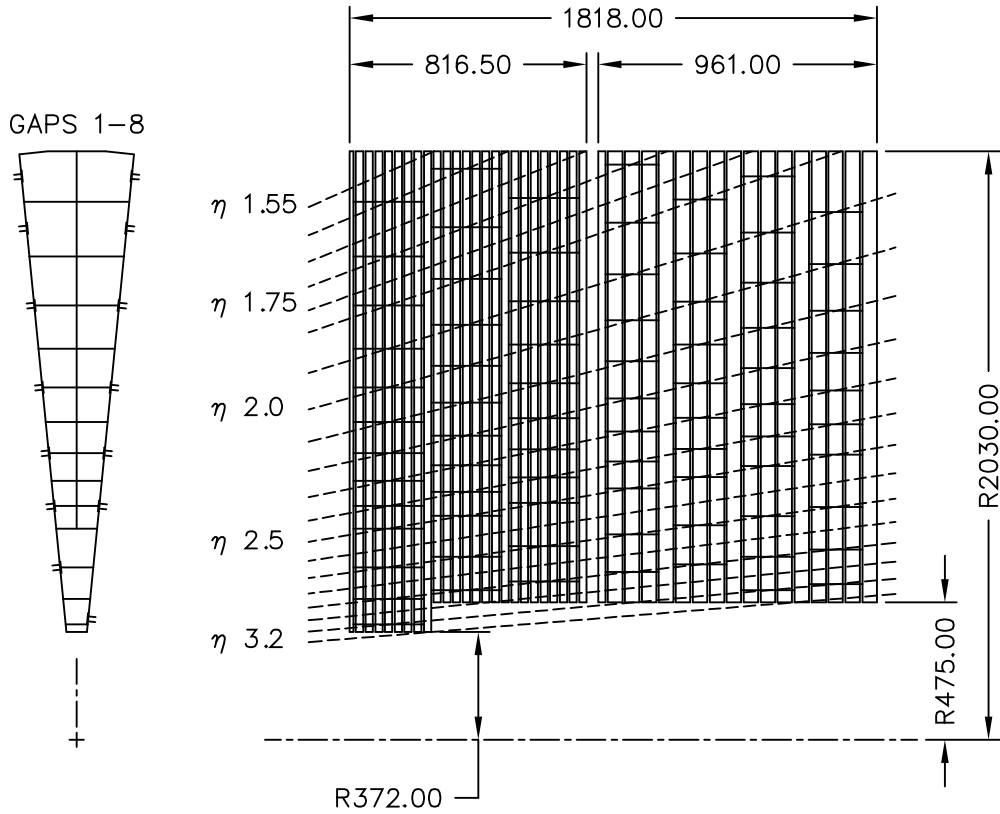
Figure 3.9: A schematic view of the geometrical structure of a single module of the LAr HEC calorimeter in the $R - \phi$ plane (left) and the as-built construction of four single modules (one per disc) in all four discs (two per wheel) presented in the $R - z$ plane (right). Both radial and axial dimensions are given in mm [3].

The HEC [121] wheels (two per end-cap) are allocated beyond the EMEC discs in the axial direction. Each wheel consists of two disc segments made of flat cooper plates (absorber) and liquid argon gaps (detector material) to form a sampling detector. The absorber plates are arranged orthogonally to the z-axis. The HEC has quite constant depth of interaction length

[4] λ, which is approximately 10λ. Each disc is composed of 32 modules with an identical trapezoidal shape. A schematic view of one module in the $R - \phi$ plane as well as the construction of all four disc modules on in the $R - z$ plane is presented in Figure 3.9. HEC covers the pseudo-rapidity range $1.5 < |\eta| < 3.2$. In total it has 5632 read-out channels.

Two identical segments of FCal [122], which also operate based on the LAr technology, are located at very closely to the beam axis and cover the pseudo-rapidity region of $3.1 < |\eta| < 4.9$. A schematic view of one FCal detector in the $R - z$ plane and its arrangement with respect to the beam pipe, the EMEC and the HEC can be seen in Figure 3.10. One detector consists of one module (FCal1) for the electro-magnetic energy measurement and two modules (FCal2 and FCal3) for the measurement of hadronic energy. Copper is used in FCal1 as an absorption material, while it is tungsten in FCal2 and FCal3. The radiation length of FCal1 module is about $27.6X_0$. The total interaction length of FCal2 and FCal3 together is about 7.3λ. Thus, FCal has enough potential for energy measurement with high resolution and it is a good shield for the muon spectrometer system. FCal has much thinner layers of liquid argon (filling the matrix of cylindrical tubes with the cathode rods inside and aligned parallel to the z-axis) than other LAr detectors. This makes its response time shorter, what is an important requirement to the detector due to the high intensity of charged particles at large pseudo-rapidity. In total FCal has 3524 read-out channels.
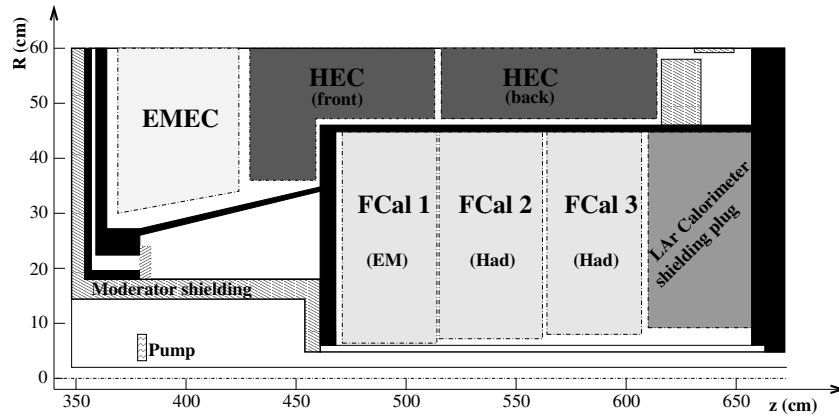
Figure 3.10: A schematic view of the modules of the FCal detector (located at the positive z-side) in the $R - z$ plane together with the parts of the other ATLAS sub-detectors [3].

Both end-cap segments of the LAr detector are contained inside the cryostat vessels. Figure 3.11 shows a cut-away view of an end-cap segment inside the cryostat.

The Tile sampling calorimeter [110] consists of the central barrel and two extended barrels (see Figure 3.7). The central barrel covers the pseudo-rapidity region of $|\eta| < 1.0$. The extended barrels coverage is $0.8 < |\eta| < 1.7$. Each of these three barrels consist of 64 identical azimuthal modules. This structure determines the Tile read-out granularity in the ϕ direction, $\Delta\phi = 0.1$, which is the size of one module in the $R - \phi$ plane.

Each Tile module is made of steel as the absorber and scintillating plates made of polystyrene (doped with the wavelength-shifting flours, PTP and POPOP) as the detector medium. Figure 3.12 shows a schematic view of the periodic structure of the absorber-scintillator plates of a single module. The total interaction length of Tile barrels in the radial direction

---

[4]The mean distance travelled by a hadronic particle before undergoing an inelastic nuclear interaction.
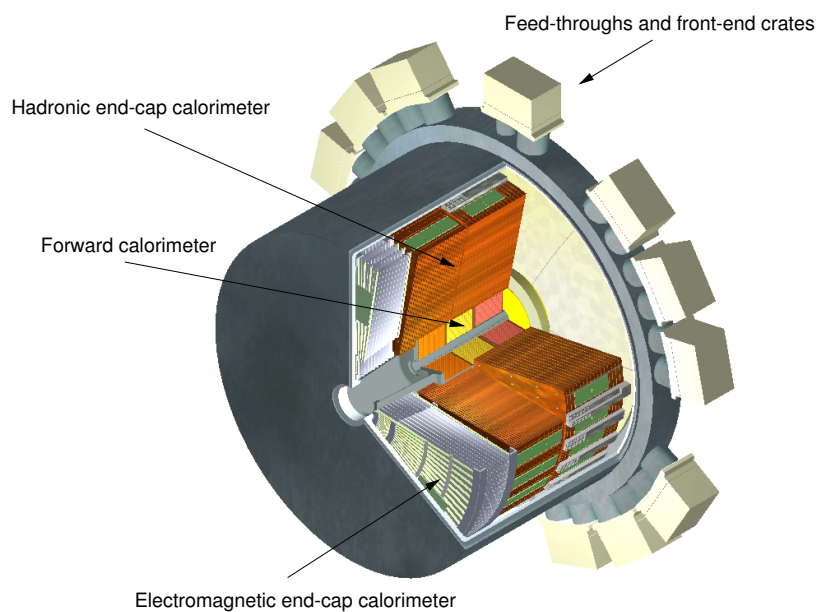
Figure 3.11: A cut-away view of one assembled end-cap segment of the LAr detector contained in the cryostat vessel. Electronic crates, which are hosted around the perimeter of the rear wall of the cryostat are also shown [3].
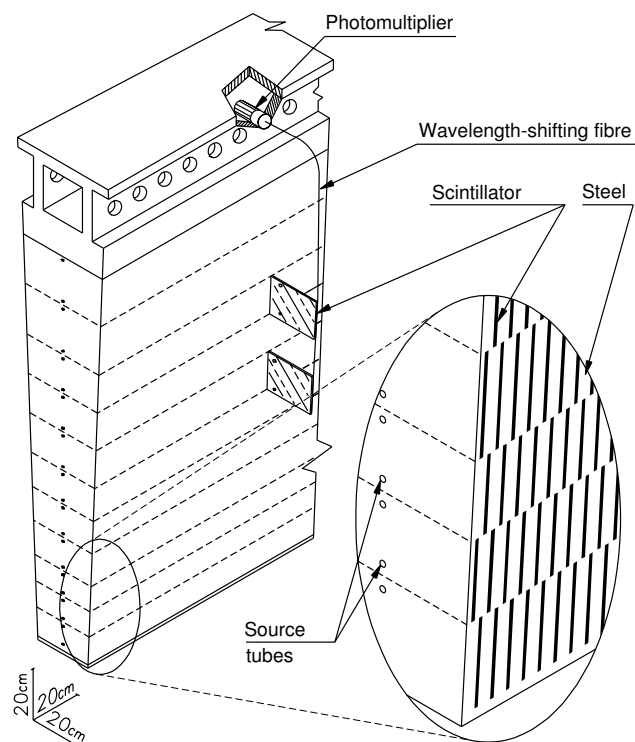
Figure 3.12: Schematic view of a single module of the Tile calorimeter and the zoomed out picture of its periodic structure of the absorber and scintillator material [3].

is approximately 7.4λ. Scintillators accumulate light as a response to the deposited energy. This light is transmitted to the photo-multipliers (PMT) using the wavelength-shifting fibers. Each of the read-out cells are served with two PMTs. The Tile read-out is divided into three radial layers as shown in Figure 3.13, which presents the read-out scheme for one symmetric half of the Tile calorimeter in the $R - z$ plane. Scintillators are grouped in read-out cells of size $\Delta\eta = 0.1$ (1-st and 2-nd layers) and $\Delta\eta = 0.2$ (3-rd layer). Each module of the extended barrel has additionally four read-out scintillator cells mounted from the inner side (see Figure 3.13). Similarly to the LAr presampler detectors, these scintillators are also aimed to measure the energy loss in the transition region between the central and extended barrels. This region has a high density of service material that leads to a significant degradation of the energy resolution. The Tile detector provides good containment for hadronic particle showers and its read-out granularity is sufficient for the measurement of the energy of hadronic jets and also, for the measurement of the missing transverse energy.
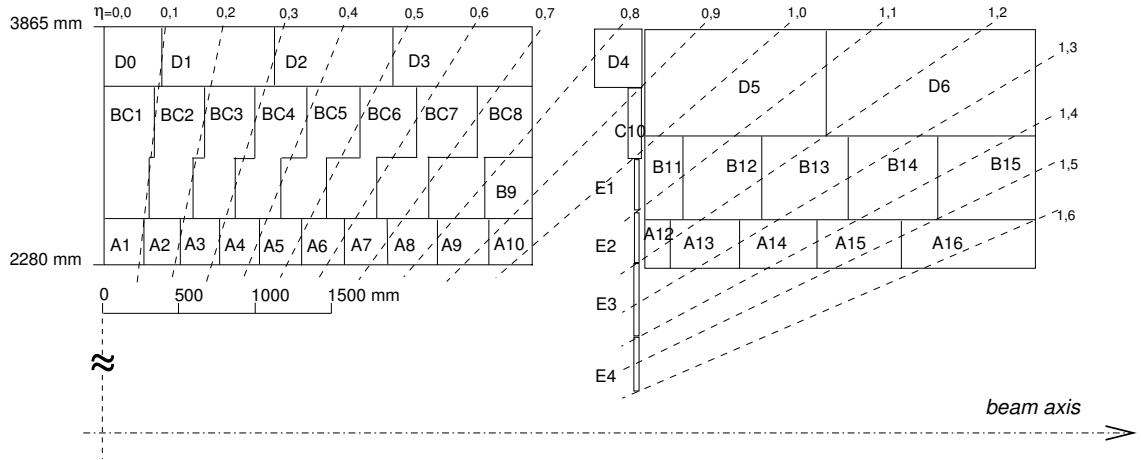
Figure 3.13: A Schematic view of the symmetric one half of the Tile read-out structure in the $R - z$ plane for the central and the extended barrel modules. The gap and crack scintillator modules, each of which is divided into two read-out cells are also shown at the inner side of the extended barrel. Boundaries of the pseudo-rapidity regions are shown by the dashed lines [3].

3.2.4 Muon spectrometer

The Muon spectrometer [111] consists of the barrel and two end-cap segments. It covers the pseudo-rapidity range $|\eta| < 2.7$ except of the small rapidity gap, $|\eta| < 0.08$, which divides the barrel segment into two identical parts. Additional acceptance holes in the $\eta - \phi$ plane are due to the feet of the support structure of the detector. Figure 3.14 shows a cut-away view of the barrel and the end-caps together with the magnet toroids. These segments are built using different types of muon detectors with different operational tasks. Monitored drift tubes (MDT) [3] and cathode strip chambers (CSC) [3] are used for the muon track reconstruction with high resolution capabilities Resistive-plate chambers (RPC) [3] in the barrel and thin-gap chambers (TGC) [3] are used for triggering muons with the time resolution of $15 - 25$ ns that helps to precisely identify a beam crossing belonging to the triggered muon. RPC and TGC together cover the pseudo-rapidity region of $|\eta| < 2.4$.

The barrel has three radial layers of MDT rectangular modules (see Figure 3.16) mounted
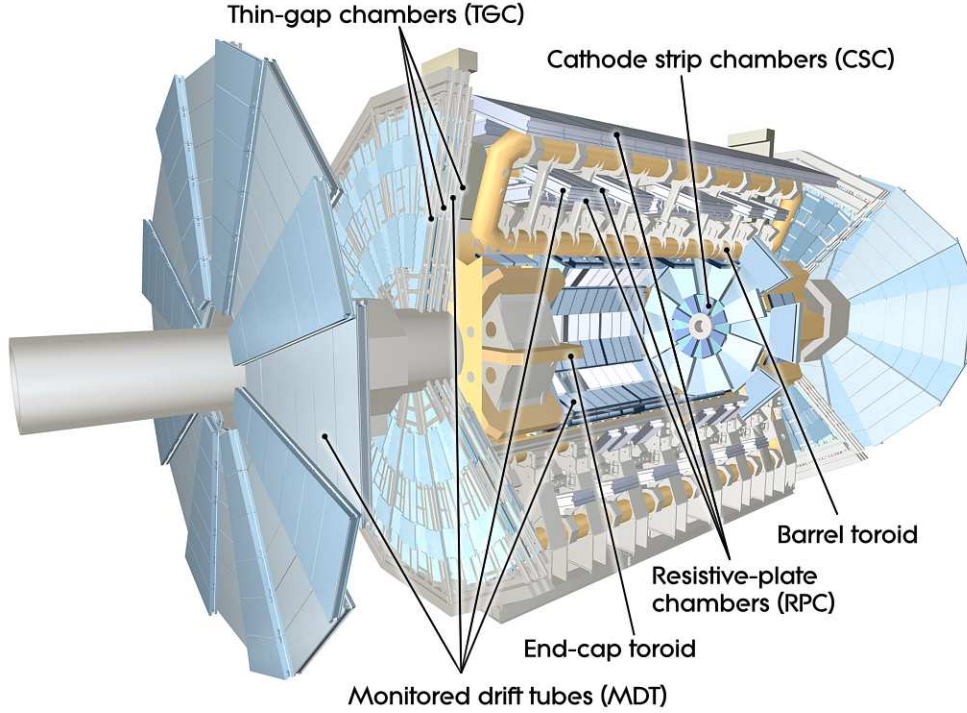
Figure 3.14: A cut-away view of the structure of the ATLAS muon spectrometer together with the toroidal magnet system [3].

in front, in the middle and behind of the central magnet toroids. The modules form eight azimuthal sectors (octants) of two sets of short and long modules as shown in Figure 3.15. The majority of modules are arranged in such a way that the perpendicular lines from their geometrical centers traverse the beam axis.

MDT modules of the barrel middle layer are covered with the rectangular RPC modules from both inner and outer sides. The third layer of RPC modules are adjusted on the outer side of the third layer of the long MDT modules (see Figure 3.16) and on the inner side of the short modules.

Each end-cap segment consists of trapezoidal modules of the MDT and the TGC, which make seven layers (discs). Figure 3.16 shows a schematic view of the barrel and the end-cap module layers on the bending $R-z$ plane for the symmetric half of the spectrometer. All seven layers are perpendicular to the beam axis. Two out of three MDT layers are located behind the end-cap magnet toroid. They both cover the pseudo-rapidity range of $|\eta| < 2.7$. The innermost MDT layer consists of two complementary discs aligned in front and co-axially to the end-cap toroid. This layer covers the pseudo-rapidity range only up to $|\eta| < 2.0$. The layer of CSC modules extends the MDT innermost layer and re-gains the coverage of $2.0 < |\eta| < 2.7$. CSC modules are not orthogonal to the beam axis rather are inclined towards the interaction point. This region is special because of intense particle fluxes, which requires high time resolution and good radiation hardness of the detector. The CSC detector satisfies these requirements.

The basic building element of the MDT detector is a drift tube [123] of radius of 3 cm. The length of tubes varies from 1 to 6 m. Figure 3.17 shows the radial cross section of a drift tube
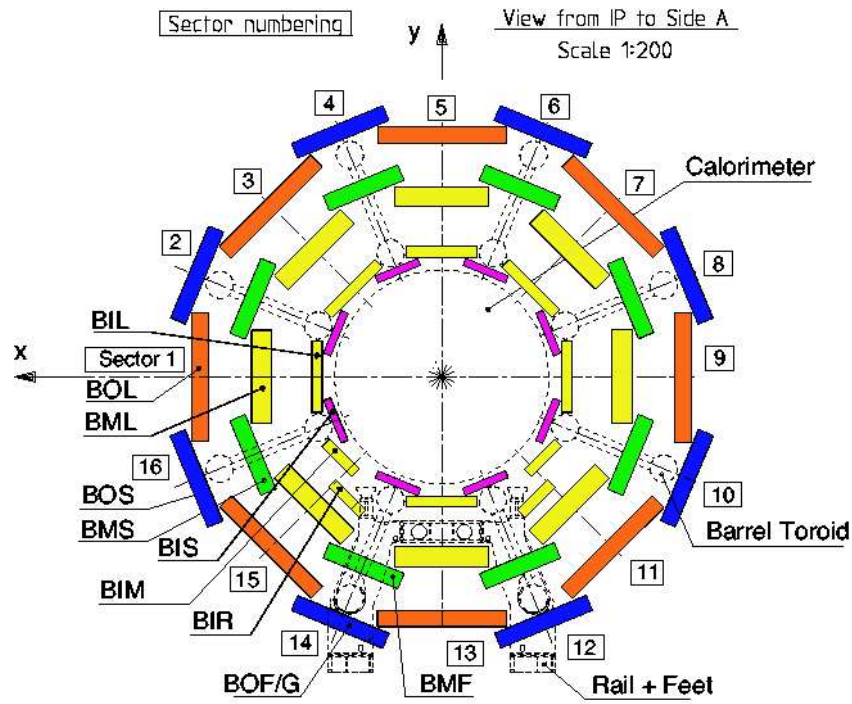
Figure 3.15: Schematic view of the three layer structure of MDT modules of the barrel segment in the $R - \phi$ plane, which includes the nominal interaction point [3].
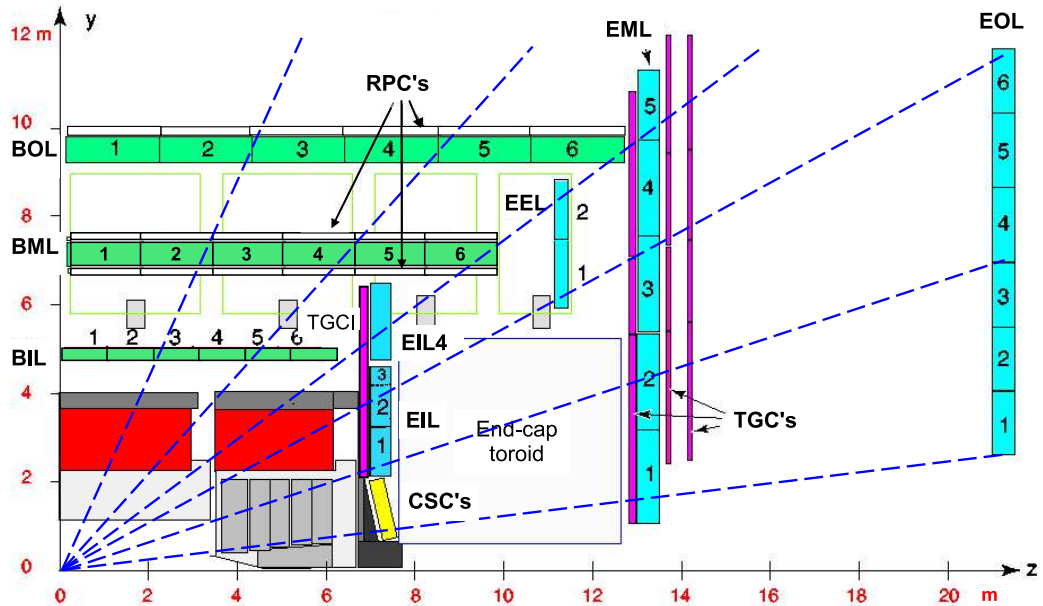
Figure 3.16: Schematic view of the muon detector layers of the half-barrel and the end-cap segments of the muon spectrometer. One sector of the layers is presented on the $R - z$ plane [3].

with an incident muon track. Tubes are filled with an Ar/CO_2 gaseous mixture. The anode is a tungsten-rhenium wire of $50\,\mu$m. Maximal drift time from the tube wall (cathode) to the anode is 700 ns [5].
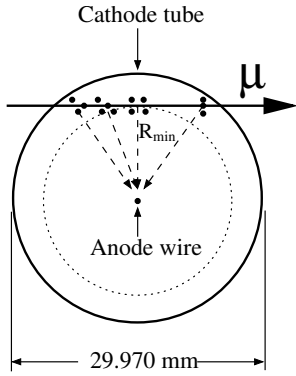
Figure 3.17: Schematic view of the radial cross section of a MDT drift tube together with an incident muon track.

MDT chambers consist of two parallel sets of drift tube layers (3 or 4 layers per set). Figure 3.18 shows a schematic cut-away view of the barrel rectangular chamber. The alignment rays, which monitor deformations of the chamber frame are also shown in red. Due to the large geometrical sizes of the chambers, especially of those, which are mounted on the outer layers of the barrel and the end-cap segments, an additional deformation of the tubes happens due to the gravitational forces. A special adjustment system corrects the gravitational sag via a central cross plane of the chamber (see Figure 3.18). The obtained averaged tolerance in the alignment of the anode wires is $\leq 20\,\mu$m in all mounted MDT chambers [124]. This translates into the $\leq 80\,\mu$m resolution in the z or R coordinate measurements in the barrel or in the end-caps respectively. This means that the resolution in the sagitta measurement is about $45\,\mu$m for muon tracks crossing all three MDT chambers. Sagitta of tracks in the barrel chambers is measured along the z-axis. In the end-caps, it is measured along the radial direction R. Muon momentum resolution is given with the formula $\Delta p/p = \Delta S \times p/500\,\mu$m. Here, ΔS is the sagitta resolution and p is assumed in the TeV units. According to this formula, the obtained resolution in the muon momentum reconstruction satisfies the design goal of having 10% resolution for 1 TeV muon tracks. In total, the muon spectrometer has 1088 MDT chambers. The total number of the MDT read-out channels is 339000.

The system of the CSC detectors consists of eight sets of small and large multi-wired proportional chambers as shown in Figure 3.19. Each chamber is composed of of four CSC segments, which are able to provide independent measurements of coordinates. Each CSC segment consists of two parallel cathode planes made of copper. Thus, there are four pairs of cathode planes in each CSC chamber. Both cathodes consist of strips, which are arranged orthogonally to each other with a constant pitch in each plane. The anode wires are made of tungsten and rhenium.

Figure 3.20 shows a schematic view of the CSC structure on the parallel to z-axis (left) and on the bending $R-z$ (right) planes. Signal is read-out from both cathode plane but not from the wires. The azimuthal strips provide high spatial resolution, which is $60\,\mu$m. In contrast, the resolution of the radial strips is 5 mm. Time resolution of the CSC detector is rather high, about 7 ns per CSC segment and about 3.6 ns for the whole chamber. Together in all its 32

---

[5]'Slowness' of the MDT detector is one of the reasons why it is replaced with the faster CSC detector in the region of $2.0 < |\eta| < 2.7$.
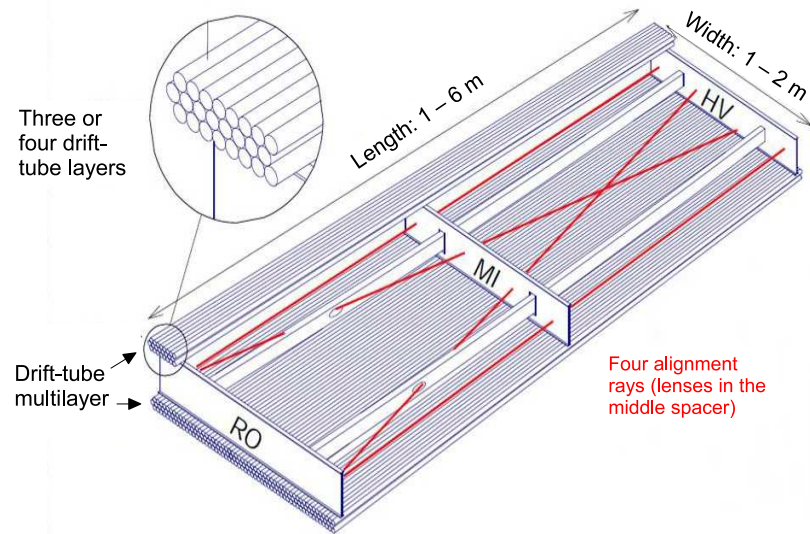
Figure 3.18: A schematic view of the MDT chamber consisting of two sets of layers of the drift tubes. The deformation monitoring rays of the chamber frame are also shown [3].
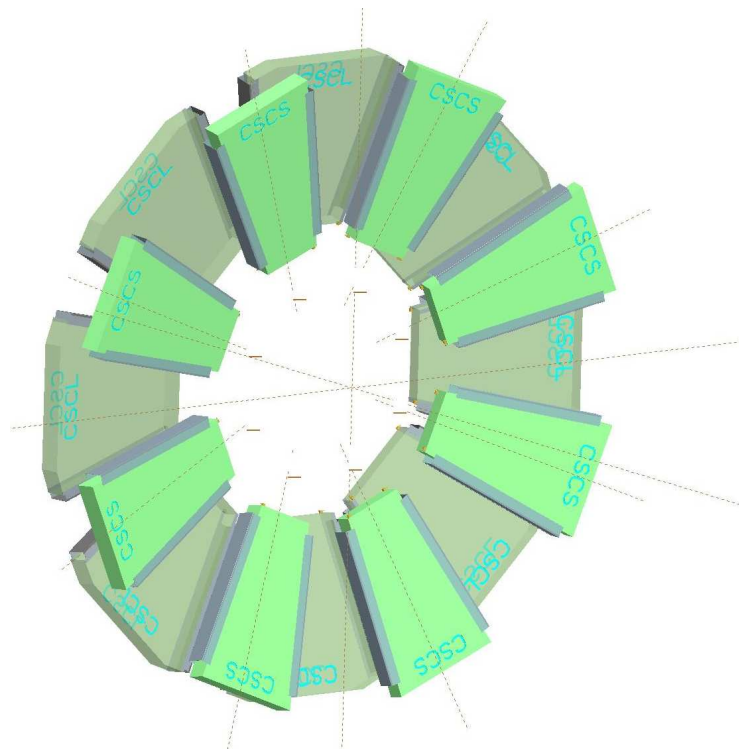
Figure 3.19: Layout of one CSC detector end-cap. The chambers are not perpendicular to the z-axis but are inclined towards the interaction point [3].

chambers, the CSC system has 30720 read-out channels.

Anode wires

S

Cathode strips

W

d

S=d=2.5 mm
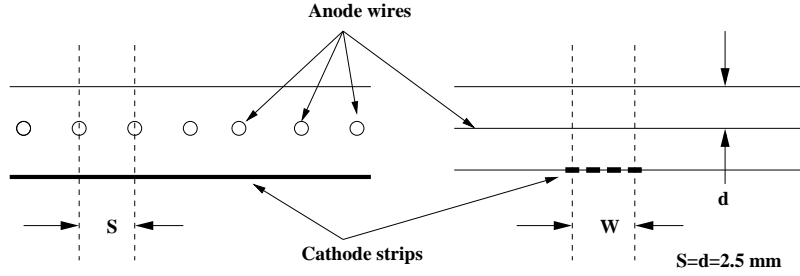
Figure 3.20: A schematic view of the CSC segment on the parallel to z-axis plane (left) and on the bending $R - z$ plane (right) [3].

A single chamber of the RPC detector consists of two or one rectangular segments. The segments are contiguous to each other. Each segment is composed of two layers, which are independent detectors. Each layer consist of two parallel resistive plates and the layer volume is filled with a gaseous mixture, which is the sensitive material of the detector. Signal from the layer is read-out from the strip electrodes, which are metallic outer covers of the resistive plates. The opposite strips are arranged in the ϕ and the z directions on the RPC modules. The pitch of both sets of strips varies between 23 and 35 mm. The gap between the plates is 2 mm and is filed with a $C_2H_2F_4$/Iso-C_4H_{10}/SF_6 gaseous mixture. At the operation voltage between the plates, 9.8 kV, the incident track induces an electron avalanche towards the anode plate. The generation time is relatively short, the signal width is about 5 ns, which allows for a good time resolution for triggering and bunch crossing identification. Three RPC layers allow to make six independent measurement of ϕ and η coordinates (two per layer, since each chamber consists of two detector layers), when a track passes through all of them. These measurements of the ϕ coordinate, with the net resolution of 10 mm, is complementary to the precise z coordinate measurement by MDT. The RPC system covers the pseudo-rapidity region of $|\eta| < 1.05$, which is the region to the comparatively homogeneous magnetic field throughout the spectrometer barrel volume. Absence of an anode wire makes its performance in terms of spatial resolution less affected with the small deviations in the alignment precision of its chambers. The RPC system consist of 544 chambers and has 359000 read-out channels.

The TGC detector operates with same principle of the multi-wired proportional detectors as the CSC detector. However, in contrast to CSC, the signal is read-out from both anode wires and cathode strips of the TGC detector layer. Each TGC end-cap consist of four discs (see Figure 3.16), which join nine layers of the TGC detector. Consequently nine measurements of coordinates per track are performed. In the TGC octants, which are the building blocks of each TGC layer, the strips are arranged radially, while the wires have azimuthal alignment. These allows to measure both ϕ and z coordinates with the strips and the wires respectively. The ϕ measurement is complementary to the MDT measurement of the R coordinate in the end-cap regions. The TGC resolution in a coordinate measurement in the azimuthal direction is about $3 - 7$ mm depending on the radial coordinate of a track. The end-caps cover the pseudo-rapidity region of $1.05 < |\eta| < 2.7$ but triggering is done only up to $|\eta| < 2.4$. The TGC detectors have good time resolution and are stably working in the conditions of intense fluxes particles. The TGC system has 3588 chambers in total and 318000 read-out channels.

3.3 Trigger system

The ATLAS trigger system [3, 125, 126] has three levels of event selection referred to as L1, L2 and EF (event filter). Often, L2 and EF trigger levels together are referred to as a high level trigger (HLT). HLT uses software algorithms for event selection in contrast to L1, which operates on hardware-based logics. L1 makes a decision in less than $2.5~\mu$m using only limited input from the detector read-out. This means that the read-out granularity of the sub-detectors is degraded in order to optimize the signal processing time, when identifying interesting physics objects like electrons, muons, high missing transverse energy and etc. It is required to keep the event acceptance rate below 75 kHz. The ATLAS data acquisition system (DAQ) [127] collects data from the front-end electronics of the sub-detectors and buffers it after L1 accepts an event. Also, L1 defines the detector 'regions of interest' (RoI) used for L1 decisions. L2 is concentrated only on data from RoI, which is a couple of percents of the total detector data. L2 refines the acceptance criteria and adds other selection criteria if applicable. It fully utilizes the detector read-out granularity in the RoIs for decision making. L2 is required to have an acceptance rate below 3.5 kHz. The event processing time is about 40 ms. Events accepted by L2 are further processed with EF, which is able to apply refined selection criteria of kinematic thresholds on energy and momentum of the interesting physics objects as well as more detailed object quality requirements. EF reduces the final rate of accepted events down to 200 Hz. It uses selection criteria for the physics objects, which are reconstructed using the procedures similar to the offline reconstruction algorithms. The processing of one event takes about four seconds in average. Both L2 and EF operates in a parallel regime of events processing using multi-node computing farms. Figure 3.21 shows a block diagram of the ATLAS trigger and data acquisition systems (TDAQ) [3, 128].
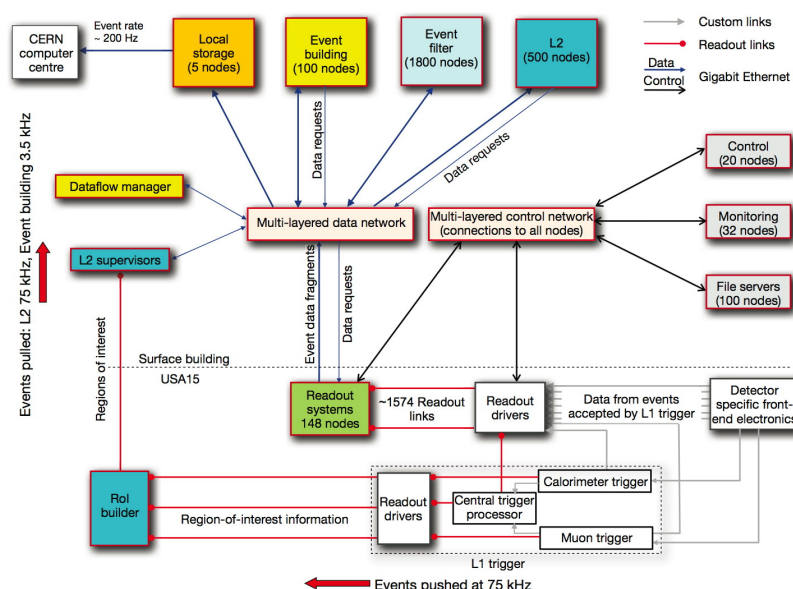
Figure 3.21: A block diagram of the trigger, the data acquisition and the data monitoring systems of the ATLAS detector [3].

As can be seen from the diagram, the L1 trigger makes a decision based on the information from the calorimeter and the muon spectrometer. The calorimeter L1 system operates using data from calorimeter sub-detectors to identify RoI with large electro-magnetic energy deposition. This energy deposition is relatively quickly converted from the calorimeter response into the electro-magnetic energy scale. The merged read-out channels of the sub-detectors allows to quickly identify $\eta - \phi$ region of RoI. The electro-magnetic shower might indicate the existence of the interesting electron, tau lepton or hadron. It is also interesting in a search of events with the high missing transverse energy. The physics studies based on an existence of muons in the final state need the trigger requirements, which are based on the muon spectrometer L1 trigger. As it was already described in the previous sections, the muon spectrometer uses the RPC system in the barrel region and the TGC system in the end-cap regions for triggering.

Different trigger requirements are collected in trigger menus. The trigger menus are composed with consideration of an optimal acceptance of the interesting physics processes on one hand and on the other hand, rates of total accepted events have to be less than the above threshold values. During the collision data taking runs, ATLAS utilizes several trigger menus to record data into several streams. For instance, the muon data stream is created from the events, which pass at least one trigger requirement of the dedicated muon trigger menu. Data streams can share the same events, since the triggers from the different menus can accept the same events. For instance, an event with a t-quark pair production, where the final particles are an electron and a muon, can 'fire' both the calorimeter based and the muon spectrometer based triggers. This event would enter in both the muon and the so called egamma [6] data streams. In our study, we use data from the egamma stream, since we are interested in the events with an electron in a final state.

---

[6]It is the combined word from the two objects, electron and γ.

Chapter 4

ATLAS Data and Monte-Carlo Simulation

4.1 Data collected in 2010

We use ATLAS data, which has been recorded during the year 2010 under conditions of stable beams of colliding protons. The instantaneous luminosity of the colliding beams was increasing from 10^{27} cm^{-2}s^{-1} to the peak luminosity $2 \cdot 10^{32}$ cm^{-2}s^{-1}, which was reached during the last period of 2010 data taking. Figure 4.1a shows the peak instantaneous luminosity as a function of the data taking period. Figure 4.1b shows the average multiplicity of collision events per bunch crossing (BX) as a function of the data taking period. As one can see from the plot, the event rate was about 1-3 events per BX. We find in our study that a small rate of additional events has no significant impact on our measurement (see Section 8.6).

(a) $\alpha \leq 0$ (b) $\alpha \geq 0$
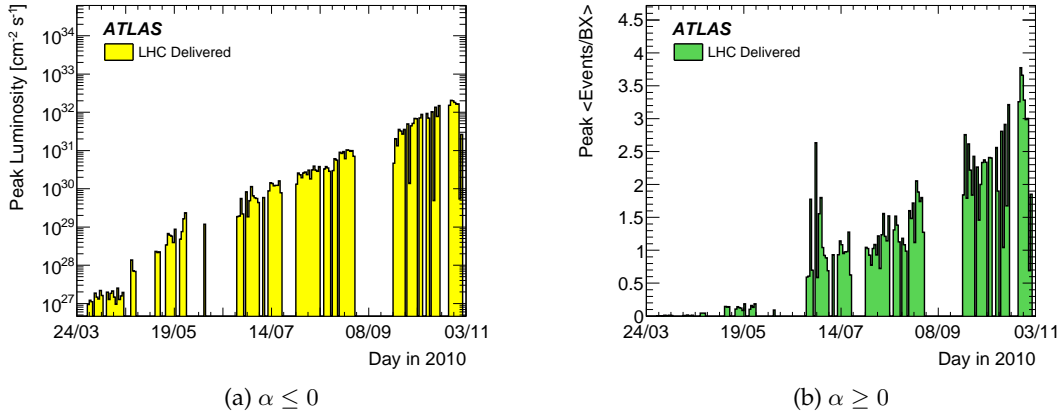
Figure 4.1: Instantaneous luminosity (left) and average number of events per bunch crossing (right) as functions of the data taking period.

Figure 4.2 present the total integrated luminosity of data recorded by ATLAS as a function of the data taking period. The plot also presents the integrated luminosity that has been delivered by the LHC machine. The ATLAS detector was able to maintain a high efficiency for data recording.

In our study, we select the part of the total recorded 45 pb^{-1} data according to data quality (DQ) requirements. These are the standard quality requirements [129], which are evaluated centrally in ATLAS. DQ are evaluated as for sub-detector systems also for the trigger system and the offline reconstruction of physics objects. The goal is to identify the data blocks, which are recorded while the hardware and software components of the detector were working properly and therefore, can be used in physics analysis. The total integrated luminosity of
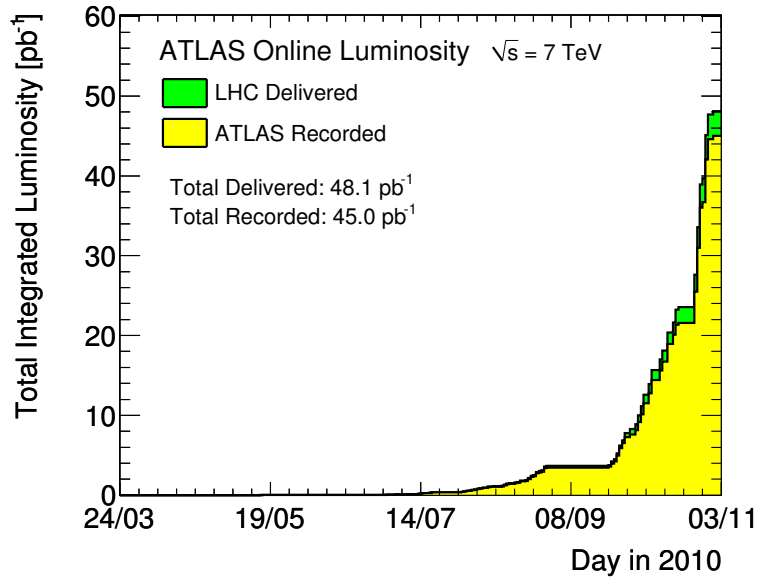
Figure 4.2: Total delivered integrated luminosity at LHC and data recorded data recorded by ATLAS as function of the data taking period in the year 2010.

data, which we select applying DQ requirements is 35.3 pb^{-1} and is known with an 3.4% uncertainty [130].

4.2 Monte-Carlo event simulation

Monte-Carlo simulation is an inevitable component of the ATLAS experiment in order to study the detector response to a wide variety of already known or still not observed, Standard Model or beyond the Standard Model physics processes. It consists of several steps [131] that should be carried out to produce simulated data to be used for the physics analysis. The first step is the detector-independent generation of collision events. It can be done by means of various external Monte-Carlo event generators interfaced by the ATLAS software framework Athena [132]. A generated event is a set of stable (at the events generation level) particles with defined four-momenta and flavors and represent our best knowledge of a real collision event. Development of a generated collision event can include productions and decays of particles, radiation of other particles and hadronization of strongly interacting particles. A particle is determined to be stable if it has a chance to reach the detector materials and interact with them before it decays. In the ATLAS detector Monte-Carlo simulation the 'stability' criterion applies to the lifetime of particles. If the lifetime of a given particle satisfies the requirement $c\tau > 10$ mm, then it is a stable particle at the event generation level. Obviously, all stable particles are colorless. Generated events are stored in a common HepMC [133] format and the record is referred to as truth.

The next step of the Monte-Carlo simulation chain is to propagate all these stable particles through the detector and simulate a realistic picture of the energy deposition in the sensitive parts of the detector [1]. Energy is deposited by the generated particles and the cascades of

---

[1]Special objects called calibration hits are designed to store energy deposition in any material of the detector and

secondary particles (normally, a few hundreds of thousands in one event) initiated by them after the interaction with the detector material. The GEANT4 toolkit [134] is used to perform this simulation. It relies on the detector geometry, which describe physical constructions and conditions (e.g. magnetic field, alignment of detector parts, dead read-out channels) of the detector. The ATLAS detector is built using the GeoModel [135] libraries [2] incorporated in the Athena framework. The detector geometry is translated into the GEANT4 format for the event simulation. The amount of deposited energy as well as the time and the position of the energy deposition are recorded in as so-called hits. Hits are associated read-out channels of any sub-detectors [3]. Truth objects of events are extended by including tracks and decays of the particles created during the detector simulation step. Figure 4.3 shows an example of the event simulation in the ATLAS detector using VP1 - a visualization software [136]. An $H \to 4\mu$ event can be viewed as the red tracks of muons passing through all sub-detectors. They deposit some fraction of their energy in the calorimeter cells presented as yellow boxes along the muon tracks. Inner detector tracks (green curves) are also visible, which belong mostly to low p_T charged particles.
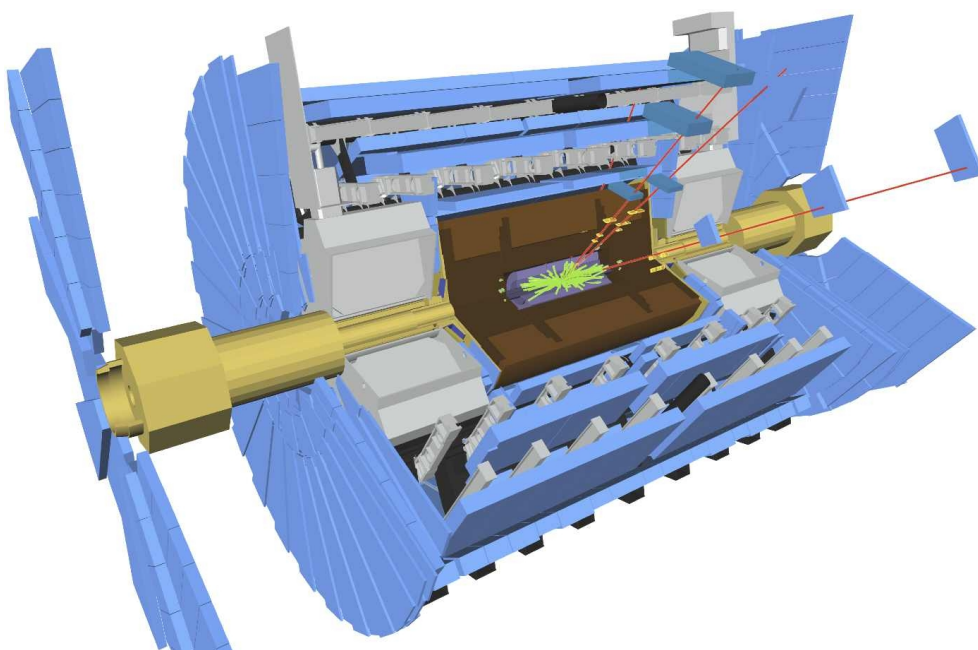
Figure 4.3: Visualization of the simulated $H \to 4\mu$ event [131] using VP1.

The last step of Monte-Carlo simulation of events is digitization of the simulation hits. At this step the energy deposited inside the sensitive parts of the detector is translated to an increase of a voltage or an electric current in a given read-out channel with further digitization

---

the supporting infrastructure. They are used for a Monte-Carlo based calibration of the calorimeter response to the incident particles.

[2] All tasks from the events simulation to the visualization of reconstructed events use GeoModel for building the detector geometry.

[3] Hits, which are geometrically contained in one readout cell of the calorimeter are merged into one final hit in the end of simulation of a given event. In contrast to that, hits in the inner detector and the muon system are not merged. The reason is that in the case of the calorimeter we are only interested in the amount of deposited energy, while in the tracking detectors we need every separated hit for reconstruction of particle tracks.

41

of this analog electronic signal. The output of digitization is recorded in so-called digits. Digits are inputs for further emulation of the detector read-out electronics, Read Out Drives (ROD), which produce the so-called Raw Data Objects (RDO). The digitization step is done by using algorithms dedicated to the corresponding sub-detectors [131, 137–139].

RDOs are the inputs for the offline reconstruction [140] of physical objects (e.g. tracks, electrons, muons and etc.) and HLT [141]. Data, which is produced by the real detector in the 'bytestream' format, is converted (optional) into the RDO format. Thus, after the digitization step, the Monte-Carlo simulated events and data are equivalently treated by the event reconstruction algorithms. L1 hardware based trigger is also simulated at the digitization step but no event rejection is done in contrast with the real situation, where useless collision events are rejected.

Up to now we were considering only the main and interesting type of collision events, which is the parton hard scattering occurring in proton-proton collisions. However, the real events seen by the ATLAS detector are overlaid with several types of background events. This overlay (superposition) is called pile-up. Proton-proton collision events, which happen during the same bunch crossing as the interesting collision event are the largest contributors in the pile-up. They are called the minimum bias events. At the nominal designed luminosity (10^{34} cm^{-2}s^{-1}) and the c.m. energy (14 TeV) of the LHC machine, the expected average number of proton-proton collision events in the ATLAS detector is 23 [3]. As we already saw in Figure 4.1b this number was smaller during the data taking period 2010, which makes less pile-up for the interesting proton-proton collision events. Minimum bias events from the preceding and the succeeding bunch crossings also contribute in pile-up, since the time windows for signal collection from the sub-detectors are usually larger [131] than the time between the neighbor bunch crossings. The signal collection time windows are determined due to the finite response time of the sub-detectors to the incident particles.

Neutrons, which are traversing the detector and are thermalized, produce the proton-electron gas in the cavern of the experiment. It is called the cavern background. The cavern background induces fake signal in the muon system. Impact on the cavern background on the other sub-detectors is negligible. Beam gas and beam halo events are the additional sources of background in the detector. Beam gas events are the collision events of the beam protons with hydrogen and other gases in the beam pipe. Similarly, beam interaction events with the material of the upstream infrastructure of the LHC ring and the ATLAS detector are called beam halo events.

Minimum bias events as well as other types of background events are simulated separately. They are mixed together with the hard scattering events at the digitization step to form realistic events with proper pile-up.

All the above described major steps of the Monte-Carlo simulation are brought together in the simulation software [142] of the Athena framework. Further processing of the simulated events, which implies reconstruction and identification of the physics objects (see Chapter 5), is done using the algorithms, which are integrated into the event reconstruction software of the Athena framework.

4.3 Monte-Carlo samples for the analysis

We use Monte-Carlo simulation for the signal (t-channel) and the SM background processes. Different Monte-Carlo event generators are used for generation of the samples. Most of the

samples, except di-bosons, are generated using two generators together. In the first place, the matrix element generators are used to generate hard scattering events. Further development of the event including initial/final state radiation and hadronization is done using a general purpose generator, which is either Herwig [143–145] or Pythia [146]. Herwig is used for generation of the di-bosons samples. Herwig and Pythia phenomenological hadronization models are tuned using the ATLAS data itself [147].

The samples are further simulated in the detector and reconstructed using the same versions of the detector geometry and conditions data bases as for data. Pile-up is added to the hard scattering events in order to simulate realistic events.

4.3.1 Top quark

All Monte-Carlo samples involving top quarks, t-channel, $t\bar{t}$ and Wt-channel are generated using the MC@NLO (version 3.41) matrix element generator [148–151]. The t-quark mass was assumed to be 172.5 GeV. The CTEQ6.6 parton distribution function set [152] is used for the description of colliding protons. Certain overlap arises between leading order $t\bar{t}$ and the next-to-leading Wt-channel diagrams in calculations [52, 53] of their cross sections[4]. MC@NLO solves the overlap by means of the dedicated diagram removal scheme [151]. Parton showering (ISR/FSR) and hadronization of the hard scattering events is done by Herwig.

Our study requires a prompt electron from the W decay in order to select the event (see Chapter 6). Events, where all heavy particles created in the hard scattering decay in hadronic modes have extremely small probability to fake the prompt leptons after the detector simulation and event reconstruction. In order to save computational time and resources the events without prompt leptons are not used. For the production of the t-channel sample it is required that $t \to bW(\to l\nu)$, where $l = e,\ \mu,\ \tau$. The $t\bar{t}$ process has two W's in events. It is required that at least one of them decays into leptons in order to be further simulated. No p_T or η cuts are applied to the leptons in the production of these three samples.

Due to the relatively smaller cross section of Wt-channel, an inclusive sample is produced for it.

We also use t-channel, Wt-channel and $t\bar{t}$ samples generated with the AcerMC matrix element generator [153] interfaced with Pythia for showering and hadronization of the hard scattering events. They are needed in order to study the systematic effect of the ISR/FSR modeling on the events selection acceptance, since the number of reconstructed jets (see Section 5.3) strongly depends on the ISR/FSR activity. AcerMC provides a way to vary the corresponding steering parameters and control the amount of ISR/FSR. In addition to the samples generated with the nominal values of the steering parameters, the additional samples are also generated with variations of these parameters. Selection of the events with prompt leptons (similarly to the above selection) is used when producing these samples. Table 4.1 summarizes the Monte-Carlo samples of the physics processes with t-quark production, their cross sections multiplied by the corresponding branching ratios (due to the selection of events with the prompt leptons) and the corresponding event generators. The NNLO inclusive cross sections are assumed for t-channel, Wt-channel and $t\bar{t}$ productions (see Table 2.1).

---

[4]In fact, the overlap exists at any higher order level corrections.

Table 4.1: Top quark production Monte-Carlo samples used in the study. The inclusive NNLO cross sections are multiplied by the corresponding branching ratios for t-channel and $t\bar{t}$ samples. For the Wt-channel sample the inclusive cross section is reported.

Sample	$\sigma \times BR$ [pb]	Generator
t-channel	20.92	MC@NLO+Herwig
Wt-channel	15.74	MC@NLO+Herwig
$t\bar{t}$	89.02	MC@NLO+Herwig
t-channel	20.92	AcerMC+Pythia
t-channel ISR/FSR	20.92	AcerMC+Pythia
Wt-channel	15.74	AcerMC+Pythia
Wt-channel ISR/FSR	15.74	AcerMC+Pythia
$t\bar{t}$	89.02	AcerMC+Pythia
$t\bar{t}$ ISR/FSR	89.02	AcerMC+Pythia

4.3.2 W/Z+jets

In general, the largest background to the t-quark signal processes [5] is the production of single vector bosons, W or Z, with accompanying hadronic jets, since they have relatively higher production cross sections and may have prompt leptons in the final states. The ALPGEN [154] leading order matrix element generator is used for generation of the hard scattering events with a single vector boson production. Showering and hadronization of the events is performed using Herwig. For the sake of an optimal usage of computational resources, only the events, where a vector boson decays leptonically (e, μ, τ) are further simulated and reconstructed. Associated partons (quarks and gluons) to a vector boson are generated at the matrix element level. Samples with different number of associated final partons (at the matrix element level) are generated separately. They are shown in Table 4.2. Corresponding cross sections, which consider the branching ratios of W/Z decays to leptons are also presented. The samples cross sections are normalized to the NLO prediction by multiplying their LO cross sections with the corresponding k-factors. The MCFM tool [56] is used to estimate the k-factors. The LO cross sections are provided by ALPGEN using CTEQ6L1 PDF set [152] in the events generation.

The W samples in the way they are produced have significant overlap between each other in the phase-space of the final state particles. For instance, an event with W, c-quark and d-quark in a final state before parton showering can exist in both samples, $W \rightarrow \ell\nu + 2\,partons$ and the $W \rightarrow \ell\nu + c + 1\,parton$. Parton showering also leads to some degree of duplication of final states between the listed samples. For instance, the same final state can occur in the $W \rightarrow \ell\nu + 1\,parton$ and the $W \rightarrow \ell\nu + b\bar{b} + 0\,parton$ production samples if in the former one the extra parton is a gluon and it splits up into a $b\bar{b}$-pair. This overlap between the samples is removed after the events are fully simulated and reconstructed. Then the samples are mixed

---

[5]Normally, it is studied in the single or the di-lepton final states with certain multiplicity of hadronic jets in association.

at the physics analysis level to form inclusive W+jets sample.

4.3.3 WW, WZ, ZZ

Di-boson events are generated using Herwig. Only the events with at least one boson decaying into a final state with electrons or muons are selected for further simulation through the detector. Corresponding branching ratios are calculated. The inclusive LO cross sections of the di-bosons samples are scaled to the NLO values using the proper k-factors calculated using the MCFM tool. Table 4.2 presents the inclusive NLO cross sections of these samples multiplied by the corresponding branching ratios.

4.3.4 QCD multi-jets

We use a data driven method to measure the QCD multi-jets background, which has a several orders of magnitude larger event production rate than other processes with t-quark, W or Z particles in the final states. We use the Monte-Carlo simulation sample called JF17 in order to test the data driven method (see Section 7.1.2). JF17 is generated using the Pythia generator and collects all hard scattering events described with $2 \rightarrow 2$ matrix elements in proton-proton collisions. Subsequent showering of partons and hadronization is performed by Pythia. Events, where at least one hadronic jet with $p_T > 17$ GeV are selected for further simulation through the detector. This sample is not a perfect model of QCD multi-jets production, since events with higher jet multiplicity are not well described using only parton showering and they should be generated at the matrix element level. However, we can still consider JF17 sample as a good model of the hard scattering events for a small number of jets. As we will see later, we are interested in this kind of events, since the t-channel signal events are also characterized with low jet activities.

Given the large expected rate of QCD multi-jets events and finite computational resources used in the production of the JF17 sample, its available number of produced events corresponds to about one-forth of the integrated luminosity of the collected data (35.3 pb^{-1}).

Table 4.2: Background non-t-quark samples used in the study. The cross-sections include the corresponding branching ratios (see the text).

Sample	$\sigma \times BR$ $[pb]$	Generator
$Z \to \ell\ell + 0$ parton	807.5	ALPGEN+Herwig
$Z \to \ell\ell + 1$ parton	162.6	ALPGEN+Herwig
$Z \to \ell\ell + 2$ partons	49.2	ALPGEN+Herwig
$Z \to \ell\ell + 3$ partons	13.7	ALPGEN+Herwig
$Z \to \ell\ell + 4$ partons	3.3	ALPGEN+Herwig
$Z \to \ell\ell+ \geq 5$ partons	1.0	ALPGEN+Herwig
$W \to \ell\nu + 0$ parton	8,400	ALPGEN+Herwig
$W \to \ell\nu + 1$ parton	1,580	ALPGEN+Herwig
$W \to \ell\nu + 2$ partons	460	ALPGEN+Herwig
$W \to \ell\nu + 3$ partons	123	ALPGEN+Herwig
$W \to \ell\nu + 4$ partons	31	ALPGEN+Herwig
$W \to \ell\nu+ \geq 5$ partons	8.5	ALPGEN+Herwig
$W \to \ell\nu + b\bar{b} + 0$ parton	55.6	ALPGEN+Herwig
$W \to \ell\nu + b\bar{b} + 1$ parton	41.1	ALPGEN+Herwig
$W \to \ell\nu + b\bar{b} + 2$ partons	20.4	ALPGEN+Herwig
$W \to \ell\nu + b\bar{b}+ \geq 3$ partons	7.7	ALPGEN+Herwig
$W \to \ell\nu + c\bar{c} + 0$ parton	155.6	ALPGEN+Herwig
$W \to \ell\nu + c\bar{c} + 1$ parton	125.9	ALPGEN+Herwig
$W \to \ell\nu + c\bar{c} + 2$ partons	63.1	ALPGEN+Herwig
$W \to \ell\nu + c\bar{c}+ \geq 3$ partons	20.6	ALPGEN+Herwig
$W \to \ell\nu + c + 0$ parton	526.2	ALPGEN+Herwig
$W \to \ell\nu + c + 1$ parton	195.3	ALPGEN+Herwig
$W \to \ell\nu + c + 2$ partons	51.8	ALPGEN+Herwig
$W \to \ell\nu + c + 3$ partons	12.1	ALPGEN+Herwig
$W \to \ell\nu + c+ \geq 4$ partons	2.8	ALPGEN+Herwig
WW	17.9	Herwig
WZ	5.4	Herwig
ZZ	1.2	Herwig

Chapter 5

Physics objects reconstruction and selection

In the following chapter details of the selection of the physics objects are discussed. These objects are used to reconstruct an event out of each proton-proton collision recorded by the ATLAS detector. Reconstructed events are later classified as signal-like or background-like based on properties of these objects.

Physics objects are the final products of the ATLAS offline reconstruction software and have well defined physics meaning. These are the tracks of charged particles and their production vertices of the interaction or the decay types, electrons, photons, muons, taus, hadronic jets, missing transverse energy $\not{E}_T$. Reconstruction and identification of these objects in data is performed in several steps of online and offline processing of proton-proton collisions. Monte-Carlo simulation of the collisions does not require online event reconstruction steps but needs Monte-Carlo generation of the events independently of a detector and later, simulation of further development of these events in the ATLAS detector (see Chapter 4). After the detector response is simulated the Monte-Carlo events are presented in the same storage format as data and all objects reconstruction and identification procedures are equivalently applied to both [155].

In this study the standard procedures of object selection are used. These procedures are common for the top quark production related searches in the ATLAS experiment, which use the same data and Monte-Carlo samples. The selection details of electrons, muons, jets and $\not{E}_T$, which are important in this measurement are provided. The b-tagged jets selection is also described.

5.1 Electrons

Electrons are reconstructed using information from the calorimeter and the inner detector. Reconstruction algorithms are defined for two separate regions of the detector. The central region is defined as $|\eta| < 2.5$, which is the inner detector coverage region and thus, provides a possibility for tracking. Electron reconstruction in the side regions, defined as $2.5 < |\eta| < 4.9$, can not use charged particle tracks and have to rely only on the calorimeter information. Only in those events, which have an electron in the central region are of interest to this study. Therefore, we will be concentrated only on issues related to the central electrons such as its reconstruction, identification, energy scale calibration and resolution. Central electrons are reconstructed and identified with a high efficiency, while keeping the fake electrons rejection at the order of 10^5 [156, 157].

Electron reconstruction starts with finding an energy cluster in the electromagnetic calorimeter ($|\eta| < 2.47$) using a 'sliding window' algorithm [158]. The window is defined in the $\eta \times \phi$ space and has a size of $(3 * 0.025) \times (5 * 0.025)$. Here, 0.025 is the granularity of the

EM middle layer in radians for both η and ϕ dimensions. If the cluster with a transverse energy (in the electromagnetic scale) above 2.5 GeV is found, then the next step is to find a matching track to the cluster within the range of $|\eta| < 2.5$. The cluster reconstruction has a very high efficiency. According to Monte-Carlo simulation it is 100% for the central electrons with $E_T > 15$ GeV [156] Therefore, this is taken as a base for the reconstruction efficiency measurement (see below).

The distance between a track and a cluster is measured in terms of η and ϕ. Namely, a difference between cluster η (ϕ) and η (ϕ) of the impact point of an extrapolated track to the EM middle layer is taken. A track matches a cluster if $\Delta\eta$ and $\Delta\phi$ are less than a given threshold value. Thresholds are tightened at the identification stage, when the quality of an electron candidate is evaluated. If there are several matching tracks, then those tracks, which have hits in the SCT detector are preferred. The matching track, which has the smallest ΔR is associated to an electron candidate. Electron cluster are re-built using a larger window, $\eta \times \phi = 3*0.025 \times 7*0.025$ ($5*0.025 \times 5*0.025$) in the barrel (end-caps) region of the electromagnetic calorimeter. Once the electron candidate is reconstructed, its energy is corrected due to the several issues. These are electron energy loss in materials in front of the calorimeter; energy deposition outside of the cluster (lateral leakage) and behind the cluster (longitudinal leakage) [155].

After corrections the cluster energy is taken for calculation of a four-momentum of the electron candidate, while the direction of the electron momentum vector is determined by η and ϕ of the matched track at its production vertex.

Calibration of the electro-magnetic calorimeter response to electrons is done using data from test-beam runs [159–162]. Energy corrections due to the material in front of the sensitive regions of the electro-magnetic calorimeter and out of cluster energy depositions are derived using Monte-Carlo simulation. In-situ inter-calibration of the electron energy scale in different pseudo-rapidity regions is made using a purified sample of $Z \to ee$ data [156] assuming the known mass of the Z boson. The scale accuracy within 1% for all pseudo-rapidity regions for electrons with $E_T > 20$ GeV is reached.

The energy resolution of electrons is found to be worse in data then in Monte-Carlo simulation. The constant term, c, of the electron energy resolution parameterization,

$$\frac{\sigma_E}{E} = \frac{a}{\sqrt{E}} \oplus \frac{b}{E} \oplus c \tag{5.1}$$

appears to be underestimated in Monte-Carlo simulation. The sampling term, $a/\sqrt{E}$ is modeled correctly with 10% uncertainty. This is confirmed by the good agreement between data and Monte-Carlo simulation for the reconstructed mean and width of the $J/\psi \to ee$ mass peak [156], which is sensitive to the sampling term due to the lower kinematic region. The noise term, b/E, has no significant impact at energies of interest and besides, it is well known from the calorimeter calibration. The constant term was estimated from a qualitative comparison of the distributions of an invariant mass of two oppositely charged electrons in the $Z \to ee$ samples extracted from data and produced by Monte-Carlo simulation. The resulting values are $c = 1.1 \pm 0.1(\text{stat}) \pm 0.2(\text{syst})$ for electrons in the $|\eta| < 1.37$ region and $c = 1.8 \pm 0.4(\text{stat}) \pm 0.2(\text{syst})$ in the $1.52 < |\eta| < 2.47$ region.

The electron energy is corrected in data. In the Monte-Carlo samples the energy of electrons is smeared in order to have the same resolution as in data. Later, we vary the energy scale correction factors and the energy smearing parameterization parameters within their

measurement uncertainties for the Monte-Carlo electrons. In such a way the corresponding systematic uncertainties of event yields of the signal and the background are evaluated (see Chapter 8).

The quality of a reconstructed electron is evaluated by checking against one or two-sided cuts on variables which characterizes a cluster, a track or both together (e.g. $\Delta\eta$ and $\Delta\phi$ between a cluster and a matching track as defined above). We use the tight quality requirements [157] in a selection of electrons.

In addition to the tight requirement for an electron candidate, it is also required to be isolated. This means that the energy deposition in those calorimeter readout cells, which are aligned around the electron cluster within some ΔR cone has to be small. Only those cells that do not belong to the cluster (out-of-cluster cells) are considered. Energy deposited in those readout cells of the hadronic calorimeter, which fall in the cone is also taken into account. The reason for this requirement is the aim to select events, where an electron comes from a W decay, a prompt electron, and reject those events, where a selection electron is a product of some heavy flavor decay within a hadronic jet, a non-prompt electron, or it is a hadronic jet itself wrongly reconstructed/identified as an electron. Both the non-prompt and fake electrons tend to have a higher amount of deposited energy in the vicinity, since they are products of hadronic jets activity, when the energy deposition expands over a larger region in the calorimeter. Electron isolation requirement is found to be an effective way of suppressing the QCD multi-jets background. QCD multi-jets production has a large cross section and because of this it is the main source of non-prompt and fake electrons.

By analogy to the calorimeter isolation definition, the tracking isolation is also defined. Here the sum of transverse momentum of those inner detector tracks, which are found within some cone around an electron track is required to be small. We use the isolation criteria optimal for rejection of fake electrons,

$$\begin{cases} E_{\text{calo}}^{\Delta R < 0.3}/E_T < 0.1 \\ p_{T\,\text{track}}^{\Delta R < 0.3}/E_T < 0.15 \end{cases} \tag{5.2}$$

Here, $E_{\text{calo}}^{\Delta R < 0.3}$ and $p_{T\,\text{track}}^{\Delta R < 0.3}$ are the total transverse energy of the out-of-cluster cells and the total transverse momentum of the extra tracks respectively. Both are calculated within the cones defined as $\Delta R < 0.3$. E_T is a module of the transverse momentum of an electron measured in the calorimeter [1].

We require that the tight isolated electron has $p_T > 20$ GeV and $|\eta| < 2.47$ but not $1.37 < |\eta| < 1.52$ that is the transition region between the central barrel and the end-caps of the electromagnetic calorimeter.

In order to minimize a possible systematic bias in a cross section measurement the electron selection efficiency in the Monte-Carlo simulation is corrected by using data-driven methods. The selection efficiency can be factorized in the reconstruction and the identification efficiencies. Both efficiencies are measured using the 'tag and probe' ($T\&P$) method [163]. In general, the method calculates an efficiency for the probe object to pass some requirements a-priori knowing that it is the interesting sort of object. This prior knowledge is based on information from the tag object. Purified $Z \to ee$ samples extracted from data and samples produced by Monte-Carlo simulation are used to measure electron reconstruction and identification efficiencies. If there is an electron in a given event, which passes all above listed

---

[1]Usually, E_T denotes the transverse energy defined as $E_T = \sqrt{p_T^2 - m^2}$. Due to the tiny mass of an electron E_T value can be replaced with the module of p_T but the E_T notation is kept.

requirements, then the $T\&P$ algorithm is looking for the other cluster, which satisfies the requirements $|\eta_{clus}| < 2.47$ and $E_{T,clus} > 2.5$ GeV. If it is found and the invariant mass of these two objects (the good electron and the cluster) lies within the predefined limits around the Z mass, then this event is selected as a $Z \to ee$ candidate. Thus, the good electron serves as a tag to the cluster to identify it as a probe electron. The ratio of the number of probes, $N_{\text{reco}}^{\text{probe}}$, which have a matching track satisfying the electron reconstruction requirements (discussed above) over the total number of probes, N^{probe}, is the reconstruction efficiency,

$$\epsilon_{\text{reco}} = \frac{N_{\text{reco}}^{\text{probe}}}{N^{\text{probe}}} \tag{5.3}$$

Reconstruction efficiencies averaged over the pseudo-rapidity and the transverse energy of electrons were measured in both data and Monte-Carlo $Z \to ee$ samples and their statistical and systematic uncertainties ware evaluated as well [156]. The corresponding scale factor, which will be used for Monte-Carlo events weighting (see Section 6.3) in order to account for the small observed difference between the reconstructed efficiencies in data and Monte-Carlo simulation was calculated [156], $SF_{\text{reco}} = \epsilon_{\text{reco}}^{\text{data}}/\epsilon_{\text{reco}}^{\text{MC}} = 1.005 \pm 0.001(\text{stat.}) \pm 0.002(\text{syst.})$.

In the next step, the electron identification efficiency is calculated in the sample of the reconstructed probe electrons, $N_{\text{reco}}^{\text{probe}}$, using the equation,

$$\epsilon_{\text{ID}} = \frac{N_{\text{reco+ID+iso}}^{\text{probe}}}{N_{\text{reco}}^{\text{probe}}} \tag{5.4}$$

Were, $N_{\text{reco+ID+iso}}^{\text{probe}}$ is the number of the probe electrons, which satisfy tight quality requirements, are isolated (Equations 5.2) and pass η and p_T selection cuts (see above). Thus, they satisfy the same selection requirements as the tag electrons. Identification efficiencies in both data and Monte-Carlo samples were calculated in 8 bins of pseudo-rapidity and in 6 bins of E_T for the probe electrons. Corresponding scale factors, SF_{ID}, were computed similarly to SF_{reco} with the same binning as the identification efficiencies. We use the identification efficiency scale factors similarly to the reconstruction scale factors for a calculation of the selected Monte-Carlo event weights (see Section 6.3). The scale factors are varied within their uncertainty ranges in order to asses corresponding systematic uncertainties of the event yields (see Chapter 8).

5.2 Muons

Muons used in this study are reconstructed using tracks in ID and MS. A muon track is formed by combining a MS track with an ID one, while both tracks are reconstructed independently from each other. The algorithm for combined muon reconstruction tries to find a matching MS track to a given ID track. When such a MS track is found, the algorithm re-fits the muon hits in ID and MS, which belong to the ID and MS tracks. Some wrongly assigned muon hits in MS can be dropped from the fit or some missing hits can be recovered. Pseudo-rapidity region, where combined muons are reconstructed is determined by the inner detector coverage, $|\eta| < 2.5$. We apply additional quality requirements [164] to a combined muon track in ID, which are related to multiplicity of muon hits in each ID sub-detectors, Pixel, SCT and TRT. This helps to increase the purity of a selection of the prompt muons.

Comparison of $Z \to \mu\mu$ samples produced by Monte-Carlo simulation and extracted from

data showed that the resolution of muon transverse momentum reconstruction is more optimistic in Monte-Carlo simulation. Similarly to the electron energy smearing procedure aiming to obtain the same resolution in data and Monte-Carlo simulation, a dedicated muon transverse momentum smearing algorithm is applied. The smearing procedure is applied to muons p_T after the ID track quality requirements (mentioned above) are applied. The acceptance and isolation cuts are applied only after this.

We are interested to select prompt muons in our analysis, which are the W decay products. Production of non-prompt muons in mainly heavy flavor hadron decay processes in hadronic jets is the important background. In order to reduce non-prompt muon background, we use calorimeter and tracking isolation requirements as it was the case of electrons,

$$\begin{cases} E_{\text{calo}}^{\Delta R < 0.3} < 4 \, \text{GeV} \\ p_{T\,\text{track}}^{\Delta R < 0.3} < 4 \, \text{GeV} \end{cases} \tag{5.5}$$

Additionally, we apply a requirement that $\Delta R > 0.4$, where ΔR is calculated between a muon and its closest hadronic jet. Only those jets, which have the calibrated (to the hadronic scale of energy) transverse momentum larger than $20\,\text{GeV}$ are considered. If a muon does not satisfy this requirement we reject the event.

Finally, we require that $p_{T\,\mu} > 20\,\text{GeV}$ and $|\eta_\mu| < 2.5$.

Detailed study of the muons reconstruction and identification efficiencies in data and Monte-Carlo simulation samples were performed [164, 165]. High precision measurements using the $T\&P$ method were performed for the different p_T ranges of combined muons and with a granularity in their pseudo-rapidity and azimuthal angle. The granularity is determined by the detector geometry considering the available amount of data. We do not provide a description of this study, since our analysis is not affected by the muon selection efficiency corresponding scale factors as it is in the case of electrons. As it will be shown later, we explicitly veto events with muons in order to reduce the di-lepton background. Therefore, muon reconstruction, identification or trigger efficiency related scale factors do not imply any corrections to the weights of selected events of Monte-Carlo signal and background samples.

5.3 Jets

Hadronic jets are reconstructed using the anti-k_T algorithm [166] with the cone size parameter 0.4. Inputs for the algorithm are the topological clusters [167]. Topological clusters (topoclusters) are built by a dedicated algorithm [158], which starts by finding a seed calorimeter cell for further clustering of the neighbor cells around the seed. A seed is required to have the deposited energy larger than some threshold number times the noise in the seed cell (in our case the threshold number is 4). Algorithm is able to split up the already created cluster if two or more seed cells are found. This helps to improve jet energy scale calibration and resolution.

Several jet energy calibration schemas have been developed. The goal of calibration is to have a jet energy, which is an unbiased estimator of the total energy of associated particles [155]. All algorithms starts calibrating a jet energy, which is already measured at the electromagnetic (EM) scale.

We use the simplest jet energy calibration. The EM+JES (electromagnetic plus jet energy scale) scheme, which is based on the corrections derived from Monte-Carlo simulation of jets or from single hadron test beam data [168]. Uncertainties of JES are induced by many detector

or physics related factors. Jet activity covers a large part of the detector and the loss of an important fraction of its energy in the non-sensitive material of the detector is unavoidable. Reconstructed topo-clusters can miss some calorimeter cells, which have deposited energy and should belong to a given jet. This out-of-cluster energy loss needs to be taken into account when calibrating JES. Also, some fraction of the energy of initial partons are taken away by neutrinos created in the weak decays of hadrons. Jet constituent hadrons (e.g. neutrons) interact with the nuclei of the detector material. A significant fraction of energy is lost (or obtained) as a compensate for the binding energy of nucleons, which are kicked out from the nuclei of the detector material. The events with high multiplicity of jets suffer from larger uncertainties of JES because of jets overlapping. On the other hand, jets multiplicity is highly correlated to the underlying physics processes. Therefore, additional corrections are applied to jets after a given event is identified as a candidate of a certain physics process. Calibration of the jet energy scale and related uncertainties were studied in the ATLAS experiment in details [169].

Jets energy and momentum are computed using the corrected energy and the momentum direction is taken with respect to the reconstructed collision point (primary vertex).

We apply no p_T cut to jets at the object selection level. Jet pseudo-rapidity has to be within the range, where the JES calibration is available, $|\eta_{jet}| < 4.5$. The jet reconstruction algorithm reconstructs also true electrons as jets. Therefore, we remove jets, which spatially overlap with one of the already selected electrons. This means that a jet is removed from the analysis if $\Delta R(\text{jet}, \text{electron}) < 0.2$.

Jets are reconstructed using the calorimeter cells, where the electronic noise can significantly fluctuate upward (burst). This behavior of the calorimeter has been studied [129] and the jet reconstruction can tag such jets as 'bad' quality. The presence of 'bad' jets in an event can introduce significant imbalance in the events kinematics [169]. Events, where such a 'bad' quality jet, with p_T(electromagnetic scale) > 10 GeV is found are rejected in data.

5.4 b-tagged jets

The top quark related studies benefit by the identification of jets, which contain b-flavored hadrons. The reason is that t-quark decays almost exclusively into W and b-quark. b-quark is energetic enough to induce a hadronic jet with high p_T in the calorimeter. A possibility to identify such a jet helps to significantly reduce other background processes characterized by light quark production. b-jet identification algorithms are based on the fact that the b-flavored hadrons have relatively long life-time and can fly some distance in the detector before decaying. The ATLAS tracking system is able to distinguish this decay vertex (called secondary) from the primary vertex. We use the so-called SV0 algorithm [155] for the identification of b-jets. It tries to find two or more tracks among those, which are associated to a given jet and have a common production vertex significantly displaced from the primary vertex. A fitting procedure is used to reconstruct the secondary vertex, which associates σ, the three dimensional uncertainty, to its distance from the primary vertex to the fitted position, denoted as L. A given jet is assigned a b-tagging weight, $w_{b-\text{tagging}}$, which is the ratio of L/σ.

Requiring $w_{b-\text{tagging}} > 5.85$ corresponds to the 50% tagging efficiency of truth b-jets in the $t\bar{t}$ Monte-Carlo sample considering all jets with $p_T > 15$ GeV and $|\eta| < 2.5$. The last requirement is naturally determined by the pseudo-rapidity coverage of the inner detector.

5.5 Missing transverse energy

The ATLAS detector cannot detect neutrinos and therefore, a vectorial sum of transverse momenta of all detected particles is not (close to) zero in all events as expected. The energy of jets is corrected for the missing contribution of the neutrinos created in hadrons weak decays inside jets. Therefore, the observed missing transverse energy can be a measure of the transverse momentum of those neutrinos, which are produced in the W leptonic decays. It serves as a good discriminating variable between the physics processes with and without W production [2]. Precise reconstruction of missing transverse energy, $\not{E}_T$, is rather challenging work. Reasons for this are the limited detector coverage, a large amount of insensitive material between the different sub-detectors of the calorimeter and its dead readout cells, pile-up, cosmic-ray and beam-halo muons, detector finite resolution in the energy reconstruction of physical objects etc.

$\not{E}_T$ is reconstructed using the calorimeter and the muon spectrometer information [170]. It relies on the final selection of objects after they are reconstructed and identified considering an overlap removal between the objects. Systematic variation of objects energy-momentum is propagated in calculation of $\not{E}_T$. The corresponding uncertainties of the Monte-Carlo event yields are obtained in such a way.

---

[2]Here, we consider only the Standard Model processes.

Chapter 6

Event selection

In this chapter the details of the event selection of the analysis are discussed. The goal of the event selection is to achieve the highest possible fraction of t-channel events in data as predicted by Monte-Carlo simulation. A level of background suppression determines precision of a signal measurement. The reason is that a background contribution is estimated from Monte-Carlo simulation or from a dedicated auxiliary measurement and has some uncertainty. If the background contribution is relatively large, then its uncertainty significantly affects a signal estimate in data. When signal has smaller cross section with respect to background often there is a trade-off between purification (in terms of a signal fraction) of data and a number of selected events. This is due to the fact that the precision of a measurement is determined by the statistical and systematic uncertainties. By tightening the event selection criteria one can reach higher purification and thus, the systematic component of the final uncertainty is reduced. But this can lead to a very small data size, which implies that the statistical uncertainty of the measurement is large. Therefore, one needs to keep an optimal balance between the two uncertainties.

Certain types of background processes are not well modeled by Monte-Carlo simulation or/and their theoretical cross section is not well known. The data driven methods for their measurement are necessary. In our study, the QCD multi-jets and W+jets production processes, which have significant impact on the measurement need to be measured using data. In parallel to searching for the best signal selection region, we also define the control regions, where QCD multi-jets contribution is extremely high. Later (see Chapter 7), we propagate the QCD multi-jets measurement in the control regions to the signal region. This itself helps to measure the W+jets contribution in in the signal regions.

6.1 Single top t-channel topology

t-channel events are characterized by one isolated lepton with a relatively high transverse momentum, which is a decay product of W[1]. An energetic b-tagged jet is expected in the central region of the detector, which is initiated by the b-quark from the t-quark decay. A spectator light quark from hard scattering, which tends to have a small transverse momentum is expected to be reconstructed as a jet in the forward region of the detector. Finally, a neutrino from the W leptonic decay also tends to be central and therefore, sizable missing transverse energy is expected. Figure 6.1 shows an illustrative drawing of a Feynman diagram [39] of a t-channel event. Initial and final state radiation changes the above idealistic configuration

---

[1]Hadronic decay modes of W are not considered, since this kind of events would be very difficult to select out of the QCD multi-jets background.

of events. Also, bottom quarks from gluon splitting can initiate an additional *b*-jet as can be seen in Figure 6.1.
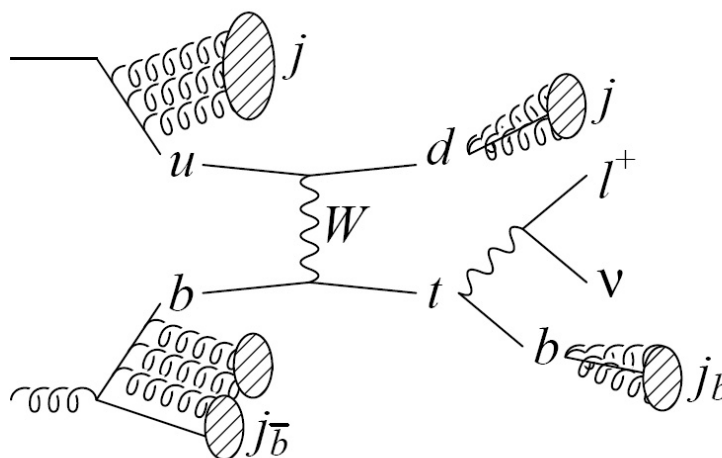
Figure 6.1: t-channel event topology [39].

We base our t-channel signal selection on the above listed characteristic features. The selection requirements are described in the following sections.

6.2 Trigger and cut selection

A HLT requirement is applied to data and Monte-Carlo events in order to select signal candidates. The trigger, which we use in our study selects events with energetic electrons of a 'medium' quality. It utilizes a dedicated L1 trigger decision if an electromagnetic cluster is reconstructed in the calorimeter with $E_T > 10$ GeV at the electromagnetic energy scale. For the HLT, the cluster object is required to have a matching track in the inner tracker and its transverse energy threshold is increased to 15 GeV. The trigger efficiency has a plateau starting from $p_T = 20$ GeV of reconstructed (offline) electrons. Its efficiency in the plateau region is found to be $\simeq 100\%$ and slightly worse in data than in Monte-Carlo simulation. This difference is accounted for by the scale factor equal to 0.995 ± 0.005.

We require that at least one of the reconstructed electrons is matched to the trigger electron candidate object, which caused the trigger to make a true decision. Matching implies the spatial coincidence of these two objects with $\Delta R < 0.15$. The requirement of matching is needed in a calculation of the trigger efficiency. Thus, in the event selection we do the same such that we can use the trigger efficiency scale factors to determine the Monte-Carlo event weights.

The leading (largest transverse momentum) electron in an event is required to have $p_T > 20$ GeV. This threshold is chosen because the trigger efficiency is not constant [2] for electrons with $p_T < 20$ GeV and on the other hand, contribution of fake electrons (originated from low energy jets) increases at low p_T. We also do not choose a higher threshold, since this

---

[2]This leads to the variable scale factor for the trigger efficiency that is hard to measure.

would lead to a reduction of signal. This can be seen in Figure 6.2, which shows the electron p_T distribution for Monte-Carlo signal and background after the trigger+matching+leading electron selection with data superimposed.
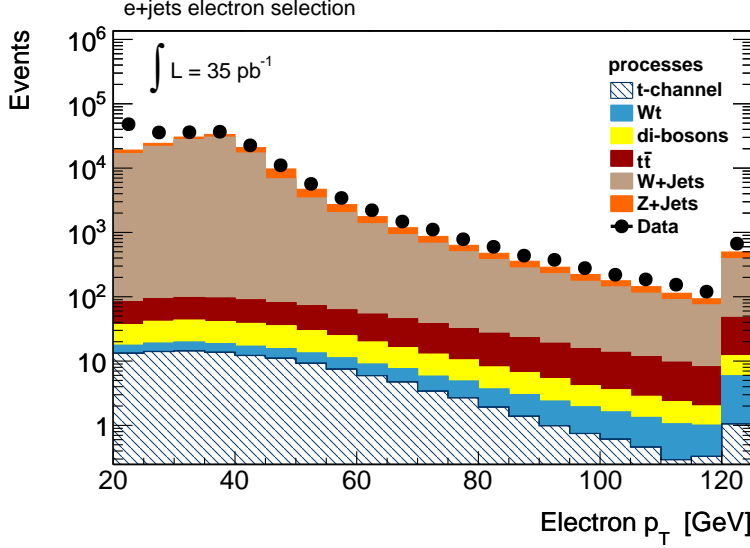
Figure 6.2: Electron p_T distribution after the trigger, the electron to trigger matching and the high p_T electron requirements are applied. The last bin contains overflow. QCD multi-jets contribution absents in the plot due to the lack of its simulated sample.

Further, we define two regions according to the pseudo-rapidity of the electron: 1) central region, $|\eta_e| < 1.37$; 2) combined sides, $1.52 < |\eta_e| < 2.47$. We use these two regions in order to account for the electron reconstruction+identification dependence on η_e or the expected signal and background fractions, which depend on η_e as well (see Table 6.2).

An event is rejected if it has more than one electron or extra muon(s) with $p_T > 20$ GeV. This helps to reduce the di-lepton background from the production of $t\bar{t}$, Wt-channel and di-bosons, while keeping the t-channel event yield unchanged (see Figure 6.8).

After selecting events with proper lepton configuration, we require two different configurations of jets, which have $p_{T\,jet} > 25$ GeV. The first selection is based on the expectation for t-channel, which predicts one central and one forward jet. Here, a jet is defined to be central if $|\eta_{jet}| < 2.5$. If $2.5 < |\eta_{jet}| < 4.5$, then the jet is forward, where the upper pseudo-rapidity threshold is determined by the availability of a calibration of the jet energy scale. The central jet pseudo-rapidity threshold is determined by the inner detector coverage and b-jets can be identified in this region only. Previous analysis [171] to our study was making use of two jet requirement without looking at the centrality of the untagged jet. We find that rejecting events with both jets in the central region significantly reduces the expected event yields of $t\bar{t}$ and other background. Comparison of the final event yields with and without the forward jet requirement can be seen in Table 6.1. The expected signal yield is also reduced but the advantage is that the measurement precision is less sensitive to the background (except of W+jets) event rate uncertainties.

The second configuration of jets is a selection of a control region and is aimed to an auxiliary measurement of QCD multi-jets and W+jets contribution in the signal selection as was already mentioned above. The requirement is to have exactly one central jet, $|\eta_{jet}| < 2.5$, in an event.

It is required to be a b-jet. Then the selected events are dominated by QCD multi-jets and the heavy flavored jets component of W+jets. This can be seen in Figure 6.3, which presents a $\not{E}_T$ distribution in events with only one b-jet.

(a) $|\eta_e| < 1.37$ (b) $1.52 < |\eta_e| < 2.47$
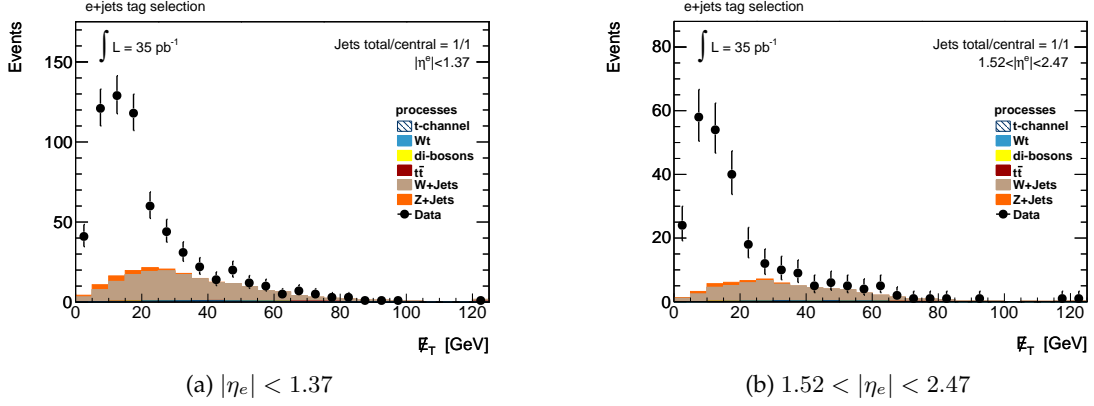
Figure 6.3: $\not{E}_T$ distributions in the selected events with one b-tagged jet. The left plot corresponds to the events, where the electron is in the central region. The right plot corresponds to the events with the electron is in one of the side regions. QCD multi-jets contribution absents in the plots due to the lack of its simulated sample.

We find that the b-jet requirement significantly reduces Z+jets and light flavored jets component of the W+jets backgrounds. Figure 6.4 presents a comparison between the $\not{E}_T$ distributions before (left plots) and after (right plots) requiring a central jet to be b-tagged in the events with one central and one forward jet. These plots show that the Z+jets contribution is significantly suppressed and the W+jets contribution is also reduced.

The last requirement of the selection is a kinematic cut on a variable introduced for QCD multi-jets suppression. The 'triangular variable' is a sum of $\not{E}_T$ and the reconstructed W boson transverse mass and we require it to be higher than 60 GeV. The W boson transverse mass depends on $\not{E}_T$ and is defined as,

$$m_T(W) = [2E_T(e)\not{E}_T(1 - \cos\Delta\phi)]^{1/2} \tag{6.1}$$

Where, $E_T(e) \simeq |p_T(e)|$ is the module of the electron transverse momentum and $\Delta\phi = \min[\phi_{\not{E}_T} - \phi_{p_T(e)}, 2\pi - (\phi_{\not{E}_T} - \phi_{p_T(e)})]$. $\phi_{\not{E}_T}$ and $\phi_{p_T(e)}$ are the azimuthal angles of $\not{E}_T$ and $p_T(e)$ vectors.

In Chapter 7 dedicated to the data driven measurements of background, we show that the triangular variable gives a powerful separation of QCD multi-jets background from the rest and the region below 60 GeV can be used as a control region. Figure 6.5 shows the two-dimensional distributions of $\not{E}_T$ versus $m_T(W)$ in data (left plot) in the simulated W+jets sample (right plot). These distributions are made in the events after the trigger (with electron matching) and the high p_T electron requirements are applied. We learn from these distributions that W like events and other events, which do not have W boson can be well separated with the triangular cut. The cut $\not{E}_T + m_T(W) > 60$ GeV is represented on the plots as red lines.

After the selection requirements are applied, good purification of the signal region is reached. All background processes except W+jets and QCD multi-jets are well suppressed. Figure 6.6

(a) w/o b-tagging, $|\eta_e| < 1.37$

(b) with b-tagging, $|\eta_e| < 1.37$

(c) w/o b-tagging, $1.52 < |\eta_e| < 2.47$

(d) with b-tagging, $1.52 < |\eta_e| < 2.47$
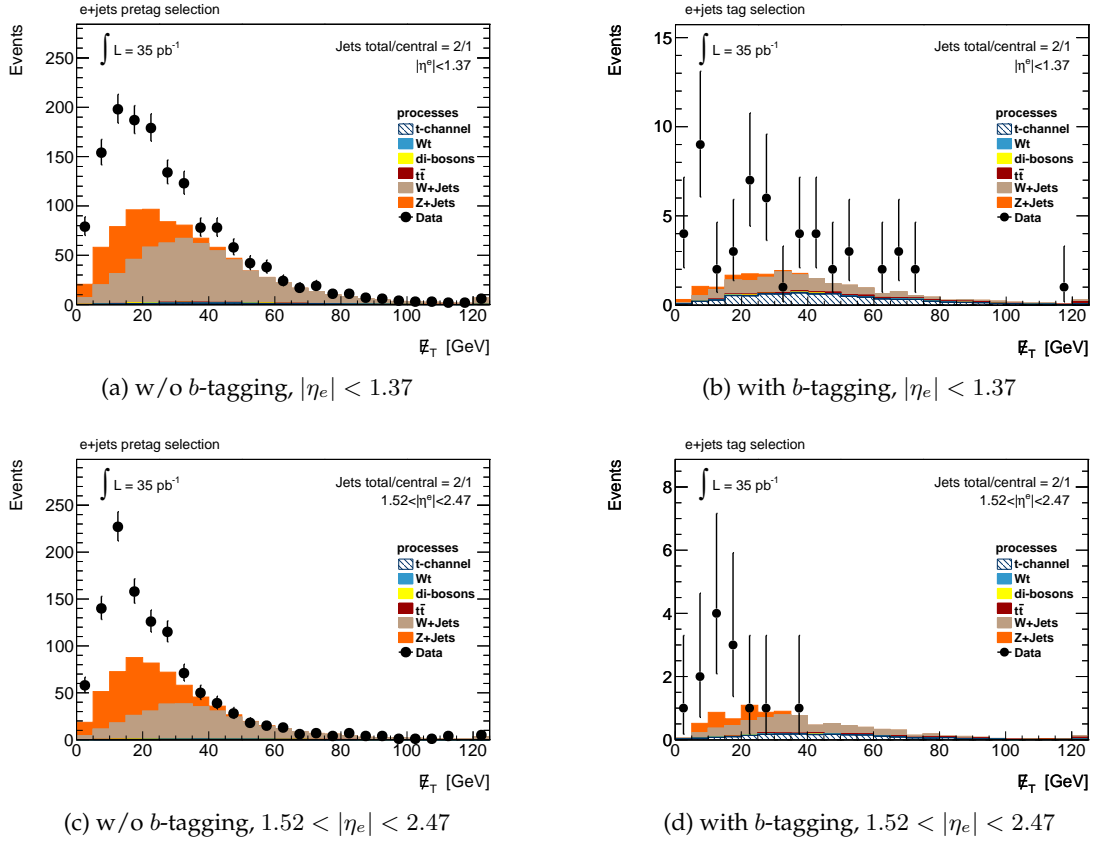
Figure 6.4: $\not{E}_T$ distributions in the selected events with 2 jets (one central and one forward) before (left plots) and after (right plots) applying the b-jet requirement. The top row plots correspond to the events, where the electron is in the detector central region. The bottom row plots correspond to the events with the electron in one of the side regions. QCD multi-jets contribution absents in the plots due to the lack of its simulated sample.

shows $\not{E}_T$ distributions in the events remaining after all selection requirements are applied. The left plot corresponds to the selected events with a central electron and the right plot is for the events with a side electron.

(a) Data

(b) W+jets, Monte-Carlo simulation
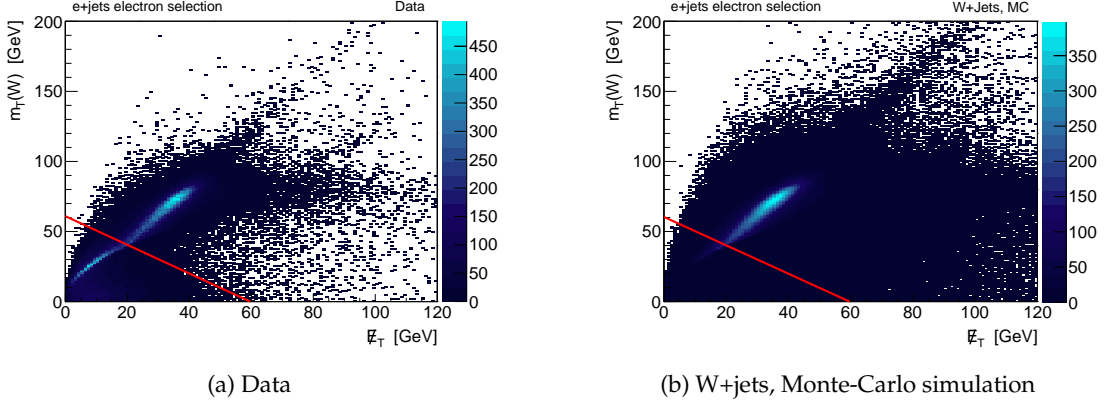
Figure 6.5: $\not{E}_T$ versus the W transverse mass distributions in data (left plot) and in the Monte-Carlo sample of W+jets. Trigger, trigger matching and high p_T electron requirements are applied to events. The red lines represent the triangular cut, $\not{E}_T + m_T(W) > 60\,\mathrm{GeV}$.

(a) $|\eta_e| < 1.37$

(b) $1.52 < |\eta_e| < 2.47$
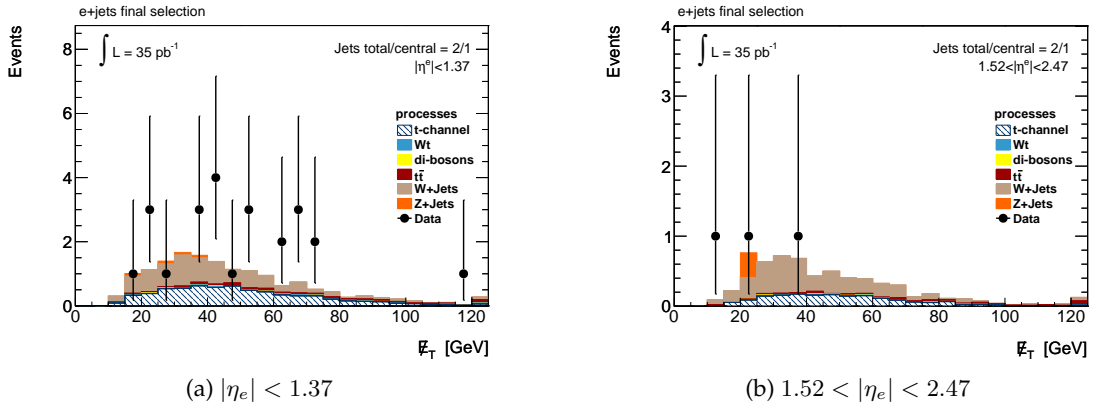
Figure 6.6: $\not{E}_T$ distributions for selected events. All selection requirements are applied. The left plot corresponds to the events, where the electron is in the central region. The right plot corresponds to the events with the electron in one of the side regions. QCD multi-jets contribution absents in the plots due to the lack of its simulated sample.

We introduce a notation for the event selection steps, which will be used throughout the document as shortcuts,

- **Electron selection**: trigger and electron trigger matching, high p_T electron requirements

- **Pretag selection**: electron selection, veto lepton and jet multiplicity requirements

- **Tag selection**: pretag selection, b-jet requirement

- **Final selection**: tag selection, cut on the triangular variable

Further, we introduce the following notation for the events with different jet configuration and the electron pseudo-rapidity region:

- **$1j/1cj$**: events with only a central jet
  - **$1j/1cj/central$**: electron is in the central region
  - **$1j/1cj/sides$**: electron is in one of the side regions

- **$2j/1cj$**: events with two jets one of which is central and the other is forward
  - **$2j/1cj/central$**: electron is in the central region
  - **$2j/1cj/sides$**: electron is in one of the side regions

We also define other notations for selected events such as $2j/2cj/central$, $2j/2cj/sides$, $3j/2cj/central$, $3j/2cj/sides$, $3j/3cj/central$ and $3j/3cj/sides$. Meaning of each of these definitions is obvious.

Figure 6.7 shows a graphical representation of the allowed configurations of jets in events. The $1j/1cj$ and $2j/1cj$ events (central jet is b-tagged) are presented on the left and the right sub-figures respectively.

(a) $1j/1cj$, central jet is b-tagged   (b) $2j/1cj$, central jet is b-tagged
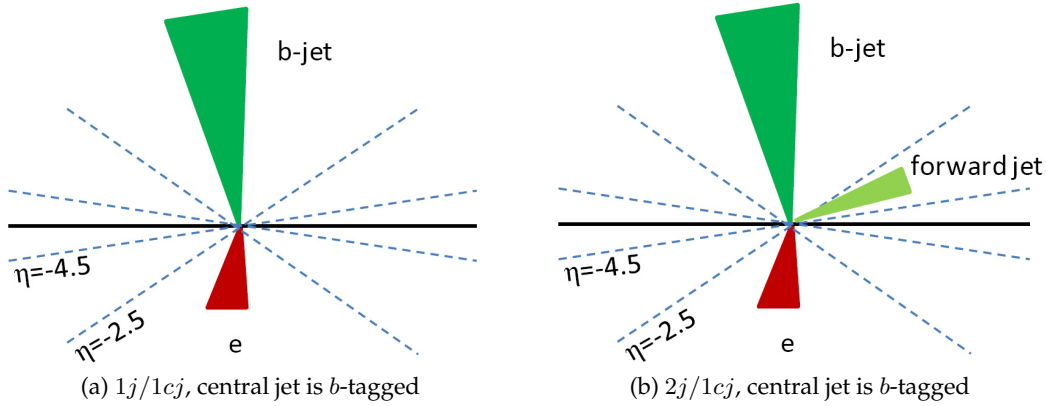
Figure 6.7: A graphical illustration of the selected event configuration. The left figure corresponds to the $1j/1cj$ events. The right figure corresponds to the $2j/1cj$ events. In addition, the central jet is required to be b-tagged.

6.3 Event yields

When giving an event yield (number of selected events) of a certain physical process predicted from Monte-Carlo simulation, we always use a weighted sum but not a simple count of the number of accepted events. The weights are computed from the Monte-Carlo generators, from the scale factors for the object selection efficiencies (see Chapter 5) and are scaled to the analysis target integrated luminosity, 35 pb^{-1}. Figure 6.8 presents the events selection 'cutflow' for the $2j/1cj$ events in data and Monte-Carlo simulation. Monte-Carlo events are properly weighted. Absolute effects of the different cuts (requirements) on the different processes can be seen.
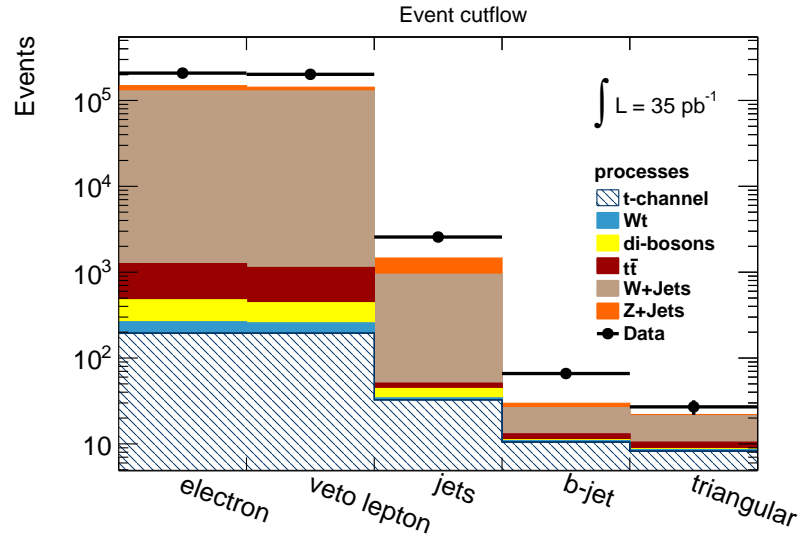
Figure 6.8: Data and Monte-Carlo simulation event cutflow for the $2j/1cj$ events, which are selected by the jet configuration requirement. QCD multi-jets contribution absents in the plot due to the lack of its simulated sample.

Table 6.1: Comparison of the expected $2j$ and $2j/1cj$ event yields for signal and background processes after the final selection. Events are weighted properly. Statistical uncertainties of the expectations due to limited sizes of the corresponding Monte-Carlo samples are small enough and therefore, not included here.

	t-channel	Wt-channel	di-bosons	$t\bar{t}$	W+jets	Z+jets	Total bkg.	S/B
2j	22.0	5.7	2.7	26.6	114	5.4	154	0.14
2j/1cj	8.1	0.34	0.17	1.69	10.9	0.70	13.8	0.59

Table 6.2: Comparison of the expected $2j/1cj$ event yields for signal and background processes after the final selection with the electron in the central or in one of the side regions. Events are weighted properly. Fractions of the expected events of each of the processes in a total event yield are provided in brackets. Statistical uncertainties of the expected event yields due to limited sizes of the corresponding Monte-Carlo samples are small enough and therefore, not included here.

	t-channel	Wt-channel	di-bosons	$t\bar{t}$	W+jets	Z+jets
2j/1cj/central	6.4 (41%)	0.26 (1.7%)	0.12 (0.8%)	1.26 (8%)	7.2 (46%)	0.35 (2.2%)
2j/1cj/sides	1.7 (27%)	0.08 (1.3%)	0.05 (0.9%)	0.43 (7%)	3.7 (58%)	0.35 (5.6%)

Table 6.1 provides a comparison between the $2j$ and the $2j/1cj$ event yields after the final selection and the obtained signal over background ratio. The optimized selection helps to reduce the overwhelming W+jets background to make its contribution comparable to the signal event yield. Besides, the contributions of the top quark pair production and the Wt-channel (not observed yet!) processes are well suppressed as well as other background processes. Table 6.2 provides additional information about the $2j/1cj$ event yield after the final selection. The event yields of the signal and the background processes are separately estimated for the central and the side electron events.

Table 6.3 presents the $1j/1cj$ and $2j/1cj$ event yields for data, signal and background after the tag and final selections except of QCD multi-jets, which will be estimated later using a data driven method. The W+jets event yield is also presented. Later, it will be corrected for its heavy flavor content using the dedicated data driven measurement. The number of Monte-Carlo simulated events are properly weighted. The t-channel cross section will be measured using the $2j/1cj$ events after the final selection. The predicted number of signal events is 8.1 and the observed data candidates are 27.

Table 6.3: The $1j/1cj$ and $2j/1cj$ event yields after the tag and final selections. The event yields, which are expected from Monte-Carlo simulation are properly weighted (see the text). The expected W+jets event yields are estimated from Monte-Carlo simulation before scaling due to the measured heavy flavor corrections. The uncertainties of the expectations are due to limited sizes of the Monte-Carlo samples. The uncertainties of the total background estimates are computed by adding uncertainties of all background components in quadrature. A QCD multi-jets event yield absents in the table.

| | $1j/1cj$ events | | | | $2j/1cj$ events | | | |
	tag		final		tag		final	
t-channel	7.7	±0.1	6.4	±0.1	9.4	±0.1	8.1	±0.1
Wt-channel	1.51	±0.05	1.31	±0.05	0.40	±0.03	0.34	±0.02
di-bosons	1.72	±0.05	1.43	±0.05	0.22	±0.02	0.17	±0.02
$t\bar{t}$	4.3	±0.1	3.8	±0.1	1.82	±0.09	1.69	±0.08
W+jets	218	±3	177	±3	13.3	±0.6	10.9	±0.5
Z+jets	20	±1	2.0	±0.4	3.6	±0.6	0.7	±0.3
Total bkg.	246	±3.2	186	±2.7	19.4	±0.8	13.8	±0.6
S/B	0.03		0.03		0.48		0.59	
Data	899		248		66		27	

Chapter 7

Data driven methods for background estimation

The t-channel signal is well hidden behind the background. Some of the background processes can be significantly reduced down to a small enough contribution with the help of the optimized signal selection. One can estimate them from Monte-Carlo simulation with some reliable systematic uncertainties. Another type of background, which is discussed in this chapter, is first of all not so significantly reducible and on the other hand it is not well modeled in Monte-Carlo simulation. This means that its contribution into a final signal selection can be wrong if one relies on Monte-Carlo simulation only. In order to study this kind of background processes the data driven methods become absolutely necessary. To some extent, almost all data driven methods rely on some Monte-Carlo based knowledge. The dependence of the data driven methods proposed in this work on Monte-Carlo simulation does not significantly affect the measurement results and is accounted by systematic uncertainties.

QCD multi-jets and W+jets processes belong to such irreducible type of background. The strategy of the analysis is to measure the QCD background first. Once this background is understood and its contribution in the interesting event selection regions is estimated, we will proceed to measure the W+jets background. However, some mutual dependence between these two measurements exist and will be also discussed. The methods, which we developed to measure the QCD multi-jets and W+jets background are described and the obtained results are presented.

7.1 QCD multi-jets

QCD multi-jets can contribute to the t-channel event selection via the presence of fake or non-prompt leptons. In case of fake electrons these are mostly the jets, which have a high fraction of electromagnetic energy. This kind of jets have a higher chance to mimic electrons and photons, since they are localized within the relatively smaller volume of the calorimeter. The ATLAS electron identification algorithm has a quite high fake electron rejection rate of the order of 10^5 (see Section 5.1). However, the jet production rate in proton-proton collisions is much higher than the production rates of the processes with real electrons among the final products of the collision events. This circumstance makes the influence of fake electrons to be not negligible in many physics analysis. In particular, the fake electron background is important for those physics analyses, which require only one electron. This is a case for the t-channel electron+jets analysis. Monte-Carlo simulation of fake electrons requires precise description of the ATLAS detector and its performance that is impossible to achieve given the complexity of the construction of the detector and its supporting infrastructure.

In contrast to the fake lepton background, the non-prompt lepton background has a comparable influence on analyses containing both electron or muon. Also, the non-prompt real leptons in Monte-Carlo simulation can be identified quite accurately. What makes the non-prompt electron background simulation hard is the poor theoretical knowledge of production rates of the underlying physics processes and distribution shapes of the key observables. QCD multi-jets production processes belong to this type of background. Of course, non-prompt production or fake identification of leptons can happen in events originated from other physics processes, too. But as it was already outlined above, the rejection efficiency of the fake leptons is high enough as well as it is for the non-prompt leptons. Thus, only the QCD multi-jets processes with very large event production rates can give a considerable contribution. For the rest of the discussion the fake and the non-prompt lepton background will be referred as QCD multi-jets (or simply QCD on the plots) background.

7.1.1 QCD multi-jets background determination with a fit method

QCD multi-jets background is often determined by means of the data driven methods. Usually, one extrapolates a background measurement in a control region into a signal region. The selection of events in these two regions has to be orthogonal. This means that the two regions do not share events. The background has to dominate in the control region. In order to ensure that the selected control region is really dominated by the background under study the reliable Monte-Carlo simulation of the rest of the physics processes contributing into the control region is necessary. Besides, there is a very important requirement to data driven methods, which is the homogeneity of the control and signal regions under the observable used for discrimination of the background. In other words, the background estimate is a function (can be analytical or empirical) of some observable and this function is equivalently valid in both the control and the signal selection regions to describe the background. This requirement to data driven methods needs to be checked by auxiliary studies using Monte-Carlo simulation or data.

The idea of the proposed method is to use the triangular variable, $\not{E}_T + m_T(W)$, to define the control and signal regions. This variable was found to be the most helpful one to discriminate between the W-like events and others (see Section 6.2). Figure 7.1 (left column) shows the triangular variable distribution after the pretag selection. The distributions correspond (from top to bottom) to $1j/1cj/central$, $1j/1cj/sides$, $2j/1cj/central$ and $2j/1cj/sides$ events respectively after the pretag selection [1]. Uncertainties in data counts are estimated from a Poisson distribution, while Monte-Carlo samples have Gaussian uncertainties due to the limited sizes. Data minus Monte-Carlo distribution (QCD multi-jets templates) uncertainties are taken as Poissonian, since they are driven by the data uncertainties rather than the smaller statistical uncertainties of the Monte-Carlo samples. The same applies to all plots of this chapter, where the QCD multi-jets templates are presented. The predictions of Monte-Carlo simulation for the different physics processes are stacked on top of each other. These plots show that the lower kinetic region ($< 60\,\text{GeV}$) of the triangular variable distribution is dominated by the QCD multi-jets background assuming the reliability of the Monte-Carlo predictions for the rest of background processes [2]. In contrast to that, a good matching of the distri-

---

[1] The notations for the event selection regions are defined in Section 6.2.

[2] The assumption applies mostly to the overall normalization of the Monte-Carlo background samples rather than their distribution shapes.
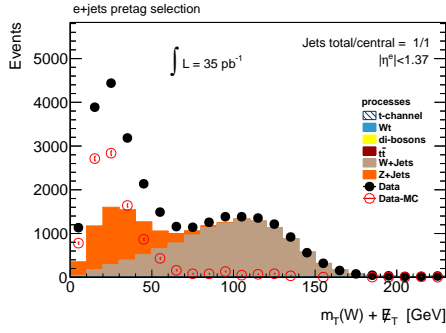
(a) $1j/1cj/central$
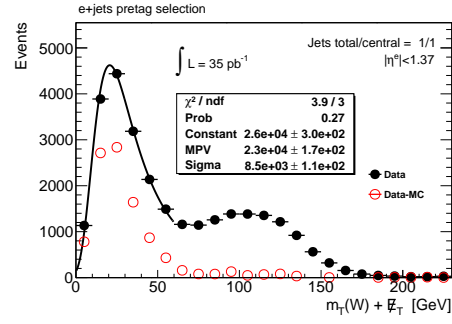
(b) $1j/1cj/central$, data fit
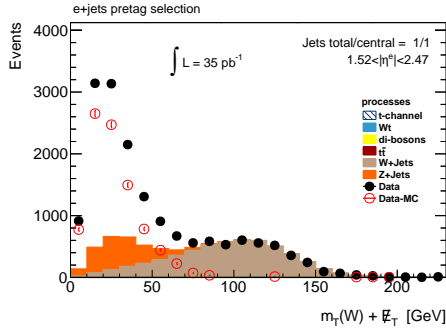
(c) $1j/1cj/sides$
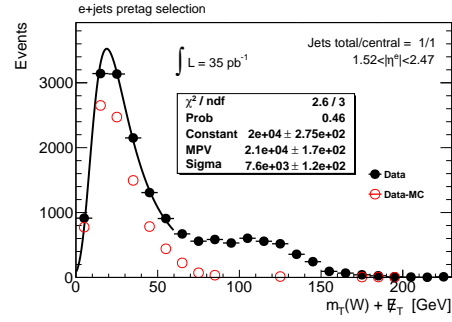
(d) $1j/1cj/sides$, data fit
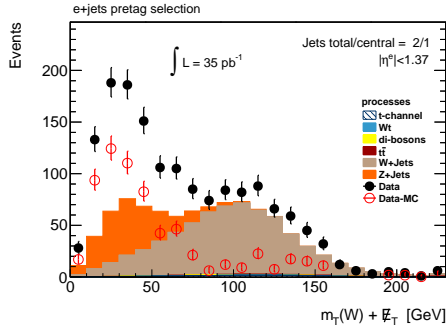
(e) $2j/1cj/central$
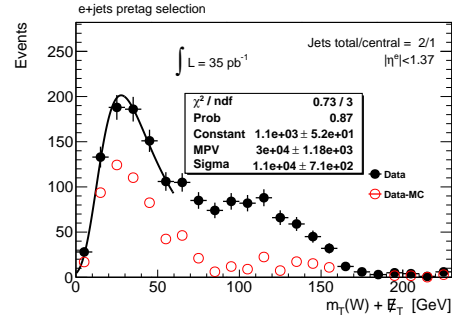
(f) $2j/1cj/central$, data fit
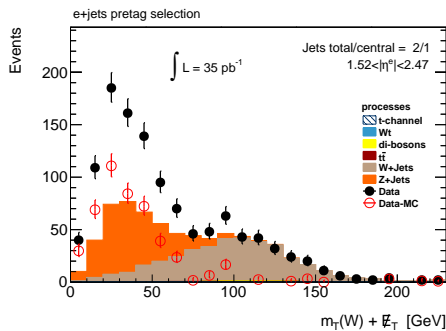
(g) $2j/1cj/sides$
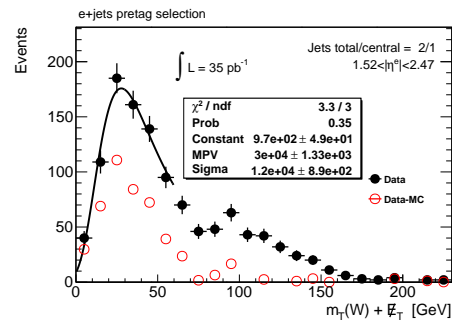
(h) $2j/1cj/sides$, data fit

Figure 7.1: Triangular variable distributions in the different events after the pretag selection. Plots on the left column present stacked distribution of the Monte-Carlo simulated samples superimposed with the QCD multi-jets templates and data. Plots on the right column show the same distributions without the Monte-Carlo simulated samples, where data is fitted with a Landau distribution in the $\not{E}_T + m_T(W) < 60$ GeV control region.

(a) $1j/1cj/central$

(b) $1j/1cj/sides$

(c) $2j/1cj/central$

(d) $2j/1cj/sides$
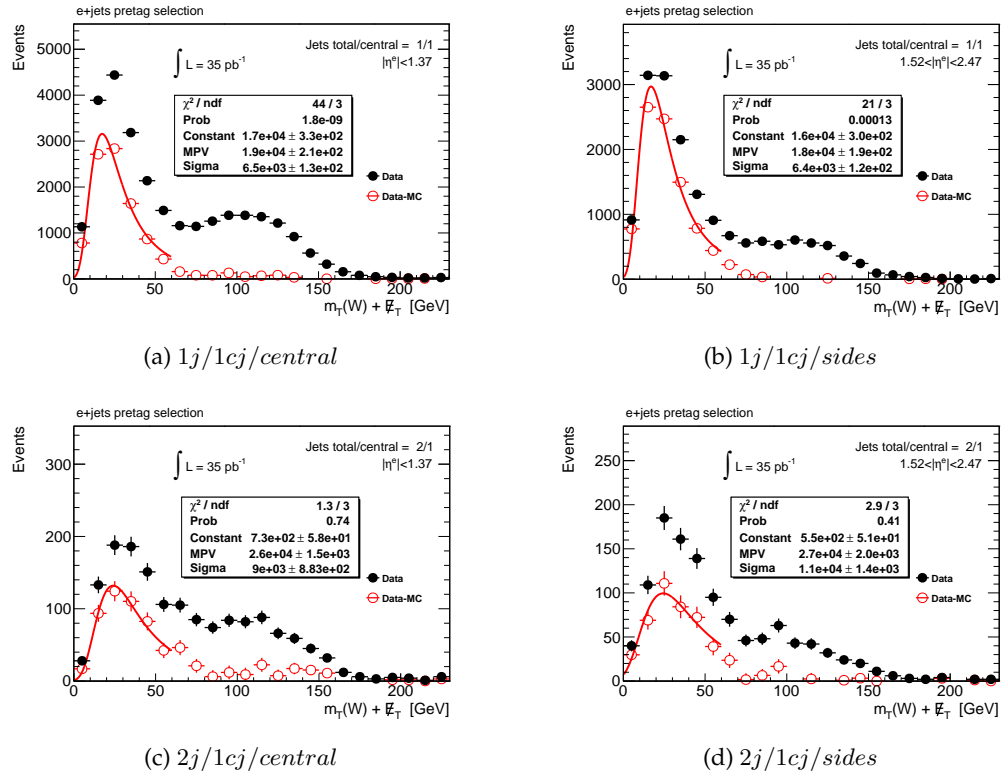
Figure 7.2: Triangular variable distributions in the different events after the pretag selection. Data and the corresponding QCD multi-jets template are presented together on each plot. QCD multi-jets templates are fitted with a Landau distribution in the $\not{E}_T + m_T(W) < 60$ GeV control region.

bution shapes in data and Monte-Carlo simulation in higher kinetic region ($> 60\,\text{GeV}$) clearly indicates that the QCD multi-jets contribution is small in there. The right column of Figure 7.1 presents the plots with the triangular variable distributions in data and QCD multi-jets templates corresponding to the same events as those on the left column. It was found empirically that the lower region ($< 60\,\text{GeV}$) of the distribution is well modeled by the Landau distribution. This can be seen from the fit results, which are included in the plots. The free parameters of the Landau fit function, the approximate most probable value (MPV) and the Landau density scale parameter (Sigma), are given in the MeV units. The Landau fit function is defined by Equation 7.1 [172],

$$L(x) = \begin{cases} \text{Constant} \cdot \int_{c-i\infty}^{c+i\infty} \exp(xs + s\log(s))\mathrm{d}s & \text{Sigma} \neq 0 \\ 0 & \text{Sigma} = 0 \end{cases} \tag{7.1}$$

Where, $s = (x - \text{MPV})/\text{Sigma}$. Equation 7.1 without the constant factor (also fit free parameter) is a probability density function of a Landau distribution.

Since the fitted region is dominated by QCD multi-jets events, we assume that the triangular variable in QCD multi-jets obeys the Landau distribution in the lower kinematic region ($< 60\,\text{GeV}$). The assumption is extended to the higher kinematic region where the signal selection is done. It should be noted that the fit region has large contribution of the W+jets and Z+jets events as predicted by Monte-Carlo simulation. This fact should be taken into account when fitting. Figure 7.2 shows fit results of the QCD multi-jets templates. The templates are not well modeled by the Landau distribution. Especially, one can see this on the upper row plots, which correspond to $1j/1cj/central$ and $1j/1cj/sides$ event selection with larger numbers of events. The reason for this discrepancy might be that the true QCD multi-jets distribution is not the Landau distribution or the Monte-Carlo shapes of W+jets and Z+jets distributions might be incorrectly modeled that affects the derived shapes of the QCD multi-jets templates. A more discriminative control region for QCD multi-jets event selection is needed.

In order to obtain a cleaner control region for QCD multi-jets, we explore events after the tag selection (pretag selection plus the b-jet requirement). Figure 7.3 shows the triangular variable distribution obtained after the events tag selection. Plots correspond (from top to bottom) to $1j/1cj/central$, $1j/1cj/sides$, $2j/1cj/central$ and $2j/1cj/sides$ events. The left column shows the distributions of the triangular variable in data and Monte-Carlo simulation as well as the QCD multi-jets templates obtained in the same way as before. The b-tagged jet requirement significantly reduces the fraction of W+jets, Z+jets and other processes in the control region as predicted by Monte-Carlo simulation. The fractions of the total expected non QCD multi-jets processes below the 60 GeV threshold is less than 10%, 9%, 15% and 27% in the $1j/1cj/central$, $1j/1cj/sides$, $2j/1cj/central$ and $2j/1cj/sides$ events respectively. This makes the QCD multi-jets triangular distribution normalization and shape prediction much less sensitive to uncertainties of the predictions of Monte-Carlo simulation for W+jets and Z+jets. The QCD multi-jets templates are fitted with a Landau distribution in the control region, $\not{E}_T + m_T(W) < 60\,\text{GeV}$. The fit results are extrapolated into the signal region. These results are shown in the right column plots in Figure 7.3.

We assumed that the triangular variable for QCD multi-jets continues to be Landau distributed in the signal region. There is no physics reason that the true distribution should have more contribution in the signal region implying an existence of some peak structure. This is expected due to the fact that in the QCD multi-jets events there is no internal physics constraints for a lepton p_T, $\not{E}_T$ and $\Delta\phi$ between the lepton and $\not{E}_T$ vectors like it is in the
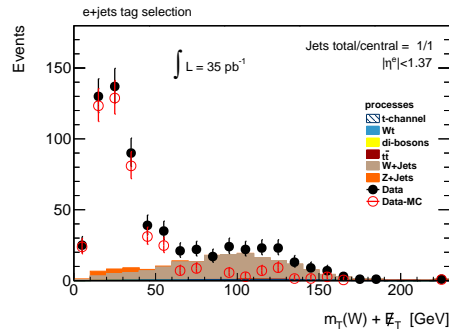
(a) $1j/1cj/central$
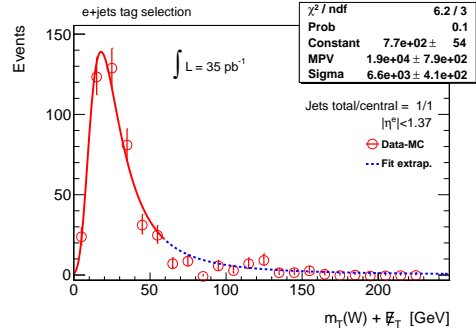
(b) $1j/1cj/central$, fit result
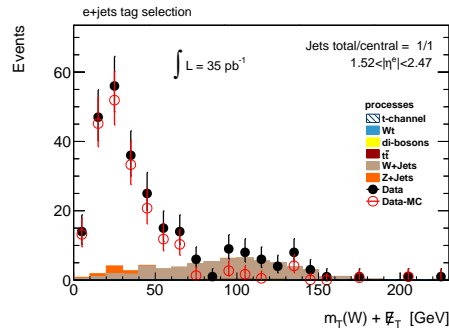
(c) $1j/1cj/sides$
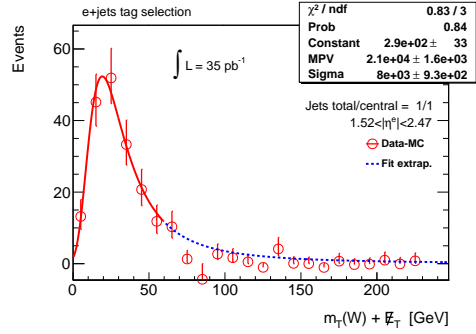
(d) $1j/1cj/sides$, fit result
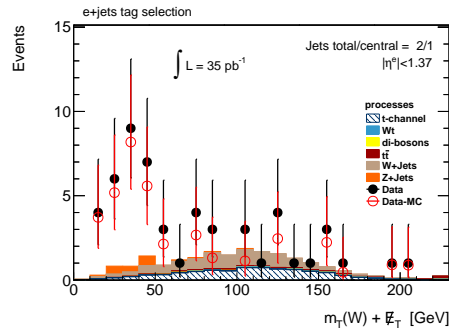
(e) $2j/1cj/central$
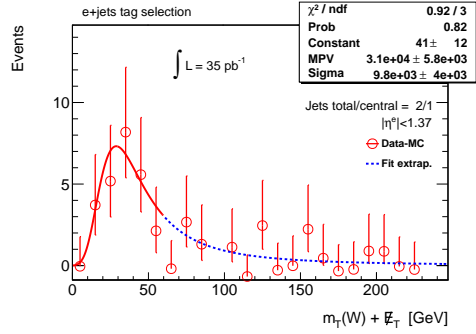
(f) $2j/1cj/central$, fit result
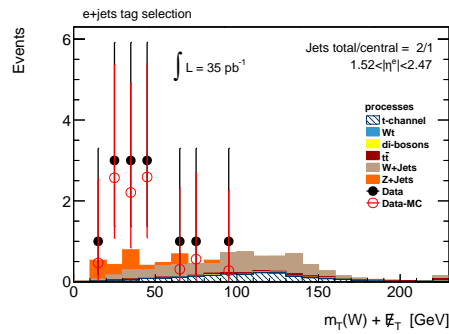
(g) $2j/1cj/sides$
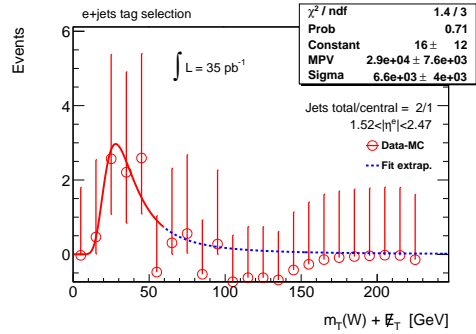
(h) $2j/1cj/sides$, fit result

Figure 7.3: Triangular variable distributions in the different events after the tag selection. The left column shows the plots with data, the stacked samples of Monte-Carlo simulation and the derived QCD multi-jets template. The right column plots show the QCD multi-jets templates fitted with a Landau distribution in the control region. Fit function is extrapolated in the signal region.

W-like and also to some extent in the *Z*-like events. Rather a monotonically falling behavior of the triangular variable distribution is expected in the QCD multi-jets events. Therefore, the Landau distribution, which describes well this variable in the control region can be consider as the optimal model of the QCD multi-jets contribution in the signal region. Later (see Section 8.1.3), we also consider an exponential model of the distribution in order to explore the model dependence of the estimated contribution of the QCD multi-jets background into the signal selection.

Figure 7.4: Simultaneous fit of two concatenated QCD multi-jets templates of the triangular variable distribution with a Landau distribution. The templates correspond to the $1j/1cj/central$ and $1j/1cj/sides$ events after the tag selection. See the text for the description of the free fitparameters.

In order to improve results a simultaneous fit of the QCD multi-jets templates (Figure 7.3, plots on the right column) is performed. The templates corresponding to the events with the same jet configuration but the different pseudo-rapidity regions of electrons are coupled in the fit. Figure 7.4 shows such a simultaneous fit with a Landau distribution of the QCD multi-jets templates corresponding to the $1j/1cj/central$ and $1j/1cj/sides$ events after the tag selection. The two distributions are concatenated. The control region parts of the two distributions are simultaneously fitted and the fit function is extrapolated in both signal regions. In the simultaneous fit, the fit free parameters, MPV and Sigma, are the same for both concatenated distributions. The free normalization parameters (the first and the last ones on the plot) of the fit correspond to the integrals from the fit Landau function in the signal regions ($> 60 \, \mathrm{GeV}$) of both concatenated distributions normalized to the x-range of integration. Thus, they are the QCD multi-jets contribution estimates obtained directly from the fit. These estimates depend on an upper limit of the integration of the Landau function. Here, the upper limit is chosen to be $230 \, \mathrm{GeV}$, which is suggested by data distribution itself [3] but remains ambiguous. As it will be shown later, the data weighting method, which uses the obtained Landau shapes of the QCD multi-jets background can be used to estimate this background in any range of the triangular variable distribution independently on the exact upper limit of the integration range.

---

[3]The upper limit of the highest bin of the corresponding distribution in data, which contains at least one entry is chosen as the upper limit of the integration.

Figure 7.5: Simultaneous fit of two concatenated QCD multi-jets templates of the triangular variable distribution with a Landau distribution. The templates correspond to the $2j/1cj/central$ and $2j/1cj/sides$ events after the tag selection. See the text for the description of the free fit parameters.

Figure 7.5 shows the results of the similar simultaneous fit of the concatenated triangular variable distributions in the $2j/1cj/central$ and $2j/1cj/sides$ events after the tag selection.

The obtained Landau fit functions will be used to derive one-dimensional maps of the QCD multi-jets event weights. These weights are used to obtain the data driven distributions for the observables of interest (see Section 7.1.3).

A similar measurement of the QCD multi-jets background is performed in those events with higher multiplicity of central jets, where the measurement is not restricted by the small amount of data. The control regions in the triangular distribution are plagued by a higher uncertainty level, since higher fractions of W+jets events are expected in the lower bins of the distribution. Figure 7.6 presents the triangular variable distribution plots after the tag selection of events. The distributions correspond to the $2j/2cj/central$, $2j/2cj/sides$, $3j/2cj/central$ and $3j/3cj/central$ events, where the available data allow to derive the QCD multi-jets templates. The fit of these templates with a Landau distribution converges.

Figure 7.7 shows simultaneous fit results of the QCD multi-jets templates for their two combinations, $2j/2cj/central$ together with $2j/2cj/sides$ events (left plot) and $2j/2cj/central$ together with $3j/2cj/central$ events (right plot). The results indicate that the method is valid for these events. It can be noted that the obtained Landau distribution shapes for QCD multi-jets events with 2 central jets have larger value for the sigma (limited) parameter than for the events with 1 central jet (see Figures 7.4 and 7.5). In general, the estimates of sigma (limited) and MPV are higher for the events with higher multiplicity of jets. This fact causes a bad quality of the simultaneous fit of the $1j/1cj/central$ and $2j/2cj/central$ events shown on Figure 7.8. The template for the QCD multi-jets $2j/2cj/central$ events is not well described by the fit function, which free parameters are mainly determined by the $1j/1cj/central$ events.
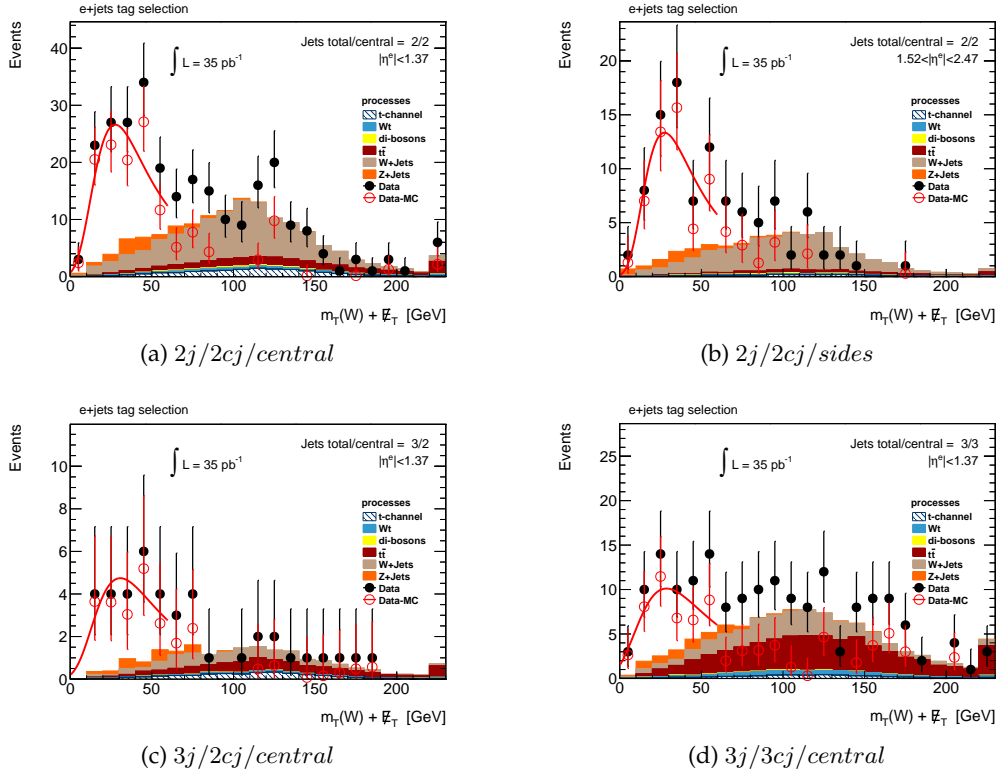
Figure 7.6: Triangular variable distributions in the different events after the tag selection. Data, the stacked samples from Monte-Carlo simulation and the QCD multi-jets templates are superimposed. The QCD multi-jets templates are fitted with a Landau distribution in the control region.
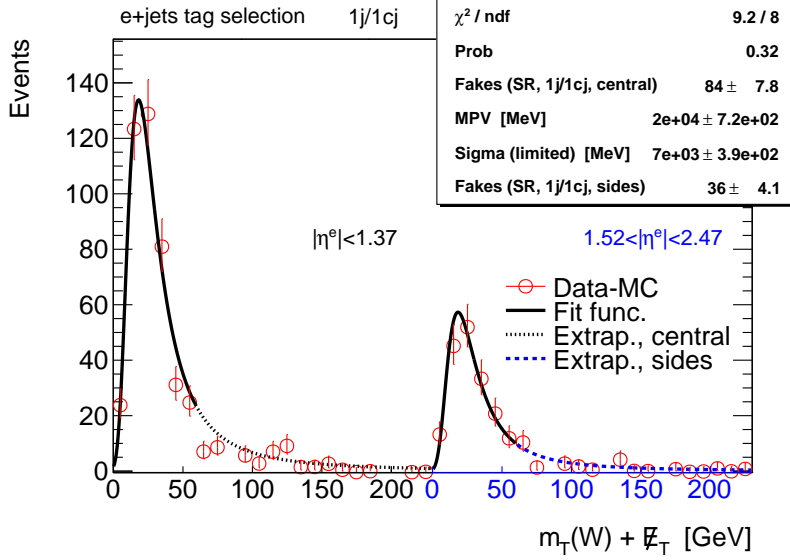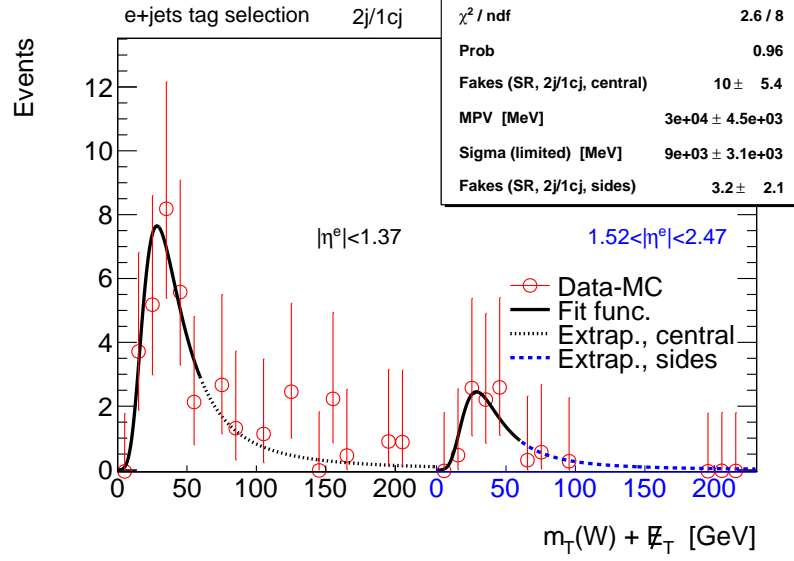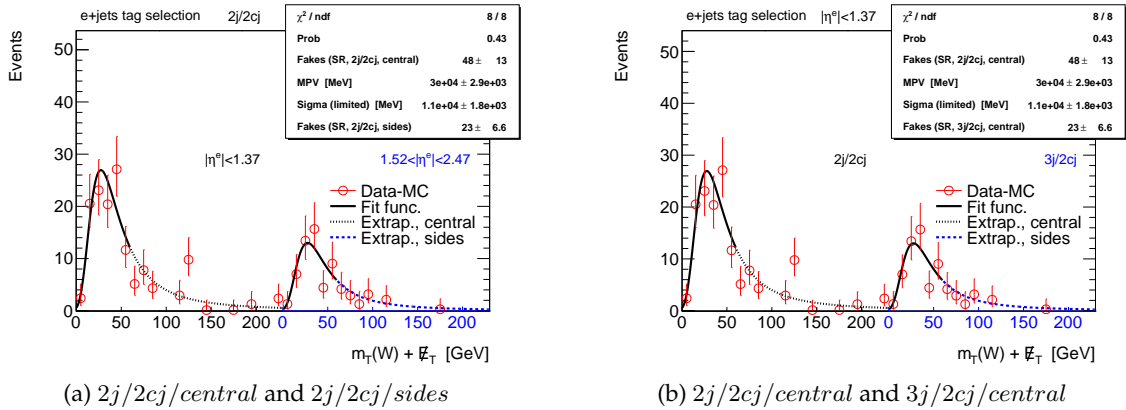

Figure 7.7: Simultaneous fit of two concatenated QCD multi-jets templates of the triangular variable distribution with a Landau distribution. The templates correspond to the different events after the tag selection. See the text for the description of the free fit parameters.
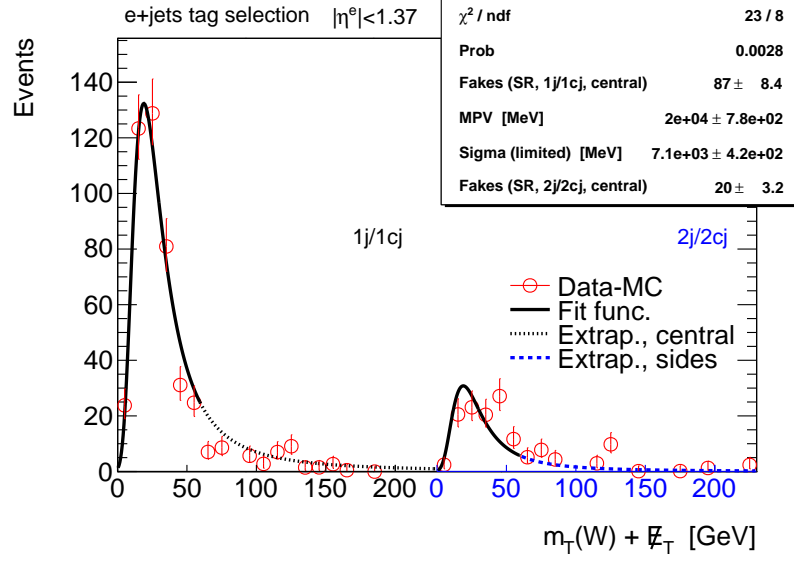
Figure 7.8: Simultaneous fit of two concatenated QCD multi-jets templates of the triangular variable distribution with a Landau function. The templates correspond to the $1j/1cj/central$ and $2j/2cj/central$ events after the tag selection. The fit fails to describe the $2j/2cj/central$ events. See the text for the description of the free fit parameters.

7.1.2 Validation of the fit method with Monte-Carlo simulation

The JF17 Monte-Carlo simulation sample (see Section 4.3.4) of QCD multi-jets produced together with other QCD processes has been used to check the performance of the fit method. The low available amount of the simulated events of the JF17 sample limits this study. In order to keep as many as possible events for validating the method, the triangular distribution is obtained after the event pretag selection. This allowed to select enough events for fitting the 1-jet events, where the jet is not necessarily in the central region of the detector. As to the events with 2 jets, only a few passes the pretag selection and due to this reason it is impossible to fit them. Besides, purification of the selected 1-jet events has been made regarding their truth origin. JF17 contains (with the appropriate fraction) W+jets, Z+jets and $t\bar{t}$ events, which have to be removed from the analysis. Events are classified by an origin of the truth electron, which matches a reconstructed electron. Matching is done by using the requirement $\Delta R < 0.05$ between the two. Sometimes the matching truth electron origin cannot be unambiguously identified in the Monte-Carlo truth record. Therefore, the reconstructed electron remains as unidentified. If the reconstructed electron does not have a matching truth electron, then it is identified as a fake electron and -1 is assigned to its origin as an identifier. Table 7.1 provides the list of the electron origin particles or processes with the corresponding (conventional) digital identifiers. Figure 7.9 presents the distributions of the origins of the matching truth electrons in the 1-jet events with the central (left plots) and side (right plots) electrons after the pretag (top plots) and tag (bottom plots) selections [4]. As one can see from these plots, the central electrons are mainly produced in B-meson decays. The corresponding events dominate after the tag selection. The side electrons are mainly produced in photon conversion. However, the b-jet requirement of the tag selection significantly reduces their re-

---

[4]The central and side events are selected according to the pseudo-rapidity of the reconstructed electrons.

Table 7.1: Conventional digital identifiers for the origin of truth electrons in Monte-Carlo simulation.

Origin	Identifier	Origin	Identifier
Undefined	0	SUSY	22
Single electron	1	Light meson	23
Single muon	2	Strange meson	24
Single photon	3	Charmed meson	25
Single tau	4	Bottom meson	26
Photon conversion	5	$c\bar{c}$ meson	27
Dalitz decay	6	J/ψ	28
Electromagnetic process	7	$b\bar{b}$ meson	29
Muon	8	Light baryon	30
Tau	9	Strange baryon	31
Top quark	10	Charmed baryon	32
Quark weak decay	11	Bottom baryon	33
W boson	12	Pion decay	34
Z boson	13	Kaon decay	35
Higgs	14	Bremsstrahlung photon	36
Higgs, MSSM	15	Prompt photon	37
W/Z, MSSM	16	Underling event photon	38
W, LRSM	17	ISR photon	39
ν_e^R	18	FSR photon	40
ν_μ^R	19	Nuclear reaction	41
ν_τ^R	20	π^0 decay	42
Light quark	21		

(a) central electron, pretag

(b) side electron, pretag

(c) central electron, tag

(d) side electron, tag
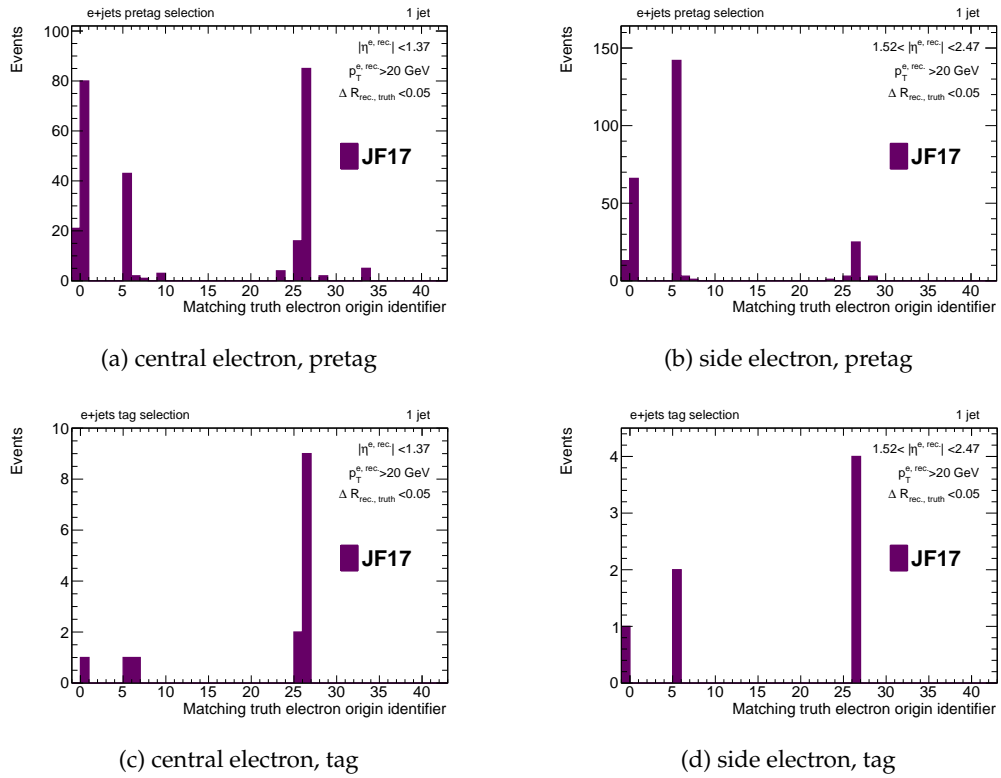
Figure 7.9: Distributions of an origin of truth electrons matched to the reconstructed electrons in 1-jet events after the pretag and tag selections.

lative contribution in the selected events as this is indicated by the distribution on the right bottom plot. The bottom row plots predict that after b-tagged jet requirement, the main part of the QCD multi-jets background should be ascribed to electrons from the B-meson decays. The top plots show that a large fraction of events has an undetermined origin of a matching truth electron. These events are not further used. A small fraction of the events with fake electrons are selected as well.

Figure 7.10 presents the triangular variable distribution in the 1-jet events after the pretag selection, where the origin of the matched truth electrons is either B-mesons (left column) or photon conversion (right column). The top row plots correspond to the events with the central electrons. The bottom row plots correspond to the events with the side electrons. All distributions are well modeled by a Landau distribution given the statistical uncertainties. The free fit parameters, MPV and sigma (limited), are provided in the MeV units.
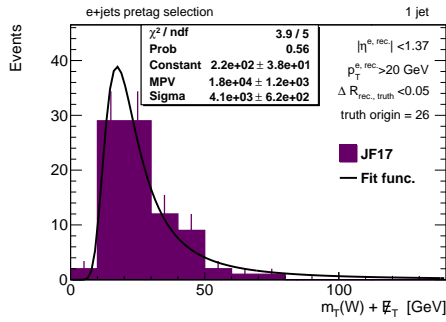
(a) central electron, matching truth electrons from B-meson decays.
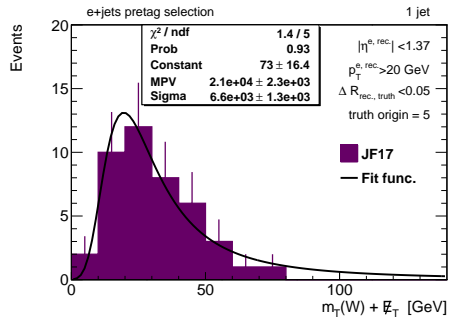
(b) central electron, matching truth electrons from photon conversion.
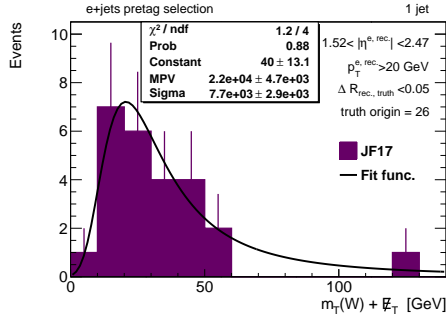
(c) side electron, matching truth electrons from B-meson decays.
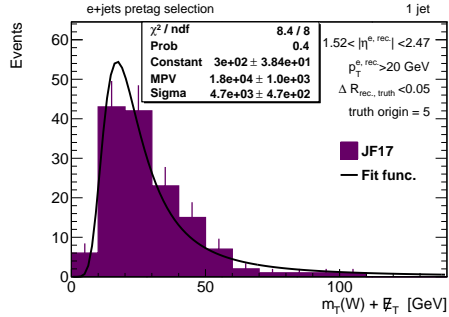
(d) side electron, matching truth electrons from photon conversion.

Figure 7.10: Triangular variable distributions in the 1-jet events after the pretag selection, where matching truth electrons are originated from B-meson decays or photon conversion.

Similarly to the data driven QCD multi-jets templates, the triangular variable distributions in the JF17 sample are taken as inputs for the simultaneous fit. The upper plot in Figure 7.11 shows the fit result of two concatenated distributions of the 1-jet events. The left part of the distributions corresponds to the events with the central electrons. The right part corresponds to the events with the side electrons. In contrast to the fitting procedure of the data templates, here the whole distributions are fitted. The quality of the fit is good and thus the Landau distribution models well the triangular variable. In the bottom plot of Figure 7.11 the events
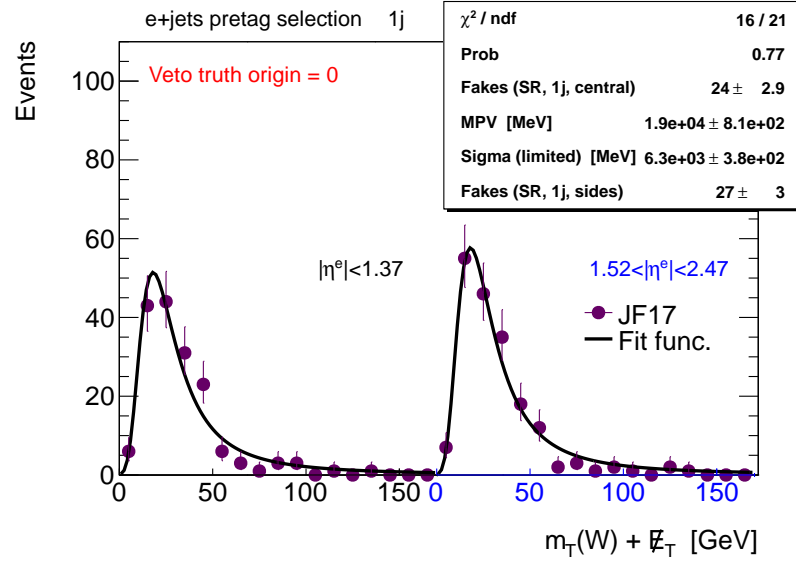
(a) events with matching truth electrons from undefined origins are dropped.
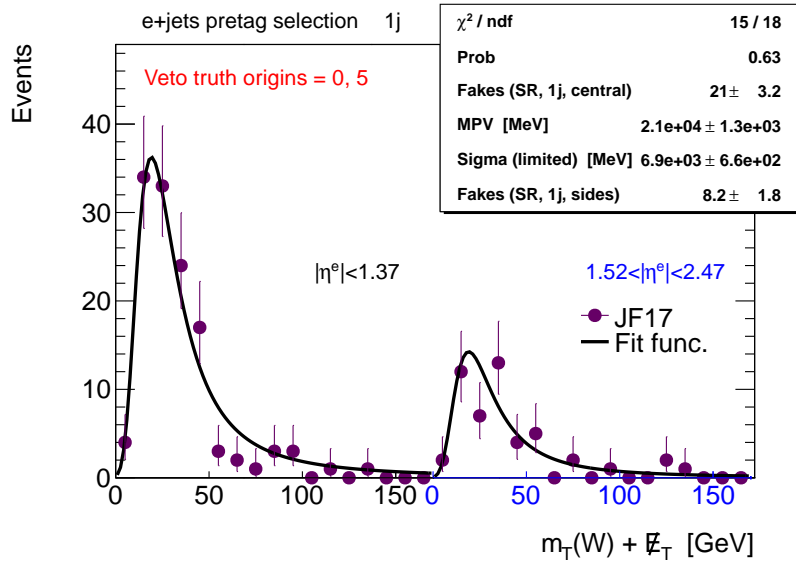
(b) events with matching truth electrons from undefined origins or from photon conversion are dropped.

Figure 7.11: Simultaneous fit of the triangular variable distribution with a Landau distribution in the Monte-Carlo QCD sample. The distribution corresponds to two concatenated independent regions of the 1-jet events with central and side electrons after the pretag selection.

with the matching truth electrons from photon conversion are removed from the distributions. As it was suggested by the distributions of the truth electron origins shown in Figures 7.9b and 7.9d the fraction of these events is expected to be significantly reduced after the tag selection. In this case the obtained distributions and the Landau fit function parameters (except of the event normalization parameters) are in agreement with the results obtained on the data driven templates, shown in Figure 7.4. Namely, in both cases the free parameters of the fit, MPV and sigma (limited) are comparable within the statistical uncertainties. The ratio of the number of the events with the central electrons estimated in the signal region ($< 60\,\mathrm{GeV}$) over the corresponding number of events with the side electrons is the same within statistical uncertainties in both cases, $21 \pm 3.2/8.2 \pm 1.8$ (Monte-Carlo simulation) and $84 \pm 7.8/36 \pm 4.1$ (data).

7.1.3 QCD multi-jet background estimation with the data event weighting method

QCD multi-jets shapes for some observables can be derived from data by using the event weighting technique. The event weights are calculated as a ratio of the QCD multi-jets estimate over a data count in a certain kinematic range of the variable, which discriminates the QCD multi-jets background. Here, we use the triangular variable.

(a) $1j/1cj/central$

(b) $1j/1cj/sides$

(c) $1j/1cj/central$, event weights

(d) $1j/1cj/sides$, event weights
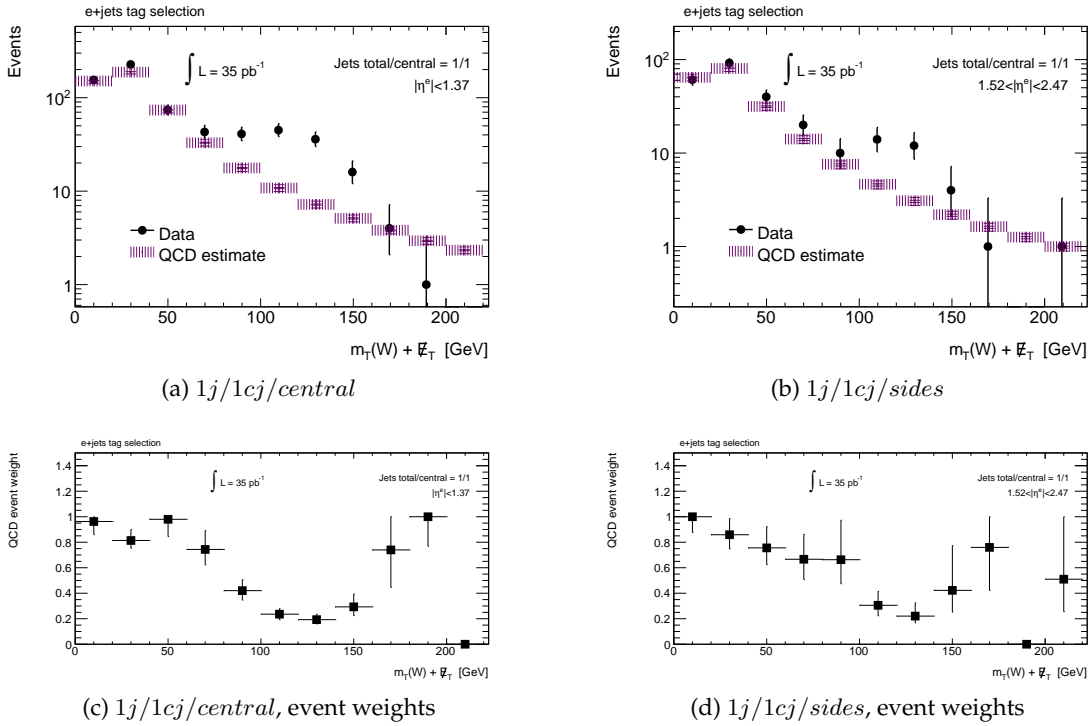
Figure 7.12: Top row: the data counts and the distributions of the QCD multi-jets event estimates as functions of the triangular variable. Each QCD multi-jets event estimate is obtained by integrating the fit Landau function within the corresponding bin limits. The plots correspond to the $1j/1cj/central$ (left) and $1j/1cj/sides$ (right) events after the tag selection. Bottom row: the event weights corresponding to the $2j/1cj/central$ (left) and $2j/1cj/sides$ (right) events after the tag selection.

(a) $2j/1cj/central$

(b) $2j/1cj/sides$

(c) $2j/1cj/central$, event weights

(d) $2j/1cj/sides$, event weights
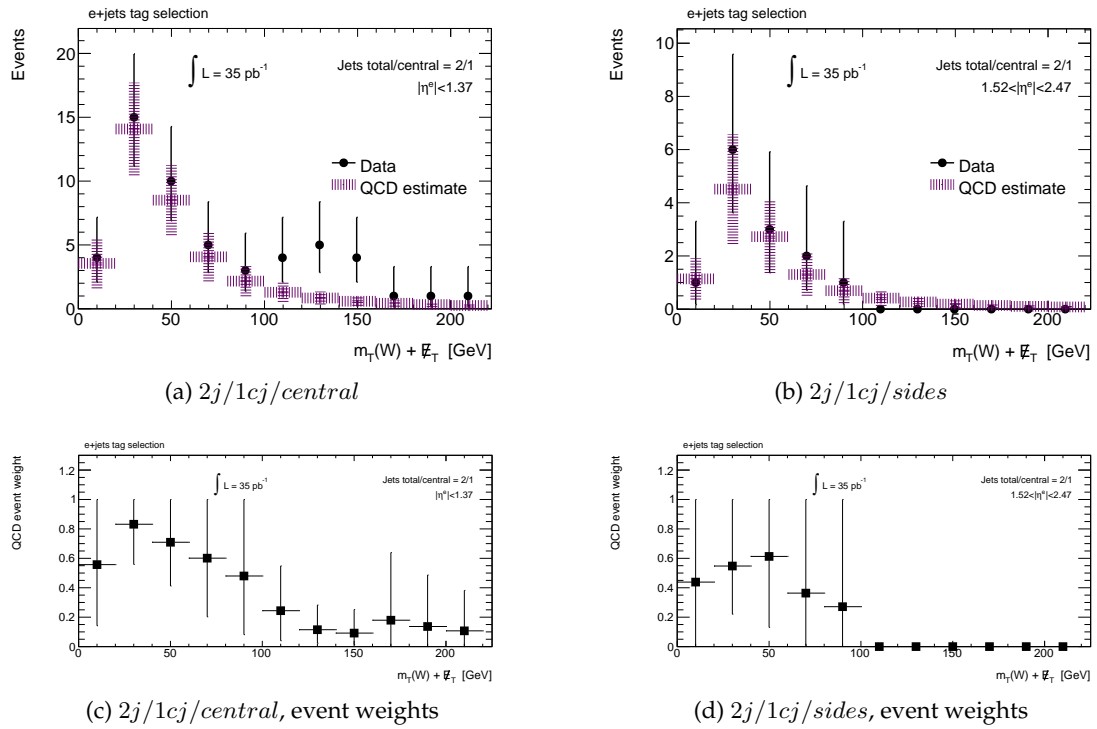
Figure 7.13: Top row: the data counts and the distributions of the QCD multi-jets event estimates as functions of the triangular variable. Each QCD multi-jets event estimate is obtained by integrating the fit Landau function within the corresponding bin limits. The plots correspond to the $2j/1cj/central$ (left) and $2j/1cj/sides$ (right) events after the tag selection. Bottom row: the event weights corresponding to the $2j/1cj/central$ (left) and $2j/1cj/sides$ (right) events after the tag selection.

Figures 7.12 and 7.13 present the details how the event weights are obtained. The top row plots in both figures show the distribution of the triangular variable in data and in the estimated QCD multi-jets background with 20 GeV binning. The binned estimate of the QCD multi-jets background is obtained by integrating the fit Landau function within the limits of the corresponding bins. The symmetric uncertainties on the estimates are due to the statistical uncertainties of the free parameters of the fit. Figure 7.12 provides the plots for the $1j/1cj/central$ (left) and $1j/1cj/sides$ (right) events after the tag selection while Figure 7.13 includes similar plots for the $2j/1cj/central$ (left) and $2j/1cj/sides$ events also after the tag selection. The bottom row plots in both figures show the calculated event weights from the corresponding distributions of data and the QCD multi-jets estimate. The plots 7.12c and 7.13c correspond to the $1j/1cj/central$ and $2j/1cj/central$ events respectively while the plots 7.12d and 7.13d correspond to the $1j/1cj/sides$ and $2j/1cj/sides$ events respectively. Each weight is calculated as a most probable value (MPV) of the distribution of the random ratio of a QCD multi-jets background estimate over the corresponding data count. The distribution is generated assuming that the data count obey a Poisson distribution while the QCD multi-jets estimate is taken to be a Gaussian quantity. The obtained MPV values are constrained, $0 \leq \text{MPV} \leq 1$. The up/down uncertainties of a given weight are calculated as the minimal up/down deviations from the constrained MPV value so that the integral from a distribution of the corresponding ratio taken within these up/down deviations covers 68.3% (one standard deviation) part of the integral from this distribution taken in the range $(0, 1)$. Meanwhile, these up/down deviations are constrained to be within the range $(0, 1)$. Thus, if a given MPV value is constrained to be 1 (0), then the up (down) uncertainty of the corresponding weight is 0.

In order to derive a distribution of some other variable besides the triangular variable using the obtained event weights certain conditions should be matched. The event weights should either depend on the variable, whose distribution is aimed to be derived from data, or this variable should not carry additional discrimination power agains QCD multi-jets. For instance, the electron p_T distribution of the QCD multi-jets background can be obtained using event weighting, since the event weights depend on the triangular variable, which itself depends on the electron p_T. It should be noted that the opposite statement would be wrong. If the weights depended on the electron p_T only, then applying them to data in order to derive a distribution of the triangular variable for QCD multi-jets would lead to a wrong result. The reason is that the triangular variable depends on $\not{E}_T$ and $\Delta\phi$ between the electron p_T and $\not{E}_T$ directions (see Equation 6.1 for the definition of the W transverse mass). These two variables carry some discriminative power (between QCD multi-jets and other processes) and cannot be properly accounted by the weights, which depend on electron p_T only. Another example of a valid weighting approach can be a jet p_T, which is sufficiently uncorrelated to the triangular variable but does not carry any discriminative power for QCD multi-jets events [5].

Figure 7.14 shows control plots, where data distributions for some key observables are compared to the corresponding distributions by superimposing data on the sum of Monte-Carlo samples and the derived QCD multi-jets background. The distributions for QCD multi-jets are derived from the corresponding distributions in data by weighting the data events using the weights described above. The plots correspond (from top to bottom) to $\not{E}_T$, electron p_T,

---

[5]In practice, this is not *a priori* knowledge about a certain variable but is obtained *aposteriori* by means of the control distributions.

(a) $1j/1cj$, $\not{E}_T$

(b) $2j/1cj$, $\not{E}_T$

(c) $1j/1cj$, electron p_T

(d) $2j/1cj$, electron p_T

(e) $1j/1cj$, H_T

(f) $2j/1cj$, H_T

(g) $1j/1cj$, t-quark reconstructed mass

(h) $2j/1cj$, t-quark reconstructed mass
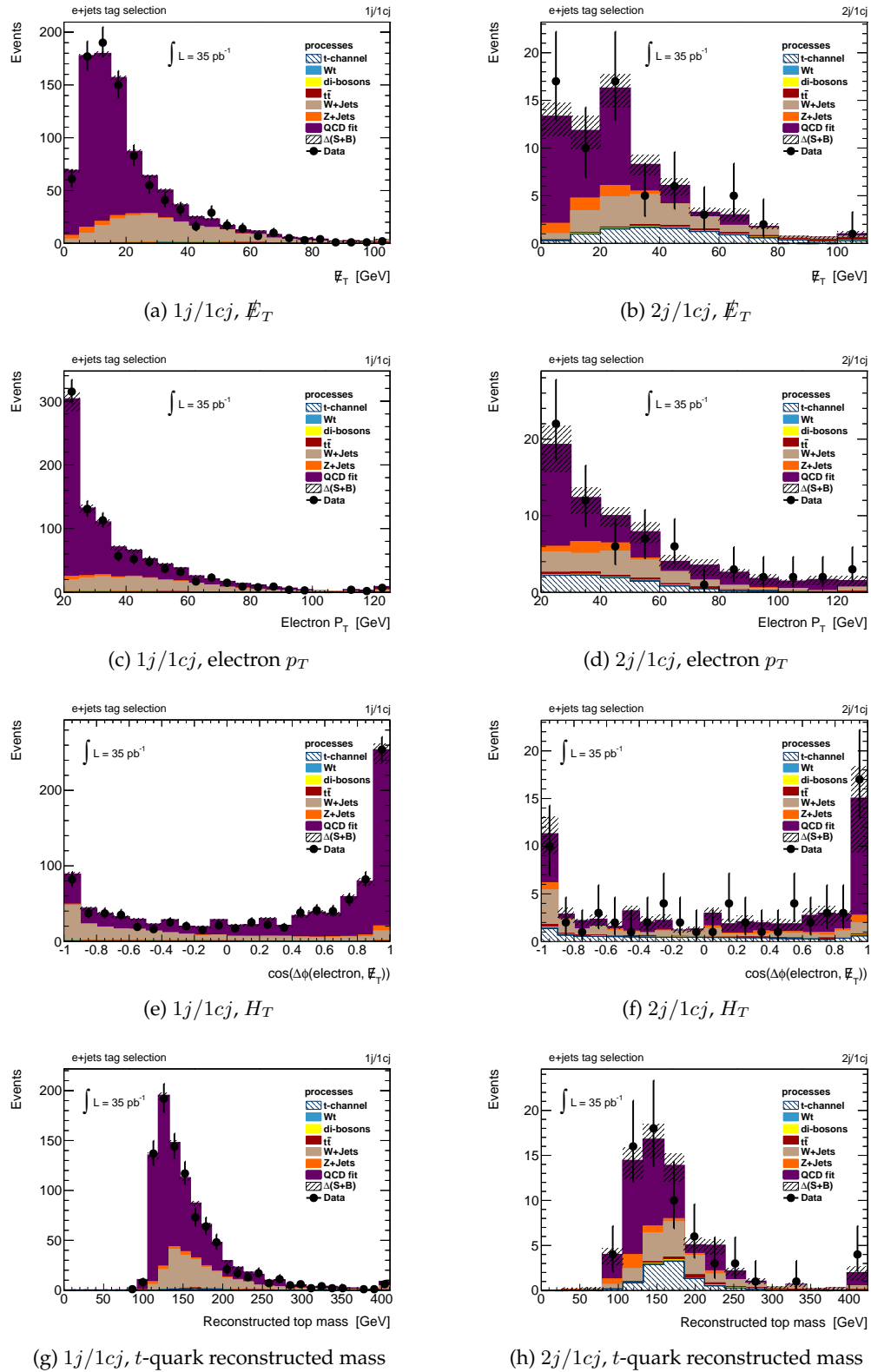
Figure 7.14: Control plots for various simple and derived variable distributions after the tag selection. The QCD multi-jets distributions are obtained by weighting the corresponding data distributions. Left column: the $1j/1cj$ events selection. Right column: the $2j/1cj$ events selection. Central and side regions of selected electrons are merged. The QCD multi-jets estimation uncertainties are combined with the uncertainties of the Monte-Carlo samples due to their limited sizes.

(a) $1j/1cj$, $\not{E}_T$

(b) $2j/1cj$, $\not{E}_T$

(c) $1j/1cj$, electron p_T

(d) $2j/1cj$, electron p_T

(e) $1j/1cj$, H_T

(f) $2j/1cj$, H_T

(g) $1j/1cj$, t-quark reconstructed mass

(h) $2j/1cj$, t-quark reconstructed mass
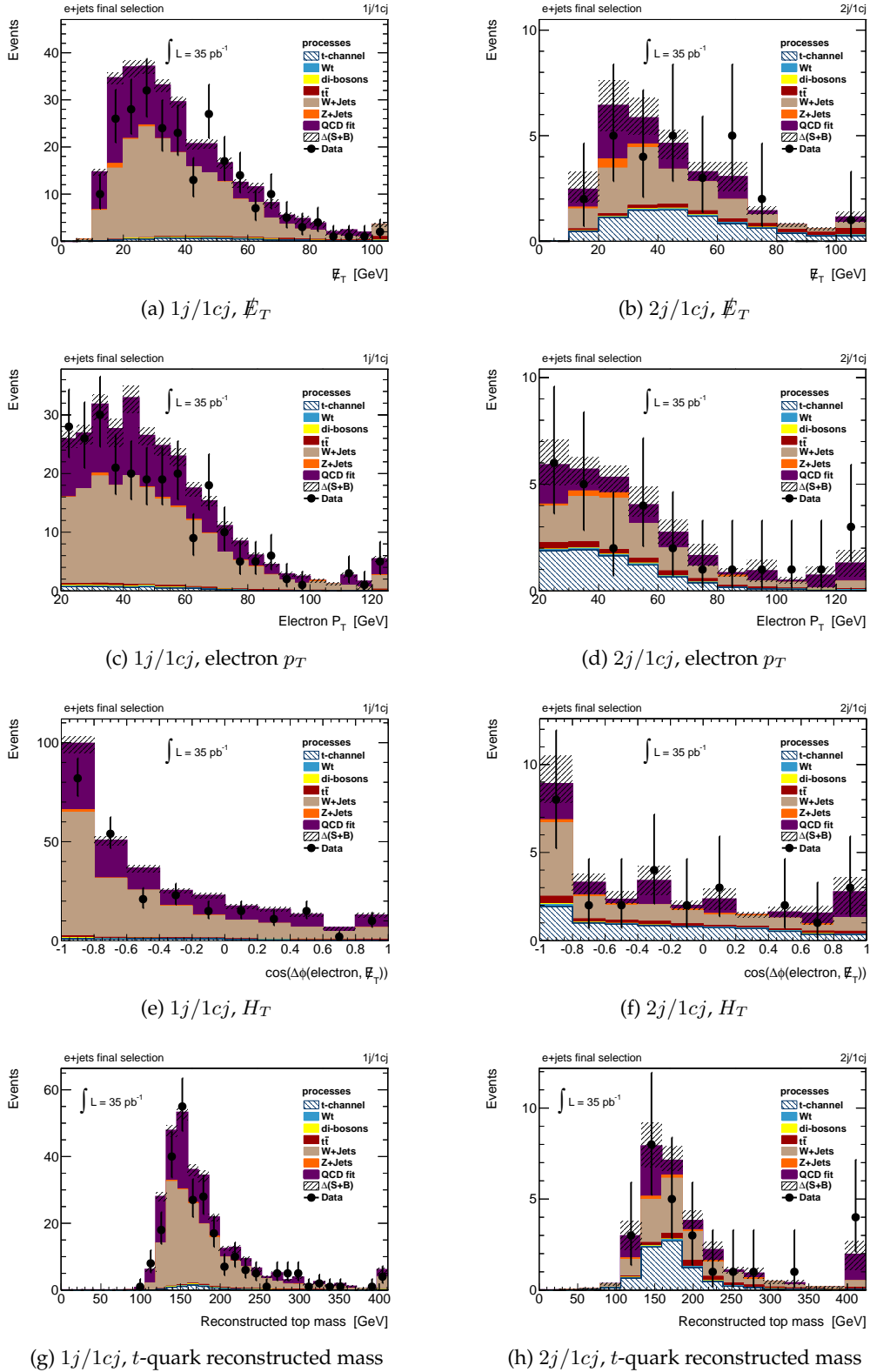
Figure 7.15: Control plots for various simple and derived variable distributions after the final selection. The QCD multi-jets distributions are obtained by weighting the corresponding data distributions. Left column: the $1j/1cj$ events selection. Right column: the $2j/1cj$ events selection. Central and side regions of selected electrons are merged. The QCD multi-jets estimation uncertainties are combined with the uncertainties of the Monte-Carlo samples due to their limited sizes.

$\Delta\phi$ between the electron p_T and $\not{E}_T$ vectors and the reconstructed t-quark mass [6]. The plots on the left column correspond to the $1j/1cj$ events while the right column provides plots, which correspond to the $2j/1cj$ events after the tag selection in both cases. Note that the events with the central and side electrons are combined. As can be seen from the plots the derived QCD multi-jets distributions together with the Monte-Carlo prediction describe data well within the uncertainties. Thus, we conclude that the developed fitting method together with event weighting technique provides a reliable measurement of the QCD multi-jets background. The uncertainties in each bin of the distributions are calculated by combining of the uncorrelated uncertainties of the Monte-Carlo samples and the QCD estimates [7].

(a) $1j/1cj$, tag selection

(b) $2j/1cj$, tag selection

(c) $1j/1cj$, final selection

(d) $2j/1cj$, final selection
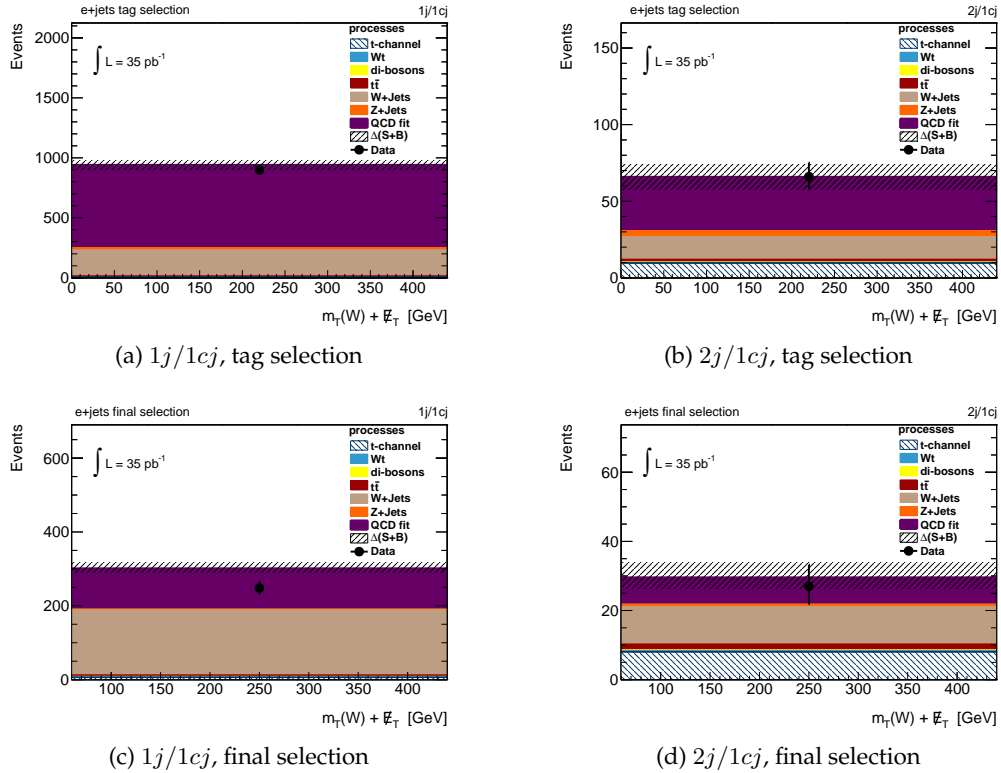
Figure 7.16: Control plots for the unbinned distribution of the triangular variable after the tag (top row) and final (bottom row) selections of the $1j/1cj$ (left column) and $2j/1cj$ (right column) events. The QCD multi-jets estimation uncertainties are combined with the uncertainties of the limited Monte-Carlo samples.

Figure 7.15 presents the same distributions as Figure 7.14 but after the final selection of

---

[6]The t-quark mass is calculated from its decay products ($bl\nu$) using W mass constraint for the only unknown $\not{E}_z$ calculation.

[7]The uncertainties of the QCD multi-jets estimates are partially correlated between the different bins of the corresponding distributions. This is caused by the fact that the a given event weight might be applied to the different events, which contribute into the different bins of the interesting distribution. Therefore, up/down variations of the given event weight leads to the correlated contribution in these bins. In order to properly take the correlation into account when calculating the uncertainty of the total estimate of QCD multi-jets contribution after the tag or final selection, the event weighting is done for the unbinned distributions. The sums of the up/down variations of the weighted events are separately calculated for each event weight. The obtained net up/down variations are combined in an uncorrelated way at the end of an event selection.

events. The distributions of the QCD multi-jets background are derived by weighting data as before. This background is significantly reduced in the $2j/1cj$ events selection (right column) after the triangular cut is applied. The combined distributions of QCD multi-jets together with the Monte-Carlo samples agree well with data in the $2j/1cj$ events. After the final selection of the $1j/1cj$ events there is an excess of the total prediction (QCD multi-jets together with Monte-Carlo samples) over data. This indicates some systematic bias, which can be caused by the overestimation of the QCD multi-jets or simulated W+jets contributions. This issue will be discussed and taken into account in the study of the systematic uncertainties of the measurement (see Section 8.1).

Figure 7.16 summarizes the QCD multi-jets measurement results after the tag (top row) and final (bottom row) selections of the $1j/1cj$ (left column) and $2j/1cj$ (right column) events. As can be seen from the plots 7.16a and 7.16c, the $1j/1cj$ events selection is dominated by the QCD multi-jets and W+jets events. Other processes have negligible contribution. The $1j/1cj$ events selection can serve as the control region for the data driven measurement of the W+jets background, since another dominant contribution of QCD multi-jets background is already estimated.

Table 7.2 provides the estimated contribution of QCD multi-jets in both $1j/1cj$ and $2j/1cj$ events after the tag and final selections. The uncertainties of the event weights are propagated into the uncertainties of the QCD multi-jets estimates, which are also presented in the table. The last row of the table presents the estimated fraction of the QCD multi-jets events in data.

Table 7.2: The measured estimates of the QCD multi-jets events and their fractions in data after the tag and final selections of the $1j/1cj$ and $2j/1cj$ events. The uncertainties are due to the uncertainties of the event weights used in estimation of the QCD multi-jets background from data.

jet multiplicity	$1j/1cj$		$2j/1cj$	
events selection	tag	final	tag	final
QCD multi-jets	690^{+37}_{-39}	111^{+14}_{-11}	35^{+8}_{-8}	$7.8^{+4.3}_{-3.2}$
fraction in data	77%	44%	53%	29%

7.2 W+jets

The production rates of W+jets events in proton-proton collisions, where some of the jets are initiated by heavy flavor quarks are predicted with larger uncertainties in Monte-Carlo simulation. As heavy flavor quarks we consider the charm and bottom quarks. They can be produced in particle - antiparticle pairs with or without an additional single heavy flavor quark. The W+jets production processes with the heavy flavor content used in this study are Wcc+jets, Wbb+jets and Wc+jets[8]. Wlight+jets refers to the events where only light quarks are produced together with a W boson. The phase space of the final states is partially overlapped

---

[8]Simulation of the Wb+jets process is not available in Monte-Carlo event generators used by the ATLAS experiment. Therefore, a part of the phase space of the production of events with single W boson and b-quark together with other types of partons in the final state is missing. However, the Wb+jets process has a relatively smaller cross section than Wcc+jets, Wbb+jets and Wc+jets and therefore, we expect that it has no significant influence on the single-top t-channel measurement.

between these samples (see Section 4.3.2). This overlap is removed before using the samples in the study.

After the tag selection the fraction of the heavy flavor component of W+jets events is significantly enhanced (see Figure 7.17 in comparison with Figure 7.20). This leads to an increased uncertainty of the Monte-Carlo simulation prediction of the contribution of the total W+jets background in the signal selection. Since we can not rely on this prediction [9], the task here is to measure W+jets background in the signal selection using a data driven method. Some theoretically motivated assumptions are used in the proposed method.

Assumption I: the uncertainties of the predictions for production rates of Wcc+jets and Wbb+jets events are taken to be completely correlated. This allows to combine the two processes, which we denote as Whf+jets. The true production rate of the Whf+jets events can be estimated by applying a scale factor to the predicted rate, where the scale factor is estimated from data.

Assumption II: the uncertainties of the predicted production rates of a given flavor component of the W+jets events with the different jet multiplicities are fully correlated. In other words, the predicted production rates of the $1j/1cj$ and $2j/1cj$ events of a given W+jets flavor (Whf+jets, Wc+jets or Wlight+jets) need a single scale factor in order to account for possible bias from the true rates. This means that we rely on the predicted ratios of the production rates of the $1j/1cj$ and $2j/1cj$ events for each W+jets flavor component and the task is to estimate the overall normalization scale factors for these components. Later, this assumption is dropped and the scale factors for the $1j/1cj$ and $2j/1cj$ events are varied relative to each other. The corresponding systematic uncertainties of the estimated yield of W+jets events are evaluated (see Section 8.1.1).

The tag and final selections of the $1j/1cj$ events are used for the W+jets background measurement. It was shown in Figures 7.16a and 7.16c that the $1j/1cj$ events are dominated by W+jets and QCD multi-jets. Contributions of other processes are taken from Monte-Carlo simulation with conservative uncertainties. The proposed method propagates the measured scale factors in the $1j/1cj$ events to the final selection of the $2j/1cj$ events. It uses the following variables,

- N_i^{pretag} - number of $1j/1cj$ events predicted by Monte-Carlo simulation for the i-th flavor component of W+jets after the pretag selection, where the index i stands for Wlight+jets, Wc+jets, Wcc+jets or Wbb+jets

- N_i^{tag} - same as above after the tag selection

- N_i^{final} - same as above after the final selection

- $N_{\text{MC}}^{\text{tag}}$ - sum of the $1j/1cj$ events of all Monte-Carlo samples except of W+jets after the tag selection (note: it does not include QCD multi-jets)

- $N_{\text{MC}}^{\text{final}}$ - same as above after the final selection

The following selection efficiencies are also defined,

- $\epsilon_i^{\text{tag}} = N_i^{\text{tag}}/N_i^{\text{pretag}}$

- $\epsilon_i^{\text{final}} = N_i^{\text{final}}/N_i^{\text{tag}}$

---

[9]The reason was explained in the beginning of this Chapter.

Similar variables for the $2j/1cj$ events are denoted by the following replacements of the letters,

- $N \rightarrow M$

- $\epsilon \rightarrow \alpha$

The true and estimated (measured) values of the above variables are denoted by putting the bar and the hat signs respectively. For instance, $\bar{N}_i^{\mathrm{pretag}}$ and $\hat{N}_i^{\mathrm{pretag}}$ are respectively the true and estimated numbers of the $1j/1cj$ events of the i-th flavor component of W+jets after the pretag selection.

In addition, we introduce corresponding variables for data, QCD multi-jets and W+jets,

- $N_{\mathrm{data}}^{\mathrm{tag}}$ - $1j/1cj$ events count after the tag selection in data

- $N_{\mathrm{data}}^{\mathrm{final}}$ - same as above after the final selection

- $\hat{N}_{\mathrm{QCD}}^{\mathrm{tag}}$ - QCD multi-jets $1j/1cj$ events estimate after the tag selection

- $\hat{N}_{\mathrm{QCD}}^{\mathrm{final}}$ - same as above after the final selection

- $\hat{N}_{\mathrm{W+jets}}^{\mathrm{tag}}$ - W+jets $1j/1cj$ events estimate after the tag selection (equals to $\sum \hat{N}_i^{\mathrm{tag}}$ by definition)

- $\hat{N}_{\mathrm{W+jets}}^{\mathrm{final}}$ - same as above after the final selection (equals to $\sum \hat{N}_i^{\mathrm{final}}$ by definition)

As before, similar variables for the $2j/1cj$ events are denoted by replacing N with M.

Using the above notations the $\hat{N}_{\mathrm{W+jets}}^{\mathrm{tag}}$ and $\hat{N}_{\mathrm{W+jets}}^{\mathrm{final}}$ estimates can be related to data through the equations,

$$\hat{N}_{\mathrm{W+jets}}^{\mathrm{tag}} = N_{\mathrm{data}}^{\mathrm{tag}} - \hat{N}_{\mathrm{QCD}}^{\mathrm{tag}} - N_{\mathrm{MC}}^{\mathrm{tag}} \tag{7.2}$$

$$\hat{N}_{\mathrm{W+jets}}^{\mathrm{final}} = N_{\mathrm{data}}^{\mathrm{final}} - \hat{N}_{\mathrm{QCD}}^{\mathrm{final}} - N_{\mathrm{MC}}^{\mathrm{final}} \tag{7.3}$$

The aim is to measure $\sum \hat{M}_i^{\mathrm{final}}$ - the net contribution of the W+jets $2j/1cj$ events after the final selection. It is the estimate for the true contribution $\sum \bar{M}_i^{\mathrm{final}}$. This later sum can be expressed using the true numbers of the $2j/1cj$ events after the tag selection and the corresponding selection efficiencies (which are actually the triangular cut efficiencies) defined above,

$$\sum \bar{M}_i^{\mathrm{final}} = \sum \bar{\alpha}_i^{\mathrm{final}} \bar{M}_i^{\mathrm{tag}} \tag{7.4}$$

Monte-Carlo simulation is used in order to estimate $\bar{\alpha}_i^{\mathrm{final}}$. Figure 7.17 shows the distributions of the triangular variable in the $1j/1cj$ (left plot) and $2j/1cj$ (right plot) events after the tag selection. According to the definition of the final selection the corresponding distributions are obtained from the distributions shown in Figure 7.17 by selecting events above 60 GeV threshold. Due to the similar shapes of the distributions the obtained selection efficiencies for the triangular cut are equal within statistical uncertainties. Figure 7.18 shows the selection efficiencies versus the W+jets flavor components for the $1j/1cj$ and $2j/1cj$ events.

The distributions are fitted by a constant function. The obtained averaged values of the efficiencies for the $1j/1cj$ and $2j/1cj$ events agree to each other within statistical uncertainties. Then, equation 7.4 can be rewritten as,

$$\sum \bar{M}_i^{\text{final}} \simeq \hat{\alpha}^{\text{final}} \sum \bar{M}_i^{\text{tag}} \simeq \hat{\epsilon}^{\text{final}} \sum \bar{M}_i^{\text{tag}} \tag{7.5}$$

Where, $\bar{\alpha}_i^{\text{final}}$ are replaced with their averaged estimate $\hat{\alpha}^{\text{final}}$ and eventually, the latter is replaced with the averaged efficiency $\hat{\epsilon}^{\text{final}}$, which can be calculated by using Equations 7.2 and 7.3,

$$\hat{\epsilon}^{\text{final}} = \frac{N_{\text{data}}^{\text{final}} - \hat{N}_{\text{QCD}}^{\text{final}} - N_{\text{MC}}^{\text{final}}}{N_{\text{data}}^{\text{tag}} - \hat{N}_{\text{QCD}}^{\text{tag}} - N_{\text{MC}}^{\text{tag}}} \tag{7.6}$$

(a) $1j/1cj$ (b) $2j/1cj$
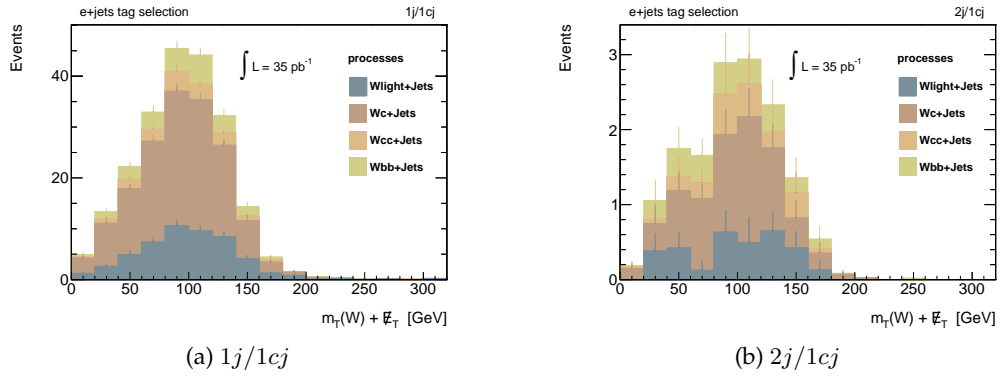
Figure 7.17: The triangular variable distribution for the different flavor components of W+jets in the $1j/1cj$ and $2j/1cj$ events after the tag selection.

The task is reduced to the problem of estimating $\sum \bar{M}_i^{\text{tag}}$ - the sum of the true number of the $2j/1cj$ events of the different flavor components of W+jets after the tag selection. We have that,

$$\bar{M}_i^{\text{tag}} = \bar{\alpha}_i^{\text{tag}} \bar{M}_i^{\text{pretag}} \simeq \alpha_i^{\text{tag}} \bar{M}_i^{\text{pretag}} \tag{7.7}$$

Where, $\bar{\alpha}_i^{\text{tag}}$ are replaced with their predicted values from Monte-Carlo simulation, α_i^{tag}. Later, the corresponding uncertainties of this replacement will be taken into account by the b-tagging uncertainties of jets in Monte-Carlo simulation.

According to assumption II the possible bias of the numbers of the $1j/1cj$ and $2j/1cj$ events after the pretag selection predicted by Monte-Carlo simulation, N_i^{pretag} and M_i^{pretag}, from their true values, $\bar{N}_i^{\text{pretag}}$ and $\bar{M}_i^{\text{pretag}}$, can be accounted by one scale factor sf_i for both $1j/1cj$ and $2j/1cj$ events,

$$\frac{\bar{M}_i^{\text{pretag}}}{M_i^{\text{pretag}}} \simeq \frac{\bar{N}_i^{\text{pretag}}}{N_i^{\text{pretag}}} \equiv \text{sf}_i \tag{7.8}$$

Equation 7.8 connects the $\bar{M}_i^{\text{pretag}}$ -unknowns to the $\bar{N}_i^{\text{pretag}}$ - unknowns. The latter can be estimated using the event numbers after the tag selection by considering the following equalities,
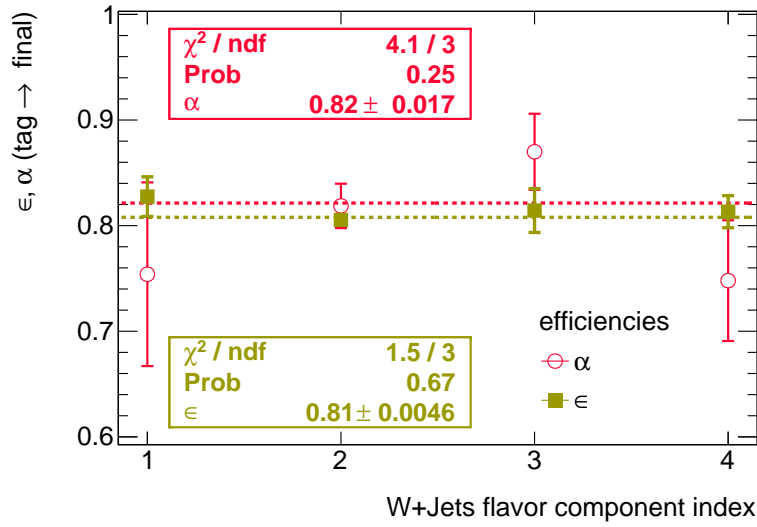
Figure 7.18: The triangular cut efficiencies for the different flavor components of W+jets in the $1j/1cj$ and $2j/1cj$ events, when the cut is applied after the tag selection. The x-axis represents integer identifiers for the W+jets flavor components: 1 - Wlight+jets; 2 - Wc+jets; 3 - Wcc+jets; 4 - Wbb+jets.

$$\bar{N}_i^{\mathrm{tag}} = \bar{\epsilon}_i^{\mathrm{tag}} \bar{N}_i^{\mathrm{pretag}} \simeq \epsilon_i^{\mathrm{tag}} \bar{N}_i^{\mathrm{pretag}} \tag{7.9}$$

Where, the true selection efficiencies, $\bar{\epsilon}_i^{\mathrm{tag}}$, are replaced with their Monte-Carlo predicted values, $\epsilon_i^{\mathrm{tag}}$, similarly to what was done in Equation 7.7. The corresponding uncertainties of the replacement $\bar{\epsilon}_i^{\mathrm{tag}} \to \epsilon_i^{\mathrm{tag}}$ will be accounted for in the measurement by the uncertainties of the jets b-tagging in Monte-Carlo simulation. The observed equality of $\bar{\epsilon}_i^{\mathrm{tag}}$ and $\bar{\alpha}_i^{\mathrm{tag}}$ in Monte-Carlo simulation that we used to derive Equation 7.5 also implies that the equalities shown by Equation 7.8 are valid for the respective number of events after the tag selection,

$$\mathrm{sf}_i \simeq \frac{\bar{N}_i^{\mathrm{tag}}}{N_i^{\mathrm{tag}}} \simeq \frac{\bar{M}_i^{\mathrm{tag}}}{M_i^{\mathrm{tag}}} \tag{7.10}$$

Now, the problem is reduced to the task to provide the estimates, $\hat{N}_i^{\mathrm{tag}}$, of the true $\bar{N}_i^{\mathrm{tag}}$ values. This will allow to estimate the scale factors sf_i and therefore, to estimate $\bar{M}_i^{\mathrm{tag}}$. The latter will be used in Equation 7.5 for the estimation of the total W+jets background in the $2j/1cj$ events after the final selection. For this goal the estimate $\hat{N}_{\mathrm{W+jets}}^{\mathrm{tag}}$ can be used. Since it is the estimate for the true net contribution of the different W+jets flavor components, we have that,

$$\hat{N}_{\mathrm{W+jets}}^{\mathrm{tag}} \simeq \bar{N}_{\mathrm{Wlight+jets}}^{\mathrm{tag}} + \bar{N}_{\mathrm{Wc+jets}}^{\mathrm{tag}} + \bar{N}_{\mathrm{Whf+jets}}^{\mathrm{tag}} \tag{7.11}$$

Where, $\bar{N}_{\mathrm{Whf+jets}}^{\mathrm{tag}} = \bar{N}_{\mathrm{Wcc+jets}}^{\mathrm{tag}} + \bar{N}_{\mathrm{Wbb+jets}}^{\mathrm{tag}}$. As it was already assumed in the beginning of the section (assumption I), the same scale factor is needed to account for the difference between the predicted and the true numbers of the Wcc+jets and Wbb+jets events. Thus, they can be combined into one sample. Equation 7.11 has three unknown quantities. We assume that the true event yields $\bar{N}_{\mathrm{Wlight+jets}}^{\mathrm{tag}}$ and $\bar{N}_{\mathrm{Whf+jets}}^{\mathrm{tag}}$ are correctly predicted by Monte-Carlo simulation

while $\bar{N}^{\text{tag}}_{\text{Wc+jets}}$ is not. This means that $\text{sf}_{\text{Wlight+jets}} = \text{sf}_{\text{Whf+jets}} = 1$ due to Equation 7.10. In other words, the observed discrepancy between $\hat{N}^{\text{tag}}_{\text{W+jets}}$ calculated using Equation 7.2 and the total prediction, $N^{\text{tag}}_{\text{Wlight+jets}} + N^{\text{tag}}_{\text{Whf+jets}} + N^{\text{tag}}_{\text{Wc+jets}}$, is due to $N^{\text{tag}}_{\text{Wc+jets}} \neq \bar{N}^{\text{tag}}_{\text{Wc+jets}}$. Since we are interested in net contributions of W+jets rather than its flavor components, we assign the observed discrepancy to the predicted contribution of only one flavor component, Wc+jets, of W+jets. We choose Wc+jets because it has largest predicted contribution in the events after the tag selection (see Figure 7.17) and therefore, the measurement is more sensitive to its contribution. Later, the scale factors of other flavor components, $\text{sf}_{\text{Wlight+jets}}$ and $\text{sf}_{\text{Whf+jets}}$, will be varied within conservative uncertainties (determined from data) in order to estimate the corresponding uncertainty of the measurement. Based on this discussion, Equation 7.11 can be re-written as,

$$\bar{N}^{\text{tag}}_{\text{Wc+jets}} \simeq \hat{N}^{\text{tag}}_{\text{W+jets}} - N^{\text{tag}}_{\text{Wlight+jets}} - N^{\text{tag}}_{\text{Whf+jets}} \tag{7.12}$$

By using Equation 7.12 in Equation 7.10 for $i = $ Wc+jets we have the following expression for $\text{sf}_{\text{Wc+jets}}$,

$$\text{sf}_{\text{Wc+jets}} \simeq \frac{\hat{N}^{\text{tag}}_{\text{W+jets}} - N^{\text{tag}}_{\text{Wlight+jets}} - N^{\text{tag}}_{\text{Whf+jets}}}{N^{\text{tag}}_{\text{Wc+jets}}} \tag{7.13}$$

Equation 7.10 also allows to derive an expression for $\bar{M}^{\text{tag}}_{\text{Wc+jets}}$ considering Equation 7.13,

$$\bar{M}^{\text{tag}}_{\text{Wc+jets}} \simeq M^{\text{tag}}_{\text{Wc+jets}} \frac{\hat{N}^{\text{tag}}_{\text{W+jets}} - N^{\text{tag}}_{\text{Wlight+jets}} - N^{\text{tag}}_{\text{Whf+jets}}}{N^{\text{tag}}_{\text{Wc+jets}}} \tag{7.14}$$

While,

$$\bar{M}^{\text{tag}}_{\text{Wlight+jets}} \simeq M^{\text{tag}}_{\text{Wlight+jets}} \tag{7.15}$$

$$\bar{M}^{\text{tag}}_{\text{Whf+jets}} \simeq M^{\text{tag}}_{\text{Whf+jets}} \tag{7.16}$$

Using Equations 7.16, 7.15, 7.14 and 7.6 in Equation 7.5, and also, considering Equation 7.2 the expression to estimate the sum of the W+jets $2j/1cj$ events after the final selection is derived,

$$
\begin{aligned}
\sum \hat{M}^{\text{final}}_i = {} & \frac{N^{\text{final}}_{\text{data}} - \hat{N}^{\text{final}}_{\text{QCD}} - N^{\text{final}}_{\text{MC}}}{N^{\text{tag}}_{\text{data}} - \hat{N}^{\text{tag}}_{\text{QCD}} - N^{\text{tag}}_{\text{MC}}} \\
& \times \Bigg[\, M^{\text{tag}}_{\text{Wc+jets}} \frac{N^{\text{tag}}_{\text{data}} - \hat{N}^{\text{tag}}_{\text{QCD}} - N^{\text{tag}}_{\text{MC}} - N^{\text{tag}}_{\text{Wlight+jets}} - N^{\text{tag}}_{\text{Whf+jets}}}{N^{\text{tag}}_{\text{Wc+jets}}} \\
& + M^{\text{tag}}_{\text{Wlight+jets}} \\
& + M^{\text{tag}}_{\text{Whf+jets}} \,\Bigg]
\end{aligned}
\tag{7.17}
$$

In order to estimate the uncertainty of the result of Equation 7.17 many pseudo experi-

ments are performed. The data counts, the QCD multi-jets estimates and the numbers of Monte-Carlo events have been randomly varied as Gaussian quantities. Uncertainty of each variable has been taken as the width (σ) of the corresponding Gauss distribution [10]. Figure 7.19 shows the resulting distribution of the interesting sum, $\sum \hat{M}_i^{\text{final}}$. The maximum probable value (MPV) of the distribution is taken as an estimate of the W+jets $2j/1cj$ events after the final selection. One standard up and down deviations from MPV are taken as the uncertainties of the estimate.
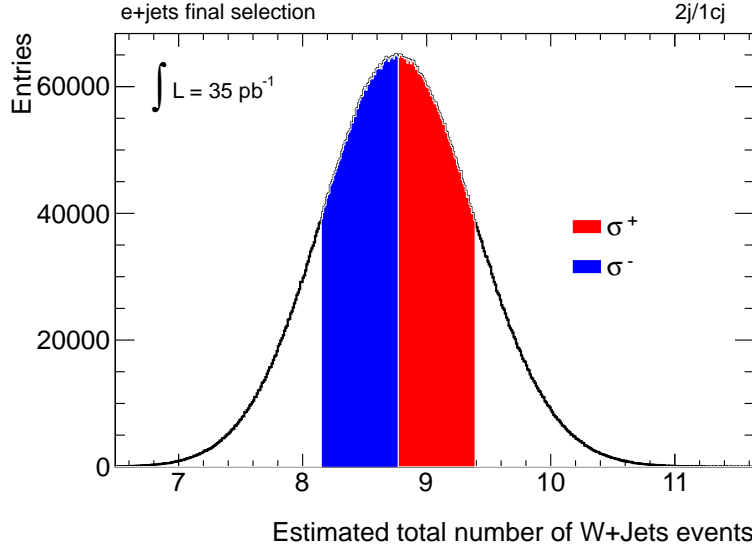
Figure 7.19: Distribution of $\sum \hat{M}_i^{\text{final}}$ - the estimated total number of the $2j/1cj$ events of W+jets after the final selection. The distribution is obtained using pseudo experiments.

Table 7.3 presents the results for the measured total contribution of the W+jets $2j/1cj$ events after the tag and final selections. The measurement uncertainties are also provided.

Table 7.3: Estimated total number of the $2j/1cj$ events of W+jets after the tag and final selections, $\sum \hat{M}_i^{\text{tag}}$ and $\sum \hat{M}_i^{\text{final}}$. The uncertainties are due to uncertainties of the data counts, the QCD multi-jets estimates and the predicted number of events used in Equation 7.17.

jet multiplicity	$2j/1cj$	
events selection	tag	final
W+jets events	12.5 ± 0.9	8.8 ± 0.7

When solving Equation 7.11 for $\bar{N}_{\text{Wc+jets}}^{\text{tag}}$, it was assumed that $\bar{N}_{\text{Wlight+jets}}^{\text{tag}} = N_{\text{Wlight+jets}}^{\text{tag}}$ and $\bar{N}_{\text{Whf+jets}}^{\text{tag}} = N_{\text{Whf+jets}}^{\text{tag}}$ implying $\text{sf}_{\text{Wlight+jets}} = \text{sf}_{\text{Whf+jets}} = 1$. Now, we vary these two scale factors independently from each other in order to estimate the corresponding systematic uncertainty of the measured sum $\sum \hat{M}_i^{\text{final}}$. The variation, $\delta \text{sf}_{\text{Wlight+jets}}$, is constrained

---

[10]Poisson uncertainties on data counts are replaced with Gaussian uncertainties, since the counts are large enough. The uncertainties of the numbers of Monte-Carlo events are due to limited size of the corresponding Monte-Carlo samples.

by the pretag measurement of $1j/1cj$ events in data. Since W+jets dominates in the tight signal region (> 70 GeV) of the triangular variable distribution after the pretag selection of the $1j/1cj$ events (see Figures 7.1a and 7.1c), we use the data count in the tight signal region (TSR) in order to determine an upper limit on the true value of the W+jets contribution, $\bar{N}_{\text{W+jets, max}}^{\text{pretag, TSR}} = N_{\text{data}}^{\text{pretag, TSR}} + \sqrt{N_{\text{data}}^{\text{pretag, TSR}}}$. Then, $\delta \text{sf}_{\text{Wlight+jets}}$ is determined from the expression , $\bar{N}_{\text{W+jets, max}}^{\text{pretag, TSR}} / N_{\text{W+jets}}^{\text{pretag, TSR}} - 1$, which gives 0.07. Here, $N_{\text{W+jets}}^{\text{pretag, TSR}}$ is the number of the W+jets $1j/1cj$ events in the tight signal region after the pretag selection. Also, since the W+jets events are dominated by Wlight+jets after the pretag selection (see Figure 7.20), we used the found upper limit as the possible variation of the scale factor for the $1j/1cj$ events of Wlight+jets after the pretag selection. As it was shown above, the scale factors are not changed by the b-jet requirement (see Equations 7.8 and 7.10) and therefore, $\delta^{\pm}\text{sf}_{\text{Wlight+jets}} = \pm 7\%$.
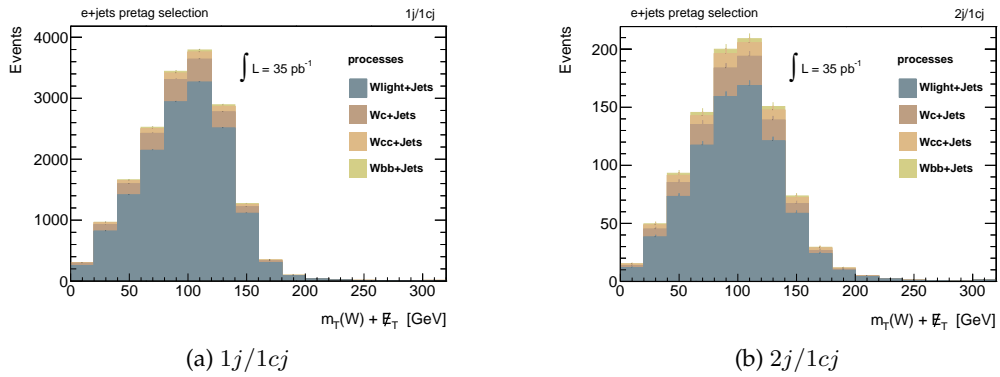
(a) $1j/1cj$

(b) $2j/1cj$

Figure 7.20: The triangular variable distribution for the different flavor components of the W+jets $1j/1cj$ and $2j/1cj$ events after the tag selection.

The up variation of the scale factor for Whf+jets is estimated from the final measurement of the $1j/1cj$ events. The $1j/1cj$ events after the final selection are dominated by QCD multi-jets and W+jets (see Figure 7.16c). We take the upper limit of the Whf+jets scale factor the following ratio, $(N_{\text{data}}^{\text{tag, TSR}} - N_{\text{Wlight+jets}}^{\text{tag, TSR}} - N_{\text{Wc+jets}}^{\text{tag, TSR}})/N_{\text{Whf+jets}}^{\text{tag, TSR}}$, where, all N-counts are obtained in TSR (defined above) of the $1j/1cj$ events after the tag selection. This leads to the estimate of the up uncertainty of the Whf+jets scale factor, $\delta^{+}\text{sf}_{\text{Whf+jets}} = +180\%$. The down variation is taken to be $\delta^{-}\text{sf}_{\text{Whf+jets}} = -100\%$.

For every single variation of $\text{sf}_{\text{Wlight+jets}}$ and $\text{sf}_{\text{Whf+jets}}$ within their uncertainties, $\text{sf}_{\text{Wc+jets}}$ is calculated in pseudo experiments by using Equation 7.13 [11]. Figure 7.21 shows the resulting distributions of $\text{sf}_{\text{Wc+jets}}$. Due to these variations of the scale factors, the MPV (obtained in the pseudo experiments) of the sum of interest, $\sum \hat{M}_i^{\text{final}}$, also varies away from the central value provided in Table 7.3. The up and down deviations from the central value are combined in an uncorrelated way in order to obtain the total systematic uncertainties. The results are $+2.9(+33\%)$ and $-1.6(-18\%)$ events as the up and down deviations from the measured central value, 8.8 events (see Table 7.3). The obtained results are only the part of the total

---

[11]Assuming that now, the predicted number of events, $N_{\text{Wc+jets}}^{\text{tag}}$ and $N_{\text{Whf+jets}}^{\text{tag}}$ are multiplied by the corresponding scale factors, $\text{sf}_{\text{Wlight+jets}}$ and $\text{sf}_{\text{Whf+jets}}$, in Equation 7.13 as well as in Equation 7.17. Also, $M_{\text{Wlight+jets}}^{\text{tag}}$ and $M_{\text{Whf+jets}}^{\text{tag}}$ are multiplied by $\text{sf}_{\text{Wlight+jets}}$ and $\text{sf}_{\text{Whf+jets}}$ respectively in Equation 7.17.
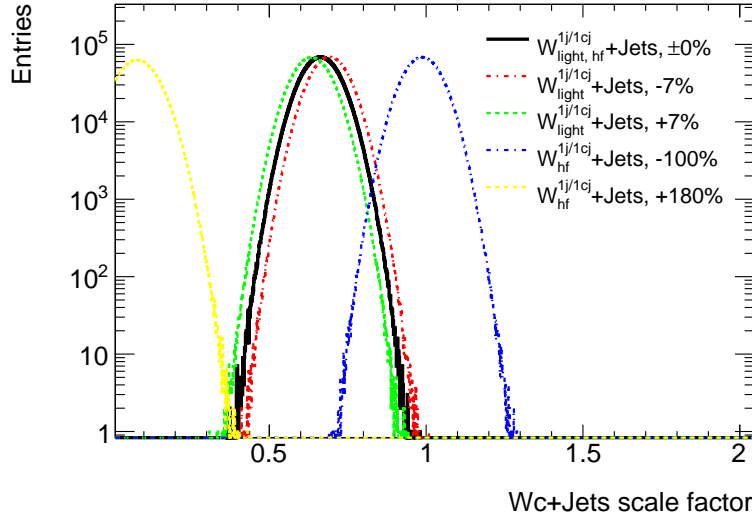
Figure 7.21: Distributions of the Wc+jets scale factor, $\mathrm{sf_{Wc+jets}}$, obtained in pseudo experiments carried out for each up and down variations of other scale factors, $\mathrm{sf_{Wlight+jets}}$ and $\mathrm{sf_{Whf+jets}}$.

systematic uncertainty of the W+jets event yield due to the scale factor uncertainties. Additional contributions come from dismissing assumption II, which was made in the beginning of this section. It will be discussed in the next chapter (Section 8.1.1) and the total systematic uncertainty will be evaluated.

Chapter 8

Systematic uncertainties of event yields

We have studied the sources of systematic uncertainties in the measurement of the t-channel cross section. Systematic The resulting uncertainties of the signal and background event yields are estimated and summarized in Table 8.9.

First, systematic uncertainties of the data driven measurement of the QCD multi-jets and the W+jets background are evaluated. This measurement has systematic uncertainties, since it rely on some predictions of Monte-Carlo simulation.

We investigated an influence of the systematic uncertainty sources due to the imperfections in the detector simulation, reconstruction and identification of physics objects on the signal and background event yields. Pile-up modeling in Monte-Carlo simulation and the luminosity related uncertainties of the event yields are also reviewed.

We also studied systematic uncertainties arising due to the theoretical uncertainties in our knowledge of the proton PDF and initial/final state radiation in proton-proton collisions. Furthermore, the alternative Monte-Carlo events generator has been used for the signal and background [1] events generation in order to evaluate the model dependent systematic uncertainties of the event acceptance in Monte-Carlo simulation.

The final uncertainties of the measured t-channel cross section will be discussed in the next chapter.

8.1 QCD multi-jets and W+jets

8.1.1 W+jets scale factors

Systematic uncertainties of the data driven measurement of W+jets was partially studied in the previous chapter (see Section 7.2). We considered independent variations of the Wlight+jets and Whf+jets scale factors from 1. The resulting variation of the Wc+jets scale factor was shown in Figure 7.21. These variations of the scale factors were evaluated as uncertainties of the measured $2j/1cj$ event yield of W+jets after the final selection.

Now, we estimate the total systematic uncertainties of the W+jets event yield due to the scale factors that means the assumption II (see Section 7.2) is dropped. By this we take into account the fact that the scale factors for the different flavor components of W+jets might differ for the $1j/1cj$ and $2j/1cj$ events.

First, the additional uncertainties of the scale factors of the W+jets flavor components for the $2j/1cj$ events are estimated. The possible variation of Wlight+jets contribution predicted by Monte-Carlo simulation is determined in the tight signal region (TSR) of the triangular

---

[1]The background processes, which contributions are estimated with the help of Monte-Carlo simulation only but not with data driven methods are assumed here.

variable distribution in the $2j/1cj$ events after the pretag selection. TSR is the region above 70 GeV of the triangular variable distribution. Since this region is dominated by W+jets (see Figures 7.1e and 7.1g), we use the same technique as was used in the case of the estimation of $\delta \mathrm{sf}_{\mathrm{Wlight+jets}}$ and $\delta \mathrm{sf}_{\mathrm{Whf+jets}}$ for the $1j/1cj$ events (see Section 7.2). This means that the upper limit of the possible contribution of W+jets in the signal region is take to be $\bar{M}_{\mathrm{W+jets,\,max}}^{\mathrm{pretag,\,TSR}} = M_{\mathrm{data}}^{\mathrm{pretag,\,TSR}} + \sqrt{M_{\mathrm{data}}^{\mathrm{pretag,\,TSR}}}$ [2], where, the data count, $M_{\mathrm{data}}^{\mathrm{pretag,\,TSR}}$, is obtained in TSR of the $2j/1cj$ events after the pretag selection. Wlight+jets has a dominant contribution in W+jets after the pretag selection of the $2j/1cj$ events (see Figure 7.20b). Therefore, the above upper limit can be used to determine $\delta \mathrm{sf}_{\mathrm{Wlight+jets}}$, which is defined as $\bar{M}_{\mathrm{W+jets,\,max}}^{\mathrm{pretag,\,TSR}}/M_{\mathrm{W+jets}}^{\mathrm{pretag,\,TSR}} - 1$. The result is $\delta^{\pm}\mathrm{sf}_{\mathrm{Wlight+jets}} = \pm 35\%$. We use the same uncertainty, 35%, for the Whf+jets and Wc+jets scale factors. This is a more conservative estimate than the result of an independent measurement [171] using the same data, which showed that the relative differences between the scale factors for $1j$ and $2j$ events are less than $10 - 15\%$.
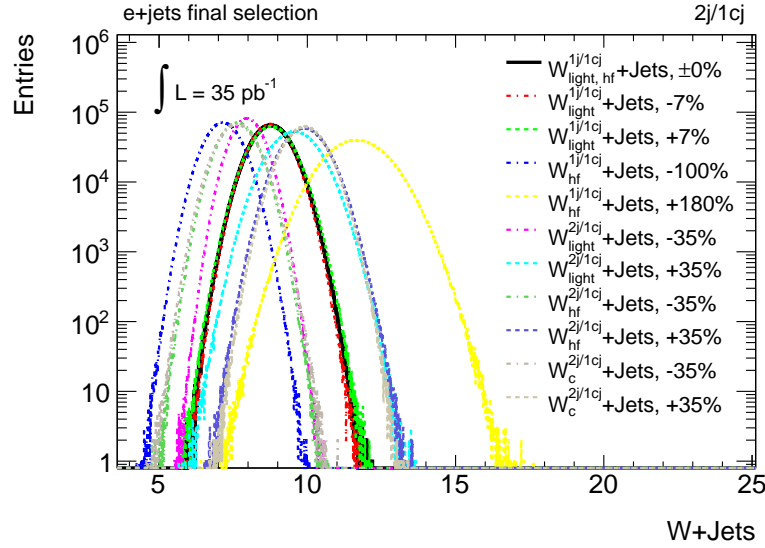
Figure 8.1: Distribution of $\sum \hat{M}_i^{\mathrm{final}}$ - the estimated number of the $2j/1cj$ events of W+jets after the final selection. A distribution for each single variation of the scale factors is obtained using pseudo experiments.

Equation 7.17 is used in pseudo-experiments to obtain the distributions of $\sum \hat{M}_i^{\mathrm{final}}$ and also $\sum_i \hat{M}_i^{\mathrm{tag}}$ for up and down variation of each scale factor separately. Figure 8.1 shows the results of the pseudo-experiments. The x-axis represents the estimated sum of $2j/1cj$ events of the different flavor components of W+jets after the final selection. The distribution obtained by using the nominal scale factors, $\mathrm{sf}_{\mathrm{Wlight+jets}} = \mathrm{sf}_{\mathrm{Whf+jets}} = 1$ and $\mathrm{sf}_{\mathrm{Wc+jets}}$ calculated with Equation 7.13, is presented with the solid black histogram on the plot and is labeled as $\mathrm{W}_{\mathrm{light,hf}}^{1j/1cj} + \mathrm{Jets}$. The distributions corresponding to the correlated variations of the scale factors between the $1j/1cj$ and $2j/1cj$ events are labeled as $\mathrm{W}_i^{1j/1cj} + \mathrm{Jets}$, where, the index i stands for only Wlight+jets and Whf+jets flavor components of W+jets. The Wc+jets scale factor varies accordingly (Equation 7.13). The plot also presents the distributions, which

---

[2]The same notations for variables as in Section 7.2 are used.

are obtained by variation of the scale factors for the $2j/1cj$ events only. They are labeled as $W^{2j/1cj}_i + \text{Jets}$, where, the index i stands for all flavor components of W+jets events, Wlight+jets, Wc+jets and Whf+jets. Deviations of the maximum probable values (MPV) of the distributions from MPV of the nominal distribution are combined in an uncorrelated way in order to obtain the up/down systematic uncertainties of the W+jets event yields. A similar measurement is also performed for W+jets events after the tag selection. Table 8.1 presents the resulting uncertainties in percents. They are the uncertainties of the W+jets event yields presented in Table 7.3 of the previous chapter.

Table 8.1: Systematic uncertainties of the $2j/1cj$ event yields, $\sum \hat{M}^{\text{tag}}_i$ and $\sum \hat{M}^{\text{final}}_i$, for W+jets due to the uncertainties of the scale factors for the W+jets flavor components.

$2j/1cj$ events	tag selection	final selection
Δ^+ W+jets	$+38\%$	$+38\%$
Δ^- W+jets	-27%	-28%

8.1.2 QCD multi-jets templates

The systematic uncertainties of the W+jets event yields in addition to those, which are shown in Table 8.1 are due to the systematic uncertainty of the measurement of QCD multi-jets in the $1j/1cj$ events [3]. Equation 7.17 shows that the estimated number of the $2j/1cj$ events of W+jets depends on the estimated numbers of the $1j/1cj$ events of QCD multi-jets after the tag and final selections, $\hat{N}^{\text{tag}}_{\text{QCD}}$ and $\hat{N}^{\text{final}}_{\text{QCD}}$. Therefore, their uncertainties cause the additional uncertainties of $\sum \hat{M}^{\text{final}}_i$. On the other hand, the uncertainty of the prediction of W+jets contribution in the $1j/1cj$ events causes an additional uncertainty in the QCD multi-jets measurement. The reason is that the QCD multi-jets templates are obtained after subtracting the contribution of W+jets and other processes predicted by Monte-Carlo simulation from data (see Section 7.1.1). This mutual dependence of the QCD multi-jets and W+jets measurements leads to the anti-correlated systematic uncertainties of the contribution of these background processes in the final selection of the $2j/1cj$ events. Below, we describe the procedure for calculation of these uncertainties.

First, we determine the possible maximal deviation of the predicted W+jets contribution in the $1j/1cj$ events after the tag selection from its true value. For this goal the triangular variable distributions shown in Figures 7.3a and 7.3c are used. The tight signal region ($>$ 70 GeV) of these distributions are dominated by W+jets events and we can use the already described technique for putting an upper limit on the true number of W+jets events using data. Namely, the upper limit is determined as $\bar{N}^{\text{tag, TSR}}_{\text{W+jets, max}} = N^{\text{tag, TSR}}_{\text{data}} + \sqrt{N^{\text{tag, TSR}}_{\text{data}}}$. The estimated maximal variations from the predictions are $+49\%$ and $+37\%$ for the $1j/1cj/central$ and the $1j/1cj/sides$ events respectively.

Then, we scale the triangular variable distribution in the $1j/1cj/central$ and $1j/1cj/sides$ events of W+jets after the tag selection by $\pm49\%$ and $\pm37\%$ respectively. QCD multi-jets tem-

---

[3]The uncertainty of the estimate of the QCD multi-jets contribution due to the uncertainties of the event weights (see Section 7.1.3) are already considered, however.

plates are re-calculated for each variation and the fit method is used to measure $\hat{N}_{\mathrm{QCD}}^{\mathrm{tag}}$ and $\hat{N}_{\mathrm{QCD}}^{\mathrm{final}}$. Figures 8.2a and 8.2b present the nominal and variation QCD multi-jets templates for the $1j/1cj/central$ and $1j/1cj/sides$ events respectively. The resulting systematic uncertainties of the estimated number of the QCD multi-jets events due to the variation of the templates in the control region ($< 60\,\mathrm{GeV}$) are shown in Table 8.2.

(a) $1j/1cj/central$ (b) $1j/1cj/sides$
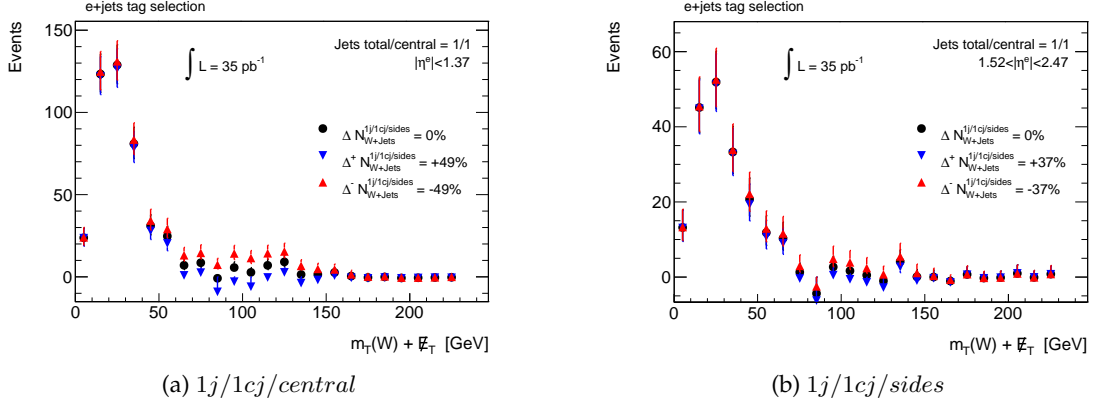
Figure 8.2: QCD multi-jets templates corresponding to the $1j/1cj/central$ (left) and $1j/1cj/sides$ (right) events after the tag selection. Templates obtained by variation of the W+jets normalization scale factors are presented together with the nominal template.

Table 8.2: Input normalization uncertainties of W+jets after the tag selection of the $1j/1cj/central$ and $1j/1cj/sides$ events and the resulting uncertainties of the estimated number of QCD multi-jets events after the tag and final selections.

events	Δ W+jets, tag	Δ QCD multi-jets, tag	Δ QCD multi-jets, final
$1j/1cj/central$	$\pm 49\%$	$\mp 4\%$	$\mp 8\%$
$1j/1cj/sides$	$\pm 37\%$	$\mp 3\%$	$\mp 7\%$

Using equation 7.17 the obtained uncertainties $\Delta\hat{N}_{\mathrm{QCD}}^{\mathrm{tag}}$ and $\Delta\hat{N}_{\mathrm{QCD}}^{\mathrm{final}}$ are propagated into the corresponding uncertainties of $\sum \hat{M}_i^{\mathrm{final}}$. The results are provided in table 8.3.

Table 8.3: Systematic uncertainties of the estimated W+jets contribution after the tag and final selection of the $2j/1cj$ events, $\sum \hat{M}_i^{\mathrm{tag}}$ and $\sum \hat{M}_i^{\mathrm{final}}$, due to the anti-correlated systematic uncertainties of the QCD multi-jets measurement of the $1j/1cj$ events after the tag selection.

$2j/1cj$ events	tag selection	final selection
Δ W+jets	$\pm 12\%$	$\pm 4\%$

When deriving the QCD multi-jets templates for the $2j/1cj$ events after the tag selection the W+jets contribution predicted by Monte-Carlo simulation was subtracted from data. This

predicted contribution of W+jets is include in Table 6.3, which is 13.3 ± 0.6 events. The results for QCD multi-jets contribution in the $2j/1cj$ events is provided in Table 7.2. Later, the W+jets contribution was estimated in the $2j/1cj$ events using data. The results of this data driven measurement are shown in Table 7.3, which provides the estimated number of $2j/1cj$ events of W+jets after the tag selection, 12.5 ± 0.9. We also estimated the systematic uncertainties of the W+jets measurement due to the uncertainties of the scale factors of the W+jets flavor components and also, due to the QCD multi-jets measurement uncertainty in the $1j/1cj$ events selection. The results are summarized in Tables 8.1 and 8.3. These data driven results of the W+jets contribution in the $2j/1cj$ events affects the QCD multi-jets measurement in the same events. In order to estimate the effect a new QCD multi-jets template is derived, where the predicted W+jets contribution is multiplied by the scale factor, $12.5/13.3$, before subtracting it from data. Additional templates of QCD multi-jets are also derived, where the predicted W+jets contribution is scaled by $12.5/13.3$ and then, scaled up or down by the corresponding uncertainties shown in Tables 8.1 and 8.3. The fit method is used to perform a new measurement of the QCD multi-jets contribution in the $2j/1cj$ events after the final selection. The new templates were used in the fit. The nominal estimate of the number of $2j/1cj$ events of QCD multi-jets after the final selection is increased by about 1.1% with respect to to the previous result (see Table 7.2) and is $7.9^{+4.3}_{-3.2}$. For each input systematic variation of the W+jets events after the tag selection the resulting anti-correlated uncertainty of the estimated QCD multi-jets events after the final selection is provided in 8.4.

Table 8.4: Systematic uncertainties of the estimated number of $2j/1cj$ events of QCD multi-jets after the final selection due to the measurement uncertainties of the $2j/1cj$ events of W+jets after the tag selection. These uncertainties of the W+jets and QCD multi-jets event yields are anti-correlated.

Δ W+jets, $2j/1cj$, tag selection	Δ QCD multi-jets, $2j/1cj$, final selection
$+38\%$	-7.2%
-27%	$+5.2\%$
$\pm 12\%$	$\mp 2\%$

8.1.3 QCD multi-jets fit model

In the previous chapter of background measurement we show that the triangular variable distribution of the QCD multi-jets events after the tag selection can be described by a Landau distribution in the lower energetic (control) region. We estimated the QCD multi-jets events contribution in the higher energetic (signal) region of the triangular variable distribution by extrapolating the Landau fit function. This approach assumes that the triangular variable for the QCD multi-jets events follows the Landau distribution in the signal region as well. This assumption is supported by the Monte-Carlo study, which was also discussed in the same chapter (section 7.1.2).

The triangular variable distribution of the QCD multi-jets events can be also fitted with an exponential function. This is the case for the Monte-Carlo sample of the QCD events, JF17. Figure 8.3 shows the same distributions as in Figures 7.10a and 7.10c now fitted with an exponential function. The low kinematic region of the distributions, below $20\,\mathrm{GeV}$, is not used

in the fit. The falling part of the distributions are well described by the exponential function.

(a) $1j/1cj/central$, matching truth electrons from B-meson decays

(b) $1j/1cj/sides$, matching truth electrons from photon conversion
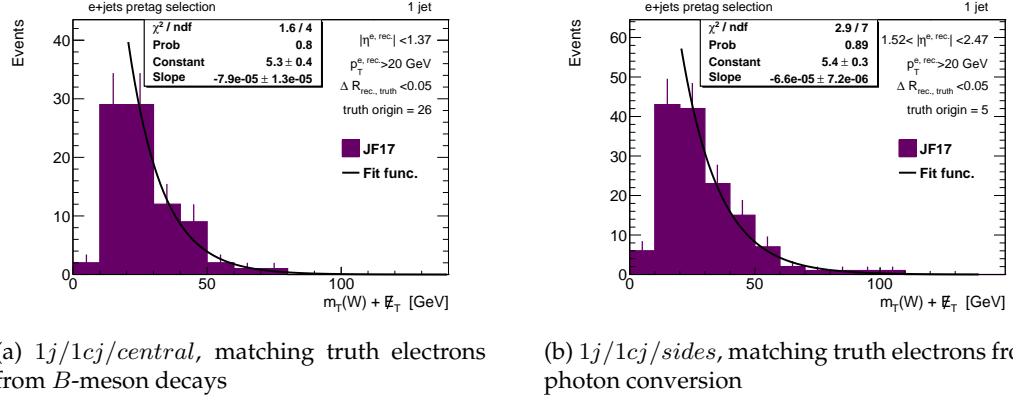
Figure 8.3: Triangular variable distribution in the $1j/1cj/central$ and the $1j/1cj/sides$ events after the pretag selection. Matching truth electrons are originated from B-meson decays or conversion. Exponential function is used to fit the falling part of the distributions.

In order to estimate the QCD multi-jets events contribution with a given jet multiplicity, we use the already described (section 7.1.1) the method of the simultaneous fit of concatenated 'central' and 'sides' templates. Figure 8.4 shows the result of the simultaneous exponential fit of the $1j/1cj/central$ and $1j/1cj/sides$ QCD multi-jets templates. The $20 - 60$ GeV control region of both templates are used in the fit.
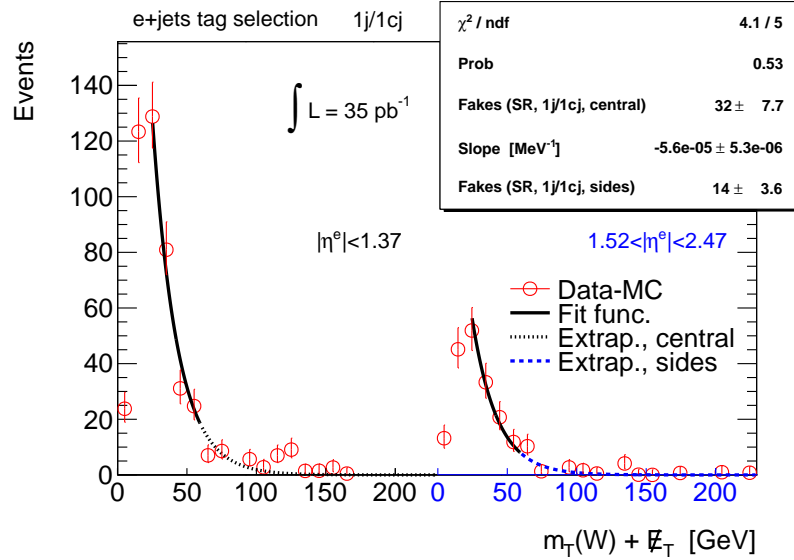
Figure 8.4: Simultaneous fit of the triangular variable distribution templates of the QCD multi-jets $1j/1cj/central$ and $1j/1cj/sides$ events after the tag selection. Templates are concatenated.

The exponential fit function is used to calculate the binned estimate of QCD multi-jets and to create maps of the corresponding event weights. The same method as before in Section 7.1.3 was used for this goal. Figure 8.5 show the triangular variable distribution (top row plots) for the $1j/1cj/central$ and $1j/1cj/sides$ events in data after the tag selection. The cor-

responding distribution of the QCD multi-jets estimate is also shown on both plots. Note, that since the exponential fit function does not cover the first bin of the distributions, the corresponding QCD multi-jets estimate is missing from the plots. We know from Monte-Carlo simulation that contributions of other physics processes such as W+jets and Z+jets are expected to be negligible in this lowest bin of the distribution. Also, It was shown by using the fit method with a Landau distribution that the QCD multi-jets contribution estimate is equal, within the one sigma statistical uncertainties, to data counts in this bin (Figures 7.12a and 7.12b). Therefore, we take the data count in this lowest bin with a Gaussian uncertainty as the QCD multi-jets estimate and calculate the corresponding event weight as well. The resulting event weight maps for the $1j/1cj/central$ and $1j/1cj/sides$ events are shown on the bottom row plots in Figure 8.5. Similar maps of event weights for the $2j/1cj/central$ and $2j/1cj/sides$ events are also created.

(a) $1j/1cj/central$

(b) $1j/1cj/sides$

(c) $1j/1cj/central$

(d) $1j/1cj/sides$
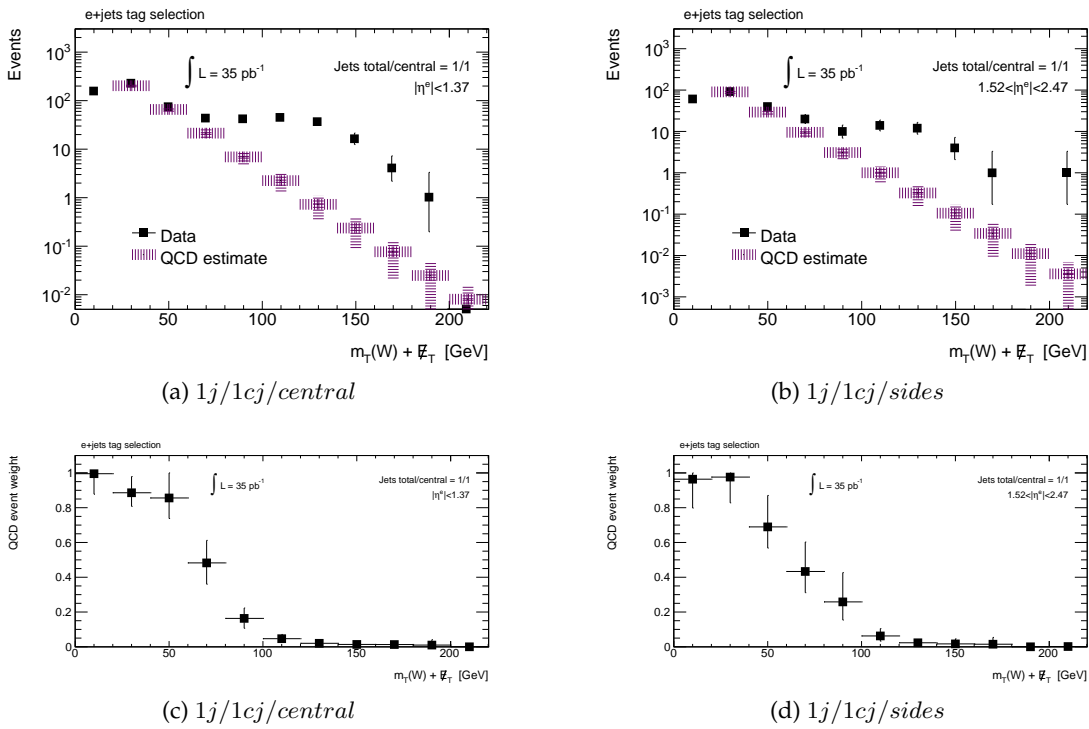
Figure 8.5: Top row: the data counts and the distribution of the QCD multi-jets estimate as functions of the triangular variable. The QCD multi-jets events estimate is obtained by integrating the exponential fit function within the corresponding bin limits. The plots correspond to the $1j/1cj/central$ (left) and $1j/1cj/sides$ (right) events after the tag selection. Bottom row: the event weights corresponding to the $2j/1cj/central$ (left) and $2j/1cj/sides$ (right) events after the tag selection.

The event weight maps are used to derive various kinematic distributions of QCD multi-jets events from data by using the event weighting method (see Section 7.1.3). Asymmetric uncertainties of the weights are propagated to uncertainties of the interesting distributions. We estimate the QCD multi-jets contribution in the $1j/1cj$ and $2j/1cj$ events after the tag and final selections using corresponding derived distributions of the triangular variable. Table 8.5 provides those estimates with their asymmetric uncertainties. Also, the relative deviations from the base measurement (Table 7.2). The results show that the estimated contribution of

the QCD multi-jets events is reduced in both $1j/1cj$ and $2j/1cj$ events with respect to the base measurement. This reduction is more significant for the final selection of events. The reduced contribution of the estimated number of QCD multi-jets events cause the opposite excess of the estimated number of the W+jets events with respect to the base measurement (Table 7.3). Results of the W+jets measurement in the $2j/1cj$ events after the tag and final selections are presented in Table 8.6. The symmetric uncertainties are due to the uncertainties of data counts, asymmetric uncertainties of the QCD multi-jets estimates and the Gaussian uncertainties of the predicted number of events of the different flavor components of W+jets. The large asymmetric uncertainties are due to uncertainties of the scale factors for the different flavor components of W+jets. The last row of the table presents nominal values of the relative deviations of the W+jets estimates from the base measurement.

Table 8.5: The measured estimates of the QCD multi-jets events and their fractions in data after the tag and final selections of the $1j/1cj$ and $2j/1cj$ events. The uncertainties are due to the uncertainties of the event weights used in estimation of the QCD multi-jets background from data. Relative deviations from the base measurement (Table 7.2) are presented in the last row.

jet multiplicity	$1j/1cj$		$2j/1cj$	
events selection	tag	final	tag	final
estimated QCD multi-jets events	644^{+31}_{-46}	45^{+10}_{-9}	34^{+8}_{-11}	$3.3^{+5.4}_{-2.9}$
fraction in data	72%	18%	52%	12%
relative deviation from the base measurement	-7%	-59%	-3%	-58%

Table 8.6: Estimated total number of the $2j/1cj$ events of W+jets after the tag and final selections. The uncertainties are due to uncertainties of the data counts, asymmetric uncertainties of the QCD multi-jets estimates and the Gaussian uncertainties of the predicted number of events of the different flavor components of W+jets. Relative deviations from the base measurement (Table 7.3) are presented in the last row.

jet multiplicity	$2j/1cj$	
events selection	tag	final
estimated W+jets events	$15.1 \pm 0.9^{+4.9}_{-4.5}$	$12.9 \pm 0.9^{+4.2}_{-3.9}$
relative deviation from the base measurement	$+19\%$	$+46\%$

By using an exponential function to model the QCD multi-jets background we obtained the results for QCD multi-jets and W+jets contributions in the $2j/1cj$ events after the final selection. The estimated number of events of these background processes deviate from the base measurement. Namely, a contribution of QCD multi-jets events is estimated to be by 58% less while the W+jets contribution is increased by 46%. However, the measurement uncertainties are large enough to cover the estimates of the base measurement. Therefore, we do not introduce additional uncertainties of the estimated event yields of QCD multi-jets and W+jets due to a choice of a fit model for the triangular variable distribution in QCD multi-jets events.

8.2 Background normalization in Monte-Carlo simulation

We use Monte-Carlo simulation based estimates of the event yields of the $t\bar{t}$, Wt-channel, di-bosons and Z+jets background processes normalized to their theoretical cross sections. It was shown (Table 6.3) that the contributions of these background processes to the final selection of events is small. The largest contribution is predicted for the $t\bar{t}$ background at about 6.3% of its fraction in the $2j/1cj$ event yield after the final selection. Therefore, using data driven methods for their determination is not as crucial as it is for the W+jets process, which contribution is estimated (in this study) to be about one third of the $2j/1cj$ event yield. The normalization uncertainties of the Monte-Carlo predicted background is aimed to cover the uncertainties of the theoretical cross sections of the background processes. This uncertainty is about 10% for the $t\bar{t}$ production cross section (see Table 2.1). Uncertainties of the differential cross section, which is reflected in the shape uncertainty of some kinematic distributions is not estimated using Monte-Carlo simulation. Instead, we take the theoretical total cross section uncertainty values of the $t\bar{t}$ process and combine it with the corresponding symmetrized uncertainty of the event yield due to the Monte-Carlo event generator choice. Uncertainties of the di-bosons and Z+jets event yields are taken $\pm100\%$, what accounts for the uncertainty of their theoretical cross sections and for a dependence of their event yields on a Monte-Carlo generator choice. Since the Wt-channel process was not measured yet, we take a larger upper uncertainty on its theoretical cross section, which is 400% and -100% as a down uncertainty. Given the small Monte-Carlo predicted contribution of Wt-channel into the final selection of the $2j/1cj$ events, the measurement of the t-channel cross section is not significantly affected by the large normalization uncertainties of the Wt-channel background.

8.3 Lepton selection

The t-channel selection is impacted by various sources of systematic uncertainties via the lepton selection. Two different types of lepton related systematic uncertainties can be distinguished. Uncertainties in the reconstruction of leptons energy and momentum belongs to one type of systematic uncertainties and are caused by uncertainties of the calibration of the energy-momentum and the parameterization of the detector resolution. They are directly propagated into leptons energy and momentum and the impact on an event selection is evaluated. $\not{E}_T$ is re-calculated in order to take into account variation of the energy and momentum of those leptons, which were originally used in the calculation of $\not{E}_T$.

The second type collects the lepton selection efficiency uncertainties. In order to match lepton selection efficiencies between data and Monte-Carlo simulation some scale factors are needed. Propagation of scale factors implies weighting of the Monte-Carlo event, which was already described in Section 6.3. Scale factors, which depend on kinematic variables of leptons are known with some uncertainties. They are varied by their up and down uncertainties and the impact on the tag and final selection of events is evaluated.

8.3.1 Electron energy calibration and resolution

We use random Gaussian smearing of the Monte-Carlo electron cluster energy in order to match the resolution between Monte-Carlo simulation and data. The width of the Gaussian is a function of the cluster energy, in the range $[10\text{ GeV}, 1\text{ TeV}]$ for the cluster transverse

energy, the cluster $|\eta|$ and a constant term. The constant term is measured in data with a certain $|\eta|$ binning and has associated up and down uncertainties. Systematic uncertainties of the selected number of Monte-Carlo events are obtained by up and down variation of the constant term. Resulting relative uncertainties are less than 1%.

Electron energy calibration in Monte-Carlo simulation is tuned by using electrons from the various processes such as $Z \to ee$ and $J/\psi \to ee$, which can be selected in data with high signal purity. Energy scale factors are estimated depending on the electron cluster η in the range $[-4.9, 4.9]$ divided in 58 non-equidistant bins. The uncertainty of the energy scale factors are provided in 8 bins of electron cluster $|\eta|$ in the range $[0, 4.9]$ and also have a dependence on the cluster transverse energy. The Monte-Carlo event selection is performed with up and down varied scale factors for the electron energy in order to estimate the corresponding uncertainties of the event yields.

8.3.2 Electron reconstruction, identification and trigger efficiency scale factors

We use the electron reconstruction, identification and trigger efficiency scale factors. The scale factors and the procedure of their propagation into the events weights were described in dedicated Sections 5.1 and 6.3. Electron reconstruction scale factor, which does not depend on the electron kinematic variables is combined with the electron identification scale factor. The electron identification scale factor is a function of the transverse energy and the cluster η of electrons. Uncertainties of the reconstruction and identification scale factors are combined in an uncorrelated way. Up and down variation of combined reconstruction and identification efficiency scale factors are propagated to the Monte-Carlo event weights. Resulting up and down variation of the number of selected (weighted) events are taken as the systematic uncertainties of the expected number of events for each Monte-Carlo process considered in this study. Uncertainty of the Monte-Carlo electron trigger efficiency scale factor is treated the same way.

The relatively large uncertainty in the acceptance due to the combined uncertainties of the reconstruction and identification scale factors indirectly affects the data driven measurement of the QCD multi-jets and W+jets background. This and similar non-negligible indirect influence on the data driven measurement from other sources of systematic uncertainties will be determined in Section 8.11. Corresponding quantitative estimates for the relative systematic uncertainties of the QCD multi-jets and W+jets events yields are provided, too.

8.3.3 Muon transverse momentum resolution

We smear muon p_T in the Monte-Carlo events in order to reach an agreement between data and Monte-Carlo simulation for the resolution of muon p_T reconstruction. Muon p_T values, which are independently measured by the inner detector and the muon spectrometer are used as inputs for the smearing procedure. Uncertainties of these values, which are partially correlated are propagated into the uncertainty of the combined muon track p_T and $\not{E}_T$ is re-calculated. Impact of each variation of the two input p_T values on the event selection is evaluated. Thus, the four estimates for the selected number of events are obtained for each Monte-Carlo process. The maximum and minimum numbers of the selected events are taken to calculate the up and down uncertainties of the events after the nominal selection. We found

that the muon p_T resolution uncertainty has a negligible effect on the signal and background yields of the $2j/1cj$ events after the final selection.

8.3.4 Muon reconstruction and identification scale factors

We use the muon reconstruction and identification scale factors to propagate them into the event weights similarly to the electron reconstruction and identification scale factors. Since our event selection implies rejecting those events, where at least one good muon is found, the weights of this kind of events can not change the selected number of weighted events after the final selection. Therefore, the uncertainties of the muon reconstruction and the identification scale factors do not cause any variation of the event yields.

8.4 Jet energy scale and resolution

Correct calibration of the jet energy scale and resolution in Monte-Carlo simulation is more challenging than it is in case of leptons. One of the reasons is the relatively larger volumes of the detector, were the energy deposition happens by the hadron constituents of the collision events. The fraction of the energy absorbed in the non-sensitive material of the detector and energy flow out of the detector is larger than in case of electro-magnetic energy deposition by electrons and photons [155]. This and other effects such as energy looses in the strong interactions of the hadrons with the detector material nuclei or the escaped energy carried away of the detector mainly by the secondary neutrinos causes larger uncertainties in the calibration of the jet energy scale and parameterization of the jets energy resolution The uncertainties of all the scale factors, which are applied to the jets energy in Monte-Carlo simulation are propagated to the $2j/1cj$ event yield after the final selection. The scale factors and their uncertainties depend on the jets momentum and angular variables. Uncertainties of the jet energy and momentum are also propagated to $\not{E}_T$, which is appropriately re-calculated. Resulting variations of the nominal yield of the $2j/1cj$ events are taken as the corresponding uncertainties.

The jet energy resolution uncertainty is estimated as the symmetrized difference between the event yields with and without smearing of the jets energy and momentum in Monte-Carlo samples. No additional uncertainties are assigned to the smearing parameters.

Soft jet energy correction uncertainties introduces an additional uncertainty in the $\not{E}_T$ calculation. Energy deposited in those detector cells, which are not included in any reconstructed jet object ('OutOfCell' energy) is not corrected on the hadronic energy scale and hence, can also bias the $\not{E}_T$ calculation if this energy is deposited in hadron activities. The both soft jet and 'OutOfCell' energy uncertainties are correlated. Their effect on the $2j/1cj$ event yield for the signal and background processes via the corresponding uncertainty of $\not{E}_T$ is evaluated.

8.5 Jet b-tagging

The b-tagged jet requirement removes a significant part of the background to the t-channel signal. Therefore, realistic identification of a jet flavor in Monte-Carlo simulation is rather crucial for our measurement in order to have a reliable event acceptance for the signal and the background. Scale factors, provided by auxiliary measurements, are introduced in order to match the heavy flavor jet identification and the light jets misidentification efficiencies between Monte-Carlo simulation and data. Similarly to the lepton identification scale factors,

these scale factors are also propagated into the event weights as described in Section 6.3. Evaluation of the uncertainties of the scale factors for each particular jet in Monte-Carlo events is done. These uncertainties are found to be one of the largest sources of systematic uncertainties of the signal and background event yields related to the detector Monte-Carlo simulation.

8.6 Pile-up

The instantaneous luminosity and the beam intensities of the LHC during the data taking period in 2010 was low (see Section 4.1) so that the small rate of multiple interactions in proton-proton collisions is observed (Figure 4.1b). Therefore, the related pile-up effect on the events acceptance is expected to be rather small and sufficiently controlled in Monte-Carlo simulation. The estimated relative uncertainty of the signal and background event yields is about 2%.

8.7 Integrated luminosity

The integrated luminosity collected in 2010 by the ATLAS detector and used in our study is known with a 3.4% overall uncertainty [130]. We apply this uncertainty to those background event yields, which are measured in Monte-Carlo simulation but not with the data driven methods. The uncertainty of the integrated luminosity is applied to the final measurement of the t-channel cross section.

8.8 Signal modeling

In this study we use Monte-Carlo samples of the t-channel signal and its background processes, such as the $t\bar{t}$ and Wt-channel production, generated by using the MC@NLO event generator interfaced to the HERWIG event generator. The latter generator is responsible for showering and hadronization of partons.

We acknowledge that some uncertainty of the Monte-Carlo based predictions for processes above exists due to a specific choice of a model of Monte-Carlo. In order to have a quantitative estimate of this uncertainty we used different Monte-Carlo event generators for production of signal and background event samples. Namely, we use the AcerMC event generator for generation of hard scattering events. The PYTHIA event generator is used for showering and hadronization of partons. These alternative signal and background samples are treated similarly to the nominal samples, following the full chain of detector simulation and event reconstruction. The choice of a model of Monte-Carlo event generation, MC@NLO +HERWIG versus AcerMC +PYTHIA, leads to a difference in the $2j/1cj$ event yields. PYTHIA parton showering model predicts more jet activity than HERWIG as this can be seen in Figure 8.6a, where the distributions of the jet multiplicity are obtained in the events after the electron selection. Therefore, more events with 2 jets are predicted by HERWIG. However, the number of 2 jet events with one ore two b-tagged jets is the same in both Monte-Carlo samples as can be seen in Figure 8.6b. This leads to the same event yield after the tag selection of the 2 jet events that implies the requirement of exactly one b-tagged jet.

The observed difference in the event yields is due to the pseudo-rapidity distribution of the second untagged jet. Figure 8.7 shows this distribution in both MC@NLO +HERWIG and

(a) jet multiplicity

(b) b-jet multiplicity in $2j$ events
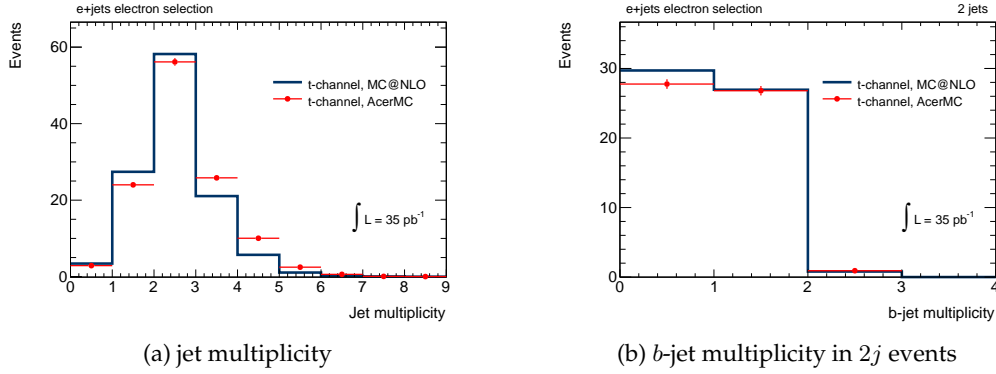
Figure 8.6: Jet (left) and b-tagged jet multiplicity in the 2 jet events (right) after the electron selection of the t-channel signal. Distributions obtained from the baseline MC@NLO +HERWIG event sample are compared with the distributions from the alternative AcerMC +PYTHIA sample.
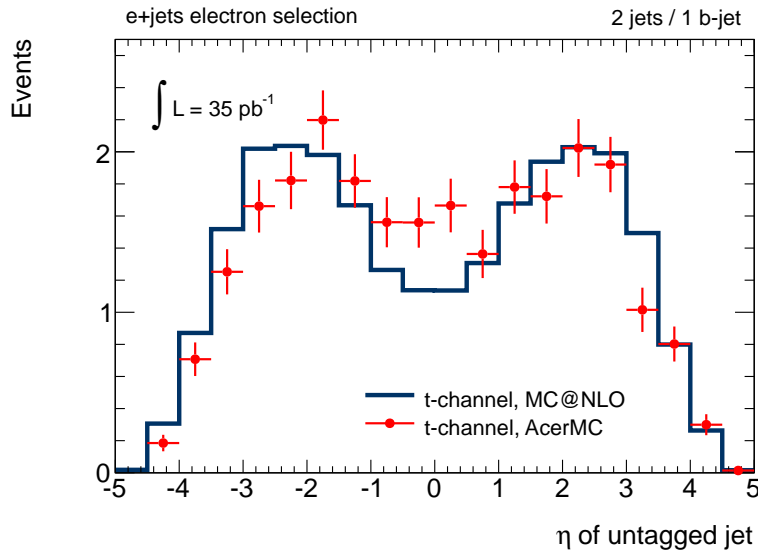

Figure 8.7: Pseudo-rapidity of the untagged jet in the 2 jet events with 1 b-tagged jet after the electron selection of the t-channel signal. The distribution obtained from the baseline MC@NLO +HERWIG event sample is compared with the distribution from the alternative AcerMC +PYTHIA sample.

AcerMC +PYTHIA samples. As can be seen from this plot, MC@NLO predicts more forward untagged jets in the 2 jet events with 1 b-tagged jet. After the selection of $2j/1cj$ events, which is done by requiring the untagged jet to be forward, $|\eta_{jet,\text{untagged}}| > 2.5$, we have a 14% larger event yield in the MC@NLO +HERWIG sample of t-channel with respect to the AcerMC +PYTHIA sample. We quote this difference as the uncertainty of the signal event yield due to the choice of the Monte-Carlo model. Similar uncertainties are estimated for $t\bar{t}$ and Wt-channel using the alternative event samples generated with AcerMC +PYTHIA.

8.9 Initial/final state radiation

Monte-Carlo modeling of the initial and final state radiation of partons in the collision events introduces an additional uncertainties of our measurement of the t-channel cross section. It has an impact on the hadron jets multiplicity in the Monte-Carlo simulated events. This can affect the selected number of events, since the selection depends on the number of jets in the central and the whole acceptance regions of the detector. In order to evaluate the uncertainty of the event acceptance due to the amount of ISR/FSR, we use t-channel, Wt-channel and $t\bar{t}$ samples generated with AcerMC interfaced by PYTHIA. PYTHIA provides possibilities to tune the amount of ISR and FSR within their experimentally available uncertainties independently to each other. Two samples with ISR and two samples with FSR variations of the tuning parameters are produced for each of the above three processes. The combinations of the ISR/FSR tuning parameters varied by their measured up and down uncertainties are selected in such a way to reach a maximum or a minimum deviations of the ISR and FSR amounts from their nominal values. We use these samples in our analysis in order to measure the corresponding difference in the event yields of signal and background with respect to to the nominal event yields. Since the ISR/FSR samples are statistically independent from each other and the numbers of their available events are restricted, the obtained uncertainty numbers are affected by the statistical fluctuations. In order to cover the pure systematic effect we take the uncertainties, which have the larger absolute values and symmetrize them. At the same time, we keep the signs of those uncertainties (which have larger absolute values) as they are. For instance, the corresponding 'up' and 'down' uncertainties of the t-channel event yield due to the FSR tuning are -11% and 11% respectively (see Table 8.9).

8.10 Parton density functions

Theoretical cross sections of signal and background processes depend on the choice of PDF. Consequently, the corresponding event yields as predicted in Monte-Carlo simulation also depend on the choice. The event kinematics, which might determine some of the distributions used in an event selection also depends on PDF. This makes an event acceptance to be sensitive to the choice of PDF that leads to additional uncertainties of in the event yields.

The parameters of a particular PDF are measured with some uncertainties. In order to account for these uncertainties some PDF sets are provided with so-called error PDFs, which are provided as 'up' and 'down' uncertainties for each parameter. The parameters are orthogonalized beforehand that means their uncertainties are uncorrelated. A theoretical cross section and an event yield of a given process depend on the error PDFs as well.

A dependence of the t-channel event acceptance on PDF was investigated. The error PDFs

of the original PDF set, CTEQ6.6 [152], which is used in generation of the t-channel events and also two other sets, MSTW2008nlo68cl [173] and NNPDF21_100 [174], are used to obtain a distribution of the t-channel event yield. The event weighting technique [175] is used for evaluating the yield of events generated at the central value PDF (defined at nominal values of the PDF parameters) for each error PDF of CTEQ6.6 and also for the central value and error PDFs of MSTW2008nlo68cl and NNPDF21_100. The variation of the vent yield due to the variation of the event acceptance but not the theoretical cross section of t-channel is estimated. The result is shown in Figure 8.8. The uncertainties of the t-channel event yield due to the error PDFs are presented on the plot as the dashed areas. The up and down uncertainties corresponding to the CTEQ6.6 and MSTW2008nlo68cl sets are calculated as the uncorrelated combination of all up and down variations of the event yield from the nominal value. The uncertainty corresponding to the NNPDF21_100 set is obtained as a width of Gaussian approximation of the spread of the event yield.

The final uncertainty of the event yield is calculated as a half of the difference between the maximum and minimum event yields. The maximum event yield is the yield obtained at the central value PDF of the NNPDF21_100 set plus the corresponding 'up' uncertainty as suggested by Figure 8.8. Then, the minimal event yield is the yield obtained at the central value PDF of the CTEQ6.6 set minus the corresponding 'down' uncertainty.
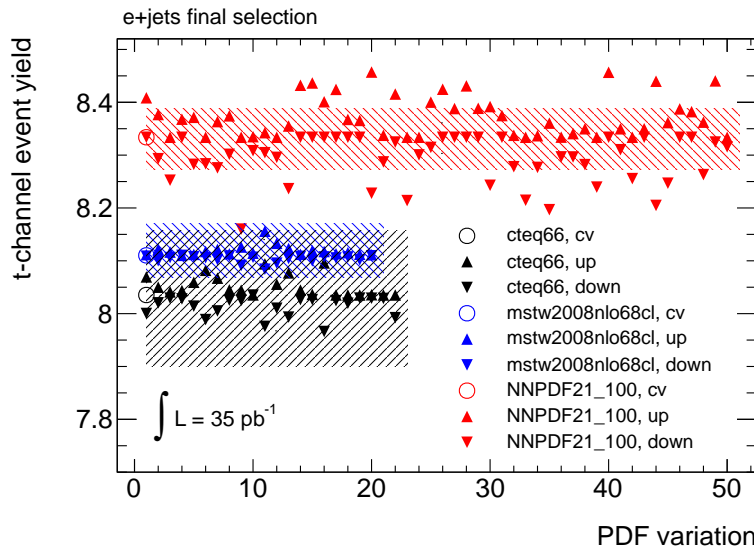
Figure 8.8: t-channel event yield obtained for each error PDF of the three different error PDF sets, CTEQ6.6, MSTW2008nlo68cl and NNPDF21_100. The resulting uncertainties of the event yield are presented on the plot as dashed areas for all three sets.

The uncertainties of the background event yields due to the choice a PDF set are combined with other systematic uncertainty sources such as factorization and re-normalization scale choices and quoted as the systematic uncertainties due the Monte-Carlo based background normalization.

8.11 Additional uncertainties in QCD multi-jets and W+jets measurement

The systematic uncertainties of the signal and background processes evaluated by using the corresponding Monte-Carlo samples can affect the data driven measurement of QCD multi-jets and W+jets. The reason is that the QCD multi-jets templates of the triangular variable are derived by subtracting the Monte-Carlo samples from data. It was shown that the contribution of W+jets and other processes in the dedicated control regions for the QCD multi-jets measurement in the $1j/1cj$ events after the tag selection are small, see Figures 7.3a and 7.3c. Nevertheless, their shape and normalization variations due to systematic uncertainties affect the templates and therefore, the QCD multi-jets estimate is also affected. We already measured the similar effect, described in Section 8.1.2, which was initiated due to the W+jets background normalization uncertainty. We do the same kind of measurement for other systematic uncertainty sources. QCD multi-jets templates are derived for the 'up' and 'down' variations of each systematic uncertainty source.

Table 8.7 presents the $1j/1cj$ event yields after the tag selection for all Monte-Carlo samples in the control region (< 60 GeV) of the triangular variable. The corresponding data events count is 651. The relative uncertainties (given in percents) of these event yields due to various systematic uncertainty sources are presented as well. The t-channel, Wt-channel, di-bosons and $t\bar{t}$ processes have negligible effect on the QCD multi-jets templates, since their contribution is predicted to be small. The W+jets and Z+jets contribution uncertainties can affect the templates. Figure 8.9 shows the triangular variable distribution in the $1j/1cj$ events of W+jets after the tag selection. The distributions corresponding to the jet energy scale (left plot) and the jets b-tagging (right plot) systematic 'up' and 'down' variations are also provided.

(a) JES up/down

(b) b-tagging up/down
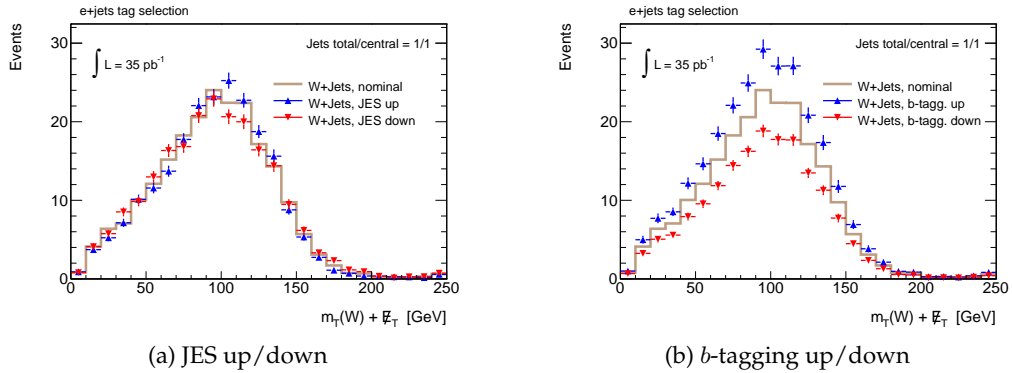
Figure 8.9: Triangular variable distribution in the $1j/1cj$ events of W+jets after the tag selection as predicted by Monte-Carlo simulation. The same distributions after the jet energy scale (left) and jets b-tagging (right) 'up' and 'down' systematic variations are superimposed on the nominal distribution.

We found that the considerable effect on the QCD multi-jets measurement comes from the uncertainties of the jets b-tagging as well as from the electron reconstruction and identification related uncertainties. The resulting uncertainties of the QCD multi-jets estimate of the $1j/1cj$ events after the tag and final selections are provided in Table 8.8. Even though the jet energy scale uncertainty also leads to the large uncertainties of the W+jets and Z+jets event yields, as shown in Table 8.7, it has no significant effect on the QCD multi-jets measurement, since

the uncertainties of the W+jets and Z+jets event yields are anti-correlated. The uncertainties of the $2j/1cj$ event yields of W+jets after the tag and final selection are calculated by using Equation 7.17.

The resulting up and down uncertainties of the W+jets estimate after the tag selection are also presented in Table 8.8. They are propagated into the uncertainty of the QCD multi-jets estimate of the $2j/1cj$ events after the final selection but the effect was found to be negligible.

Table 8.7: Relative systematic uncertainties of the estimated number of $1j/1cj$ events of the signal and background processes in the control region. Uncertainty numbers are provided in percents. These uncertainties correspond to the 'up' and 'down' variation of each source of systematic uncertainties except of the jet energy resolution.

	t-ch.	Wt-ch.	di-bosons	$t\bar{t}$	W+jets	Z+jets
Expected event yields	1.3	0.2	0.3	0.4	41	19
e - energy res.	-0.6	0.0	0.0	0.9	0.4	0.0
	0.0	0.0	0.2	-0.9	0.2	0.0
e - energy scale	-0.8	0.0	-0.1	0.0	-1.3	0.1
	0.0	1.0	0.5	0.0	0.9	-1.4
e - reco+ID SF	±3.8	±3.8	±3.8	±3.8	±3.8	±3.8
e - trig. SF	±0.5	±0.5	±0.5	±0.5	±0.5	±0.5
μ p_T res.	0.0	1.1	0.0	0.0	0.0	0.0
Jet energy res.	-1.7	3.3	4.7	-9.9	1.5	1.5
Jet energy scale	28	39	19	59	-4.9	3.9
	-28	-23	-23	-38	3.8	-6.0
Jet b-tagging	±10	±13	±17	±13	±21	±21
Soft + 'OutOfCell'	-0.7	-1.0	-0.4	-0.7	-0.3	-0.4
	-0.6	1.6	-0.2	3.5	0.3	-1.1

Our study of systematic uncertainties of the t-channel cross section measurement showed that the main uncertainty on the cross section measurement is caused by the large uncertainties of the QCD multi-jets contribution to the final selection of the $2j/1cj$ events. These up and down uncertainties are $+54\%$ and -41% respectively. Given the high fraction, $\simeq 29\%$, of the estimated QCD multi-jets background, its large uncertainties significantly affect the signal cross section measurement (see Section 9.2).

Table 8.8: Relative systematic uncertainties of the estimated number of $1j/1cj$ events of QCD multi-jets after the tag and final selections and the $2j/1cj$ events of W+jets after the tag selection presented in percents. The uncertainties correspond to the 'up' and 'down' variations of each source of systematic uncertainties. The corresponding estimated number of events of QCD multi-jets and W+jets are provided (copied from Tables 7.2 and 7.3).

| | QCD multi-jets, $1j/1cj$ | | W+jets, $2j/1cj$ |
	tag	final	tag
Estimated event yields	690	111	12.5
e - reco+ID SF	-0.4 0.9	∓ 0.9	0.9 -1.5
Jet energy scale	0 -0.14	0.2 -0.6	0 0.3
Jet b-tagging	∓ 2.7	∓ 5.0	± 6.6

Table 8.9: Summary of the systematic uncertainties of the $2j/1cj$ event yields presented in percents. The uncertainties correspond to the 'up' and 'down' variations of each systematic uncertainty source, except of the jet energy resolution and the Monte-Carlo generator choice. The asymmetric uncertainties are presented in two rows, where the top row corresponds to the 'up' variation of the given source and the bottom row corresponds to the 'down' variation. All uncertainty numbers are rounded to 0 if they are less than 0.1%. The empty fields in the columns mean that the corresponding uncertainty sources are either irrelevant to the measurement of a given physics process or they have negligible effects on it. The content of Tables 6.3, 7.3, 8.1, 8.3 and 8.4 are used.

	t-ch.	Wt-ch.	Di-bosons	ttbar	Z+jets	W+jets	QCD
Statistical	8.1	0.34	0.17	1.69	0.7	8.8	7.9
limitations	±0.1	±0.02	±0.02	±0.08	±0.3	±0.7	+4.3 / − 3.2
Luminosity	±3.4	±3.4	±3.4	±3.4	±3.4		
W+jets heavy						38	−7.2
flavor SF						−28	5.2
W+jets						±4	∓2
norm., CR							
e - energy res.	0.0	0.6	0.0	0.0	0.0		
	0.0	−0.6	0.1	0.0	0.0		
e - energy scale	0.3	0.6	0.1	0.0	0.0		
	−0.3	−0.6	0.0	−0.2	0.0		
e - reco+ID SF	±3.8	±3.8	±3.8	±3.8	±3.9	0.4	
						−0.3	
e - trig. SF	±0.5	±0.5	±0.5	±0.5	±0.5		
μ p_T res.	0.0	0.0	0.0	0.0	0.0		
Jet energy res.	0.3	4.0	0.9	0.9	12.1		
Jet energy scale	−12	−8.1	−25	10	−62	−0.1	
	6.5	−7.8	48	−9.1	63	0.3	
Jet b-tagging	±12	±13	±19	±14	±17	±2.0	
Soft +	0.0	1.2	−0.1	−0.7	−13		
'OutOfCell'	0.0	0.0	−0.3	0.0	0.0		
Pile-up	±2	±2	±2	±2	±2		
MC generator	−14	−68	n/a	−39	n/a		
ISR	−8.8	47	n/a	−6.3	n/a		
	15	134		10			
FSR	−11	121	n/a	−18	n/a		
	−1.4	−5.3		−11			
PDF effect	±5.1						
on acceptance							
MC background		400	100	7	100		
normalization		−100	−100	−10	−100		

Chapter 9

t-channel cross section measurement

The methods to measure the t-channel cross section and its uncertainty are described in this chapter. Details of the measurement as well as the final results are presented. The impact of the various systematic uncertainties on the results is studied and evaluated into the final uncertainties of the measurement.

9.1 Maximum likelihood method

We use the maximum likelihood method [25, 176] to estimate the t-channel cross section and its measurement uncertainty. In order to estimate the uncertainty or the confidence intervals, the profile log-likelihood ratio method is used. This method has theoretically known asymptotic approximation for determination of confidence intervals when a size of a data sample increases. We do use the asymptotic formalism in our analysis to estimate uncertainties of the t-channel cross section. In contrast, the cross section upper limit is estimated using a more reliable procedure based on pseudo experiments, which utilizes the profile log-likelihood ratio as a test statistics. Both approaches lead to the same result in estimation of confidence intervals when data statistics reaches asymptotic values.

9.1.1 Likelihood function

In order to fit data we construct a ratio of a t-channel cross section estimate over its theoretical value, $\mu = \sigma^{\mathrm{obs}}/\sigma^{\mathrm{theory}}$, as a free parameter of a likelihood function. This ratio is also called a signal strength. $\hat{\mu}$ is the global maximum of the likelihood function and describes the compatibility of the measured cross section to the theoretically expected value. Confidence intervals for μ obtained using the profiling method allows to extract uncertainties on the t-channel cross section measurement.

Due to the limited count of the selected events we perform the measurement using an unbinned likelihood function. The total number of selected events, $N^{\mathrm{obs}} = 27$, is considered to be distributed according to a Poisson distribution with the expectation value of the total selected number of events, $N_{\mathrm{total}}^{\mathrm{exp}}$. Its probability density function (p.d.f.) is denoted as $P(N^{\mathrm{obs}}; N_{\mathrm{total}}^{\mathrm{exp}})$. A precision of the knowledge of $N_{\mathrm{total}}^{\mathrm{exp}}$ is affected by the various sources of systematic uncertainties. Below, we determine this dependence on the systematic uncertainty sources introducing the nuisance parameters of the likelihood function and use it in evaluation of the confidence intervals for the measured t-channel cross section.

$N_{\mathrm{total}}^{\mathrm{exp}}$ can be re-written in terms of the expectation values for the signal and background processes as shown by Equation 9.1,

$$N_{\text{total}}^{\text{exp}} = N_{\text{t−ch.}}^{\text{exp}} + \sum_{k \in \text{bkg.}} N_k^{\text{exp}} \tag{9.1}$$

Where, $N_{\text{t−ch.}}^{\text{exp}}$ and N_k^{exp} are the expectation values for the signal and the k-th background event yields respectively. They themselves are parameterized as given by Equations 9.2,

$$N_{\text{t−ch.}}^{\text{exp}} = l\mu N_{\text{t−ch.}}^{\text{exp}}(L_0)$$

$$N_k^{\text{exp}} = l N_k^{\text{exp}}(L_0) \tag{9.2}$$

Where, $l = L/L_0$ is the ratio of a variable integrated luminosity over its measured value and is a nuisance parameter, which accounts for the uncertainty on the integrated luminosity measurement [1]. When maximizing the likelihood function, we constrain it with a Gaussian p.d.f. denoted as $G(l_0; l, \sigma_l)$, where, $l_0 = 1$ and $\sigma_l = 0.034$ is the uncertainty of the measured integrated luminosity (see Table 8.9). $N_{\text{t−ch.}}^{\text{exp}}(L_0)$ and $N_k^{\text{exp}}(L_0)$ are the expectation values of the selected signal and background normalized to the nominal integrated luminosity L_0. Their nominal expectation values, $\tilde{N}_{\text{t−ch.}}(L_0)$ and $\tilde{N}_k(L_0)$, are predicted from Monte-Carlo simulation or estimated using the data driven methods and are provided in the first row of Table 8.9. They have uncertainties due to the data driven measurements or the limited sizes of Monte-Carlo samples as well as the uncertainties due to the various systematic uncertainty sources affecting their measurement/prediction. We denote the systematic uncertainty sources as $\{\alpha_j\}_{j \in \text{syst.}}$ without including the luminosity uncertainty. Below we use α_j to denote a nuisance parameter of the likelihood function, which characterizes the j-th source of the systematic uncertainty. The expectation values of the signal and background processes are differently affected from a certain source of a systematic uncertainty. From the study of systematic uncertainties, we know how much the 'up' and 'down' variations, denoted as $\sigma_{m,j}^{\pm}$, where, $m \in (\text{t − ch.}, \text{bkg.})$ and $j \in \text{syst.}$, change the given expectation value (see Table 8.9). The corresponding expectation values are denoted as $\tilde{N}_{m,j}(\sigma_{m,j}^{\pm}; L_0)$. Deviations of these values from the nominal values are denoted as $\Delta\tilde{N}_{m,j}(\sigma_{m,j}^{\pm}; L_0)$.

Extrapolation of the expectation values at any variation of each given systematic uncertainty source is done using a linear piece-wise equation system 9.3,

$$N_{m,j}^{\text{exp}}(\alpha_j; L_0) = \begin{cases} \tilde{N}_m(L_0) + \alpha_j(\tilde{N}_{m,j}(\sigma_{m,j}^+; L_0) - \tilde{N}_m(L_0)) & \text{if } \rho_{m,j}\alpha_j > 0 \\ \tilde{N}_m(L_0) & \text{if } \rho_{m,j}\alpha_j = 0 \\ \tilde{N}_m(L_0) - \alpha_j(\tilde{N}_{m,j}(\sigma_{m,j}^-; L_0) - \tilde{N}_m(L_0)) & \text{if } \rho_{m,j}\alpha_j < 0 \end{cases} \tag{9.3}$$

Or alternatively, an exponential piece-wise equation system 9.4,

$$N_{m,j}^{\text{exp}}(\alpha_j; L_0) = \begin{cases} \tilde{N}_m(L_0)(1 + \Delta\tilde{N}_{m,j}(\sigma_{m,j}^+; L_0)/\tilde{N}_m(L_0))^{\alpha_j} & \text{if } \rho_{m,j}\alpha_j > 0 \\ \tilde{N}_m(L_0) & \text{if } \rho_{m,j}\alpha_j = 0 \\ \tilde{N}_m(L_0)(1 + \Delta\tilde{N}_{m,j}(\sigma_{m,j}^-; L_0)/\tilde{N}_m(L_0))^{\alpha_j} & \text{if } \rho_{m,j}\alpha_j < 0 \end{cases} \tag{9.4}$$

Where, $m \in (\text{t − ch.}, \text{bkg.})$, $j \in \text{syst.}$ and $\rho_{m,j}$ are the correlation factors and can obtain only two values, $+1$ or -1. They are necessary in order to correctly consider correlation or anti-correlation between the different processes when systematically varying them. The detailed

---

[1] Applied to only those background processes, which are estimated from Monte-Carlo simulation.

procedure is explained below.

Both equation systems imply that the parameterization of the α_j nuisance parameters is done in such a way that the $\alpha_j = 0, \pm 1$ values map to the $\tilde{N}_m(L_0)$ and $\tilde{N}_{m,j}(\sigma_{m,j}^{\pm}; L_0)$ expectation values respectively. We use a normalized Gaussian p.d.f., $G(0; \alpha_j, 1)$, in order to constrain the α_j nuisance parameters and thus, ensure physically meaningful variation of the expectation values of the event yields.

Different sources of systematic uncertainties are uncorrelated. But the effect of some of them on the expectation values of the different processes can be correlated or anti-correlated as was shown in the previous chapter describing the study of systematic uncertainties. Fully correlated or anti-correlated systematic variation of the signal and background expectation values can be parameterized in such a way, that the corresponding nuisance parameter, α_j, is constrained with a single normalized Gaussian p.d.f.. The correlation sign between any couple of the processes is taken into account by using $\rho_{m,j}$, which was already defined above. It is always $+1$ for t-channel. Further, $\rho_{k,j} = +1$ for all those k-th background processes, which have fully correlated variation with t-channel due to the given j-th source of systematic uncertainties. For fully anti-correlated background processes it is -1.

Those systematic uncertainty sources, which have uncorrelated effects on the event yields of different processes are treated differently. The Monte-Carlo based background normalization uncertainty, $\alpha_{\text{norm.}}$, is uncorrelated between the different processes. Its effect on each background process known from Monte-Carlo simulation is parameterized with the separate normalized Gaussian p.d.f., $G(0, \alpha_{k,\text{norm.}}, 1)$, where, $k \in \text{MC bkg.}$. The joint p.d.f. is the product of all single p.d.f., $\prod_{k \in \text{MC bkg.}} G(0; \alpha_{k,\text{norm.}}, 1)$.

The uncertainties of the signal and background event yields due to limited sizes of the Monte-Carlo samples or due to the data driven measurements of some background processes are uncorrelated between these processes. We denote them as $\alpha_{m,\text{stat.}}$, where, $m \in (\text{t} - \text{ch.}, \text{bkg.})$. They are parameterized with the normalized Gaussian p.d.f., $G(0; \alpha_{m,\text{stat.}}, 1)$, separately for each process. The joint p.d.f. is $\prod_{m \in (\text{t}-\text{ch.},\text{bkg.})} G(0; \alpha_{m,\text{stat.}}, 1)$.

Having Equations 9.3 and 9.4 and the prescription for proper handling of correlations we can calculate $N_{\text{t}-\text{ch.}}^{\text{exp}}(L_0)$ and $N_k^{\text{exp}}(L_0)$ at any variation of each of the α_j nuisance parameters. Plugging them into Equations 9.2 and using the results of these later in Equation 9.1, we calculate $N_{\text{total}}^{\text{exp}}$. Note, that $N_{\text{total}}^{\text{exp}}$ depends on $\{\alpha_j\}_{j \in \text{syst.}}$ as well as on l and μ.

A likelihood function, which depends on μ, the parameter of interest, and on the nuisance parameters l and $\{\alpha_j\}_{j \in \text{syst.}}$ is given by Equation 9.5,

$$
\begin{aligned}
\mathcal{L}(\mu, l, \alpha_j) = P(N^{\text{obs}}; & N_{\text{total}}^{\text{exp}}) \\
& \times G(l_0; l, \sigma_l) \\
& \times \prod_{k \in \text{MC bkg.}} G(0; \alpha_{k,\text{norm.}}, 1) \\
& \times \prod_{m \in (\text{t}-\text{ch.},\text{bkg.})} G(0; \alpha_{m,\text{stat.}}, 1) \\
& \times \prod_{i \in (\text{syst.} \not\supset (\text{stat.},\text{norm.}))} G(0; \alpha_i, 1)
\end{aligned}
\tag{9.5}
$$

Where, α_j implies the set of all $\alpha_{m,\text{stat.}}$, $\alpha_{k,\text{norm.}}$ and α_i nuisance parameters. By maximization of the likelihood function with respect to all its parameters (μ, l and α_j) we obtain the

maximum likelihood estimate (MLE) for the t-channel cross section deviation from the theory predicted value, which we denote as $\hat{\mu}$. It is well-known that MLE is a *consistent* estimator that means if a data sample size increases, then $\hat{\mu} \to \mu^t$, where, μ^t is the true value of μ.

9.1.2 Profile likelihood ratio

In order to determine confidence intervals of μ^t given $\hat{\mu}$ the profile likelihood ratio is constructed as given by Equation 9.6,

$$\lambda(\mu) = \frac{\mathcal{L}(\mu, \hat{\hat{l}}, \hat{\hat{\alpha}}_j)}{\mathcal{L}(\hat{\mu}, \hat{l}, \hat{\alpha}_j)} \tag{9.6}$$

Where, $\mathcal{L}(\hat{\mu}, \hat{l}, \hat{\alpha}_j)$ is the maximum of the likelihood function with respect to all parameters; $\mathcal{L}(\mu, \hat{\hat{l}}, \hat{\hat{\alpha}}_j)$ is a conditional (profiled) maximum of the likelihood function with respect to the l and α_j nuisance parameters, while holding μ fixed at any arbitrary value.

It is common practice in high energy physics to use two times negative natural logarithm of the profile likelihood ratio, $-2ln\lambda(\mu)$, as a frequentist test statistics for estimating confidence intervals [2]. The reason for this choice is a well-known asymptotic behavior of $-2\ln\lambda(\mu)$, when the data sample size increases. Then according to Wald's results [177, 178]) the following relation is true,

$$-2\ln\lambda(\mu) = \left(\frac{\mu - \hat{\mu}}{\sigma}\right)^2 + \mathcal{O}(1/\sqrt{N^{\text{obs}}}) \tag{9.7}$$

if $\hat{\mu}$ is distributed as a Gaussian with a mean equal to the true value μ^t and a standard deviation σ. Wald's equation implies the *consistency* and *asymptotic normality* properties of MLE, when a data sample size is large enough and some general conditions [3] are matched [176].

By 'scanning' the μ parameter, one finds its values, μ_{lim}, for which $-2\ln\lambda(\mu_{\text{lim}}) = 1$. Thus, one estimates $\sigma = |\mu_{\text{lim}} - \hat{\mu}_0|$, the standard deviation of $\hat{\mu}$. It is an *efficient* estimator of the variance of $\hat{\mu}$ [176]. This means that the interval $[-\sigma + \hat{\mu}, \hat{\mu} + \sigma]$ is the smallest one among all intervals, which have a 68.3% probability to cover the true value μ^t.

In practice, we observe that $-2\ln\lambda(\mu)$ is not a symmetric function with respect to $\mu - \hat{\mu}$, which is due to asymmetric systematic uncertainties entering via the nuisance parameters into the likelihood function. This leads to a non-Gaussian $p.d.f.(\hat{\mu})$ and therefore, Wald's equation is not valid. It can be shown [179, 180] that in the asymptotic regime an interval determined by the equation $-2\ln\lambda(\mu) = 1$ and leading to non-equal up and down standard deviations for the $\hat{\mu}$ estimator can be still considered as a good estimator of 68.3% coverage probability for μ^t. However, the right coverage is not always guarantied. It is recommended to validate an obtained confidence interval with other methods. We discuss such an additional method in the next section, which we use in our analysis. It still uses a (constrained) profile log-likelihood ratio (Equation 9.6) as a test statistics but is based on Monte-Carlo simulation of pseudo-experiments for a construction of a p.d.f. of the test statistics.

---

[2]Depending on the type of a problem it can be used for estimation of exclusion limits or discovery significance as well.

[3]In practice, we do not explicitly check these conditions rather assume that they are satisfied given the type of problem described by a likelihood function.

9.1.3 Confidence interval with $\mu \geq 0$ constraint

We showed in the previous section that the profile log-likelihood ratio is a powerful test statistics for estimating confidence intervals for parameters of an assumed model of a data distribution. From a statistics point of view, there are no constrains on these parameters. This means that the obtained knowledge about parameters and their confidence intervals is a measure of the information that one gets from the observed data. On the other hand, when one deals with a concrete physics problem, these parameters naturally can have physically allowed regions. For instance, in a cross section measurement (the focus of this study) the signal strength parameter has a constraint $\mu \geq 0$. It can happen that the estimated confidence interval covers also a negative value region for μ based on pure statistical inferences. Putting constraints on μ can be thought of as a distortion of the information (see a discussion in [181]) and special care (depending on the details of a particular problem) should be taken to obtain still correct estimates for confidence intervals. That is to preserve their statistical meaning in terms of coverage probability for a parameter (or parameters) true value given the desired confidence levels.

A non-physical coverage of estimated confidence intervals is characteristic to problems with low size of a data sample. Also, in such a case the usage of asymptotic formulae for obtaining confidence intervals for a tested hypothesis is questionable. A solution can be Monte-Carlo simulation of many pseudo-experiments. One chooses test values of the parameters of interest, denoted as μ, and the model nuisance parameter conditional MLE values, denoted as $\hat{\hat{\alpha}}(\mu, \text{obs})$, in order to generate a statistical ensemble of pseudo-data. If the nuisance parameter values fluctuate within their estimated uncertainties in each generation cycle of pseudo-data, then it is called an *unconditional ensemble* of pseudo-data. Using this pseudo-data one can construct p.d.f. of the chosen test statistics [4], denoted as t_μ (e.g. $t_\mu = -2ln\lambda(\mu)$), by performing a maximum likelihood fit to every sample of pseudo-data and each time calculating t_μ. All parameters are allowed to float in a fit considering the possible constraints, though. The generated p.d.f. of the given test statistics depends on data via the conditional MLE of nuisance parameters and on the assumed values of the parameters of interest, μ. We denote it as $f(t_\mu | \mu, \hat{\hat{\alpha}}(\mu, \text{obs}))$ or simply $f(t_\mu | \mu)$. It can be used to determine a confidence interval for μ with a specified confidence level assuming μ is the true value. More details of this procedure will be discussed later based on the specifications of our particular problem.

Obviously, one wants to construct t_μ in such a way that it considers the physical constraints on one hand and on the other hand guarantees the same results of the asymptotic approach. We do this for our problem, where we have only one parameter of interest, which has a physical constraint to be not negative. It can be shown [178] that

$$
\tilde{t}_\mu = -2ln\tilde{\lambda}(\mu) = \begin{cases} -2ln\frac{\mathcal{L}(\mu,\hat{\hat{l}},\hat{\hat{\alpha}}_j)}{\mathcal{L}(\hat{\mu},\hat{l},\hat{\alpha}_j)} & \hat{\mu} \geq 0 \\ -2ln\frac{\mathcal{L}(\mu,\hat{\hat{l}},\hat{\hat{\alpha}}_j)}{\mathcal{L}(0,\hat{\hat{l}}(0),\hat{\hat{\alpha}}_j(0))} & \hat{\mu} < 0 \end{cases}
\tag{9.8}
$$

fulfils the requirement of the asymptotic consistency if its p.d.f. is obtained from pseudo-experiments with generation of the *unconditional ensemble* (see the definition above) of pseudo data. It is assumed that if $\hat{\mu} < 0$, then $\mu = 0$ is in best agreement with the data given the physics constraint on μ.

---

[4]It is constructed in such a way that it depends only on the parameters of interest but not on the nuisance parameters

A p.d.f. obtained for $\tilde{t}_\mu$ can be used to determine a confidence interval for a given confidence level. However, as it often happens due to the lack of data, the lower limit of a confidence interval can hit an unphysical region and has to be constrained on the boundary $\mu = 0$. Then the goal is to determine only the upper limit of μ in such a way that the proper coverage for the true value is achieved. For this goal, we use a modified version (suggested in [178]) of the test statistics 9.8,

$$\tilde{q}_\mu = \begin{cases} -2ln\tilde{\lambda}(\mu) & \hat{\mu} \le \mu \\ 0 & \hat{\mu} > \mu \end{cases} \tag{9.9}$$

Where, $-2\ln\tilde{\lambda}(\mu)$ is defined by Equation 9.8.

By definition higher values of $\tilde{q}_\mu$ correspond to higher disagreement between the tested value μ and data. That is the reason setting it to 0, when the observed data with $\hat{\mu} > \mu$ should be considered to be well compatible to the tested value μ [178]. A p.d.f. of $\tilde{q}_\mu$ distribution is denoted as $f(\tilde{q}_\mu|\mu)$.

To estimate the upper limit of μ we calculate the p-value, which is the probability of having $\tilde{q}_{\mu,\text{obs}}$ observed given μ is the true value,

$$\tilde{p}_\mu = \int_{\tilde{q}_{\mu,\text{obs}}}^\infty f(\tilde{q}_\mu|\mu)\mathrm{d}\tilde{q}_\mu \tag{9.10}$$

Where, the integral lower threshold, $\tilde{q}_{\mu,\text{obs}}$, is calculated on the observed data assuming μ. It is a monotonically increasing quantity as μ is getting larger. In other words, incompatibility between data and tested value μ increases. Thus, $\tilde{p}_\mu$ monotonically decreases. $f(\tilde{q}_\mu|\mu)$ also changes by increasing μ but it does not completely compensate the effect of increasing $\tilde{q}_{\mu,\text{obs}}$ in the calculation of $\tilde{p}_\mu$. For a certain $\mu_{up,\text{obs}}$ value $\tilde{p}_\mu$ becomes equal to 0.05. We take $\mu_{up,\text{obs}}$ as the observed upper limit of μ at the $1 - \tilde{p}_\mu$ confidence level.

The above method of an upper limit calculation is called the CL_{s+b} method. We use its modified version called CL_s [182], which is more suitable for our analysis due to the small size of selected data. In the CL_s method p-value is constructed in the following way,

$$\tilde{p}'_\mu = \frac{\tilde{p}_\mu}{1 - \tilde{p}_b} \tag{9.11}$$

Where, $\tilde{p}_b$, also known as CL_b is calculated with Equation 9.12,

$$\tilde{p}_b = \int_{-\infty}^{\tilde{q}_{\mu,obs}} f(\tilde{q}_\mu|0)\mathrm{d}\tilde{q}_\mu \tag{9.12}$$

Where, the background only hypothesis corresponding p.d.f., $f(\tilde{q}_\mu|0)$ is constructed using pseudo data generated with $(\mu = 0, \hat{\hat{\alpha}}(\mu = 0, \text{obs}))$.

CL_s upper limit at 95% C.L. is found by scanning μ and selecting its value, $\mu_{up,\text{obs}}$, for which $\tilde{p}'_{\mu_{up,\text{obs}}} = 0.05$. We also calculate the expected upper limit (median upper limit of background only experiments) for μ and its $\pm 1\sigma$ and $\pm 2\sigma$ error bands.

9.1.4 Software tools

The described mathematical formalism for the maximal likelihood and the profile log-likelihood ratio methods are implemented in the RooFit/RooStats [183, 184] software package. Fitting

of data with a likelihood function and all related calculations is done using the MINOS technique of the MINUIT [185] software.

9.2 Results

The likelihood function (Equation 9.5) incorporates Gaussian constraints on the α_j nuisance parameters, which determine the variation of the expected event yields. Dependence of the yields on each of the nuisance parameters is described by Equation 9.3 or 9.4. The former way of the linear extrapolation of the yields is a sufficiently good approach if the uncertainties of the yields due to $\pm 1\sigma$ variation of the α_j parameters are not large. Then the yields are distributed according to a Gaussian. If the uncertainties are sizeable, i.e., they are comparable to the yields themselves, this leads to an unphysical behavior of the profile log-likelihood ratio. In our study we have such a situation, for instance, with the Wt-channel background event yield and the large uncertainties, -100% and $+400\%$, assigned to the yield. The linear extrapolation method leads to a negative yield when $\alpha_{\mathrm{Wt,norm.}} < -1$ and the yield needs to be constrained to 0. For the distribution of the expected Wt-channel event yield we would obtain a shape, which has two maxima at 0 and at 0.34 (the nominal Wt-channel event yield), which is not realistic. Figure 9.1 shows the Wt-channel event yield as a function of $\alpha_{\mathrm{Wt,norm.}}$. The results obtained by using both the linear (black solid curve) and the exponential (red long-dashed curve) extrapolation methods are presented. The left plot 9.1a corresponds to the downward variation of the $\alpha_{\mathrm{Wt,norm.}}$ nuisance parameter. As one can see from this plot, the exponential extrapolation method guarantees a positive event yield. Therefore, we use the exponential extrapolation method for the nuisance parameters. However, this leads to a significant increase of the yield for the upward variation of $\alpha_{\mathrm{Wt,norm.}}$ as can be seen on the right plot 9.1b. In case of relatively smaller uncertainties the two methods lead to the same distributions of the event yields [5].

The exponential approximation provides a physical shape of an event rate distribution. This can be seen in Figure 9.2, where two simulated p.d.f. of the expected Wt-channel event yield are compared to each other. An unconstrained p.d.f. obtained with the linear extrapolation method predicts on one hand a negative expectation of the event yield in a significant fraction of times and on the other hand has a prominent discontinuity of the first kind at the nominal expectation value of the event yield. In contrast, the exponential method leads to a more physically meaningful shape of the p.d.f. in a natural way. This implies the positively defined expectation for the event yield and smooth transition between the left and right sides of the p.d.f. with respect to the nominal expectation value.

The negative profile log-likelihood ratio (Equation 9.6) curves of μ are presented in Figure 9.3. The plot presents a function corresponding to the final measurement (blue solid curve), which includes all nuisance parameters in the maximum likelihood fit and in profiling. The dashed red curve is obtained by fitting data and making a profile with the nuisance parameters fixed at their nominal values ($l = 1$ and $\alpha_j = 0$ for all $j \in \mathrm{syst.}$). This allows to evaluate confidence intervals for the measured cross section determined only by the data amount. The light blue dash-dotted curve is a distribution to illustrate the influence of the main source of systematic uncertainties, the QCD multi-jets background measurement uncertainty. It is

---

[5]This is expected, since the linear extrapolation formulae can be derived from the exponential ones by their Taylor expansion.
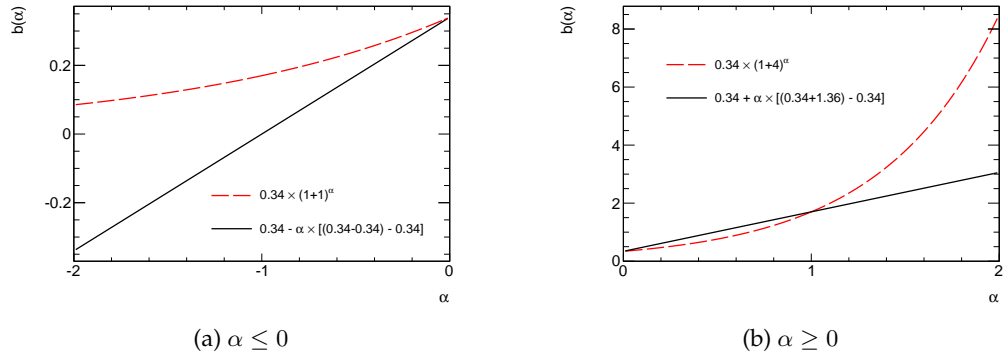
(a) $\alpha \leq 0$ (b) $\alpha \geq 0$

Figure 9.1: Wt-channel event yield $N_{\mathrm{Wt}}^{\mathrm{exp}}(L_0)$ (denoted as $b(\alpha)$) dependence on the $\alpha_{\mathrm{Wt,norm.}}$ nuisance parameter (denoted as α), which distribution is described by a normalized Gaussian p.d.f.. Two models, the linear (black solid curve) and the exponential (red long-dashed curve) extrapolation of the $b(\alpha)$ event yield are compared to each other. The left plot presents the distributions for $\alpha \leq 0$ and the right plot corresponds to $\alpha \geq 0$. The legends on the plots provide the extrapolation Equations 9.3 and 9.4 with the actual values of the nominal Wt-channel event yield as well as its uncertainties due to the Wt-channel normalization up/down uncertainties. The corresponding ratios of these uncertainties over the nominal yield are provided on the legends for Equation 9.4.
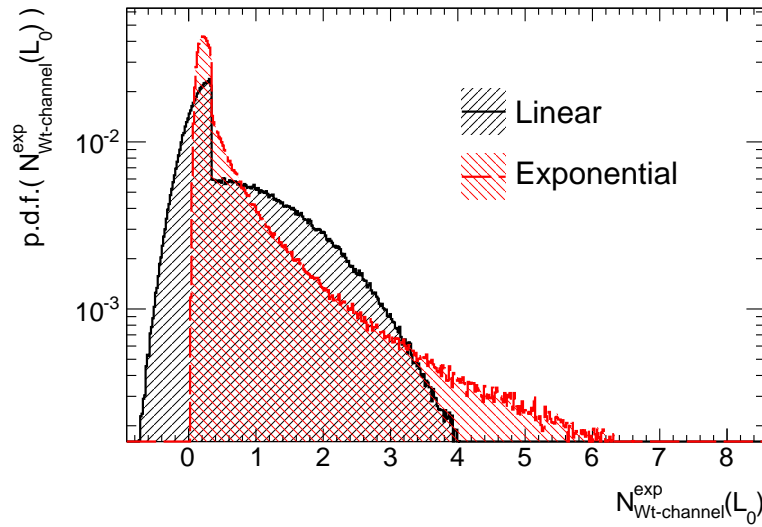

Figure 9.2: Simulated p.d.f. of the Wt-channel event yield obtained by using with the linear and the exponential extrapolation methods for the event yield.

obtained with a condition that the corresponding nuisance parameter is fixed at its nominal value, $\alpha_{\text{QCD,stat.}} = 0$, when constructing Equation 9.6.

The intersection of the curves in Figure 9.3 with the green line representing the 68.3% confidence level gives one standard deviation limits for the measured cross section, which is $59 \,^{+77}_{-55}$ (stat. + syst.) pb. Table 9.1 provides detailed information about the measurement uncertainties.

The observed upper limit for the t-channel signal strength, $\mu^{\text{obs}}_{\text{upp. limit @ 95\% C.L.}} = 3.6$, is obtained at the intersection point of the profiled log-likelihood curve (blue solid curve) with the green line representing the 95% confidence level. More precise determination of the upper limit is done using the method of pseudo-experiments for obtaining p.d.f. of test statistics (see below).

The above result for the upper limit is obtained using the asymptotic approach based on Equation 9.7. We obtain the observed upper limit with more precise methods, CL_{s+b} and CL_s. Both methods give only a little smaller observed upper limit than the asymptotic method [6]. We quote the result of the CL_s method, which is a more conservative estimate than the result of CL_{s+b}, as an observed upper limit of the t-channel cross section.

In order to calculate an upper limit of μ with CL_{s+b} and CL_s methods, we follow the instructions described in Section 9.1.3 for constructing a p.d.f. of the $\tilde{q}_\mu$ test statistics defined with Equations 9.9 and 9.8. Pseudo-data is generated assuming different values of μ including $\mu = 0$, which correspond to a background only hypothesis. Figure 9.4 shows examples of the resulting p.d.f. of $\tilde{q}_\mu$ for two particular values of the parameter of interest, $\mu = 1.5$ (left plot) and $\mu = 3.5$ (right plot). In both cases the p.d.f. is constructed assuming the background only model (blue dashed histogram) and $\mu = 1.5, 3.5$ (red solid histogram) when generating pseudo-data. Black vertical lines are set on the observed values of the test statistic, $\tilde{q}_{\mu,\text{obs}}$. The dashed areas of the histograms on the right of $\tilde{q}_{\mu,\text{obs}}$ represent the $CL_{s+b} = \tilde{p}_\mu$ and the $CL_b = 1 - \tilde{p}_b$ probabilities, where $\tilde{p}_\mu$ and $\tilde{p}_b$ are defined by Equations 9.10 and 9.12 respectively. This example shows that by increasing μ the observed test statistics becomes less compatible to observed data that is $\tilde{p}_{\mu=3.5} < \tilde{p}_{\mu=1.5}$. We find that (see Figure 9.5) for $\mu = 3.5$, $\tilde{p}'_\mu = 0.05$, where $\tilde{p}'_\mu$ is defined by Equation 9.11. Thus, $\mu_{\text{up,obs}} = 3.5$ is the CL_s upper limit on the t-channel signal strength at 95% C.L.

Figure 9.5 presents the result of the search in terms of an upper limit. The p-value dependence on test values of $\sigma/\sigma^{\text{theory}} \equiv \mu$ are presented for the CL_{s+b} (curve with solid blue circle markers) and the CL_s (curve with solid black rectangle markers) methods. The values of μ, at which the curves representing the methods cross the red horizontal line, p-value = 0.05, are the corresponding observed upper limits. The expected upper limit as a function of μ is also presented on the plot (black dashed curve). In order to estimate an expected limit at the test value of μ, one finds the median, $\tilde{q}_{\mu,\text{median}}$, of the p.d.f. of background only hypothesis, $f(\tilde{q}_\mu|0)$ (e.g., blue dashed histograms in Figure 9.4a and Figure 9.4b). The corresponding p-value is calculated from the p.d.f. of signal+background hypothesis with the value μ under test, $f(\tilde{q}_\mu|\mu)$ (e.g. the red solid histograms in Figure 9.4a and Figure 9.4b),

$$\tilde{p}_{\mu,\text{median}} = \int_{\tilde{q}_{\mu,\text{median}}}^{\infty} f(\tilde{q}_\mu|\mu)\mathrm{d}\tilde{q}_\mu \tag{9.13}$$

If $\tilde{p}_{\mu,\text{median}} = 0.05$, then the corresponding value of μ is the expected upper limit, $\mu_{up,\text{median}}$. Obviously, the larger the incompatibility between data and the background only model is

---

[6]This indicates that the cross section uncertainties estimated using the asymptotic method are reliable.
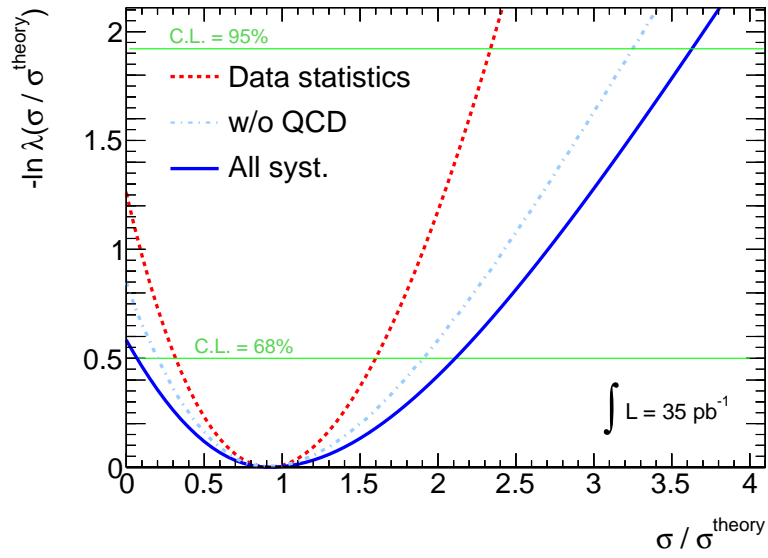
Figure 9.3: Distribution of the negative profile log-likelihood ratio as a function of the $\mu \equiv \sigma/\sigma^{\mathrm{theory}}$ signal strength parameter. The minimum of the distribution corresponds to the measured t-channel cross section (in terms of its relative deviation from the expected value from theory). The red dashed distribution corresponds to the case, when all nuisance parameters are fixed at their nominal values. The solid blue curve is obtained by profiling all nuisance parameters. The light blue dash-dotted curve is obtained by profiling all but the $\alpha_{\mathrm{QCD,stat.}}$ nuisance parameters. It is fixed at the nominal value, $\alpha_{\mathrm{QCD,stat.}} = 0$. Confidence levels corresponding to 68% and 95% are presented on the plot as two green horizontal lines. Intersections of the curves with these lines determine the corresponding confidence intervals for the true value of $\sigma/\sigma^{\mathrm{theory}}$.

Table 9.1: Statistical and systematic uncertainties of the measured cross section of t-channel, 59 pb, presented in the picobarn units. The uncertainties are obtained with the profile likelihood method.

Uncertainty source	$\Delta^+\sigma$, pb	$\Delta^-\sigma$, pb
Statistics	44	-39
Luminosity	6.0	0
Monte-Carlo samples size	5.2	0
QCD multi-jets (dd)	36	-32
W+jets (dd)	19	-21
Electron energy resolution	0	0
Electron energy scale	0	0
Electron reco + id efficiency scale factors	6.0	0
Electron trigger efficiency scale factors	0.8	0
Jet energy resolution	1.3	-1.0
Jet energy scale	17.3	0
Jet b-tagging	18.5	-5.8
Soft jet energy scale + 'OutOfCell' corrections	0.8	0
Pile-up	3.0	-1.0
Monte-Carlo generator for t-channel	15.5	0
Monte-Carlo generator for $t\bar{t}$	6.7	-4.2
ISR	18.4	-3.9
FSR	15.1	-4.1
t-channel acceptance due to PDFs	6.4	0
Wt-channel normalization	6.1	-4.3
Di-bosons normalization	4.0	0
$t\bar{t}$ normalization	3.5	0
Z+jets normalization	11.0	-2.2
Total systematics	63	-39
Statistics + systematics	77	-55

(good evidence of signal) the stronger is the inequality $\tilde{q}_{\mu,\text{obs}} < \tilde{q}_{\mu,\text{median}}$ due to the definition of $\tilde{q}_\mu$. That is the two p.d.f. $f(\tilde{q}_\mu|\mu)$ and $f(\tilde{q}_\mu|0)$ are well separated. Therefore, the expected upper limit is smaller than the observed one if a signal is presented in data and the analysis has enough sensitivity to observe it.
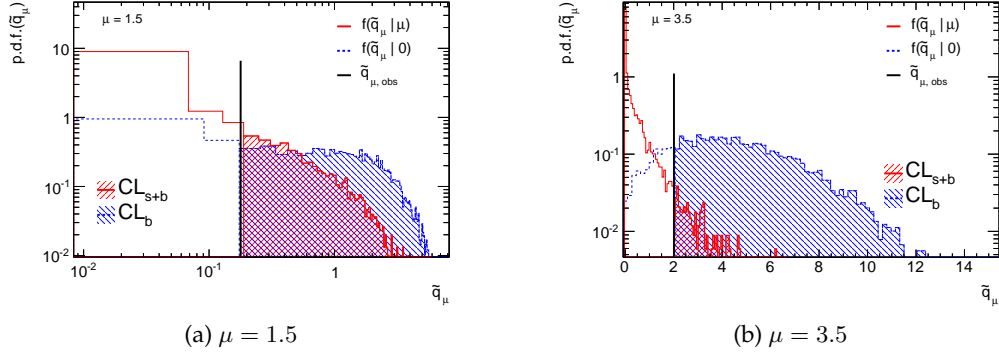

(a) $\mu = 1.5$ (b) $\mu = 3.5$

Figure 9.4: P.d.f. of the $\tilde{q}_\mu$ test statistics corresponding to the signal+background (red solid histogram) and the background only (blue dashed histogram) models. The black solid lines represent the measured values of the test statistics, $\tilde{q}_{\mu,\text{obs}}$. The dashed areas of the histograms correspond to the observed CL_{s+b} (signal+background model) and CL_b (background only model) probabilities.

Uncertainties of $\tilde{p}_{\mu,\text{median}}$ are estimated by evaluating Equation 9.13 at the values of $\tilde{q}_\mu$ at $\pm1\sigma$ and $\pm2\sigma$ from $\tilde{q}_{\mu,\text{median}}$. Here σ is a generalized notation for upper and lower one standard deviations of $\tilde{q}_{\mu,\text{median}}$, which might not be equal. Figure 9.5 presents the corresponding $\pm1\sigma$ (green) and $\pm2\sigma$ (yellow) uncertainty belts of p-value. Projection of the intersection points of these belts with the p-value $= 0.05$ line on the μ-axis represents $\pm1\sigma$ and $\pm2\sigma$ uncertainties of the expected upper limit.

We assigned a large normalization uncertainty (see Table 8.9) to the Wt-channel event yield in order to account for the fact that it is not observed yet by ATLAS at the 7 TeV c.m. energy[7] as its cross section is not yet measured, while a highly precise theoretical calculation exist (see Section 2.1). Our event selection significantly reduces expected contribution of Wt-channel in the $2j/1cj$ events. Thus, its large normalization uncertainties has little impact on the measured t-channel cross section. Figure 9.6 shows the dependence of the observed upper limits (equivalently, the exclusion regions) at 68% C.L. (boundary to the yellow dashed region) and 95% C.L. (boundary to the red dotted region) of the t-channel μ on the Wt-channel estimate $\hat{\sigma}_{\text{Wt}}/\sigma_{\text{Wt}}^{\text{theory}}$. The limits are calculated using the profile likelihood ratio method for different fixed values of the $\hat{\sigma}_{\text{Wt}}/\sigma_{\text{Wt}}^{\text{theory}}$ estimator. As can be seen from the plot, there is a weak dependence for the upper limits of μ on this estimator. The observed MLE of the t-channel signal strength, $\hat{\sigma}_{\text{t-ch.}}^{\text{obs}}/\sigma_{\text{t-ch.}}^{\text{theory}}$ (open circle graph) is also presented on the plot with one standard deviation uncertainties (vertical error bars). Projection of the graph point on the x-axis corresponds to MLE of the Wt-channel background strength, $\hat{\sigma}_{\text{Wt}}/\sigma_{\text{Wt}}^{\text{theory}}$, presented with the corresponding uncertainties (horizontal error bars). Note, that the lower uncertainty of $\hat{\sigma}_{\text{Wt}}/\sigma_{\text{Wt}}^{\text{theory}}$ is much smaller than the input normalization 'down' uncertainty of the Wt-channel background , -100% (see Table 8.9). The reason is that we use the exponential ex-

---

[7]TEVATRON experiments, CDF and D0, also did not measure Wt-channel because of its small production cross section at 1.96 TeV c.m. energy.
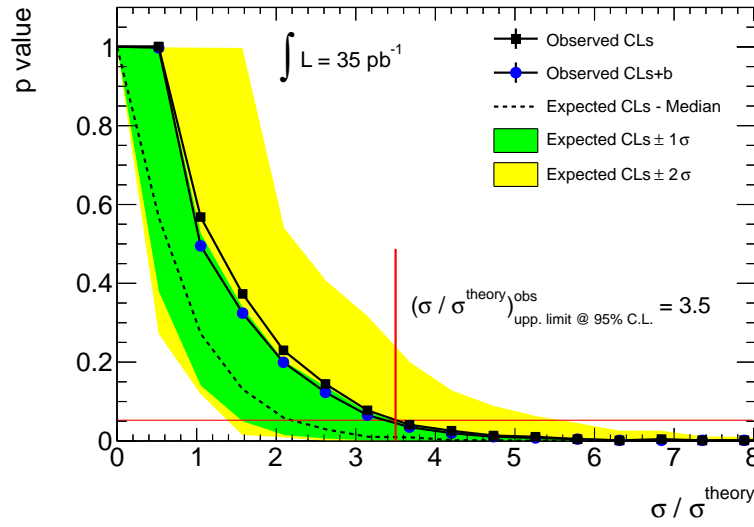
Figure 9.5: Distribution of the observed CL_{s+b} (curve with solid blue circle markers) and more conservative CL_s (curve with solid black rectangular markers) probabilities as well as the expected CL_s (black dashed line) probability distribution corresponding to the background only hypothesis. The latter is presented with 1σ (green) and 2σ (yellow) uncertainty bands obtained from pseudo-experiments. The x-axis represents the t-channel cross section upper limit in terms of $\sigma/\sigma^{\text{theory}} \equiv \mu$. The red vertical line represents the value of observed upper limit with 95% C.L., $\sigma/\sigma^{\text{theory}} = 3.5$, which corresponds to the x-value of the intersection point of the observed CL_s curve and the threshold p-value $= 0.05$ represented by the red solid horizontal line.

trapolation method 9.4 to vary the expectation values of the event yields. The method leads to the reduced initial values of 'down' uncertainties.

The plot also shows the uncertainties, red rectangle, of the theory (NNLO) predicted cross section values of t-channel and Wt-channel.
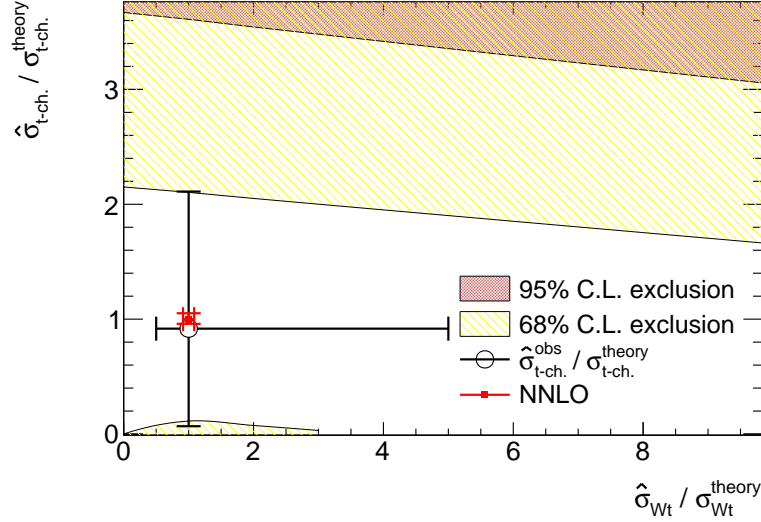

Figure 9.6: Dependence of the observed upper limits of the t-channel cross section (in terms of $\hat{\sigma}_{t-ch.}/\sigma_{t-ch.}^{theory}$) at 68% C.L. and 95% C.L. on the fixed values of the Wt-channel cross section estimator (in terms of $\hat{\sigma}_{Wt}/\sigma_{Wt}^{theory}$) used in the maximum likelihood fit with profiling. The observed MLE of the t-channel cross section, $\hat{\sigma}_{t-ch.}^{obs}/\sigma_{t-ch.}^{theory}$, is presented on the plot as a black open circle with 1σ uncertainties. The horizontal uncertainties are for MLE of the Wt-channel cross section, $\hat{\sigma}_{Wt}/\sigma_{Wt}^{theory}$. The theoretical uncertainties of the t-channel and Wt-channel cross sections calculated at NNLO and normalized to these cross sections are presented as the red solid error bars.

9.3 Summary

In the present study we measured the inclusive cross section of t-channel production in proton-proton collisions at 7 TeV c.m. energy, using data collected by the ATLAS detector with 35pb^{-1} of integrated luminosity. The measurement was performed using selected events with an electron plus two hadronic jets in the final state. One jet was required to be in the central region of the detector and to be tagged as a b-jet. A second untagged jet was required to be in the forward region of the detector. Due to the topology of t-channel events the above criteria of jet selection was found to determine the highest predicted fraction of t-channel events in data. Additional requirements (selection cuts) were applied to the events in order to maximize the signal fraction in the selected events and thus, perform an as much as possible precise measurement. Monte-Carlo simulation of the t-channel signal and the Standard Model background processes has been used to predict the event rates in selected data. The final selection resulted in 27 candidates in data, while the expected number is 8.1 (t-channel signal) plus 19.6 (background) events under the assumption of the t-channel theory (approximate NNLO) predicted cross section, $\sigma_{t-ch.}^{theory} = 64.6 \, ^{+3.3}_{-2.6}$. Production of W bosons with associated hadronic

jets and QCD multi-jets was found to be the largest background. We developed and used a data driven template fit method to estimate the contribution of both background processes to the data in the selected region. All possible systematic effects on the signal and the background were studied and quantitatively evaluated. The uncertainty of the data driven measurement of QCD multi-jets was found to have largest impact on a precision of the t-channel cross section measurement.

We used a maximum likelihood method to extract the t-channel inclusive cross section from the observed data given the Monte-Carlo simulation based or data driven predictions for the expected signal and background event rates, considering also their systematic uncertainties. Frequentist confidence intervals for the measured cross section were calculated using the profile likelihood ratio method. We obtain a measurement of the Standard Model t-channel inclusive cross section and its one standard deviation statistical and systematic uncertainties. An upper limit of the cross section has been also estimated.

$$\sigma^{\mathrm{obs}}_{\mathrm{t-ch.}} = 59 \; \left(^{+44}_{-39}\right)_{\mathrm{stat.}} \; \left(^{+63}_{-39}\right)_{\mathrm{syst.}} \; \mathrm{pb}$$

$$\sigma^{\mathrm{obs}}_{\mathrm{t-ch.}}(\text{upper limit @ 95\% C.L.}) = 226 \; \mathrm{pb}$$

Thus, we can conclude that in our study we found that the observed single top-quark t-channel production agrees with the Standard Model predicted value within uncertainties. The obtained results are also in agreement with the t-channel cross section measurement [171] (preliminary) of the combined electron+jets and muon+jets final states of selected events and carried out using the same 35 pb^{-1} integrated luminosity of data collected by ATLAS. The both measurements are presented on the summary plot in Figure 9.7 as the black solid circle (thesis) and the black open rectangle (ATLAS preliminary). The t-channel cross section measurement performed using the LHC proton-proton collision data of 36 pb^{-1} of integrated luminosity recorded by the CMS detector [186] is also presented on the plot as the black solid star. The red open cross represents the t-channel theoretical cross section (see above) calculated at the approximate NNLO [42]. A dependence of the t-channel theoretical cross section (NLO) on the c.m. energy of proton-proton collisions calculated using the MCFM tool [56] is presented as the green solid band. These theoretical calculations and the measurements based on ATLAS data are performed assuming $m_{t\text{-quark}} = 172.5$ GeV. The CMS measurement assumed a different mass of t-quark, $m_{t\text{-quark}} = 173$ GeV [8]. The plot also presents the t-channel cross section of the single top production in proton-antiproton collisions [187] as the blue solid band in the TEVATRON range of the c.m. energy of collisions, $1.8 - 2.0$ TeV, assuming $m_{t\text{-quark}} = 175$ GeV. The approximate NNNLO cross section of the single top production in t-channel in proton-antiproton collisions at $\sqrt{s} = 1.96$ TeV and assuming $m_{t\text{-quark}} = 173$ GeV [188] is presented as the red open star. The latest measurements of the t-channel cross section by the TEVATRON experiments, D0 [189] and CDF [190] (preliminary), using proton-antiproton collision data at $\sqrt{s} = 1.96$ TeV and assuming $m_{t\text{-quark}} = 172.5$ GeV are presented on the plot as the black solid triangles.

All these measurements are in agreement with the Standard Model predictions within uncertainties.

---

[8]As it was shown in Section 2.1 (see Figure 2.5) the SM t-channel cross section has a negligible dependence on the t-quark mass.
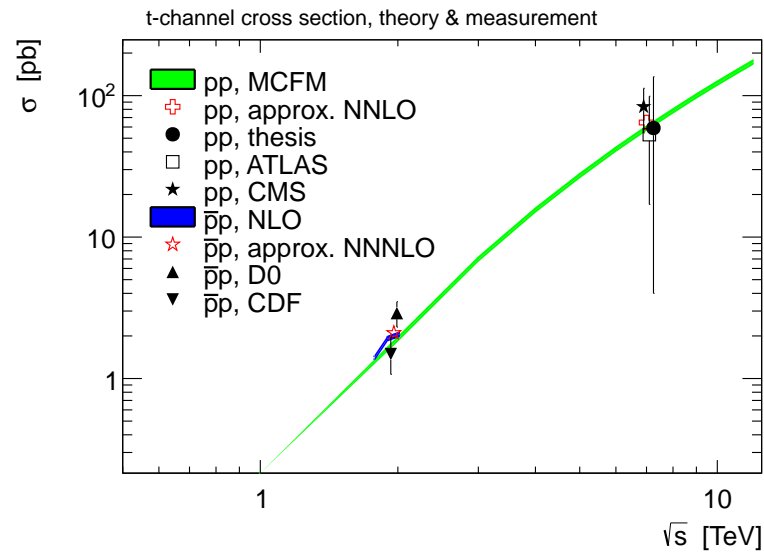
Figure 9.7: Summary plot of the cross section measurements of the single top production in t-channel using the LHC proton-proton collision data at $\sqrt{s} = 7\,\text{TeV}$ recorded by the ATLAS and the CMS detectors in 2010. The t-channel theoretical cross section is also presented on the plot including its dependence on the c.m. energy of proton-proton collisions. The similar measurements from the TEVATRON experiments, D0 and CDF, are also presented together with the corresponding theoretical calculations of the t-channel cross section. See the text for more information.

Bibliography

[1] L. Evans et al., *LHC Machine*, JINST **3** (2008) S08001.

[2] S. Holmes et al., *Overview of the Tevatron collider complex: goals, operations and performance*, JINST **6** (2011) T08001.

[3] ATLAS Collaboration, *The ATLAS Experiment at the CERN Large Hadron Collider*, JINST **3** (2008) S08003.

[4] CMS Collaboration, *CMS Physics Technical Design Report Volume I: Detector Performance and Software*, CERN-LHCC-2006-001, Geneva: CERN, (2006).

[5] CMS Collaboration, *CMS Physics Technical Design Report, Volume II: Physics Performance*, J. Phys. G **34** (2007) 995.

[6] S. Glashow, *Partial Symmetries of Weak Interactions*, Nucl. Phys. **22** (1961) 579.

[7] S. Weinberg, *A Model of Leptons*, Phys. Rev. Lett. **19** (1967) 1264.

[8] A. Salam, *Weak and Electromagnetic Interactions*, Elementary particle theory. Relativistic groups and analyticity. Proceedings of the Eighth Nobel Symposium, Almquist & Wiksell, (1968) 367.

[9] P. W. Higgs, *Broken symmetries, massless particles and gauge fields*, Phys. Lett. **12** (1964) 132–133.

[10] P. W. Higgs, *Broken Symmetries and the Masses of Gauge Bosons*, Phys. Rev. Lett. **13** (1964) 508–509.

[11] P. W. Higgs, *Spontaneous Symmetry Breakdown without Massless Bosons*, Phys. Rev. **145** (1966) 1156–1163.

[12] H. Fritzsch, M. Gell-Mann and H. Leutwyler, *Advantages of the Color Octet Gluon Picture*, Phys. Lett. B **47** (1973) 365–368.

[13] D. J. Gross and F. Wilczek, *Asymptotically Free Gauge Theories. I*, Phys. Rev. D **8** (1973) 3633–3652.

[14] D. J. Gross and F. Wilczek, *Asymptotically free gauge theories. II*, Phys. Rev. D **9** (1974) 980–993.

[15] S. Weinberg, *Non-Abelian Gauge Theories of the Strong Interactions*, Phys. Rev. Lett. **31** (1973) 494–497.

[16] S. Weinberg, *Current Algebra and Gauge Theories. II. Non-Abelian Gluons*, Phys. Rev. D **8** (1973) 4482–4498.

[17] H. D. Politzer, *Reliable Perturbative Results for Strong Interactions?*, Phys. Rev. Lett. **30** (1973) 1346–1349.

[18] J. D. Bjorken and S. D. Drell, *Relativistic Quantum Mechanics*, ISBN 0-07-232002-8, New York: McGraw-Hill, (1964).

[19] M. E. Peskin and D. V. Schroeder, *An Introduction to Quantum Field Theory*, ISBN 0-201-50397-2, Boston: Addison-Wesley, (1995).

[20] CDF Collaboration, *Observation of Top Quark Production in $\bar{p}p$ Collisions with the Collider Detector at Fermilab*, Phys. Rev. Lett. **74** (1995) 2626–2631.

[21] D0 Collaboration, *Observation of the Top Quark*, Phys. Rev. Lett. **74** (1995) 2632–2637.

[22] DONUT Collaboration, *Observation of tau neutrino interactions*, Phys. Lett. B **504** (2001) 218–224.

[23] S. W. Herb and et al., *Observation of a Dimuon Resonance at 9.5 GeV in 400-GeV Proton-Nucleus Collisions*, Phys. Rev. Lett. **39** (1977) 252–255.

[24] M. L. Perl and et al., *Evidence for Anomalous Lepton Production in $e^+ - e^-$ Annihilation*, Phys. Rev. Lett. **35** (1975) 1489–1492.

[25] K. Nakamura et al., *Particle Data Group*, J. Phys. G **37** (2010), and 2011 partial update for the 2012 edition 075021.

[26] N. Cabibbo, *Unitary Symmetry and Leptonic Decays*, Phys. Rev. Lett. **10** (1963) 531–533.

[27] M. Kobayashi and T. Maskawa, *CP-Violation in the Renormalizable Theory of Weak Interaction*, Progress of Theoretical Physics **49** (1973) 652–657.

[28] K. Nakamura et al., *Particle Data Group, 11. The CKM quark-mixing matrix*, J. Phys. G **37**. 075021 (2010), and 2011 partial update for the 2012 edition.

[29] M. Beneke et al., *Top quark physics*, (2000), arXiv:hep-ph/0003033 [hep-ph].

[30] S. Dawson et al., *Associated Higgs boson production with top quarks at the CERN Large Hadron Collider: NLO QCD corrections*, Phys. Rev. D **68** (2003) 034022.

[31] W Bernreuther, *Top-quark physics at the LHC*, J. Phys. G **35** (2008) 083001.

[32] K. Nakamura et al., *Particle Data Group, 16. Structure functions*, J. Phys. G **37** (2010), and 2011 partial update for the 2012 edition 075021.

[33] ATLAS Collaboration, *Measurement of the top quark pair production cross section in pp collisions at $\sqrt{s}$ = 7 TeV in dilepton final states with ATLAS*, Phys. Lett. B **707** (2012) 459–477, arXiv:hep-ex/1108.3699 [hep-ex].

[34] S. Dawson, *The effective W approximation*, Nucl. Phys. B **249** (1985) 42–60.

[35] S. S. D. Willenbrock and D. A. Dicus, *Production of heavy quarks from W-gluon fusion*, Phys. Rev. D **34** (1986) 155–161.

[36] C. P. Yuan, *New method to detect a heavy top quark at the Fermilab Tevatron*, Phys. Rev. D **41** (1990) 42–51.

[37] R. K. Ellis and S. Parke, *Top-quark production by W-gluon fusion*, Phys. Rev. D **46** (1992) 3785–3788.

[38] G. Bordes and B. van Eijk, *Calculating QCD corrections to single top production in hadronic interactions*, Nucl. Phys. B **435** (1995) 23–58.

[39] T. Stelzer, Z. Sullivan and S. Willenbrock, *Single-top-quark production via W-gluon fusion at next-to-leading order*, Phys. Rev. D **56** (1997) 5919–5927.

[40] D. O. Carlson and C.-P. Yuan, *Studying the top quark via the W-gluon fusion process*, Phys. Lett. B **306** (1993) 386–390.

[41] T. Stelzer, Z. Sullivan and S. Willenbrock, *Single-top-quark production at hadron colliders*, Phys. Rev. D **58** (1998) 094021.

[42] N. Kidonakis, *Next-to-next-to-leading-order collinear and soft gluon corrections for t-channel single top quark production*, Phys. Rev. D **83** (2011) 091503, arXiv:`hep-ph/1103.2792` `[hep-ph]`.

[43] S. Cortese and R. Petronzio, *The single top production channel at Tevatron energies*, Phys. Lett. B **253** (1991) 494–498.

[44] T. Stelzer and S. Willenbrock, *Single-top-quark production via $qq \to tb$*, Phys. Lett. B **357** (1995) 125–130.

[45] M. C. Smith and S. S. Willenbrock, *QCD and Yukawa corrections to single-top-quark production via $q\bar{q} \to t\bar{b}$*, Phys. Rev. D **54** (1996) 6696–6702.

[46] S. Mrenna and C.-P. Yuan, *Effects of QCD resummation on W+h and $t\bar{b}$ production at the Tevatron*, Phys. Lett. B **416** (1998) 200–207.

[47] N. Kidonakis, *Next-to-next-to-leading logarithm resummation for s-channel single top quark production*, Phys. Rev. D **81** (2010) 054028, arXiv:`hep-ph/1001.5034 [hep-ph]`.

[48] G. A. Ladinsky and C. P. Yuan, *W-boson $-$ top-quark background to heavy-Higgs-boson production*, Phys. Rev. D **43** (1991) 789–793.

[49] S. Moretti, *Single-top-quark production in the $\mathrm{tW}^{\pm}$ channel and Higgs boson signals via $H \to W^+W^-$ at the CERN Large Hadron Collider*, Phys. Rev. D **56** (1997) 7427–7433.

[50] A. P. Heinson, A. S. Belyaev and E. E. Boos, *Single top quarks at the Fermilab Tevatron*, Phys. Rev. D **56** (1997) 3114–3128.

[51] A. S. Belyaev, E. E. Boos and L. V. Dudko, *Single top quark at future hadron colliders: Complete signal and background study*, Phys. Rev. D **59** (1999) 075001.

[52] A. Belyaev and E. Boos, *Single top quark $tW + X$ production at the CERN LHC: A closer look*, Phys. Rev. D **63** (2001) 034012.

[53] T. M. P. Tait, *tW^- mode of single top quark production*, Phys. Rev. D **61** (1999) 034001.

[54] N. Kidonakis, *Two-loop soft anomalous dimensions for single top quark associated production with a W^- or H^-*, Phys. Rev. D **82** (2010) 054018, arXiv:`hep-ph/1005.4451` `[hep-ph]`.

[55] Calculation at approximate NNLO in QCD using Hathor 1.2 (M. Aliev et al., Comput.Phys.Commun. 182, 1034–1046, 2011) using the MSTW2008 90% NNLO PDF sets (A.D. Martin et al. Eur.Phys.J. C63, 189–285, 2009) incorporating PDF and α_S uncertainties according to the MSTW prescription (Eur.Phys.J. C64, 653–680, 2009). Cross checked with the NLO+NNLL calculation (M. Cacciari et al., hep-ph/1111.5869v2) as implemented in Top++ 1.0 (M. Czakon and A. Mitov, hep-ph/1112.5675v2).

[56] J. M. Campbell and R. Ellis, *MCFM for the Tevatron and the LHC*, Nucl.Phys.Proc.Suppl. **205-206** (2010) 10–15, arXiv:`hep-ph/1007.3492 [hep-ph]`.

[57] V. N. Gribov and L. N. Lipatov, *Deep inelastic e p scattering in perturbation theory*, Sov. J. Nucl. Phys. **15** (1972) 438–450.

[58] G. Altarelli and G. Parisi, *Asymptotic Freedom in Parton Language*, Nucl. Phys. B **126** (1977) 298.

[59] Y. L. Dokshitzer, *Calculation of the Structure Functions for Deep Inelastic Scattering and e^+e^- Annihilation by Perturbation Theory in Quantum Chromodynamics*, Sov. Phys. JETP **46** (1977) 641–653.

[60] J. M. Campbell et al., *Next-to-Leading-Order Predictions for t-Channel Single-Top Production at Hadron Colliders*, Phys. Rev. Lett. **102** (2009) 182003, arXiv:`hep-ph/0903.0005v2 [hep-ph]`.

[61] P. Falgari, P. Mellor and A. Signer, *Production-decay interferences at next-to-leading order in QCD for t-channel single-top-quark production*, Phys. Rev. D **82** (2010) 054028, arXiv:`hep-ph/1007.0893 [hep-ph]`.

[62] R. Schwienhorst et al., *Single top quark production and decay in the t channel at next-to-leading order at the LHC*, Phys. Rev. D **83** (2011) 034019, arXiv:`hep-ph/1012.5132 [hep-ph]`.

[63] P. Falgari et al., *Off-shell effects for t-channel and s-channel single-top production at next-to-leading order in QCD*, Phys. Rev. D **83** (2011) 094013, arXiv:`hep-ph/1102.5267 [hep-ph]`.

[64] D0 Collaboration, *Simultaneous Measurement of the Ratio $R = \mathcal{B}(t \to Wb)/\mathcal{B}(t \to Wq)$ and the Top-Quark Pair Production Cross Section with the D0 Detector at $\sqrt{s} = 1.96$ TeV*, Phys. Rev. Lett. **100** (2008) 192003, arXiv:`hep-ex/0801.1326v1 [hep-ex]`.

[65] CDF Collaboration, *Measurement of $\mathcal{B}(t \to Wb)/\mathcal{B}(t \to Wq)$ at the Collider Detector at Fermilab*, Phys. Rev. Lett. **95** (2005) 102002.

[66] D0 Collaboration, *Observation of Single Top-Quark Production*, Phys. Rev. Lett. **103** (2009) 092001, arXiv:`hep-ex/0903.0850v2 [hep-ex]`.

[67] CDF Collaboration, *Observation of Electroweak Single Top-Quark Production*, Phys. Rev. Lett. **103** (2009) 092002, arXiv:`hep-ex/0903.0885v3 [hep-ex]`.

[68] CDF Collaboration, *Search for single top quark production in $p\bar{p}$ collisions at $\sqrt{s} = 1.96$ TeV in the missing transverse energy plus jets topology*, Phys. Rev. D **81** (2010) 072003, arXiv:`hep-ex/1001.4577 [hep-ex]`.

[69] T. M. P. Tait and C.-P. Yuan, *Single top quark production as a window to physics beyond the standard model*, Phys. Rev. D **63** (2000) 014018, arXiv:`hep-ph/0007298v2 [hep-ph]`.

[70] S. Weinberg, *Phenomenological Lagrangians*, Physica A: Statistical Mechanics and its Applications **96** (1979) 327–340.

[71] H. Georgi, *On-shell effective field theory*, Nucl. Phys. B **361** (1991) 339–350.

[72] J. Wudka, *Electroweak effective lagrangians*, Int. J. Mod. Phys. **A**. **9** (1994) 2301–2361, arXiv:`hep-ph/9406205v1 [hep-ph]`.

[73] R. Peccei and X. Zhang, *Dynamical symmetry breaking and universality breakdown*, Nucl. Phys. B **337** (1990) 269–283.

[74] E. Malkawi and C.-P. Yuan, *Global analysis of the top quark couplings to gauge bosons*, Phys. Rev. D **50** (1994) 4462–4477.

[75] W. Wagner, *Top quark physics in hadron collisions*, Rep. Prog. Phys. **68** (2005), arXiv:`hep-ph/0507207v2 [hep-ph]`.

[76] M. Luke and M. J. Savage, *Flavour changing neutral currents, weak-scale scalars and rare top decays*, Phys. Lett. B **307** (1993) 387–393.

[77] S. Béjar, J. Guasch and J. Solà, *Loop induced flavor changing neutral decays of the top quark in a general two-Higgs-doublet model*, Nucl. Phys. B **600** (2001) 21–38.

[78] W.-S. Hou, *Tree level $t \to ch^0$ or $h^0 \to t\bar{c}$ decays*, Phys. Lett. B **296** (1992) 179–184.

[79] J. A. Aguilar-Saavedra, *Effects of mixing with quark singlets*, Phys. Rev. D **67** (2003) 035003.

[80] D. Delépine and S. Khalil, *Top flavour violating decays in general supersymmetric models*, Phys. Lett. B **599** (2004) 62–74.

[81] J. J. Liu et al., *via SUSY FCNC couplings in the unconstrained MSSM*, Phys. Lett. B **599** (2004) 92–101.

[82] J. J. Cao et al., *Supersymmetry-induced flavor-changing neutral-current top-quark processes at the CERN Large Hadron Collider*, Phys. Rev. D **75** (2007) 075021.

[83] J. M. Yang, B.-L. Young and X. Zhang, *Flavor-changing top quark decays in R-parity-violating supersymmetric models*, Phys. Rev. D **58** (1998) 055001.

[84] J. Guasch et al., *Single top-quark production by direct supersymmetric flavor-changing neutral-current interactions at the LHC*, Application of Quantum Field Theory to Phenomenology - Radcor 2005. Proceedings of the 7th International Symposium on Radiative Corrections, vol. **157**, (2006) 152–156.

[85] G. Lu et al., *Rare top quark decays $t \to cV$ in the top-color-assisted technicolor model*, Phys. Rev. D **68** (2003) 015002.

[86] A. Arhrib et al., *Single top quark production in flavor-changing Z' models*, Phys. Rev. D **73** (2006) 075015, arXiv:hep-ph/0602175v2 [hep-ph].

[87] E. Nardi, *Z', new fermions, and flavor-changing processes: Constraints on E_6 models from $\mu \to eee$*, Phys. Rev. D **48** (1993) 1240–1247.

[88] K. S. Babu, C. Kolda and J. March-Russell, *Implications of generalized $Z - Z'$ mixing*, Phys. Rev. D **57** (1998) 6788–6792.

[89] K. Leroux and D. London, *Flavour-changing neutral currents and leptophobic Z' gauge bosons*, Phys. Lett. B **526** (2002) 97–103.

[90] P. Langacker and M. Plümacher, *Flavor changing effects in theories with a heavy Z' boson with family nonuniversal couplings*, Phys. Rev. D **62** (2000) 013006.

[91] V. Barger et al., *Z' mediated flavor changing neutral currents in B meson decays*, Phys. Lett. B **580** (2004) 186–196.

[92] V. Barger et al., *$B_s - \bar{B}_s$ mixing in models with flavor-changing neutral currents*, Phys. Lett. B **596** (2004) 229–239.

[93] V. Barger et al., *Solution to the puzzle in a flavor-changing model*, Phys. Lett. B **598** (2004) 218–226.

[94] R. S. Chivukula, E. H. Simmons and J. Terning, *Limits on noncommuting extended technicolor*, Phys. Rev. D **53** (1996) 5258–5267.

[95] D. B. Kaplan and H. Georgi, *SU(2) × U(1) breaking by vacuum misalignment*, Phys. Lett. B **136** (1984) 183–186.

[96]   H. Georgi and D. B. Kaplan, *Composite Higgs and custodial SU(2)*, Phys. Lett. B **145** (1984) 216–220.

[97]   J. Ruppert et al., *Partonic scattering cross sections in the QCD medium*, Phys. Lett. B **520** (2001) 233–242.

[98]   D. E. Kaplan and M. Schmaltz, *The little Higgs from a simple group*, JHEP **0310** (2003) 039.

[99]   M. Schmaltz and D. Tucker-Smith, *Little Higgs theories*, Annual Review of Nuclear and Particle Science **55** (2005) 229–270.

[100] P. Batra et al., *The Higgs mass bound in gauge extensions of the minimal supersymmetric standard model*, JHEP **0402** (2004) 043.

[101] E. Boos et al., *Interference between and W in single-top quark production processesi*, Phys. Lett. B **655** (2007) 245–250, arXiv:hep-ph/0610080v3 [hep-ph].

[102] C.-X. Yue, Y.-P. Kuang and G.-R. Lu, *Corrections to the $W\bar{t}b$ coupling in the top-color-assisted multiscale technicolor model*, Phys. Rev. D **56** (1997) 291–294.

[103] H.-J. He and C.-P. Yuan, *New Method for Detecting Charged Scalars at Colliders*, Phys. Rev. Lett. **83** (1999) 28–31.

[104] J. Cao, Z. Xiong and J. M. Yang, *Probing top-color-assisted technicolor from top-charm associated production at the CERN Large Hadron Collider*, Phys. Rev. D **67** (2003) 071701.

[105] ATLAS Collaboration, *ATLAS inner detector: Technical Design Report, 1*, Technical Design Report ATLAS,   CERN-LHCC-97-016, Geneva: CERN, (1997).

[106] ATLAS Collaboration, *ATLAS inner detector: Technical Design Report, 2*, Technical Design Report ATLAS,   CERN-LHCC-97-017, Geneva: CERN, (1997).

[107] ATLAS Collaboration, *The silicon microstrip sensors of the ATLAS semiconductor tracker*, NIM A **578** (2007) 98–118.

[108] ATLAS Collaboration, *The ATLAS Transition Radiation Tracker (TRT) proportional drift tube: design and performance*, JINST **3** (2008) P02013.

[109] ATLAS Collaboration, *ATLAS liquid-argon calorimeter: Technical Design Report*, Technical Design Report ATLAS,   CERN-LHCC-96-041, Geneva: CERN, (1996).

[110] ATLAS Collaboration, *ATLAS tile calorimeter: Technical Design Report*, Technical Design Report ATLAS,   CERN-LHCC-96-042, Geneva: CERN, (1996).

[111] ATLAS Collaboration, *ATLAS muon spectrometer: Technical Design Report*, Technical Design Report ATLAS,   CERN-LHCC-97-022, Geneva: CERN, (1997).

[112] ATLAS Collaboration, *ATLAS magnet system: Technical Design Report, 1*, Technical Design Report ATLAS,   CERN-LHCC-97-018, Geneva: CERN, (1997).

[113] A. Yamamoto et al., *The ATLAS central solenoid*, rm NIM A **584** (2008) 53–74.

[114] ATLAS Collaboration, *ATLAS central solenoid: Technical Design Report*, Technical Design Report ATLAS,   CERN-LHCC-97-021, Geneva: CERN, (1997).

[115] J. P. Badiou et al., *ATLAS barrel toroid: Technical Design Report*, Technical Design Report ATLAS,   CERN-LHCC-97-019, Geneva: CERN, (1997).

[116] ATLAS Collaboration, *ATLAS end-cap toroids: Technical Design Report*, Technical Design Report ATLAS, CERN-LHCC-97-020, Geneva: CERN, (1997).

[117] H. H. J. ten Kate, *The ATLAS superconducting magnet system at the Large Hadron Collider*, Physica C: Superconductivity **468** (2008) 2137–2142.

[118] ATLAS Collaboration, *ATLAS pixel detector electronics and sensors*, JINST **3** (2008) P07007.

[119] F. Campabadal et al., *Beam tests of ATLAS SCT silicon strip detector modules*, NIM A **538** (2005) 384–407.

[120] B. Aubert et al., *Construction, assembly and tests of the ATLAS electromagnetic barrel calorimeter*, NIM A **558** (2006) 388–418.

[121] ATLAS Hadronic End-Cap Calorimeter Group et al., *Construction, assembly and testing of the ATLAS hadronic end-cap calorimeter*, JINST **3** (2007) P05005.

[122] ATLAS Forward Calorimeter Group et al., *The ATLAS Forward Calorimeter*, JINST **3** (2008) P02010.

[123] J. Wotschack, *ATLAS Muon Chamber Construction Parameters for CSC, MDT, and RPC chambers*, ATL-MUON-PUB-2008-006, CERN, (2008).

[124] R. Avramidou et al., *The accuracy of the ATLAS muon X-ray tomograph*, NIM A **496** (2003) 83–101.

[125] H. von der Schmitt et al., *A configuration system for the ATLAS trigger*, JINST **1** (2006) P05004, arXiv:`physics.ins-det/0602180v1 [physics.ins-det]`.

[126] M. Abolins et al., *The ATLAS Trigger: Commissioning with cosmic rays*, 022014, 2008.

[127] ATLAS Collaboration, *ATLAS high-level trigger, data-acquisition and controls: Technical Design Report*, Technical Design Report ATLAS, CERN-LHCC-2003-022, Geneva: CERN, (2003).

[128] M. Abolins et al., *Integration of the Trigger and Data Acquisition Systems in ATLAS*, tech. rep. 022001, 2008.

[129] ATLAS Collaboration, *Data-Quality Requirements and Event Cleaning for Jets and Missing Transverse Energy Reconstruction with the ATLAS Detector in Proton-Proton Collisions at a Center-of-Mass Energy of sqrts = 7 TeV*, ATLAS-CONF-2010-038, CERN, (2010).

[130] ATLAS Collaboration, *Updated Luminosity Determination in pp Collisions at root(s)=7 TeV using the ATLAS Detector*, ATLAS-CONF-2011-011, CERN, (2011).

[131] ATLAS Collaboration, *The ATLAS Simulation Infrastructure*, Eur. Phys. J. C **70** (2010) 823–874, arXiv:`physics.ins-det/1005.4568 [physics.ins-det]`.

[132] ATLAS Collaboration, *Atlas Computing: technical design report*, CERN-LHCC-2005-022, Geneva: CERN, (2005).

[133] M. Dobbs and J. B. Hansen, *The HepMC C++ Monte Carlo event record for High Energy Physics*, Comput. Phys. Commun. **134** (2001) 41–46.

[134] S. Agostinelli et al., *Geant4-a simulation toolkit*, NIM A **506** (2003) 250–303.

[135] J. Boudreau and V. Tsulaia, *The GeoModel Toolkit for Detector Description*, Computing in High Energy Physics and Nuclear Physics 2004, Geneva: CERN, (2005) 353.

[136] T. Kittelmann et al., *The Virtual Point 1 event display for the ATLAS experiment*, J. Phys.: Conf. Ser. **219**. 032012 (2008).

[137] S. Gadomski, *Model of the SCT detectors and electronics for the ATLAS simulation using Geant4*, ATL-SOFT-2001-005, CERN, (2001).

[138] W. Lampl et al., *Digitization of LAr calorimeter for CSC simulations*, ATL-LARG-PUB-2007-011, CERN, (2007).

[139] D. Rebuzzi et al., *Geant4 Muon Digitization in the ATHENA Framework*, ATL-SOFT-PUB-2007-001, CERN, (2007).

[140] V. Boisvert et al., *Final Report of the ATLAS Reconstruction Task Force*, ATL-SOFT-2003-010, CERN, (2003).

[141] S. Armstrong et al., *Architecture of the ATLAS High Level Trigger Event Selection Software*, NIM A **518** (2004) 537–541.

[142] E. Obreshkov et al., *Organization and management of ATLAS offline software releases*, NIM A **584** (2008) 244–251.

[143] G. Marchesini et al., *HERWIG 5.1 - a Monte Carlo event generator for simulating hadron emission reactions with interfering gluons*, Comput. Phys. Commun. **67** (1992) 465–508.

[144] G. Corcella et al., *HERWIG 6: An Event generator for hadron emission reactions with interfering gluons (including supersymmetric processes)*, JHEP **0101** (2001) 010, arXiv:`hep-ph/0011363 [hep-ph]`.

[145] G. Corcella et al., *HERWIG 6.5 Release Note*, CERN-TH-2002-270, CERN, (2002).

[146] T. Sjöstrand, S. Mrenna and P. Skands, *PYTHIA 6.4 Physics and Manual*, JHEP **0605** (2006) 026, arXiv:`hep-ph/0603175 [hep-ph]`.

[147] ATLAS Collaboration, *ATLAS Monte Carlo tunes for MC09*, ATL-PHYS-PUB-2010-002, CERN, (2010).

[148] S. Frixione and B. R. Webber, *Matching NLO QCD computations and parton shower simulations*, JHEP **0206** (2002) 029, arXiv:`hep-ph/0204244 [hep-ph]`.

[149] S. Frixione, P. Nason and B. R. Webber, *Matching NLO QCD and parton showers in heavy flavor production*, JHEP **0308** (2003) 007, arXiv:`hep-ph/0305252 [hep-ph]`.

[150] S. Frixione et al., *Single-top production in MC@NLO*, JHEP **0603** (2006) 092, arXiv:`hep-ph/0512250 [hep-ph]`.

[151] S. Frixione et al., *Single-top hadroproduction in association with a W boson*, JHEP **0807** (2008) 029, arXiv:`hep-ph/0805.3067 [hep-ph]`.

[152] J. Pumplin et al., *New generation of parton distributions with uncertainties from global QCD analysis*, JHEP **0207** (2002) 012, arXiv:`hep-ph/0201195 [hep-ph]`.

[153] B. P. Kersevan and E. Richter-Was, *The Monte Carlo event generator AcerMC version 2.0 with interfaces to PYTHIA 6.2 and HERWIG 6.5* (2004), arXiv:`hep-ph/0405247 [hep-ph]`.

[154] M. L. Mangano et al., *ALPGEN, a generator for hard multiparton processes in hadronic collisions*, JHEP **0307** (2003) 001, arXiv:`hep-ph/0206293 [hep-ph]`.

[155] ATLAS Collaboration, *Expected Performance of the ATLAS Experiment - Detector, Trigger and Physics* (2009), arXiv:`hep-ex/0901.0512 [hep-ex]`.

[156] ATLAS Collaboration, *Electron performance measurements with the ATLAS detector using the 2010 LHC proton-proton collision data*, Eur. Phys. J. C **72** (2012) 1909, arXiv:hep-ex/1110.3174 [hep-ex].

[157] ATLAS Collaboration, *Expected electron performance in the ATLAS experiment*, ATL-PHYS-PUB-2011-006, CERN, (2011).

[158] W. Lampl et al., *Calorimeter Clustering Algorithms: Description and Performance*, ATL-LARG-PUB-2008-002, CERN, (2008).

[159] E. Abat et al., *Combined performance studies for electrons at the 2004 ATLAS combined test-beam*, JINST **5** (2010) 11006.

[160] M. Aharrouche et al., *Energy linearity and resolution of the ATLAS electromagnetic barrel calorimeter in an electron test-beam*, NIM A **568** (2006) 601–623.

[161] M. Aharrouche et al., *Response uniformity of the ATLAS liquid argon electromagnetic calorimeter*, NIM A **582** (2007) 429–455.

[162] M. Aharrouche et al., *Measurement of the response of the ATLAS liquid argon barrel calorimeter to electrons at the 2004 combined test-beam*, NIM A **614** (2010) 400–432.

[163] D0 Collaboration, *Measurement of the shape of the boson rapidity distribution for $p\bar{p} \rightarrow Z/gamma^* \rightarrow e^+e^- + X$ events produced at $\sqrt{s}$ of 1.96 TeV*, Phys. Rev. D **76** (2007) 012003, arXiv:hep-ex/0702025 [hep-ex].

[164] ATLAS Collaboration, *Muon reconstruction efficiency in reprocessed 2010 LHC proton-proton collision data recorded with the ATLAS detector*, ATLAS-CONF-2011-063, CERN, (2011).

[165] ATLAS Collaboration, *Determination of the muon reconstruction efficiency in ATLAS at the Z resonance in proton-proton collisons at $\sqrt{s}$=7 TeV*, ATLAS-CONF-2011-008, CERN, (2011).

[166] M. Cacciari, G. P. Salam and G. Soyez, *The Anti-k(t) jet clustering algorithm*, JHEP **0804** (2008) 063, arXiv:hep-ph/0802.1189 [hep-ph].

[167] C. Cojocaru et al., *Hadronic calibration of the ATLAS liquid argon end-cap calorimeter in the pseudorapidity region in beam tests*, NIM A **531** (2004) 481–514.

[168] E. Abat et al., *Study of energy response and resolution of the ATLAS barrel calorimeter to hadrons of energies from 20-GeV to 350-GeV*, NIM A **621** (2010) 134–150.

[169] ATLAS Collaboration, *Jet energy measurement with the ATLAS detector in proton-proton collisions at $\sqrt{s}$ = 7 TeV* (2011), arXiv:hep-ex/1112.6426 [hep-ex].

[170] ATLAS Collaboration, *Performance of missing transverse momentum reconstruction in proton-proton collisions at $\sqrt{s}$ = 7 TeV with ATLAS*, Eur. Phys. J. C **72** (2012) 1–35.

[171] ATLAS Collaboration, *Searches for Single Top-Quark Production with the ATLAS Detector in pp Collisions at $\sqrt{s}$ = 7 TeV*, ATLAS-CONF-2011-027, CERN, (2011).

[172] R. Brun and F. Rademakers, *ROOT: An object oriented data analysis framework*, NIM A **389** (1997) 81–86, URL: http://root.cern.ch.

[173] A. Martin et al., *Parton distributions for the LHC*, Eur. Phys. J. C **63** (2009) 189–285, arXiv:arXiv/0901.0002 [hep-ph].

[174] R. D. Ball et al., *A first unbiased global NLO determination of parton distributions and their uncertainties*, Nucl. Phys. B **838** (2010) 136–206, arXiv:`hep-ph/1002.4407` `[hep-ph]`.

[175] G. Khoriauli, *Study of Systematic Uncertainties of Single Top Production at ATLAS*, Nuovo Cim. B **123** (2008) 1327–1330, arXiv:`hep-ex/0808.2568 [hep-ex]`.

[176] G. Cowan, *Statistical Data Analysis*, ISBN 0-19-850155-2, New York: Oxford University Press, (1998).

[177] A. Wald, *Tests of Statistical Hypotheses Concerning Several Parameters When the Number of Observations is Large*, Transactions of the American Mathematical Society **54** (1943) 426–482.

[178] G. Cowan et al., *Asymptotic formulae for likelihood-based tests of new physics*, Eur. Phys. J. C **71** (2011) 1–19, arXiv:`physics.data-an/1007.1727 [physics.data-an]`.

[179] F. James, *Statistical Methods in Experimental Physics*, ISBN 10-981-270-527-9, Singapore: World Scientific, (2008).

[180] A.G. Frodesen and O. Skjeggestad and H. Tøfte, *Probability and Statistics in Particle Physics*, ISBN 8200019063, Oslo: Universitetsforlaget, (1979).

[181] F. Porter, *Interval estimation using the likelihood function*, NIM A **368** (1996) 793–803.

[182] A. L. Read, *Presentation of search results: The CL_s technique*, J. Phys. G **28** (2002) 2693–2704.

[183] W. Verkerke and D. Kirkby, *The RooFit toolkit for data modeling* (2003), arXiv:`physics.data-an/0306116 [physics.data-an]`.

[184] L. Moneta and et al., *The RooStats Project* (2010), arXiv:`physics.data-an/1009.1003 [physics.data-an]`.

[185] F. James and M. Roos, *Minuit: A System for Function Minimization and Analysis of the Parameter Errors and Correlations*, Comput. Phys. Commun. **10** (1975) 343–367.

[186] CMS Collaboration, *Measurement of the t-Channel Single Top Quark Production Cross Section in pp Collisions at $\sqrt{s} = 7$ TeV*, Phys. Rev. Lett. **107** (2011) 091802.

[187] B. W. Harris et al., *Fully differential single-top-quark cross section in next-to-leading order QCD*, Phys. Rev. D **66** (2002) 054024.

[188] N. Kidonakis, *Higher-order corrections to top-antitop pair and single top quark production* (2009), arXiv:`arXiv/0909.0037 [hep-ph]`.

[189] D0 Collaboration, *odel-independent measurement of t-channel single top quark production in collisions at*, Phys. Lett. B **705** (2011) 313–319.

[190] CDF Collaboration, *Measurement of Single Top Quark Production in 7.5 fb^{-1} of CDF Data Using Neural Networks*, CDF/PUB/TOP/PUBLIC/10793, FNAL, (2012).